


INDUSTRIAL APPLICATIONS OF PLASMA SYSTEMS



by  
Tuba Şen

Submitted to Graduate School of Natural and Applied Sciences  
in Partial Fulfillment of the Requirements  
for the Degree of Doctor of Philosophy in  
Physics

Yeditepe University  
2016

## INDUSTRIAL APPLICATIONS OF PLASMA SYSTEMS

APPROVED BY:

Prof. Dr. Necdet Aslan  
(Thesis Supervisor)

  
.....

Prof. Dr. Gürcan Oraltay

  
.....

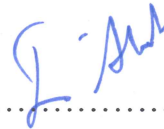
Prof. Dr. Uğur Yahşi

  
.....

Assoc. Prof. Dr. Sinan Keskin

  
.....

Assist. Prof. Dr. Ercüment Akat

  
.....

DATE OF APPROVAL: ....../....../2016

## ACKNOWLEDGEMENTS

I would like to thank a lot of people for their contributions to my thesis.

Firstly, I would like to thank my PhD supervisor Professor Doctor Necdet Aslan who supports me from start to finish and directs on each aspect of my thesis.

I would also like to thank Professor Gürcan Oraltay in Marmara University for his advice and help to my thesis.

I thank Dr. Kenan Şentürk, Research Assistants Melda Patan Alper, Mehmet Torun, Ergun Eray Akkaya, Damla Bulut, Berç Deruni and İsmail Şişman, and PhD student Turgay Çoruhlu.

Dr. Ercüment Akat for giving of his own time to proof my thesis, I would like to thank a lot.

And finally my parents, my sisters Nefise and Neslihan Şen; my little nephew Ahmet Kırayt for their support.

This thesis is dedicated to my dear sister Ayşe Şen which passed away in the 1st October 2011.

## ABSTRACT

### INDUSTRIAL APPLICATIONS OF PLASMA SYSTEMS

This thesis is concerned with some of the applications of magnetron sputtering system. Electron temperatures at different pressures and at different distances from cathode to anode were calculated by using Langmuir probe system. Optical emission spectroscopy was also used to calculate electron temperatures. The resistances on the deposited textiles were measured by using multimeter. Scanning electron microscopy, electron dispersive spectroscopy, and atomic force microscopy methods were used to investigate deposited materials; optical emission spectroscopy was used to investigate the reflectivity of the metals. Contact angle measurements were done by a goniometer. Contact angles before and after abrasion test were measured by the help of this system. Thus, wettability of the textiles was determined. In addition to this, antibacterial properties of the textiles were studied, and it was seen that silver coated textiles were more antibacterial than copper coated textiles. Both silver and copper coated textiles were more effective toward *E. coli* than *S. aureus*. Reflectivity of the metals were also studied by using optical emission spectroscopy.



## ÖZET

### PLAZMA SİSTEMLERİNİN ENDÜSTRİYEL UYGULAMA ALANLARI

Bu tezde magnetron sıçratıcı sistemin bazı uygulama alanları ele alınmıştır. Langmuir probu kullanılarak farklı basınçlarda ve katottan anoda doğru farklı mesafelerde electron sıcaklığı hesaplandı. Electron sıcaklığı hesaplanmasında optik emisyon spektroskopisinden de yararlanıldı. Multimetre kullanarak kaplanmış kumaşlarda direnç hesaplandı. Kaplanmış malzemeleri incelemek için taramalı elektron mikroskobu, elektron dağıtıcı spektroskopi ve atomik kuvvet mikroskopisinden yararlanıldı. Temas açısı ölçümü için gonyometre kullanıldı. Bu system vasıtasıyla aşındırmadan önce ve sonraki temas açıları ölçüldü. Buna ek olarak, kumaşların antibakteriyel özellikleri incelendi ve gümüşle kaplanan kumaşların bakırla kaplanana göre daha antibakteriyel olduğu gözlemlendi. Gümüş ve bakır kaplı kumaşların her ikisi de *E. coli* bakterisine *S. aureus* bakterisinden daha etkiliydi. Metallerin yansıtıcılığı da optik emisyon spektroskopisi aracılığıyla ölçüldü.

## TABLE OF CONTENTS

ACKNOWLEDGEMENTS.....	iii
ABSTRACT.....	iv
ÖZET .....	v
LIST OF FIGURES .....	xi
LIST OF TABLES.....	xix
LIST OF SYMBOLS ABBREVIATIONS.....	xxi
1. INTRODUCTION .....	1
1.1. NANOTECHNOLOGY.....	1
1.2. WHAT IS PLASMA.....	2
1.3. HISTORY OF PLASMA .....	3
1.4. HISTORY OF ELECTRICAL DISCHARGES.....	5
1.5. IMPORTANCE OF INDUSTRIAL PLASMA APPLICATIONS.....	8
2. PHYSICS OF PLASMA.....	10
2.1. ELECTRON AND ION TEMPERATURES.....	10
2.2. PLASMA POTENTIAL AND SHEATH AT A FLOATING SUBSTRATE .....	15
2.3. DEBYE SHIELDING .....	20
2.4. SHEATH FORMATION AND THE BOHM CRITERION .....	24
2.5. THE DEPENDENCE OF THE ELECTRON TEMPERATURE TO THE PRESSURE.....	29
3. DC GLOW DISCHARGES.....	37
3.1. THE DISCHARGE .....	37
3.2. EMISSION OF SECONDARY ELECTRONS .....	39
3.3. THE CATHODE REGION .....	39
3.3.1. Ionization in the Sheath.....	40
3.3.1.1. Electron Impact Ionization.....	40
3.3.1.2. Ion Impact Ionization .....	41
3.3.1.3. Sheath Ionization .....	42

3.3.2.	Exchange of Charge in the Sheath .....	42
3.4.	ANODE REGION.....	42
3.4.1.	Anode Sheath .....	42
3.4.2.	Secondary Electron Emission .....	43
3.4.3.	Polarity of Anode Sheath.....	43
3.4.4.	Main Effects in the Anode Region .....	43
3.5.	THE GLOW REGION .....	44
3.5.1.	Electrons in the Glow Region .....	44
3.5.2.	Ionization in the Negative Glow .....	44
4.	SPUTTERING .....	45
4.1.	INTERACTIONS OF IONS WITH SURFACES.....	45
4.2.	APPLICATIONS OF SPUTTERING.....	46
4.2.1.	Sputter Etching.....	46
4.2.2.	Sputter Deposition .....	46
4.3.	LIMITATIONS OF SPUTTERING .....	47
4.4.	A CONVENTIONAL DC SPUTTERING SYSTEM.....	47
4.4.1.	Choosing the Sputtering Gas .....	49
4.4.2.	Choosing the Sputtering Gas Pressure.....	49
4.4.3.	Choosing Electrical Conditions for the Glow Discharge.....	50
4.5.	DEPOSITION OF INSULATORS .....	51
4.5.1.	RF Sputtering .....	51
4.5.2.	Reactive Sputtering.....	52
4.6.	SPUTTERING SYSTEMS .....	52
4.6.1.	Ground Shields .....	52
4.6.2.	Shutters .....	52
4.6.3.	Target Cooling .....	53
4.6.4.	Substrate Temperature Control.....	53
4.6.5.	Electrode Voltage Measurement.....	54
4.7.	DEPOSITION WITH SPUTTERING METHOD .....	55
4.7.1.	Thin Film Formation.....	55
4.7.2.	The Nature of the Substrate .....	56
4.7.2.1.	Sputtered Atoms and Contaminants.....	57

4.7.2.2.	Sputtering Gas Atoms .....	57
4.7.2.3.	Excited Neutrals .....	58
4.7.2.4.	Positive Ions .....	58
4.7.2.5.	Negative Ions .....	58
4.7.2.6.	Electrons.....	58
4.7.2.7.	Photons .....	59
4.8.	RADIATION DAMAGE .....	59
4.9.	BIAS TECHNIQUES.....	59
4.10.	DEPOSITION OF MULTICOMPONENT FILMS.....	60
4.11.	THIN FILM ADHESION .....	60
5.	MAGNETICALLY ENHANCED SPUTTERING SYSTEMS .....	61
5.1.	MAGNETIC FIELDS .....	62
5.1.1.	Axial Magnetic Fields.....	63
5.1.2.	Magnetron Fields .....	64
5.2.	MAGNETRONS .....	69
5.3.	MAGNETRON SPUTTERING SYSTEM.....	70
6.	DIAGNOSTICS OF LANGMUIR PROBE .....	72
6.1.	PROBE CHARACTERISTICS .....	72
6.2.	APPLICATION OF LANGMUIR PROBE METHOD TO FIND ELECTRON AND ION TEMPERATURE.....	74
7.	OPTICAL EMISSION SPECTROSCOPY .....	80
8.	BOLTZMANN PLOT FOR TEMPERATURE .....	82
9.	SEM ANALYSIS .....	88
10.	ENERGY-DISPERSIVE X-RAY SPECTROSCOPY (EDS) .....	90
11.	ATOMIC FORCE MICROSCOPY .....	91
12.	CONTACT ANGLE MEASUREMENT .....	92
13.	ANTIBACTERIAL TESTS .....	94
14.	RESULTS AND DISCUSSION.....	96
14.1.	ELECTRICAL PROPERTIES OF PLASMA SYSTEMS .....	96

14.1.1.	Hysterisis.....	96
14.1.2.	Langmuir Probe Results.....	100
14.1.2.1.	The Change of Electron Temperature with Pressure .....	100
14.1.2.2.	The Change of Electron Temperature from Cathode to Anode ....	106
14.1.3.	Measurement of the Electron Temperature by Boltzman Method.....	112
14.2.	INVESTIGATION OF SURFACE PROPERTIES OF DEPOSITED TEXTILES WITH MAGNETRON SPUTTERING METHOD .....	120
14.2.1.	Coating Processes For Textiles .....	120
14.2.2.	SEM Results.....	121
14.2.3.	EDS Results .....	128
14.2.4.	Results of Wettability of The Surfaces .....	131
14.2.5.	The Measurement of the Resistance .....	133
14.2.6.	Antibacterial Textile Results.....	140
14.2.6.1.	Parallel Streak Method.....	140
14.2.6.1.1.	<i>Escherichia coli</i> Inactivation for the Cu Coated Textiles .....	141
14.2.6.1.2.	<i>Escherichia coli</i> Inactivation for the Ag Coated Textiles.....	142
14.2.6.1.3.	<i>Staphylococcus aureus</i> Inactivation for the Cu Coated Textiles .	144
14.2.6.1.4.	<i>Staphylococcus aureus</i> Inactivation for the Ag Coated Textiles .	145
14.2.6.1.5.	Results of Parallel Streak Method.....	146
14.2.6.2.	Suspension Test.....	146
14.2.6.2.1.	Procedure of Suspension Test .....	146
14.2.6.2.2.	Result of Suspension Test .....	147
14.3.	THE COMPARISON OF SURFACE CHARACTERISTICS OF TEXTILES (COTTON AND POLYESTER) COATED BY SILVER AND COPPER.....	148
14.3.1.	Antibacterial Activity.....	148
14.3.2.	Contact Angle Measurements .....	149
14.3.3.	Abrasion Tests.....	152
14.3.4.	Washing Tests .....	154
14.3.4.1.	Antibacterial Results .....	154
14.3.4.2.	Contact Angle Results.....	155
14.3.4.3.	Roughness Analysis of Washed Textiles .....	155

14.4. OPTICAL EMISSION SPECTROSCOPY OF GLASS, ALUMINIUM AND  
TEXTILE COATED WITH COPPER AND SILVER..... 158

15. CONCLUSION AND FUTURE WORK..... 166

REFERENCES ..... 170

APPENDIX A..... 174



## LIST OF FIGURES

Figure 1.1. Glow discharge plasma .....	2
Figure 1.2. The figure of Leyden jar.....	4
Figure 1.3. The figure of electric egg .....	6
Figure 1.4. The figure of Hittorf tube .....	6
Figure 1.5. An electrical discharge tube .....	7
Figure 1.6. The figure of railway tube .....	7
Figure 2.1. Electric field effect on an electron and on a positive ion .....	10
Figure 2.2. Potential energies of ions and electrons around a floating substrate.....	17
Figure 2.3. Sheat voltage in front of a floating substrate.....	18
Figure 2.4. Debye shielding.....	21
Figure 2.5. Change of potential around the perturbation.....	22
Figure 2.6. Change of potential close to a negative electrode .....	24
Figure 2.7. Momentum transfer on the wall of the container .....	29
Figure 2.8. The cross section of the wall .....	30
Figure 3.1. The normal glow discharge .....	38

Figure 3.2. Diagram of a discharge loss .....	40
Figure 4.1. Interaction of ions with target surface .....	45
Figure 4.2. Schematic diagram of a DC sputtering system .....	48
Figure 4.3. Schematics of the magnetron sputtering system with argon gas .....	49
Figure 4.4. Thin film formation .....	55
Figure 4.5. Particles which bombard a substrate .....	57
Figure 5.1. The cross product of electric field and magnetic field .....	61
Figure 5.2. Top view of magnetron sputtering system .....	61
Figure 5.3. The vacuum system with a mechanical and turbo pump .....	62
Figure 5.4. Helical motion of particle .....	64
Figure 5.5. An electron with nonzero magnetic field and zero electric field .....	65
Figure 5.6. An electron with nonzero magnetic field and nonzero electric field .....	65
Figure 5.7. Magnetron sputtering system in plasma laboratory .....	70
Figure 5.8. Schematic of the Yeditepe magnetron sputtering system .....	71
Figure 6.1. Current density versus voltage graph of a probe .....	73
Figure 6.2. Schematic diagram of Langmuir probe system .....	75
Figure 6.3. Langmuir probe in the plasma environment during sputtering process .....	76



Figure 6.4. The set up of our Langmuir probe measurement system.....	76
Figure 6.5. Typical current-voltage characteristics of Lagmuir probe .....	77
Figure 7. Diagram of optical emission spectroscopy.....	81
Figure 8.1. Energy level diagram of two level system .....	82
Figure 8.2. (a) Induced absorption, (b) Induced emission, (c) Spontaneous emission.....	83
Figure 9.1. Diagram of a scanning electron microscope .....	89
Figure 9.2. Electrons and X-rays which are ejected from the sample .....	89
Figure 11. Diagram of an atomic force microscopy .....	91
Figure 12. Contact angle measurement method.....	92
Figure 14.1. The graph of current versus voltage at $10^{-2}$ Torr with a content of 100% pure argon.....	98
Figure 14.2. The graph of current versus voltage at $10^{-2}$ Torr with a content of 80% argon and 20% air.....	98
Figure 14.3. The graph of current versus voltage at $10^{-2}$ Torr with a content of 50% argon and 50% air.....	99
Figure 14.4. The graph of current versus pressure at 400 V.....	100
Figure 14.5. Probe current versus voltage graph at $9 \times 10^{-3}$ Torr.....	102
Figure 14.6. $I_{\text{probe}} - I_{\text{sat}}$ versus voltage graph at $9 \times 10^{-3}$ Torr.....	102

Figure 14.7. $\ln(I_{\text{probe}}-I_{\text{sat}})$ versus voltage graph at $9 \times 10^{-3}$ Torr.....	103
Figure 14.8. $\ln(I_{\text{probe}}-I_{\text{sat}})$ versus voltage graph at $2 \times 10^{-2}$ Torr.....	104
Figure 14.9. $\ln(I_{\text{probe}}-I_{\text{sat}})$ versus voltage graph at $6 \times 10^{-2}$ Torr.....	104
Figure 14.10. The change of electron temperature with pressure.....	105
Figure 14.11. Langmuir probe method to measure electron temperature.....	106
Figure 14.12. Current versus voltage graph on the first probe at $2 \times 10^{-2}$ Torr.....	107
Figure 14.13. $I_{\text{probe}}-I_{\text{sat}}$ versus voltage graph on the first probe at $2 \times 10^{-2}$ Torr.....	108
Figure 14.14. $\ln(I_{\text{probe}}-I_{\text{sat}})$ versus voltage graph on the first probe at $2 \times 10^{-2}$ Torr.....	108
Figure 14.15. $\ln(I_{\text{probe}}-I_{\text{sat}})$ versus voltage graph on the fourth probe at $2 \times 10^{-2}$ Torr.....	109
Figure 14.16. $\ln(I_{\text{probe}}-I_{\text{sat}})$ versus voltage graph on the eight probe at $2 \times 10^{-2}$ Torr.....	110
Figure 14.17. The Graph of electron temperature from cathode to anode.....	111
Figure 14.18. Measurement of emission of plasma by using Baki spectroscopy in front of the window.....	112
Figure 14.19. Intensity versus wavelength at the voltages 300V, 400V and 500V.....	113
Figure 14.20. The webpage of the NIST.....	114
Figure 14.21. The values which were obtained from the website of the NIST.....	115
Figure 14.22. The graph of $\ln(I\lambda / gA)$ versus $E_k$ at 300 V.....	116

Figure 14.23. The graph of $\ln(I\lambda / gA)$ versus $E_k$ at 400 V.....	117
Figure 14.24. The graph of $\ln(I\lambda / gA)$ versus $E_k$ at 500 V.....	118
Figure 14.25. Electron temperature versus voltage .....	119
Figure 14.26. SEM images (a) coated polycotton fiber, (b) coated cotton fiber .....	122
Figure 14.27. SEM images of Cu coatings for 15 minutes.....	122
Figure 14.28. SEM images of Ag coatings for 8 minutes.....	123
Figure 14.29. The SEM images of the cotton fibers coated by copper (a) 90 magnification, (b) 200 magnification.....	123
Figure 14.30. The SEM images of the cotton fibers coated by copper, (a) 1000 magnification, (b) 2000 magnification.....	124
Figure 14.31. The SEM images of the cotton fibers coated by copper, (a) 5000 magnification, (b) 10000 magnification.....	124
Figure 14.32. The SEM images of the cotton fibers coated by copper (a) 25000 magnification, (b) 70000 magnification.....	125
Figure 14.33. SEM Picture of lateral view of the glass coated by copper .....	126
Figure 14.34. The diagram of the glass deposited by copper .....	127
Figure 14.35. SEM images of (a) Ag coatings for 4 minutes and (b) Ag coatings for 10 minutes.....	128

Figure 14.36. The results of EDS which were taken from a cotton textile coated by silver.....	129
Figure 14.37. The results of EDS of a cotton textile coated by silver and copper.....	130
Figure 14.38. The results of EDS which were taken from a glass coated by copper.....	131
Figure 14.39. The conditions of droplets after $t=0$ , $t=3$ and $t=5$ minutes on Ag coated polycotton samples.....	132
Figure 14.40. The conditions of droplets after $t=0$ , $t=2$ and $t=4$ minutes on Cu coated polycotton samples.....	132
Figure 14.41. SEM images of Ag coatings on polycotton for 4 minutes.....	134
Figure 14.42. The nonwoven fabric before and after coating by Ag and resistance measurement.....	135
Figure 14.43. Resistances of nonwoven textiles deposited by silver without surface treatment for 5 minutes at different lengths.....	135
Figure 14.44. Resistances of nonwoven textiles deposited by silver for 5 minutes with surface treatment at different lengths.....	136
Figure 14.45. Resistances of nonwoven textiles deposited by silver for 10 minutes without surface treatment at different lengths.....	136
Figure 14.46. Resistances of nonwoven textiles deposited by silver for 10 minutes with surface treatment at different lengths.....	137

Figure 14.47. Resistances of nonwoven textiles deposited by silver for 20 minutes without surface treatment at different lengths.....	137
Figure 14.48. Resistances of nonwoven textiles deposited by silver for 20 minutes with surface treatment at different lengths.....	138
Figure 14.49. <i>Escherichia coli</i> inactivation for (a) control sample, (b) Cu coated textile sample.....	141
Figure 14.50. <i>E. coli</i> control .....	141
Figure 14.51. <i>Escherichia coli</i> inactivation for (a) control sample, (b) Ag coated textile sample.....	143
Figure 14.52. <i>Staphylococcus aureus</i> inactivation for (a) control sample, (b) Cu coated textile sample.....	144
Figure 14.53. <i>Staphylococcus aureus</i> inactivation for (a) control sample, (b) Ag coated textile sample.....	145
Figure 14.54. The drop shape on (a) 1 min. silver deposited cotton, (b) 4 min. silver deposited cotton, (c) 10 min. silver deposited cotton.....	150
Figure 14.55. Contact angle measurements versus deposition times of silver on cotton ..	150
Figure 14.56. The drop shape on (a) 1 min. copper deposited cotton, (b) 4 min. copper deposited cotton, (c) 10 min. copper deposited cotton.....	151
Figure 14.57. Contact angle measurements versus deposition times of copper on cotton..	152
Figure 14.58. Contact angle measurement on 10 minutes silver coated cotton.....	153

Figure 14.59. Contact angles at different times, (a) 1 min. silver deposited cotton after abrasion, (b) 4 min. silver deposited cotton after abrasion, (c) 10 min. silver deposited cotton after abrasion.....	154
Figure 14.60. Afm analysis after 1 washing cycle.....	156
Figure 14.61. Afm analysis after 5 washing cycles .....	156
Figure 14.62. Afm analysis after 10 washing cycles .....	157
Figure 14.63. Measuring reflectivity by using optical emission spectroscopy.....	158
Figure 14.64. Diagram of measuring reflectivity .....	159
Figure 14.65. Intensity versus wavelength for single glass and copper coated glass .....	159
Figure 14.66. Intensity versus wavelength graph for single aluminium and copper coated aluminium.....	160
Figure 14.67. Intensity versus wavelength graph for single glass, 10 and 20 minutes silver coated aluminium.....	161
Figure 14.68. Intensity versus wavelength graph for single glass and 5, 10 and 20 minutes silver coated glasses.....	163
Figure 14.69. Intensity versus wavelength graph for single textile and 1, 4 and 10 minutes silver coated textiles.....	164
Figure 14.70. Intensity versus deposition time graph for 1, 4 and 10 min. silver coated textiles.....	165

## LIST OF TABLES

Table 14.1. The change of current values with voltage values at $9 \times 10^{-3}$ Torr.....	101
Table 14.2. Electron temperature calculated with respect to the pressure.....	105
Table 14.3. The change of current with voltage on first probe.....	107
Table 14.4. The change of electron temperature with the probe number .....	111
Table 14.5. The values calculated at 300 V .....	116
Table 14.6. The values calculated at 400 V .....	117
Table 14.7. The values calculated at 500 V .....	118
Table 14.8. The electron temperature change with respect to the voltage.....	119
Table 14.9. Deposition conditions for Ag and Cu .....	121
Table 14.10. The mass of the samples before and after deposition of copper .....	127
Table 14.11. The values of resistances with the time of deposition .....	139
Table 14.12. Measurement of the distance where <i>E. coli</i> move away from the both sides of textile coated by copper.....	142
Table 14.13. Measurement of the distance where <i>E. coli</i> move away from the both sides of textile coated by silver.....	143

Table 14.14. Measurement of the distance where <i>S. aureus</i> move away from the both sides of textile coated by copper.....	144
Table 14.15. Measurement of the distance where <i>S. aureus</i> move away from the both sides of textile coated by silver.....	145
Table 14.16. Colony forming units (cfu) at $10^{-7}$ dilution.....	147
Table 14.17. Typical deposition parameters for Ag and Cu coatings. ....	148
Table 14.18. The relationship between the roughness and the contact angle. ....	157



## LIST OF SYMBOLS/ABBREVIATIONS

$a$	Acceleration
$A$	Area
$A_1, A_2$	Normalization constants
$A_{21}, B_{12}, B_{21}$	Einstein coefficients
$B$	Magnetic field
$c$	Speed of light
$\bar{c}$	The average thermal velocity of neutral gas atoms
$\bar{c}_e$	The average thermal velocity of electrons
$\bar{c}_i$	The average thermal velocity of ions
$e$	Electron charge
$E$	Energy
$E$	Electric field
$f$	Distribution function
$F$	Force
$g$	Degeneracy
$h$	Planck constant
$j$	Current density
$I$	Intensity
$I_{\text{sat}}$	Saturation current
$I_{\text{probe}}$	Probe current
$k$	Boltzman constant
$K$	Kinetic energy
$L$	Length
$m$	Mass
$m_i$	Ion mass
$m_e$	Electron mass
$n$	Particle number density
$n_e$	Number density of electrons
$n_i$	Number density of ions
$N$	Number of particles

$p$	Momentum
$P$	Pressure
$q$	Charge
$S$	Sputtering yield
$t$	Time
$T$	Temperature
$T_e$	Electron temperature
$T_i$	Ion temperature
$v$	Speed
$\bar{v}$	Velocity
$V$	Potential
$V_f$	Floating potential
$V_p$	Plasma potential
$x$	Distance
$Z$	Partition function
$\epsilon_0$	Permittivity of plasma
$\Gamma$	Flux
$\lambda$	Wavelength
$\nu$	Frequency
$\omega$	Oscillation frequency
AFM	Atomic force microscopy
Aq	Silver
Cu	Copper
EDS	Electron diffraction spectroscopy
K	Kelvin
nm	Nanometer
SEM	Scanning electron microscopy

## **1. INTRODUCTION**

This thesis is concerned with the application of magnetron sputtering method in the vacuum coating technology to search the surface properties of coated materials such as textiles, metals and glasses. For diagnostics, Langmuir probe measurements were done to calculate electron temperature of the plasma at different pressures and at different distances. Optical emission spectroscopy of the plasma system was taken to find the electron temperature at different voltages by using the Boltzmann method. Contact angles were measured for the purpose of understanding whether the coated surfaces are hydrophilic or not. Abrasion tests were done and then hydrophobicity of textiles coated at different times was studied before and after abrasion tests. Whether the coated textile surfaces are antibacterial or not was shown by parallel streak method and suspension test. In addition to this, the light reflectivity of the substrates which were coated by different metals were studied by using optical emission spectroscopy. These tests will be shown by the results, conclusions and publications.

### **1.1. NANOTECHNOLOGY**

Richard Feynman was the first scientist who talked about nanotechnology and said “there is plenty of room at the bottom” in 1959 [1].

The structures which have dimensions between 1 and 100 nanometers are known as nanostructures. Nanoscience is the study of the main principles of these nanostructures. Application of the nanostructures into the nanoscale machines is called as nanotechnology. Nanotechnology has an interest to the characteristics of mechanical, chemical, quantum or physical structures on the nanoscale. The main characteristics of the materials are size dependence and their properties change at the nanoscale. This is an advantage to develop new structures with better properties. Everything such as the melting point and chemical properties change from the macro scale to the nanoscale. Because, the nature of the interactions among the atoms changes. Therefore, the properties of nanostructures are not the same as their bulk materials. Scientists and engineers are concerned with the

applications of these properties in the fabrication of new materials such as in the environment, industry or medicine [2].

## 1.2. WHAT IS PLASMA?

A plasma is a partially ionized gas with equal numbers of negative and positive charges and distinct number of unionized neutrals, which show collective behaviour. Ionization leads to the creation of an “ion-electron” pair and recombination leads to its removal. Due to the interactions among plasma species, the photons are also produced, so that the plasma can be made visible [3].

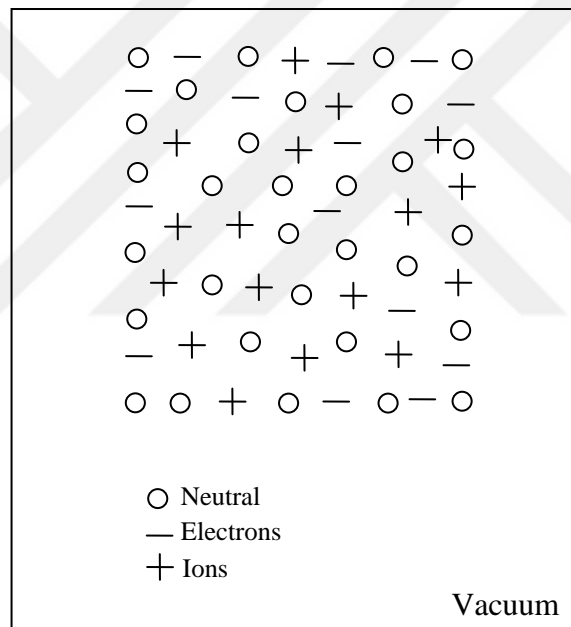


Figure 1.1. Glow discharge plasma

The crystal lattice structure of the atoms is perturbed by the thermal motion, if the solid is heated enough. A gas is created, if a liquid is heated adequately. In the gas cases, the atoms collide with each other and knock the electrons off when the gas is heated enough. As a conclusion, formation of a plasma, “the fourth state of the matter” is obtained. A plasma shows unique characteristics of being quasineutral and collective. The reason of why a plasma shows collective behaviour is as follows: although the forces between near-neighbour regions of the material determines the dynamics of the motion in most of the

materials, electric fields in the plasma is increased by the charge separation between the electrons and ions; magnetic fields and currents are increased by charged particle flows. The action of these fields results forces long distances [3]. The particle's motion is determined by the collision of the atoms and molecules with each other. Collisions help the transmissions of a macroscopic force applied to a neutral gas to the individual atoms. However, the situation is very different for the condition of plasma having charged particles. Local concentrations of positive and negative charge are created (as these charges move around) and they cause the increase of local electric fields. Currents and magnetic fields are also created by the motion of these charges. The motion of other charged particles is then influenced by these fields. A force is exerted by the elements of plasma even at larger distances. It is a long-ranged Coulomb force. Collective behaviour is also related with the motions depending on the state of plasma in remote regions in addition to the local conditions [4]. Quasineutral behaviour of the plasma will be described in Section 2.3.

A plasma can be obtained in different pressure conditions such as atmospheric or low pressure. DC, low-frequency, radio-frequency, or microwaves can be used in plasma applications as power. The general application of plasma technology is in textile or metal industry to obtain such as hydrophobic, hydrophilic, unscratchable, resistive or antibacterial materials [5].

### **1.3. HISTORY OF PLASMA**

The study of the plasma was initiated by Sir Humphry with the development of the steady-state DC discharge in 1808 and by Michael Faraday with the development of high voltage DC electrical discharge tube in 1830's.

The definition of the plasma made by Sir William Crookes in 1879 was "the fourth state of matter". If heat is added to solid matter which is at low temperature, it becomes a liquid by melting and a gas by vapourizing. If more heat is added, the temperature increases and fourth state of matter is produced by breaking apart the individual atoms into positively charged ions and electrons.

Irving Langmuir introduced the term of plasma in 1928: Electrically neutral collection of electrons and ions which does or does not contain a background neutral gas.

Sir William Gilbert introduced some of the basic concepts at the start of the 17th century. A primitive capacitor which was called as Leyden jar was invented by E G von Kleist in 1745, and it was shown in Figure 1.2. Thus, important amounts of charge were stored and high static electric potentials were obtained.

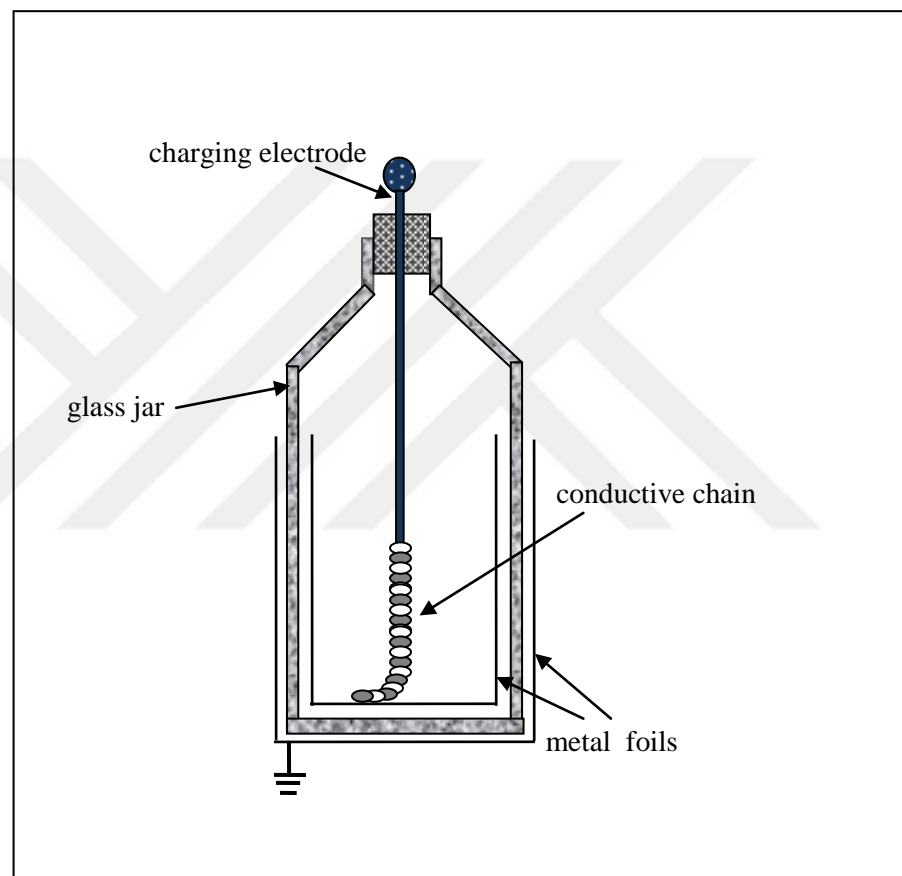


Figure 1.2. The figure of Leyden jar

Benjamin Franklin did some experiments to prove single fluid theory by using the Leyden jar and lightning was identified as a form of electricity. In addition to this, positive and negative polarity was explained by Franklin. A negative polarity implied a deficit of the electrical fluid, positive polarity implied an excess of the positive fluid in the single fluid theory.

Electrical discharge physics proceeded in the 19th century rapidly. Michael Faraday and Sir Humphry Davy worked on the electrical arcs and DC electrical discharge tubes at low pressure at the Royal Institution in London in the early 19th century.

G J Stoney introduced the term of electron in the year of 1891. According to him, electron was a massless, photon-like collection of charge. Sir Joseph John Thomson defined and observed the electron quantitatively in 1895. However, scientists suspected the existence of the electron for many years before 1895. Sir William Crookes defined the ionization as the break up of a neutral atom into a positive ion and an electron in 1898.

Irving Langmuir identified the sheath and the plasma in the 1920's. DC electrical and arc discharge plasmas were studied in details in 19th century. The magnetoionic theory was developed in the 1920's. It was a main theoretical progress in modern plasma physics. Commercial investigations on MHD power generators started in the USA in 1930's. Microwave technology for radar was developed in the years of Second World War. Then microwave discharges produced plasmas in the late 1940's. Fusion studies began in the main industrialized countries at the 1950's. Plasmas started to be used in the microelectronics industry for the etching and deposition processes in the 1970 [6].

#### **1.4. HISTORY OF ELECTRICAL DISCHARGES**

Many European physicists worked on the low pressure DC electrical discharges in gases in the 19th century. The effect of lowering the pressure on an electrical discharge was investigated in the electric egg in 1870. Paschen effect was used to prove by the Hittorf tube at 1884. Figure 1.4 shows the image of Hittorf tube. The discharge was created through the long tube at low pressures instead of the small gap between the electrodes. Fluorescence of the glass wall of the vacuum vessel was seen due to cathode rays, if an electrical discharge is created between two electrodes in an evacuated tube. J W Hittorf did one experiment about cathode rays in 1869. He showed that cathode rays travel in straight lines and left a shadow of the anode on the fluorescing glass surface.



Figure 1.3. The figure of electric egg [7]



Figure 1.4. The figure of Hittorf tube [8]



The travel of cathode rays was shown in an electrical discharge tube by Brown in 1978. The cathode rays which are in straight lines lead to the shadow of anode on the fluorescing glass.

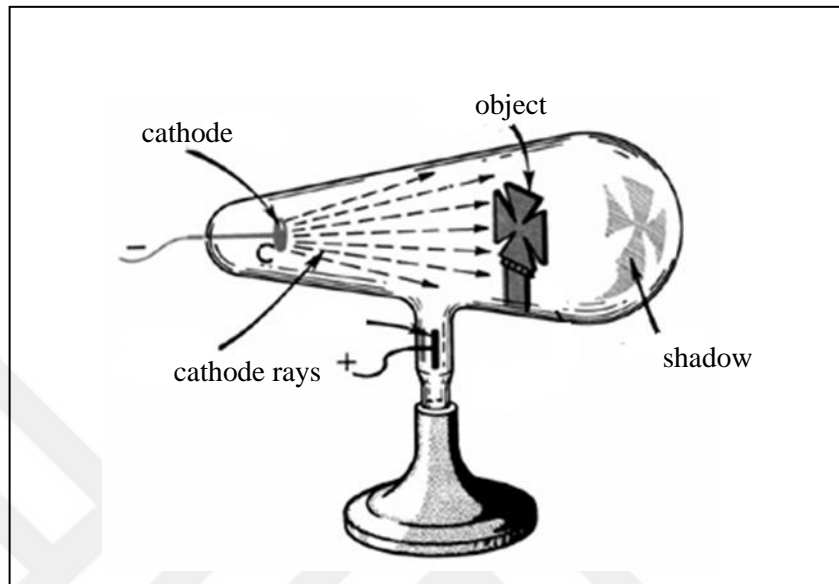


Figure 1.5. An electrical discharge tube [9]

W. Crookes showed the mechanical effects of cathode rays by the help of railway tube in 1879 as in Figure 1.6. Cathode rays emerging from the negative electrode hit the mica vanes of a small paddlewheel and it goes through the positive electrode of the tube.

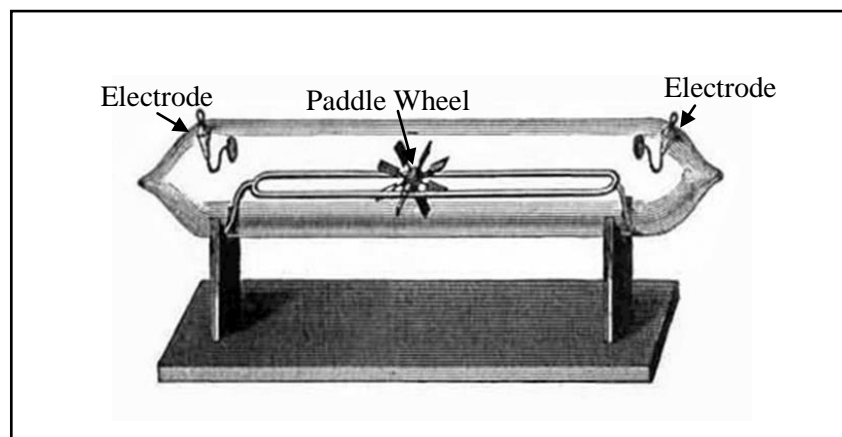


Figure 1.6. Figure of railway tube [10]

It was proved that cathode rays have heating effects by the help of a tube designed by G H Wiedemann. Cathode rays emerging from the concave cathode focused on a platinum foil, and an incandescence was seen on the foil.

Thomas Edison designed an electrical discharge tube in which a current is applied between an incandescent cathode filament and another metallic electrode in a glass envelope. There was a deflection of cathode rays by a magnetic and electric field. It is known as Edison effect.

Crookes designed a tube in 1895. Cathode rays were sent to the anode and travel through the glass wall of the tube. X-rays were emitted with an angle. Fluorescence of the minerals was seen. This design also helped Röntgen to investigate x-rays.

One of the significant progresses in the electrical discharges is the design of vacuum pumps. August Toepler decreased the pressure down to 1 mTorr in the mercury piston pump with a slow pumping speed at 1890's. German engineer Wolfgang Gaede designed the rotary mercury pump which decreases the pressure down to  $10^{-5}$  Torr in 1905. He also designed the mercury diffusion pump in 1911 and the modern rotary oil forepump in 1935 [6]. Then the modern technology helped for the development of diffusion and turbo molecular pumps which are currently being used to produce low pressure plasmas.

## **1.5. IMPORTANCE OF INDUSTRIAL PLASMA APPLICATIONS**

Industrial plasma applications are important to increase the efficiency of the main energy-consuming processes. Plasmas are preferable in the industry due to their two properties: Their *temperatures* and *energy densities* so different than chemical or other processes. In addition to this, active species are produced by plasmas. These species can initiate the chemical or physical changes which are created with difficulty in other methods. Charged particles such as ions, electrons and free electrons, highly reactive neutral species such as reactive atoms, excited atomic states and molecular fragments and ultraviolet or visible photons are examples of the active species.

The plasma has some advantages over other methods. It does not create too much unwanted byproducts or waste materials. It involves very low quantities of chemicals and

only uppermost atomic layers of materials are changed without interfering with its bulk properties. It accomplishes the results more cheaply and effectively than other processes [11]. In industry, low temperature plasma has already been used for the treatment of polymers and metals. The application of plasma on the deposition of textiles are more complicated due to their structures. However, nowadays, deposition of textiles by plasma method has a great interest [12]. The importance of plasma applications is highlighted in the following list:

- More effective energy use is established by plasma lighting devices such as fluorescent lamps.
- Production with minimal toxic wastes are plasma deposition and etching, plasma chemistry, ion implantation and plasma chemistry.
- Using the plasma, material surface modification and paint spraying can be established successfully.

Plasma physics is related with the basic laws and processes of the plasma. Electrohydrodynamics and magnetohydrodynamics are significant sub-areas of plasma physics. Electrohydrodynamics is related with the behaviour of electrically charged fluids or particles in electric fields and magnetohydrodynamics is related with the behaviour of electrically conducting fluids such as plasma in magnetic fields.

Plasma chemistry is related with the chemical reactions in the presence of a plasma. Only a plasma can be a participant or the components of a plasma or a plasma-chemical reaction products interact with solid surfaces or liquids in these kinds of chemical reactions [6].

## 2. PHYSICS OF PLASMA

### 2.1. ELECTRON AND ION TEMPERATURES

Excitation, relaxation, ionization and recombination are main processes that take place during the interactions among the plasma particles. An energy source is needed for these processes. Usually, this source is the electric or magnetic field which has direct effects on the charged particles.

If an electric field is applied, the energy is transferred from the electric field ( $\vec{E}$ ) to the electrons and ions as seen in Figure 2.1.

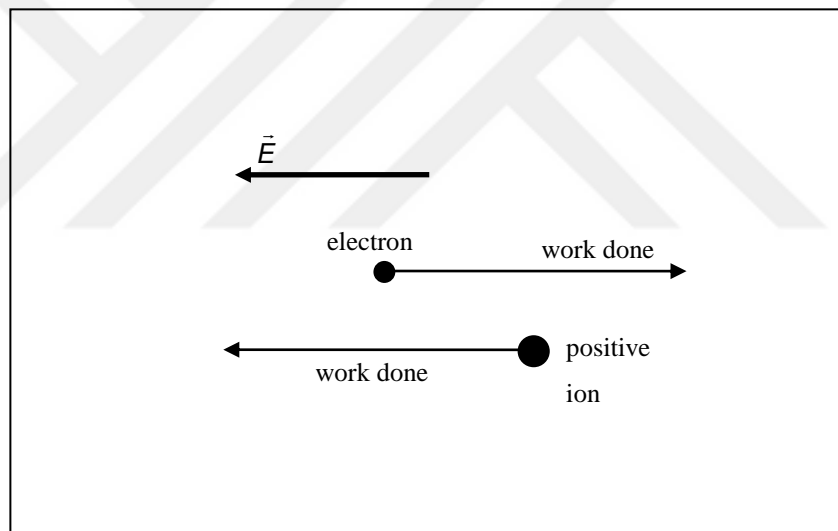


Figure 2.1. Effect of electric field on an electron and on a positive ion

If an electric field  $\vec{E}$  acts on an initially stationary ion particles of charge  $q$ , the work done by the electric field on the ion is  $q\vec{E}x$  where  $x$  is the distance travelled given by:

$$x = \frac{1}{2} at^2 \quad (2.1)$$

where  $t$  is the time and  $a$  is the acceleration. Thus the force,  $F$  on the charge  $q$  with a mass,  $m$  can be written as:

$$F = qE = ma . \quad (2.2)$$

So that the work done by the electric field is given by:

$$qEx = qE \frac{1}{2} \left( \frac{qE}{m} \right) t^2 = \frac{(qEt)^2}{2m} . \quad (2.3)$$

This relationship holds for both electrons and ions. However, the field primarily gives energy to the electrons, because  $m_e \leq m_i$ . Although the collisions were ignored in the equations above for simplicity, there are usually collisions in the plasma depending on the pressure and temperature.

When the electrons collide with ions and neutral atoms, there is a small energy transfer among them. The energy is shared by the neutral atoms and the ions efficiently in the collision processes and is lost to the walls of the chamber, when they hit.

Neutral molecules have an energy a little lower than that of ions. They obtain energy by collisions with the electrons (inefficiently) and ions (effectively) and mainly remain at room temperature.

For the neutral gas atoms, the average thermal energy is given by :

$$\frac{1}{2} m v_{av}^2 = \frac{3}{2} kT \quad (2.4)$$

where  $v_{av}$  is the average thermal velocity,  $k$  is Boltzmann constant and  $T$  is the temperature.

The concept of the temperature can also be applied to the electrons:

$$\frac{1}{2} m v_e^2 = \frac{3}{2} kT_e \quad (2.5)$$

where  $T_e$  is the effective temperature with the electron motion and  $v_e$  is the average electron velocity.

An average electron energy is around 2 eV ( $2 \times 11600$  K) in the glow discharge plasmas so that Eq. (2.5) produces an electron temperature of about  $2.32 \times 10^4$  K. Although this is a very high temperature, the vacuum vessel that keeps plasma electrons will not melt. Because the masses and heat capacity of the electrons are very small.

As in electrons, the ions can also receive energy from the external electric field, and for such plasmas, their temperatures may go up to 500 K which is above the room temperature of 300 K [3]. With these temperatures, cooling must be employed since ions are able to heat the vacuum chamber.

For a Maxwellian gas distributions, the root mean square and average velocities are given by  $v_{rms} = (3kT/m)^{1/2}$ ,  $\bar{v} = 2(2kT/\pi m)^{1/2}$ , and  $|\bar{v}_x| = (2kT/\pi m)^{1/2}$  respectively.

The derivations of these velocities are given below:

It is assumed that plasma has a Maxwellian velocity distribution:

$$f(\mathbf{v}) = A_1 e^{-v^2/v_{th}^2} \quad (2.6)$$

where  $v_{th} = \sqrt{\frac{2kT}{m}}$  is the thermal velocity and  $A_1 = \left(\frac{m}{2\pi kT}\right)^{3/2}$  is the coefficient which normalizes the distribution. The average velocity square is defined as:

$$\langle v^2 \rangle = \int f v^2 d^3v \quad (2.7)$$

where

$$v^2 = (v_x^2 + v_y^2 + v_z^2). \quad (2.8)$$

If Eq. 2.6 and Eq. 2.8 are plugged into Eq. 2.7, one gets:

$$\langle v^2 \rangle = A_1 \int e^{-a(v_x^2 + v_y^2 + v_z^2)} (v_x^2 + v_y^2 + v_z^2) dv_x dv_y dv_z \quad (2.9)$$

where

$$a = 1/v_{th}^2 = \frac{m}{2kT}. \quad (2.10)$$

Inserting Eq. 2.10 into Eq. 2.9, one gets:

$$\begin{aligned} \langle v^2 \rangle &= A_1 \int_{-\infty}^{\infty} e^{-av_x^2} v_x^2 dv_x \int_{-\infty}^{\infty} e^{-av_y^2} dv_y \int_{-\infty}^{\infty} e^{-av_z^2} dv_z + A_1 \int_{-\infty}^{\infty} e^{-av_y^2} v_y^2 dv_y \int_{-\infty}^{\infty} e^{-av_x^2} dv_x \int_{-\infty}^{\infty} e^{-av_z^2} dv_z + \\ &A_1 \int_{-\infty}^{\infty} e^{-av_z^2} v_z^2 dv_z \int_{-\infty}^{\infty} e^{-av_x^2} dv_x \int_{-\infty}^{\infty} e^{-av_y^2} dv_y. \end{aligned} \quad (2.11)$$

Noting that:

$$\int_{-\infty}^{\infty} e^{-av_\alpha^2} dv_\alpha = \sqrt{\frac{\pi}{a}} \quad (2.12)$$

where  $\alpha \equiv x, y, z$ , one can put Eq. 2.12 into Eq. 2.11, to get:

$$\langle v^2 \rangle = 3A_1 \frac{\pi}{a} \int_{-\infty}^{\infty} e^{-av_x^2} v_x^2 dv_x. \quad (2.13)$$

Using the following identity:

$$-\frac{\partial}{\partial a} (e^{-av_x^2}) = v_x^2 e^{-av_x^2} \quad (2.14)$$

and by using Eq. 2.14, Eq. 2.13 can be written as:

$$\langle v^2 \rangle = -\frac{3A_1\pi}{a} \frac{\partial}{\partial a} \int_{-\infty}^{\infty} e^{-av_x^2} dv_x. \quad (2.15)$$

Again by using Eq. 2.12, one gets:

$$\langle v^2 \rangle = -\frac{3A_1\pi}{a} \frac{\partial}{\partial a} \left( \sqrt{\frac{\pi}{a}} \right) = -\frac{3A_1\pi}{a} \sqrt{\pi} \left( -\frac{1}{2} a^{-3/2} \right) = \frac{3}{2} A_1 \pi^{3/2} a^{-5/2} \quad (2.16)$$

So that:

$$\langle v^2 \rangle = \frac{3}{2} \left( \frac{m}{2\pi kT} \right)^{3/2} \pi^{3/2} \left( \frac{m}{2kT} \right)^{-5/2} = \frac{3kT}{m}. \quad (2.17)$$

Then the root-mean-square velocity  $v_{rms}$  is then given by:

$$\langle v^2 \rangle^{1/2} = \sqrt{\frac{3kT}{m}}. \quad (2.18)$$

The average magnitude of the velocity  $\bar{v}$  is found as :

$$\bar{v} = \int_{-\infty}^{\infty} f v d^3v. \quad (2.19)$$

The volume element of each spherical shell is  $4\pi v^2 dv$ . If  $f$  is put into the equation:

$$\bar{v} = \int_0^{\infty} (m/2\pi kT)^{3/2} e^{-v^2/v_{th}^2} v 4\pi v^2 dv \quad (2.20)$$

and

$$\bar{v} = (m/2\pi kT)^{3/2} \int_0^{\infty} e^{-v^2/v_{th}^2} 4\pi v^3 dv \quad (2.21)$$

If  $v_{th} = (2kT/m)^{1/2}$  is put into Equation 2.21, one gets:

$$\bar{v} = 4\pi (\pi v_{th}^2)^{-3/2} \int_0^{\infty} e^{-v^2/v_{th}^2} v^3 dv. \quad (2.22)$$

If we define  $v/v_{th} = y$ ,  $v = v_{th}y$  and  $dv = v_{th}dy$ , then Equation 2.22 can be written as:

$$\bar{v} = 4\pi (\pi v_{th}^2)^{-3/2} \int_0^{\infty} e^{-y^2} v_{th}^3 y^3 v_{th} dy = 4\pi (\pi v_{th}^2)^{-3/2} v_{th}^4 \int_0^{\infty} e^{-y^2} y^3 dy. \quad (2.23)$$



The definite integral was found by integration by parts to give  $1/2$ . Then  $\bar{v}$  becomes:

$$\bar{v} = 2\pi^{-1/2}v_{th} = 2(2kT/\pi m)^{1/2} \quad (2.24)$$

Although  $\bar{v}_x$  vanishes,  $|\bar{v}_x|$  is not for an isotropic distribution.

$$|\bar{v}_x| = \int |v_x| f d^3v = \left(\frac{m}{2\pi kT}\right)^{3/2} \int_{-\infty}^{\infty} dv_y e^{-v_y^2/v_{th}^2} \int_{-\infty}^{\infty} dv_z e^{-v_z^2/v_{th}^2} \int_0^{\infty} 2v_x e^{-v_x^2/v_{th}^2} dv_x \quad (2.25)$$

First of the two integrals is  $\pi^{1/2}v_{th}$ . If we define  $\frac{v_x^2}{v_{th}^2} = u$ , and  $2v_x dv_x = v_{th}^2 du$  in the last integration, the result of it becomes  $v_{th}^2$ . Thus we have:

$$|\bar{v}_x| = (\pi v_{th}^2)^{-3/2} \pi v_{th}^4 = \pi^{-1/2} v_{th} \quad (2.26)$$

Putting  $v_{th} = \sqrt{\frac{2kT}{m}}$  into Eq. 2.26, then we obtain:

$$|\bar{v}_x| = (2kT/\pi m)^{1/2} \quad (2.27)$$

## 2.2. PLASMA POTENTIAL AND SHEATH AT A FLOATING SUBSTRATE

Since the masses of ions, electrons and neutrals are different, their temperatures will also be different. The densities of the electrons and ions are equal on average and are called as the ‘‘plasma density’’, but the neutral density is much higher for weakly ionized plasmas.

The average speed of electrons is much higher than those of the ions and neutrals. Since the electrons have higher temperature and lower mass.

The random flux crossing an imaginary plane from one side, to the other is found by:

$$\Gamma = \frac{1}{2} n |\bar{v}_x| = \frac{1}{4} n \bar{v} \quad (2.28)$$

Current density can then be found by using Eq. 2.28:

$$j = q\Gamma = \frac{qn\bar{v}}{4} \quad (2.29)$$

If a small isolated substrate is placed into plasma, the electrons and ions will hit their surfaces with random current densities given by:

$$j_e = \frac{en_e\bar{c}_e}{4} \quad (2.30)$$

and

$$j_i = \frac{en_i\bar{c}_i}{4} \quad (2.31)$$

where  $n$  is the number density,  $\bar{c}_e$  and  $\bar{c}_i$  are the average thermal velocity of electrons and ions respectively.

Note that, although number density of electrons and ions may be nearly the same, the ion average thermal velocity  $\bar{c}_i$  is much less than that of electrons, so that  $j_e \geq j_i$ . Since the electron flux is higher in that case, a negative charge and negative potential with respect to the plasma will be built on this substrate. Due to this negative charge, further electrons are repelled and ions are attracted. Then, the electron flux decreases. Substrate charging negatively continues until the electron flux is reduced by repulsion.

Plasma is virtually electric field free and equipotential everywhere due to local charge neutrality. This potential is known as “plasma potential”  $V_p$  and sometimes called the space potential. There is also a floating potential,  $V_f$  associated with the isolated substrate (see Figure 2.3). The floating potential and wall potential are related, because the insulating walls of the container require zero steady state net flux. This floating potential is smaller than the plasma potential. Because  $V_f$  repels electrons due to negative charges. A potential energy hill can be seen in front of the substrate due to the charging of the substrate. It is an uphill plot for electrons from the plasma to the substrate and a downhill plot for the ions (see Figure 2.2). Therefore, only electrons with enough kinetic energy can overcome the potential barrier.

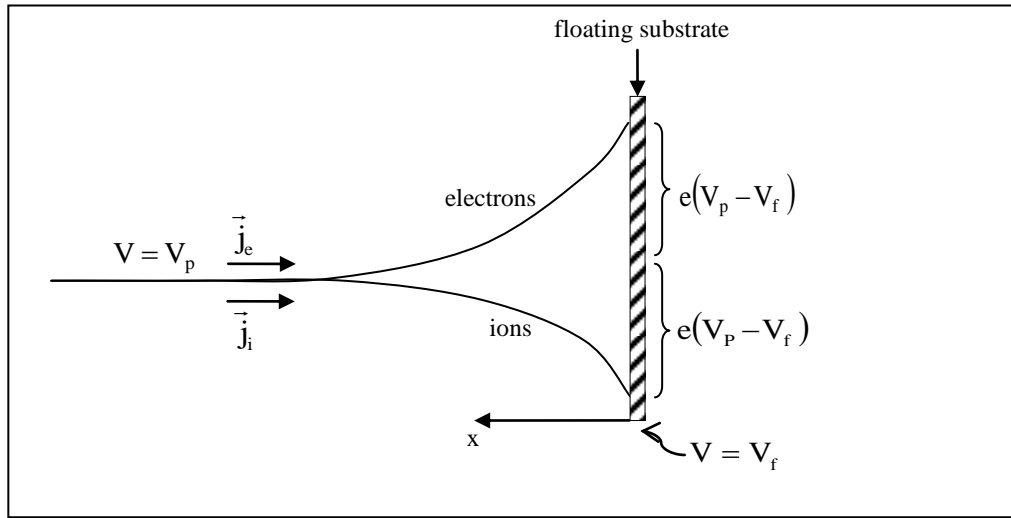


Figure 2.2. Potential energies of ions and electrons around a floating substrate

In order to understand this mechanism, one can get the variation of potential  $V$  with the distance  $x$  across regions of the net space charge using one dimensional Poisson's equation (see Figure 2.3)

$$\frac{d^2V}{dx^2} = -\frac{\rho}{\epsilon_0} \quad (2.32)$$

where  $\rho = n_e q_e + n_i q_i$  is the charge density and  $\epsilon_0$  is the permittivity of the plasma.

In one dimension, electric field can be written as:

$$E = -\frac{dV}{dx} \quad (2.33)$$

so that Poisson's equation becomes:

$$\frac{dE}{dx} = \frac{\rho}{\epsilon_0} \quad (2.34)$$

As soon as a floating substrate is inserted in the plasma, initial particle fluxes at the surface are  $\frac{n_e \bar{c}_e}{4}$  for electrons,  $\frac{n \bar{c}}{4}$  for neutrals and  $\frac{n_i \bar{c}_i}{4}$  for ions are created. This means that the

electric field across the surface changes through the regions of the net charge. The electron density decreases in the region, called sheath since the sheath obtains a net positive charge.

Glow is seen outside the sheath region due to the relaxation of the atoms excited by electron impact. Therefore, the energy of the electrons which are excited determines the glow intensity.

The sheath region does not glow, because the electron density is lower in the sheath. Therefore, it is seen as a region with lower luminosity than the glow region. A dark space surrounds the substrate as in the case of the sheath around all objects in contact with the plasma.

The potential difference;  $V_p - V_f$  behaves as a barrier to electrons. An electron must obtain potential energy of  $e(V_p - V_f)$  to achieve this barrier in order to reach the inserted substrate surface. Only electrons with kinetic energies which exceeding this quantity can reach the substrate.

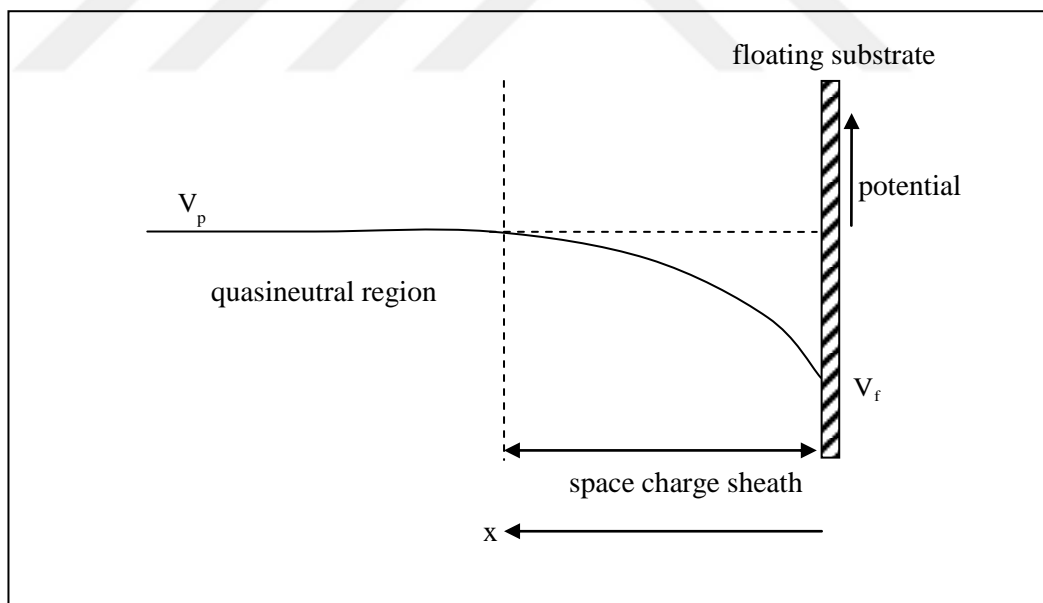


Figure 2. 3. Sheath voltage in front of a floating substrate

According to this Maxwell-Boltzmann statistics, the density ratio in surface region bulk plasma is given by:

$$\frac{n'_e}{n_e} = \exp\left(-\frac{e\phi}{kT_e}\right) \quad (2.35)$$

where  $\phi = V_p - V_f$  is the potential difference,  $n'_e$  is density of the electrons close to the substrate and  $n_e$  is density of electrons in the bulk plasma. When the charge flux balance at the object just achieved by the density  $n'_e$ , one can write:

$$\frac{n'_e \bar{c}'_e}{4} = \frac{n_i \bar{c}_i}{4}. \quad (2.36)$$

It could be thought that  $n'_e$  electrons lose the kinetic energy of  $e(V_p - V_f)$  in crossing the sheath, so  $n'_e$  electrons would have lower mean speed  $\bar{c}'_e$  than  $n_e$  electrons. However,  $n'_e$  electrons have higher energies than average.

According to Maxwell-Boltzmann kinetic theory, the differential density of electron in the sheath region is given by:

$$dn'_e = 4\pi n_e \left(\frac{m_e}{2\pi kT_e}\right)^{3/2} c_e^2 \exp\left[-\frac{1/2 m_e c_e^2 + e\phi}{kT_e}\right] dc_e = \exp\left(-\frac{e\phi}{kT_e}\right) dn_e \quad (2.37)$$

Using this distribution, one can show the mean speed of  $n'_e$  electrons close to the substrate:

$$\bar{c}'_e{}^2 = \frac{\int c_e^2 \exp\left(-\frac{e\phi}{kT_e}\right) dn_e}{\int \exp\left(-\frac{e\phi}{kT_e}\right) dn_e} = \bar{c}_e^2 \quad (2.38)$$

showing that the thermal energy of electrons is the same everywhere in plasma.

By integrating Eq. 2.37, one gets:

$$n'_e = n_e \exp\left(-\frac{e\phi}{kT_e}\right) = n_e \exp\left[-\frac{e(V_p - V_f)}{kT_e}\right]. \quad (2.39)$$

By substituting  $n'_e$  and  $\bar{c}'_e$  into Eq. 2.36 , one gets :

$$n_e \exp\left(-\frac{e(V_p - V_f)}{kT_e}\right) \frac{\bar{c}_e}{4} = \frac{n_i \bar{c}_i}{4} \quad (2.40)$$

However,  $n_e = n_i$  and  $\bar{c} = \left(\frac{8kT}{\pi m}\right)^{1/2}$  and from the charge balance (local charge neutrality).

So that, one gets:

$$V_p - V_f = \frac{kT_e}{e} \ln \frac{\bar{c}_e}{\bar{c}_i} \quad (2.41)$$

and

$$V_p - V_f = \frac{kT_e}{2e} \ln \left( \frac{m_i T_e}{m_e T_i} \right) \quad (2.42)$$

showing that the difference between  $V_p$  and  $V_f$  depends on the temperatures of electron and ion.

Negatively charged floating substrate repels electrons and attracts positive ions. The energy with which the ion strikes the substrate is affected by the voltage across the sheath. The ion with low energy is then accelerated by the sheath voltage, and the kinetic energy of the ions would be equal to the sheath voltage. Note that when the inserted metal surface is not floating but biased by a variable voltage  $V$ , it can be used as a Langmuir probe as will be shown in Sec.6.

### 2.3. DEBYE SHIELDING

One of the most important characteristics of a plasma is that it will shield out the electric potentials which are applied to it. If two charged balls which are connected to a battery and put in the plasma (Figure 2.4) negative ball is surrounded by a cloud of ions and positive ball is surrounded by a cloud of electrons. The shielding would be excellent, if the plasma were cold and there were no thermal motions. There would be a lot of charges in the cloud but there would not be an electric field in the bulk plasma outside the clouds (charge neutrality). On the other hand, the particles at the edge of the cloud (the electric field is

weak there) have adequate thermal energy and can escape from the electrostatic potential well, if the temperature is finite. This causes the plasma to be at slightly negative plasma potential, called  $V_p$ . The edge of the cloud is at the radius where the potential energy is nearly equal to the thermal energy,  $kT$ . Potentials of the order of  $kT/e$  can escape to the plasma, and lead to the finite electric fields there [4].

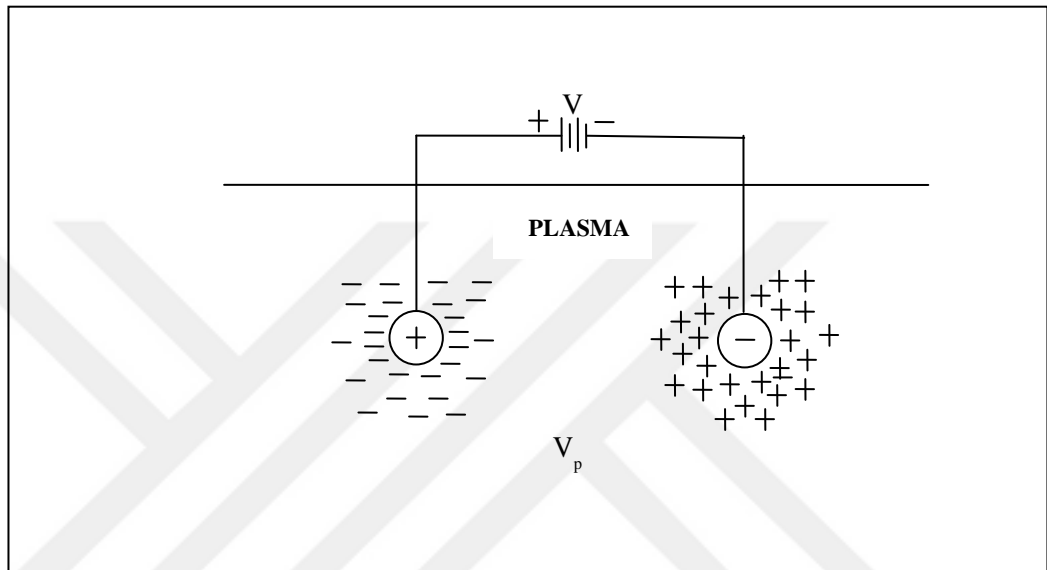


Figure 2.4. Debye shielding

The thickness of such a charge cloud can be computed as follows. If the numbers of ions and electrons are very high and equal, then the Coulomb interaction with a particular charge is equal to zero. However, due to some disturbance in the plasma, instantaneous potential at a point may differ from zero. For a surface placed at  $x=0$ , the change of potential  $\Delta V = V - V_p$  with respect to  $x$  can be seen in Figure 2.5:  $\Delta V_0$  (at  $x=0$ ) is more negative than  $V_p$ . The ions are heavier and do not almost move, but generate a uniform positive charge cloud in the background.

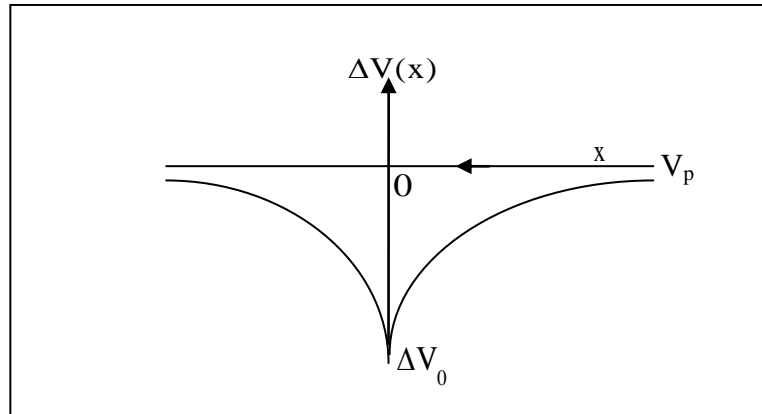


Figure 2.5. Change of potential around the perturbation

The Poisson's equation in one dimension (Eq. 2.32) can be written as the equation below:

$$\frac{d^2V}{dx^2} = -\frac{\rho}{\epsilon_0} = -\frac{e}{\epsilon_0}(n_i - n_e(x)) \quad (2.43)$$

where  $\epsilon_0$  is the permittivity of the free space, and  $n_e(x)$  is the electron density distribution that can be found from the Boltzmann equation :

$$\frac{n_e(x)}{n_e} = \exp\left[-\frac{E}{kT_e}\right] = \exp\left[-\frac{e\Delta V(x)}{kT_e}\right] \quad (2.44)$$

Inserting Eq 2.44 into Eq 2.43, one gets (note that  $n_e = n_i$  in the bulk plasma):

$$\frac{d^2V}{dx^2} = -\frac{en_i}{\epsilon_0} \left(1 - \exp\left[-\frac{e\Delta V(x)}{kT_e}\right]\right). \quad (2.45)$$

Since electrons are highly energetic,  $\Delta V(x) \leq kT_e$ , so that Eq. 2.45 can be expanded into Taylor series:

$$\epsilon_0 \frac{d^2\Delta V}{dx^2} \cong en_i \left[ \frac{e\Delta V(x)}{kT_e} + \frac{1}{2} \left( \frac{e\Delta V(x)}{kT_e} \right)^2 + \dots \right] \quad (2.46)$$



where since  $V_p$  is constant  $\frac{d^2V}{dx^2} = \frac{d^2\Delta V}{dx^2}$  was used.

The potential decreases very quickly in this region, so the second term in the expansion is very small and it can be ignored. This gives:

$$\frac{d^2\Delta V}{dx^2} \cong \frac{e^2 n_i}{kT_e \epsilon_0} \Delta V(x) \quad (2.47)$$

The solution to this equation can be written as:

$$\Delta V(x) = \Delta V_0 \exp\left[-\frac{|x|}{\lambda_D}\right] \quad (2.48)$$

where

$$\lambda_D = \left(\frac{kT_e \epsilon_0}{n_e e^2}\right)^{1/2} \quad (2.49)$$

$\lambda_D$  is called as Debye length which is a measure of the thickness of the sheath around the object placed at  $x=0$ . The change of  $\Delta V(x)$  with respect to  $x$  shows that if the potential in the plasma is perturbed, plasma opposes to that change.  $\lambda_D$  decreases if the density increases and it increases if  $kT_e$  increases.

The plasma is quasineutral. If the dimensions of a system  $L$  is much larger than  $\lambda_D$ , the external potentials or local concentrations of charge are shielded out in a shorter distance than  $L$ . The bulk of plasma is left free of large electric fields or potentials.  $\nabla^2\phi$  is very small outside the sheath [4].

One of the three conditions for an ionized gas to be a plasma is that  $\lambda_D \ll L$ . The concept of Debye shielding is not valid if there are only a few particles in the sheath region. It is valid, if there are sufficient number of particles in the sheath cloud.

The number of particles in the “Debye sphere” can be written as:

$$N_D = n \frac{4}{3} \pi \lambda_D^3 \quad (2.50)$$

The other one of the conditions for a gas to be called plasma is  $N_D \gg 1$ . The third criterion for a gas to behave like a plasma is  $\omega\tau > 1$  where  $\omega$  is the frequency of the oscillations and  $\tau$  is the mean time between collisions with neutral atoms.

#### 2.4. SHEATH FORMATION AND THE BOHM CRITERION

It was found by Bohm [1949] that there is an increase of the velocity of the ions which enter the sheath, Bohm sheath criterion [13]. In order to get some idea of velocity and potential distribution near the sheath region, assume the negatively charged electrode is inserted in the plasma at  $x=d$  (see Figure 2.6). Here,  $x=0$  refers to the boundary between the quasi-neutral transition and positive space charge region.  $n_i(0) = n_e(0)$  in this region. If the ions traverse the positive space charge sheath, it feels that the potential  $V(x)$  decreases monotonically. This sheath region is supposed to be collisionless.

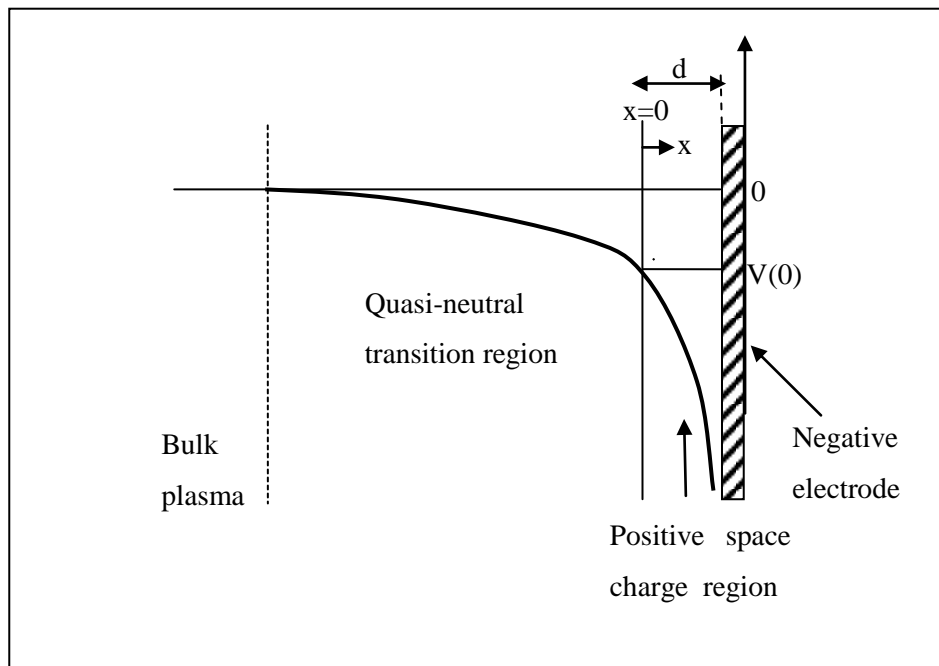


Figure 2.6. Change of potential close to a negative electrode.

From the conservation of the energy for the ions moving from  $x = 0$  to any  $x$  closer to the negative electrode, one can write :

$$1/2 m_i u(x)^2 = 1/2 m_i u(0)^2 - e[V(x) - V(0)] \quad (2.51)$$

From which one can get:

$$u(x) = \left( u(0)^2 - \frac{2e[V(x) - V(0)]}{m_i} \right)^{1/2}. \quad (2.52)$$

Since the fluxes are equal at  $x = 0$ ,  $n_i(x)u(x) = n_i(0)u(0)$ , the ion density becomes:

$$n_i(x) = \frac{n_i(0)u(0)}{u(x)} = n_i(0) \left( 1 - \frac{2e[V(x) - V(0)]}{m_i u(0)^2} \right)^{-1/2}. \quad (2.53)$$

It is known that, the electron density is obtained from the Boltzmann relation, as given earlier in Eq. 2.35:

$$n_e(x) = n_e(0) \exp \frac{e[V(x) - V(0)]}{kT_e}. \quad (2.54)$$

Thus, one dimensional Poisson equation in the positive space charge region can be written from Eq.2.43 as :

$$\frac{d^2V}{dx^2} = -\frac{\rho}{\epsilon_0} = \frac{e}{\epsilon_0} (n_e(x) - n_i(x)) \quad (2.55)$$

$$= en_e(0) \left( \exp \frac{e[V(x) - V(0)]}{kT_e} - \left( 1 - \frac{2e[V(x) - V(0)]}{m_i u(0)^2} \right)^{-1/2} \right) \quad (2.56)$$

$x=0$  corresponds to the boundary between the two regions, so that  $n_i(0) = n_e(0)$ .

$d^2V/dx^2$  must be zero or negative for all the values of  $x > 0$ , if this is a positive space charge sheath. In this case, one can write:

$$\left(1 - \frac{2e[V(x) - V(0)]}{m_i u(0)^2}\right)^{-1/2} \geq \exp\left[\frac{e[V(x) - V(0)]}{kT_e}\right]. \quad (2.57)$$

If it is squared and inverted, one gets:

$$\exp\left(-\frac{2e[V(x) - V(0)]}{kT_e}\right) \geq 1 - \frac{2e[V(x) - V(0)]}{m_i u(0)^2} \quad (2.58)$$

Since,  $V(x) - V(0)$  in this region is very small compared to  $kT_e$ , one can use Taylor's expansion of the exponential term Eq. 2.58 to get :

$$1 - \frac{2e[V(x) - V(0)]}{kT_e} \geq 1 - \frac{2e[V(x) - V(0)]}{m_i u(0)^2} \quad (2.59)$$

which results in:

$$u(0) \geq \left(\frac{kT_e}{m_i}\right)^{1/2}. \quad (2.60)$$

This means that the velocity of the ion which enters the sheath is equal to or larger than  $\left(\frac{kT_e}{m_i}\right)^{1/2}$ . The ions obtain this velocity due to the electric field across the transition region.

When the random motion of the ions is ignored, the conservation of energy at  $x = 0$  gives:

$$1/2 m_i u(0)^2 = eV(0) \quad (2.61)$$

where  $V(0)$  is the potential with respect to the plasma at the sheath boundary. Using this equation, one gets the potential at sheath boundary at  $x = 0$  as:

$$eV(0) = \frac{m_i u(0)^2}{2} = \frac{m_i k T_e}{2m_i} = \frac{k T_e}{2} \quad (2.62)$$

The ion density at the sheath boundary can then be found using Eq. 2.62:

$$n_e(0) = n_e e^{-eV(0)/kT_e} \quad (2.63)$$

$$n_e(0) = n_e e^{-1/2} = 0.6n_e \quad (2.64)$$

If we put an object into a plasma, the object becomes electrically floating, this leads to the floating sheath. The floating potential can be found by equating the electron flux to the ion flux. Since electron and ion densities are equal through the presheath ( $n_e(0) = n_i(0)$ ), the ion flux becomes:

$$\Gamma_i = n_i(0)u(0) = 0.6n_e \left( \frac{kT_e}{m_i} \right)^{1/2} \quad (2.65)$$

The electron flux to the floating object at floating potential,  $V_f$  is found by using:

$$\Gamma_e = \int_{v_{\min}}^{\infty} v_x f d^3v \quad (2.66)$$

where the electrons which have enough energy to overcome the potential.

If we put  $v_{\min} = \left( \frac{2e(V_p - V_f)}{m_e} \right)^{1/2}$  into the  $x$ -integral, Eq. 2.66 becomes:

$$\Gamma_e = n_e \left( \frac{m_e}{2\pi k T_e} \right)^{3/2} \int_{-\infty}^{\infty} \int_{-\infty}^{\infty} \int_{\sqrt{\frac{2e(V_p - V_f)}{m_e}}}^{\infty} v_x e^{\left[ \frac{-m_e(v_x^2 + v_y^2 + v_z^2)}{2kT_e} \right]} dv_x dv_y dv_z \quad (2.67)$$

The last two integrals are calculated as:

$$\int e^{-av^2} dv = \sqrt{\frac{\pi}{a}} \quad (2.68)$$

where  $a = m_e/2kT_e$ . Then, integration becomes:

$$\Gamma_e = n_e \left( \frac{m_e}{2\pi k T_e} \right)^{3/2} \left( \frac{2k\pi T_e}{m_e} \right) \int_{v_{\min}}^{\infty} v_x e^{\left[ \frac{-m_e(v_x^2)}{2kT_e} \right]} dv_x = n_e \left( \frac{m_e}{2\pi k T_e} \right)^{1/2} \int_{v_{\min}}^{\infty} v_x e^{\left[ \frac{-m_e(v_x^2)}{2kT_e} \right]} dv_x. \quad (2.69)$$

The integral looks like  $\int_c^{\infty} v_x e^{-av_x^2} dv_x$ . If we define  $u = av_x^2$  and  $dv = 2av_x dv_x$ , it can be written

as  $\frac{1}{2a} \int_{v_{\min}}^{\infty} e^{-u} du$  which gives  $\frac{1}{2a} \int_{v_{\min}}^{\infty} e^{-u} du = \frac{1}{2a} e^{-v_{\min}}$  or:

$$\Gamma_e = n_e \left( \frac{kT_e}{2\pi m_e} \right)^{1/2} e^{-\left( \frac{e(V_p - V_f)}{kT_e} \right)}. \quad (2.70)$$

The ion flux to any object negatively biased with respect to the plasma is increased by the effect of the Bohm criterion. Bohm criterion will change the ion flux to a floating substrate. Floating potential was found in Equation 2.42. However, it is changed to allow for this changed ion flux, and the criterion for net zero current (or  $\Gamma_i = \Gamma_e$ ) is found by equating Eq. 2.65 and 2.70 :

$$\left( n_e \left( \frac{kT_e}{2\pi m_e} \right)^{1/2} \exp\left( -\frac{e(V_p - V_f)}{kT_e} \right) \right) = n_i 0.6 \left( \frac{kT_e}{m_i} \right)^{1/2} \quad (2.71)$$

which leads to:

$$V_p - V_f = -\frac{kT_e}{e} \ln 2.4 \left( \frac{kT_e}{m_i} \right)^{1/2} \left( \frac{\pi m_e}{8kT_e} \right)^{1/2} = -\frac{kT_e}{2e} \ln \left( \frac{2.26.m_e}{m_i} \right) \quad (2.72)$$

This equation can be used to get electron temperature, if  $V_p$  and  $V_f$  are measured.

## 2.5. THE DEPENDENCE OF THE ELECTRON TEMPERATURE TO THE PRESSURE

Regardless of being neutral or ionized, the gas molecules in a container bounce around freely as a result of collisions with each other and walls. The collisions on the walls lead to the pressure exerted on the surface. Some momentum is transferred to the wall by gas molecules in each collision as in Figure 2.7. This momentum transfer leads to the force per unit area: the gas pressure.

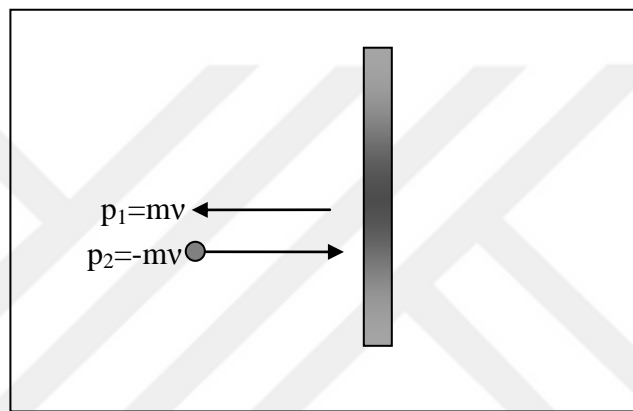


Figure 2.7. Momentum transfer on the wall of the container

Consider each gas particle has the mass,  $m$  and the speed,  $v$ . The change of momentum is  $2mv$ . Since, the atom is bounced back with the same speed ( $\Delta p = 2mv$ ). A momentum of  $+2mv$  is transferred to the wall of the container.

The force on the wall is the time rate of change of this momentum:  $F = dp/dt$ . Consider a cylinder with a base area  $A$  (see Figure 2.8.). The distance in which the particles striking the wall travels in the cylinder per unit time is  $v\Delta t$ , so that the volume of the cylinder is  $v\Delta tA$  and the number of particles which travels toward to the right is then given by :

$$N = \frac{n}{6}V = \frac{n}{6}v\Delta tA \quad (2.73)$$

where  $n$  is particle number density. (Note that the entrance plane in Fig. 6.7 is only one of the total of 6 planes of the 3 dimensional cube. This is the reason of having 6 on the denominator of Eq. 2.73).

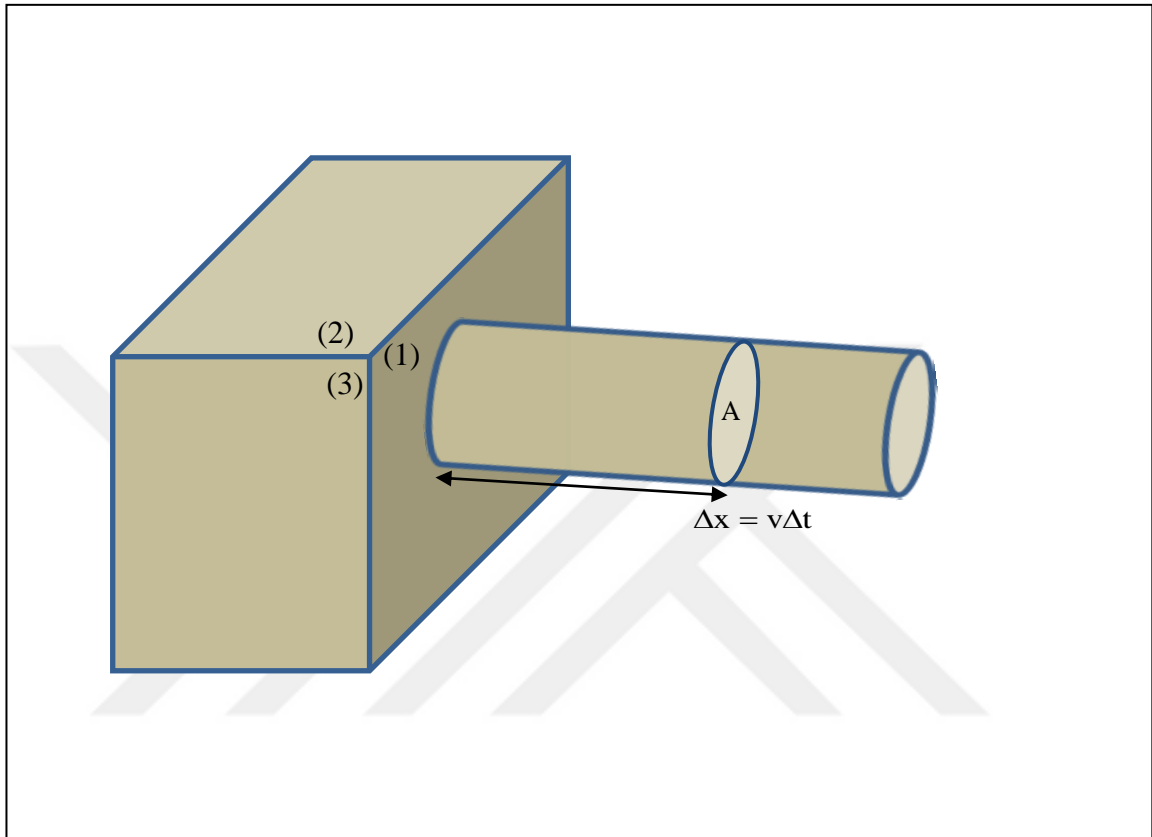


Figure 2.8. The cross section of the wall

The pressure is total momentum transfer per unit area per unit time ( $N\Delta p$ ):

$$P = \frac{N\Delta p}{\Delta t A} \quad (2.74)$$

By substituting equation 2.73. into equation 2.74, one gets:

$$P = \frac{nmv^2}{3} \quad (2.75)$$



This shows that the pressure in a vacuum chamber is directly related to the density of the gas atoms  $n$  and mean kinetic energy. The equation 2.75 can also be written as :

$$P = \frac{2}{3} n \frac{mv^2}{2} = \frac{2}{3} nK \quad (2.76)$$

where  $K$  is kinetic energy. If this average kinetic energy is obtained from a distribution function, then the pressure can be found from Eq. 2.76. A plasma includes particles of neutrals  $n$ , ions  $i$  and electrons  $e$  with different velocities and positions. Along with the internal collision processes such as Coulomb interaction, ionization and exchange of charge, external forces such as gravity and electromagnetic fields also affect the motion of the particles. Macroscopic parameters such as current density  $j$ , electron density  $n_e$ , ion temperature  $T_i$ , electron temperature  $T_e$  and pressure  $P$  are averages over the distribution of particle positions or velocities [17]. Now let us see how these averaged values can be obtained from the distribution function:

A single particle in phase space can be described by a velocity vector in cartesian coordinate system:

$$\vec{v} = v_x \hat{i} + v_y \hat{j} + v_z \hat{k} \quad (2.77)$$

and a position vector in coordinate space:

$$\vec{r} = x \hat{i} + y \hat{j} + z \hat{k} \quad (2.78)$$

producing 6 independent components :  $x, y, z, v_x, v_y, v_z$  making the phase space. Each point in phase space represents a particle at a particular point at a particular time at a particular velocity.

The number of particles in a unit volume of this phase space is specified by a distribution function.

$$dn = f(\vec{r}, \vec{v}, t) d^3r d^3v \quad (2.79)$$

$$n(\vec{r}, t) = \int_{-\infty}^{\infty} f(\vec{r}, \vec{v}, t) d^3r d^3v \quad (2.80)$$

where  $d^3r$  and  $d^3v$  are the volume elements:

$$d^3r = dx dy dz \quad (2.81)$$

$$d^3v = dv_x dv_y dv_z. \quad (2.82)$$

If a system is not subject to external forces, equilibrium distribution is obtained eventually. If the system is in thermodynamic equilibrium, ion temperature is not equal to electron temperature for cold plasmas. But these temperatures will be nearly the same for hot plasmas, not in our interest.

The plasma particles get distributed according to the Maxwell-Boltzmann distribution given by :

$$f(E) = A_2 e^{-E/kT} \quad (2.83)$$

where  $E$  is the energy,  $A_2$  is the normalization constant. For ideal gas (no interactions), this energy is just the kinetic energy so that  $E = K = \frac{1}{2}mv^2$ , the distribution function can be written:

$$f(v) = A_2 \exp\left(-\frac{1}{2}mv^2/kT\right). \quad (2.84)$$

The density can be specified by putting the distribution function into the equation 2.80, one gets:

$$n_0 = \int_{-\infty}^{\infty} \int_{-\infty}^{\infty} \int_{-\infty}^{\infty} f(v_x, v_y, v_z) dv_x dv_y dv_z \quad (2.85)$$

by assuming that temperature  $T$  does not change and for the velocities of interest, one gets:

$$n_0 = \int_{-\infty}^{\infty} \int_{-\infty}^{\infty} \int_{-\infty}^{\infty} A_2 \exp\left[-\frac{1/2mv_x^2}{kT} - \frac{1/2mv_y^2}{kT} - \frac{1/2mv_z^2}{kT}\right] dv_x dv_y dv_z \quad (2.86)$$

or

$$n_0 = A_2 \int_{-\infty}^{\infty} e^{-K_x/kT} dv_x \int_{-\infty}^{\infty} e^{-K_y/kT} dv_y \int_{-\infty}^{\infty} e^{-K_z/kT} dv_z \quad (2.87)$$

By using  $\int_{-\infty}^{\infty} e^{-ax^2} dx = \sqrt{\frac{\pi}{a}}$  the density integral turns into:

$$n_0 = A_2 \sqrt{\frac{2\pi kT}{m}} \sqrt{\frac{2\pi kT}{m}} \sqrt{\frac{2\pi kT}{m}} = A_2 \left(\frac{2\pi kT}{m}\right)^{3/2} \quad (2.88)$$

so that the normalization constant is found as:

$$A_2 = n_0 \left(\frac{m}{2\pi kT}\right)^{3/2}. \quad (2.89)$$

Therefore, the normalized Maxwell Boltzmann velocity distribution function can be written as :

$$f(\vec{v}) = n_0 \left(\frac{m}{2\pi kT}\right)^{3/2} \exp\left(-\frac{1}{2}mv^2 / kT\right). \quad (2.90)$$

Using this distribution function, the average velocity can be obtained from:

$$\langle \vec{v} \rangle = \frac{\int \vec{v} f(\vec{r}, \vec{v}, t) d^3v}{\int f(\vec{r}, \vec{v}, t) d^3v} = \frac{1}{n_0} \int \vec{v} f(\vec{r}, \vec{v}, t) d^3v. \quad (2.91)$$

Thus, for example average velocity in  $x$  direction:

$$\langle v_x \rangle = \frac{1}{n_0} A_2 \iiint v_x f(\vec{v}) d^3v = \frac{A_2}{n_0} \int_{-\infty}^{\infty} v_x e^{-\frac{1}{2}mv_x^2/kT} dv_x \int_{-\infty}^{\infty} e^{-\frac{1}{2}mv_y^2/kT} dv_y \int_{-\infty}^{\infty} e^{-\frac{1}{2}mv_z^2/kT} dv_z \quad (2.92)$$

$$= \frac{A_2}{n_0} \left( \frac{2\pi kT}{m} \right)^{1/2} \left( \frac{2\pi kT}{m} \right)^{1/2} \left( -\frac{kT}{m} \right) \exp\left( -\frac{mv_x^2}{2kT} \right) \Bigg|_{-\infty}^{\infty} = 0 \quad (2.93)$$

showing that average velocities in all directions are zero; i.e.,

$$\langle v_x \rangle = \langle v_y \rangle = \langle v_z \rangle = 0. \quad (2.94)$$

A plasma in thermal equilibrium is characterized by a homogeneous, isotropic and time-independent distribution function. If the distribution function  $f$  is independent of the direction of  $v$ , the distribution is isotropic. By using speed distribution, one can get averages of scalars ( $K, v, \dots$ ) and by using velocity distribution, one can get averages of vectors ( $\vec{v}, \vec{p}, \vec{l}, \dots$ ).

Transformation from Cartesian velocity space to spherical velocity space is obtained by differentiation as below:

$$d^3v = v^2 (\sin\theta d\theta d\phi) dv \quad (2.95)$$

where  $\theta$  is the polar angle of the velocity vector, and  $\phi$  is the azimuthal angle. In that case,

$$d^3v = \int_0^{\pi} \int_0^{2\pi} \sin\theta d\theta d\phi v^2 dv = 4\pi v^2 dv \quad (2.96)$$

and

$$n(\vec{r}, t) = \int_0^{\infty} 4\pi v^2 f(\vec{r}, \vec{v}, t) dv = \int_0^{\infty} f(\vec{r}, v, t) dv \quad (2.97)$$

Note that,  $g(v) = f(\vec{r}, v, t)$  is speed distribution, while  $f(\vec{r}, \vec{v}, t)$  is velocity distribution function. The speed distribution is then given by:

$$f(\vec{r}, v, t) = 4\pi n_0 v^2 \left( \frac{m}{2\pi kT} \right)^{3/2} \exp(-1/2mv^2 / kT). \quad (2.98)$$

Average kinetic energy is then found from:

$$\langle K \rangle = \frac{1}{n_0} \int \left( \frac{1}{2}mv^2 \right) f(\vec{r}, v, t) d^3v. \quad (2.99)$$

Putting Maxwell Boltzmann speed distribution function into equation 2.100, kinetic energy is:

$$\langle K \rangle = \frac{1}{n_0} \int_0^\infty 4\pi n_0 v^2 \left( \frac{m}{2\pi kT} \right)^{3/2} \left( \frac{1}{2}mv^2 \right) \exp(-1/2mv^2 / kT) dv \quad (2.100)$$

$$= \frac{2\pi m^{5/2}}{(2\pi kT)^{3/2}} \int_0^\infty v^4 e^{-1/2mv^2 / kT} dv. \quad (2.101)$$

By applying gamma function:  $\int_0^\infty x^n e^{-ax^2} dx = \frac{\Gamma(n+1/2)}{2a^{(n+1)/2}}$  into  $f(\vec{r}, v, t) = 4\pi v^2 f(\vec{r}, \vec{v}, t)$ ,

one gets:

$$\langle K \rangle = \frac{2\pi m^{5/2}}{(2\pi kT)^{3/2}} \frac{\Gamma(5/2)}{2 \left( \frac{m}{2kT} \right)^{5/2}}. \quad (2.102)$$

Using the properties of gamma function  $\Gamma(5/2) = \frac{3}{4}\sqrt{\pi}$ , one gets the kinetic energy as a function of temperature:

$$\langle K \rangle = \frac{2\pi m^{5/2}}{(2\pi)^{3/2} (kT)^{3/2}} \frac{\frac{3}{4}\sqrt{\pi}}{2 \cdot \frac{m^{5/2}}{(2kT)^{5/2}}} = \frac{3}{2} kT. \quad (2.103)$$

The pressure can then be obtained as a function of temperature by putting  $\langle K \rangle = \frac{3}{2}kT$  into the pressure equation of:

$$P = \frac{2}{3}nK = \frac{2}{3}n\frac{3}{2}kT = nkT. \quad (2.104)$$

This equation clearly states that the pressure is directly related to the temperature. If the pressure of the system increases, the temperature of gas increases in a fixed volume. This is because as the kinetic energy of the gas molecules increases, they move faster and the number of collisions per second increases.

The condition is the same for the electrons [3]. If the pressure of the system increases, electron temperature also increases.

### 3. DC GLOW DISCHARGES

#### 3.1. THE DISCHARGE

The DC sputtering system used in this study is indeed a DC glow discharge which utilizes a cathode including target and an anode including substrate. A DC glow discharge is obtained by applying a potential difference between two electrodes in a gas, see Figure 3.1.

A bright glow filled most of the space between the two electrodes. This negative glow is the result of the excitation and recombination. The space next to the cathode is called the dark space which is generated in front of the cathode. There is also a thin sheath in front of the anode. The minimum inter-electrode separation should be a few times the cathode dark space thickness in order to obtain a sustainable DC glow discharge. The region of the discharge is the positive column and it is made of plasma particles. The currents at two electrodes are equal, since the current must be continuous in a system. Plasma is more positive than anode and anode is more positive than floating potential. The plasma potential  $V_p$  is the same as the potential of the sheath at the cathode.

Ions and electrons are lost to each of the electrodes. Ion neutralization by Auger emission at the target, electron loss onto the external circuit at the anode and electron-ion recombination take place in the plasma and there must be an equal number of ion-electron pair generation to continue steady state discharge in the plasma.

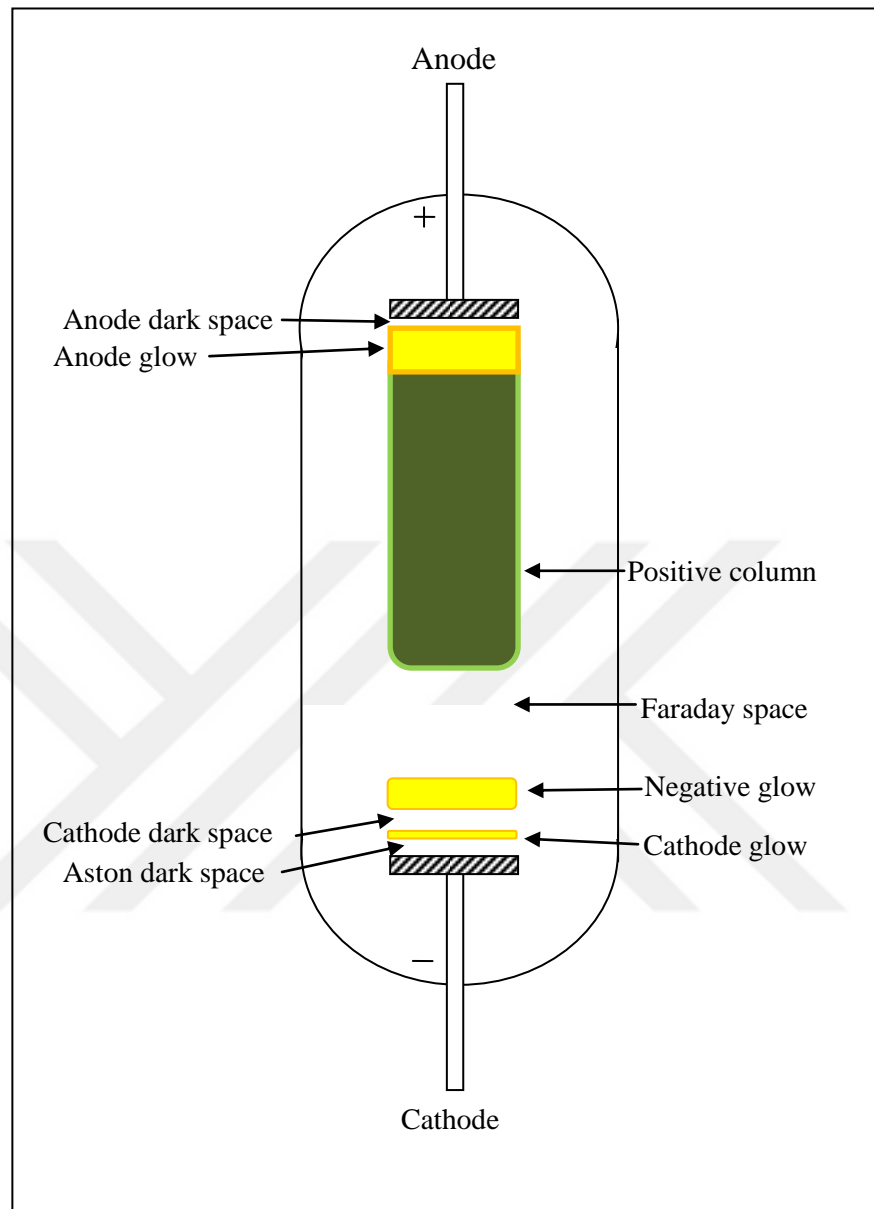


Figure 3.1. The normal glow discharge

Energetic particles hit on the electrodes and walls of the system and they cause heat increase, thus energy loss. There should also be enough amount of a balancing energy input to the discharge to sustain it. This is provided by applying an external potential between cathode and anode.

Electrons absorb energy from the applied electric field and these accelerated electrons obtain enough energy to ionize gas atoms producing a background conductive plasma.



Most of background ionization occurs in the glow region. Excitation has lower threshold than ionization. Excitation and subsequent emission from de-excitation usually participate to the ionization. This leads to visible photons that can be seen by the naked eye through the inspection window of vacuum chamber.

### **3.2. EMISSION OF SECONDARY ELECTRONS**

The secondary electron coefficient or yield is the number of electrons ejected per incident particle from an electrode. The bombardment of ions, photons, electrons and neutrals cause a different secondary electron emission coefficient and a different energy dependence.

These electron bombardment processes are very important in glow discharge, since they all contribute to the number of electrons in the discharge. The sheath helps to accelerate electrons from the surface to the glow and give energy to the discharge. Both electron and ion bombardment are important at the anode, but only ion bombardment at the cathode. The ion bombardment at the cathode is the main source for sputtering the target material placed above the cathode.

### **3.3. THE CATHODE REGION**

Sputtering target is located at the cathode. Therefore, it is very important to know the processes in the cathode region. Along with primary electrons, the secondary electrons are also created by the cathode and these electrons help to maintain the discharge which keeps sputtered ions for growing thin films. A discharge with a constant voltage and constant current density can be obtained at lower applied voltages and lower currents. This is called as “normal glow discharge”. If more power is applied, the size of the cathode region which carries current increases until all the cathode is used. This DC discharge is called as “abnormal glow discharge”. To initiate the discharge, one usually starts with higher power and abnormal discharge, then normal discharge is obtained by lowering power. This can be done automatically by the power supply or by the user. The cathode sheath region includes ionization, charge exchange and production of fast electrons.

The loss and gain of energy in a discharge system are explained in Figure 3.2. The ions bombard both cathode and anode as well as the wall boundaries. The light emitted through plasma interaction also contributes to the wall heating mainly done by ion impact. For some processes, the wall temperatures increase to very high values which need cooling.

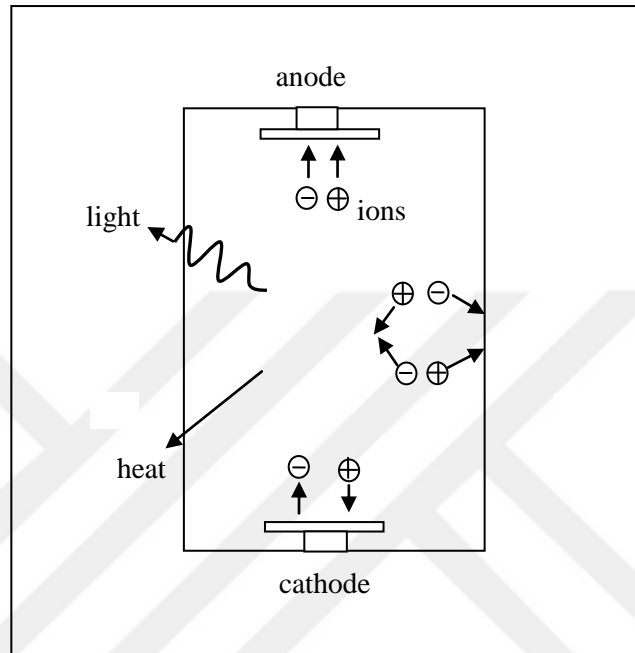


Figure 3.2. Diagram of a discharge loss

### 3.3.1. Ionization in the Sheath

#### 3.3.1.1. Electron Impact Ionization

The glow discharge process can be described by the ionization caused by the secondary electrons ejected from the target, if they are accelerated towards the dark space.

A flux of electrons  $N_e(x)$  which pass through a thin slab with a thickness  $\Delta x$  located at a distance  $x$  of from the cathode determines the amount of the ionization. If  $q$  is the ionization cross-section and  $n$  is the density of the neutrals, number of ionizing collisions =  $N_e(x)nq\Delta x$  gives.

so that:

$$\frac{dN_e(x)}{dx} \Delta x = N_e(x) n q \Delta x \quad (3.1)$$

and

$$\int \frac{dN_e}{N_e} = \int n q dx. \quad (3.2)$$

This results in:

$$N_e(x) = N_e(0) e^{nqx} \quad (3.3)$$

showing that ionization in the plasma increases exponentially from the cathode surface.

The electric field is very strong in this region and so that electrons will move in a straight line across the dark space. The multiplication of each electron which is ejected from the target by  $\exp(nqL)$  by the time it goes to the edge of the dark space gives the number of ionizing collision at a distance  $L$ .

Ions form for each electron which is ejected from the target. Secondary electrons are also ejected for each ion which hits to the target (with a yield of  $\gamma$ ). Thus, each ion which hits to the target causes to the formation of electrons with the equation:  $\gamma(\exp nqL - 1)$  in the dark space region.

### **3.3.1.2. Ion Impact Ionization**

Some possible ionization processes are photoionization and ion impact on neutrals. To calculate ion impact ionization, the factor  $\exp(nqL)$  is used as well as used for the electron impact ionization.

### 3.3.1.3. Sheath Ionization

The ionization which becomes in the sheath is not adequate to maintain ion flux to the target. The cathode sheath field is polar, so ions in the cathode sheath can not reach to the anode. Therefore, a large ionization source is necessary in the anode sheath or in the negative glow.

### 3.3.2. Exchange of Charge in the Sheath

The kinetic energy of the ion which reaches the interface between the glow and the sheath can be ignored. If there is no any collision, ion is accelerated through the sheath. When travelling through the sheath, it loses potential energy and hits to the electrode.

However, the ions generally collide with other particles in the plasma. This changes the energy distributions of the particles which hit the electrodes and the substrate. The energy distribution of the ions which hit the cathode is modified due to ionizing collisions in the sheath region in addition to the charge exchange. The electric field decreases linearly across the sheath and becomes zero at the dark space. If the voltage of the target is increased, the thickness of the dark space decreases. Thus, high energy ions with larger proportion will hit the cathode.

## 3.4. ANODE REGION

### 3.4.1. Anode Sheath

The thickness of the sheath in front of the anode is very small. Since it is much less than the thickness of the cathode sheath. Therefore, it should be collisionless. It repels some of the random flux,  $\frac{n_e c_e}{4}$  of electrons and decreases the current density to a small value.

The sheath voltage at the anode is not as large as the one in front of the floating substrate, although the sheath structure in front of the anode is the same as the one in front of the floating substrate.

### **3.4.2. Secondary Electron Emission**

Due to ion impacts, the secondary electrons are emitted from the anode too. They are accelerated back into the glow due to the polarity of the anode sheath, and they act as a source of electrons and energy. The ions, electrons and photons from the glow bombard the anode. However, a small fraction of them are the fast electrons which are formed in the cathode sheath. These electrons mostly do not collide in the glow, but they produce an important power input to the anode, after hitting the anode with a very large energy.

### **3.4.3. Polarity of Anode Sheath**

Anode sheath is polar, so the anode will always be more negative than the plasma potential. There are some reasons of the polarity of the anode sheath. One reason is that the dimension of the anode is small. If the anode size decreases, the current density at the anode increases. This can be achieved by reducing the anode voltage. Then fewer electrons are repelled become fewer. Electron current can increase until the saturation, when the anode is at the plasma potential. By decreasing the ion current, further increases in the net electron current are prevented. The second reason of the polarity of the anode is high secondary electron coefficient at the anode.

### **3.4.4. Main Effects in the Anode Region**

The acceleration of the secondary electrons from the anode back to the glow, and the acceleration of the ions from the glow to the anode and onto any substrate is due to the polarity of the anode. The secondary electrons accelerated behave like an electron and energy source, although the thickness of the sheath is too small to be an ionization source.

The ion flux at both of the electrodes are the same, but there is a little ionization in the cathode sheath and less in the anode sheath.

## **3.5. THE GLOW REGION**

The glow is anisotropic plasma. Because, the beam of the fast electrons which reach the glow from the cathode sheath penetrate through the sheath.

### 3.5.1. Electrons in the Glow Region

There are three types of electrons in the glow:

- Primary electrons which are also electrons coming from the cathode sheath with high energies.
- Secondary electrons that have lower energy. They are produced by ionizing collisions or primaries which lost a lot of energy.
- Ultimate electrons which have the highest intensity. The collision cross-sections decrease, if the energy increases at high energies. Forward scattering is the result of the weak interaction. Therefore, the initial path of the incident particles are not deflected much.

### 3.5.2. Ionization in the Negative Glow

The contributions of the ionization mechanisms in the glow region are by fast electrons by thermal electrons, by ions and metastables.

The electron impact ionization of ground state background atoms (such as argon) in the negative glow is the most important source of ionization in the discharge. The contributions of the electron impact ionization and ion impact ionization in the cathode sheath, and ionization of metastables in the glow are also important. The ionization is done by fast and thermal electrons.

The fast electrons which arrive into the glow cause some ionization, but do not lead to the ionization to maintain the glow directly.

Ionization by ion impact can be neglected in the glow, because ionization by ion impact on neutrals has a small contribution.

A metastable can be ionized by more electrons in the glow than a ground state atom. The ionization of a metastable is a two step ionization, because a metastable is excited by some energy input before. The density of metastables and their ionization cross-section is needed for the calculations.

## 4. SPUTTERING

### 4.1. INTERACTIONS OF IONS WITH SURFACES

When an ion impinges on the surface of a solid (target), the overall results of these target processes are listed below (see Figure 4.1)

- The ion may be reflected from the surface as a neutral. The principle of ion scattering spectroscopy is based on this reflection process. By using this spectroscopy, the surface layers of the material can be determined.
- The impact of the ion may lead to the ejection of an electron. This is called as secondary electron.
- The ion may be buried in the target. This is called ion implantation.
- The ion impact may cause structural reordering on the surface of target material. (altering the position of atoms on the target or radiation damage).
- A target atom may be sputtered and get ejected by the impact of ion. This process is called as sputtering. This is the main source of sputtering of the target atoms in order to get their thin films on the substrate placed at anode.

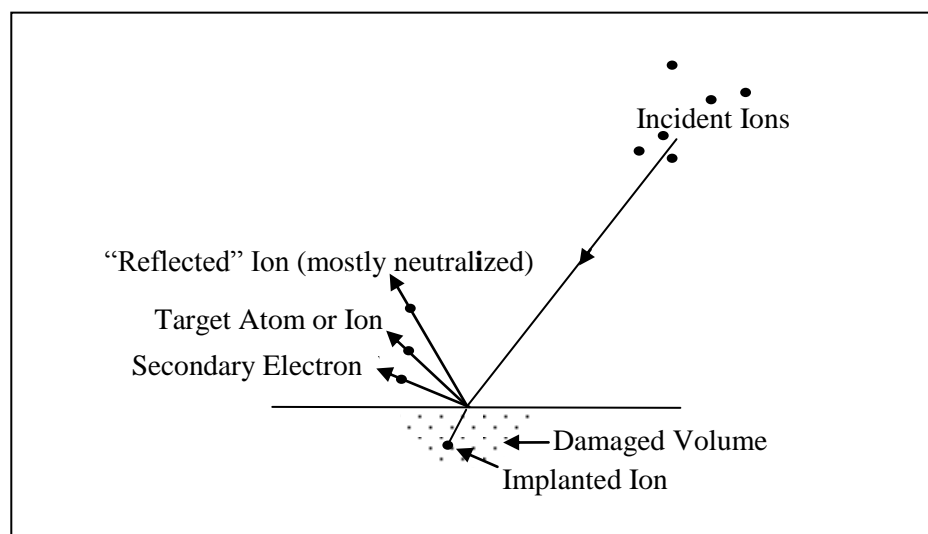


Figure 4.1. Interaction of ions with target surface

The particle which is incident can be an ion or a neutral atom, but ions are preferable. Because, they can easily be accelerated by an electric field. However, the impacting species are usually neutralized by the Auger emission from the target.

The number of collisions in the target due to primary collision at the surface is called as collision cascade. This cascade may lead to the sputter ejection of an atom from the surface of the target or heading off into the target. The collision phenomena occurring in a target may cause sputter deposition, ion implantation and radiation damage.

## **4.2. APPLICATIONS OF SPUTTERING**

### **4.2.1. Sputter Etching**

In sputtering process, the target atoms are knocked out of the surface of a target by the impact of accelerated carrying gas ions, usually Ar or N<sub>2</sub>. The target can be sputter etched by repeating this process. This process wear the target surface until it can not be used anymore.

### **4.2.2. Sputter Deposition**

A material is ejected from a "target" onto the surface of a receiver which is known as a "substrate". Many atomic or molecular layers of target material on the surface of substrate can be coated by repeating the process over and over. This process is the basis of sputtering and called as sputter deposition. The deposition which is less than about 1 μm is called thin film.



### 4.3. LIMITATIONS OF SPUTTERING

Sputtering is done in a partial vacuum. Some materials are not proper to the vacuum condition. Organic solids can not withstand the bombardment in sputtering. Target materials which contain volatile component have problems in the presence of vacuum. Although powders and liquids are sometimes used, the target is generally solid [3].

In addition the metals that can be magnetized produce undesirable effect due to the magnetic field configuration in the cathode magnetron head.

The plasma treatment is controlled by applied potential for gas discharge, nature of the gas, position of the fabric inside plasma and exposure time [14].

### 4.4. A CONVENTIONAL DC SPUTTERING SYSTEM

In a conventional DC sputtering system, sputtering target is the cathode of a circuit, and high voltage,  $V$  is applied to it. The substrate is placed on a grounded anode. These electrodes are put in a vacuum chamber. The system is well evacuated and argon gas is sent into the chamber. Electrons are accelerated by applying the electric field and they collide with argon atoms by making some of them argon ions. More electrons produce the glow discharge and move towards the anode. The ions move towards the cathode and rotationally hit on the target surface by the  $\vec{E} \times \vec{B}$  force. (see Figure 5.3) When the ions strike to the target, some of the target atoms may be sputtered and sputtered atoms have a wide range of energy distribution. Some of the sputtered atoms energetically impact on the substrate and form a thin film. (see Figure 4.3) The ions which strike the cathode may liberate secondary electrons from the target, too.

The amount of sputtering, ion flux at the target and current determine the rate of thin film formation. Sputtering yield  $S$ , ion energy and voltage determines the sputtering rate.

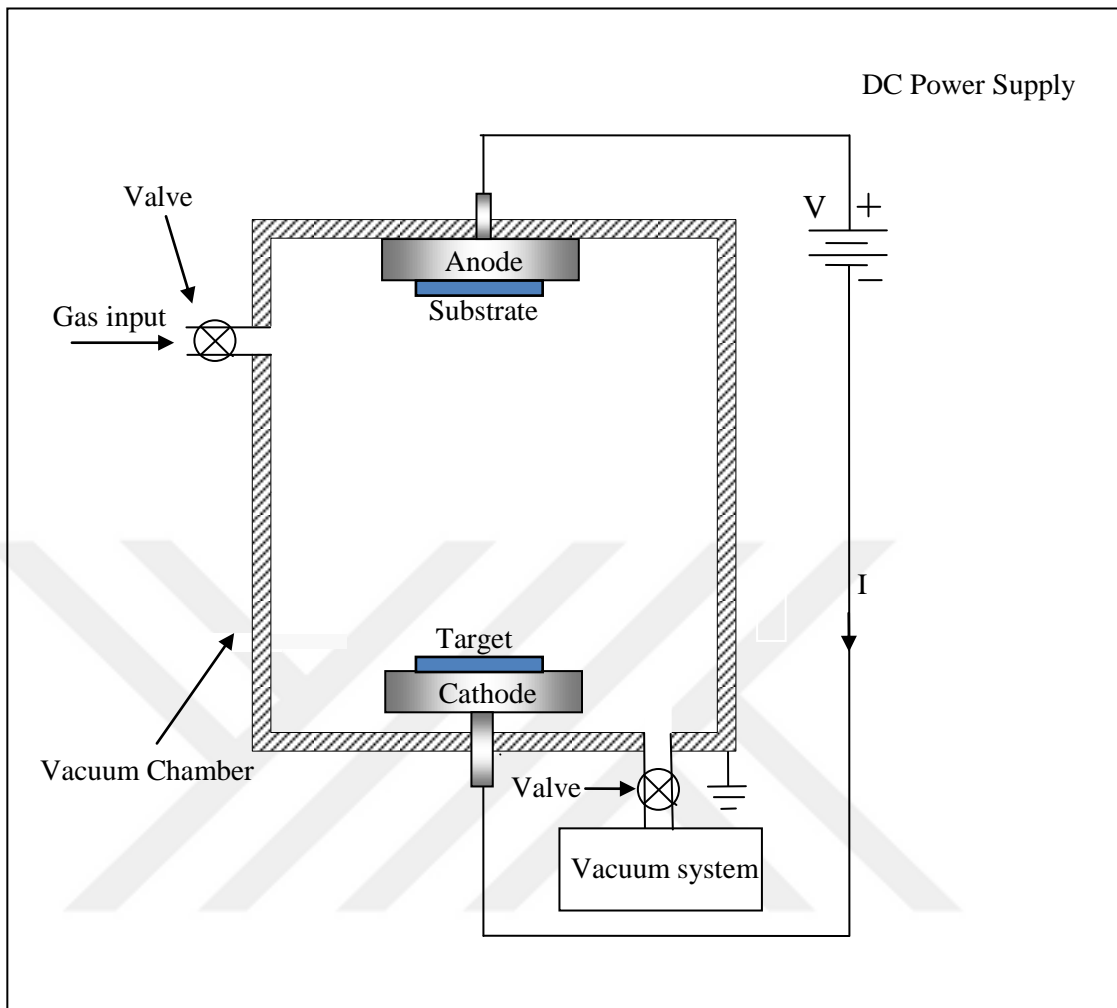


Figure 4.2. Schematic diagram of a DC sputtering system

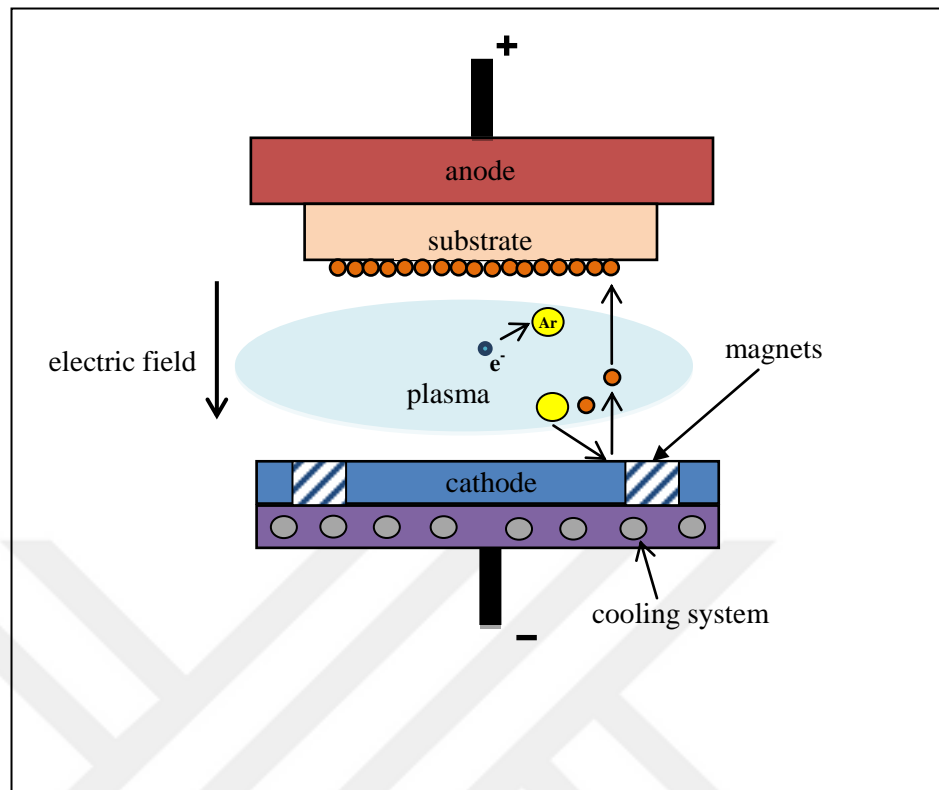


Figure 4.3. Schematics of the magnetron sputtering system with argon gas

#### 4.4.1. Choosing the Sputtering Gas

The sputtering is usually established by ions not by neutrals; since, it is very difficult to accelerate the neutral atoms.

Noble gas ions are used in vacuum system, since they do not cause reactions with the target and substrate. Noble gas ions have closed shell structure and they are not chemically active. Therefore, using such gases (Ar, Ne), the thin films which are produced can be made more cleaner. Argon (18) is cheap and easily available, so it is more preferable than other noble gases. This is the gas utilized in our vacuum system.

#### 4.4.2. Choosing the Sputtering Gas Pressure

Pressure inside the vacuum chamber can be controlled by the gas input. Both the glow discharge and film deposition determines the operating pressure. Lower pressure limit is

necessary for glow discharge. With decreasing gas pressure, the number of ionizing collisions and the discharge current will also decrease. The rate of sputtering and current in a DC discharges is very small below about 30 mTorr. This is the reason, the sputtering is carried at between 50-100 mTorr of gas pressure.

However, some problems can also arise at high pressures (more than 120 mTorr). Sputtered material from the target may collide with the argon atoms, before it reaches the substrate surface. The rate of these collisions can increase with increasing pressure, so that the deposition rate decreases. When the rate of collision increases the sputtered atom may be deflected back to target. This backscattering is high above about 120 mTorr. Therefore, 30-120 mTorr should be selected as operating range [3]. In our coatings, usually 100 mTorr of Ar pressure is utilized.

#### **4.4.3. Choosing Electrical Conditions for the Glow Discharge**

The flux of ions, the sputtering yield and energetic neutrals determine the rate of sputtering. Target bombardment flux is also due to neutrals as well as ions. There is a specific voltage-current relationship for each target material, sputtering gas and operating pressure.

If the ion energy rises up to 10 keV, the sputtering yield increases monotonically and after 10 keV, it starts to decrease. Voltages below 10 keV of energy should be used. If high energy input is used fast ions and the electrons may create X-rays on metal surface. Other criteria (for example the material of substrate and target etc.) are also important. V-I relationship can be changed by varying the operating pressure of system. Setting up this condition, the same power input is supplied. Therefore, constant yield per energy input,  $S/E$  is obtained. According to sputtering target kinetics,  $S$  increases linearly with  $E$  until 1 keV. Above 1 keV,  $S/E$  decreases with increasing energy. It was shown in this thesis that there exists an hysteresis effect in the current, if the pressure is increased and decreased as voltage is kept constant. Similar hysteresis effect was also observed in this study when pressure is kept constant but the voltage is increased and decreased.

Cathode current is also carried by secondary electrons and some of the sputtering particles are neutral. Therefore, the flux of sputtering particles at the cathode does not produce to

the total current. Sputtering particles collide with gas atoms and slow down. These mean that target do not take all of the V-I power input. According to the sputtering yield per unit energy input data ( $S/E$ ) the sputtering is not true below about 100 V [3].

## **4.5. DEPOSITION OF INSULATORS**

Insulators should be deposited by RF sputtering or reactive sputtering method. Because, there may be some problems of excess surface charges and stress produced in the target by resistive heating.

### **4.5.1. RF Sputtering**

In RF sputtering, the sputtering target is alternately bombarded by ions and electrons, thus charge build up is prevented. An alternating voltage power supply with frequency about 13.5 MHz is used in an RF sputtering system, since this is one of the allowed frequencies by the law. RF discharge uses electron impact ionization more efficiently. Therefore, operating pressure may be below 1 mTorr. The amount of scattering of material is reduced by lower operating pressure. The lower pressure also causes less ion energy attenuation due to charge exchange. Because, the sheath mechanism of RF system is more different than that of DC system.

There are some advantages in RF systems. Arching may not be formed in RF discharges, since the field changes its direction continuously and reduces to zero charge. However, arching is a problem in DC sputtering systems due to dirt patches (with higher secondary electron coefficient), asperities or pockets of outgassing. Therefore, conditioning of a target is necessary before general usage, by sputtering away or evaporating the arc defect and increasing the power applied. However, conditioning of target in RF systems is also important.

### **4.5.2. Reactive Sputtering**

Reactive sputtering also prevents the target charging. The DC sputtered material is mixed with a chemical in gas phase (e.g. oxygen or nitrogen). It is used for the purpose of deposition of multicomponent materials. For example, by sputtering a titanium in DC glow which contains oxygen, a titanium oxide compound can be created on the surface.

## **4.6. SPUTTERING SYSTEMS**

Some other practical factors which affect the sputtering systems are listed below.

### **4.6.1. Ground Shields**

There is a dark space shield (ground shield) around the target which focuses the ion bombardment and sputtering to only the target. It prevents the contamination of the mounting clips, target backing plate and mechanical supports. The thickness of the dark space should be more than the size of the gap between the target and the ground shield to prevent ion bombardment of these region. The thickness of the dark space decreases with the frequency. Therefore, systems with the frequency above 13.56 MHz should have closer ground shields. The space between the target and shield sets an upper pressure limit. Because, the dark space thickness also decreases with pressure.

A lot of systems can apply electrical power to the substrate. This technique is called as bias sputtering. In this condition, there should also be a ground shield around that electrode.

### **4.6.2. Shutters**

Shutters can be used during a presputtering process, for the purpose of removing the first few atomic layers of the target by sputtering to clean it. The target can be contaminated by atmospheric pollution or handling, if the system is in contact with air to load or unload. This is prevented by the shutter during the initial process to avoid the deposition on the

substrate. During this pre-sputter period, powering the substrate is also very important, as well as the application of the bias during the sputtering deposition.

#### **4.6.3. Target Cooling**

A lot of power input to the sputtering system are lost as target heating. This can damage the bonding between the target and backing electrode. Therefore, cooling the target with water or another suitable liquid is very important. Because of this cooling system is very complex, if the power input to the system is not much, it can be avoided. It is not very difficult to put a cooling system to the substrate platform, but a partial electrical short of the target by the liquid flow must be prevented by excessive resistive or capacitive coupling to the ground.

#### **4.6.4. Substrate Temperature Control**

To control the temperature of a target is very important, but difficult parameter. The structure of a thin film and gas corporation in the bias technique is influenced by substrate temperature. Therefore, target cooling is very important.

A circulating hot liquid or electrical resistance can enable the substrate platform to be heated. The resistance heater can be decoupled with a proper isolation transformer, if electrical isolation is needed. A thermocouple feeding a power controller can control the temperature of the substrate. However, the thermoelectric emf of the couple should be preserved while removing DC and RF offset components. So, electrical isolation is more difficult in this case.

Whole assembly of the heater, temperature controller and the thermocouple can run at the DC target voltage by a single isolation transformer at the power source, in a DC sputter etch system. Therefore, electrical isolation between the thermocouple and substrate is not required.

There are some problems in the control of substrate temperature. The most required part of the substrate to measure the temperature is the surface, and the latter is difficult due to

thermal barriers. (e.g. thermal isolation between the substrate and substrate platform or electrical isolation between the substrate and a thermocouple pressed onto it.)

Another problem is that the power input to the substrate from the discharge can cause the surface temperature to become greater than the bulk. Evaporation of a thin film thermocouple onto the surface of the substrate can be done. An infrared thermometer is a good way to measure the temperature of the substrate. It can measure the infrared radiation emission from the substrate behind the window of the sputtering system, but the transmission characteristics of window should be known. Since, it may affect the infrared rays.

#### **4.6.5. Electrode Voltage Measurement**

The control of many RF systems can be done by the power input to matching network and chamber. However, the measurement of the target voltage is also important. Measuring the DC offset voltage is more general than the RF peak-to-peak. The LC circuit can filter out the RF components. Therefore, DC voltage can be obtained with an LC circuit . A high voltage probe (resistive network divider) can show the RF voltage waveform using an oscilloscope.

The resistive probes are used to find the AC and DC waveforms, although clamping circuits are used to find only RF peak to peak magnitude.

There are a great amount of RF currents in the external circuitry and the inductance of even a straight piece of wire can be important for radio frequencies. There are important voltage drops along the cables. Voltage changes can be noticed very easily by using the probe. The probe should be connected to the back of the electrode to prevent drops. The same processes can be applied for the measurement of the substrate voltage. The DC offset of the applied RF is measured as in a bias sputtering system.



## 4.7. DEPOSITION WITH SPUTTERING METHOD

### 4.7.1. Thin Film Formation

Figure 4.4 shows that material reaches to the substrate in an atomic or molecular form. The motion of the atom is determined by its binding energy to the substrate. Density of a single atom or deposition rate determines the formation of an atomic pair. The doublets are joined by other single atoms and form triplets, quadruplets and so on. This is known as nucleation stage. Then quasi-stable islands contain tens or hundreds of atoms. The size of the islands increases during the island growth stage. At the end, they start to touch each other. This step is called as agglomeration or coalescence stage. The islands show liquid-like behaviour during coalescence. Coalescence stage continues until continuity and the film contains valleys and hills during the coalescence stages.

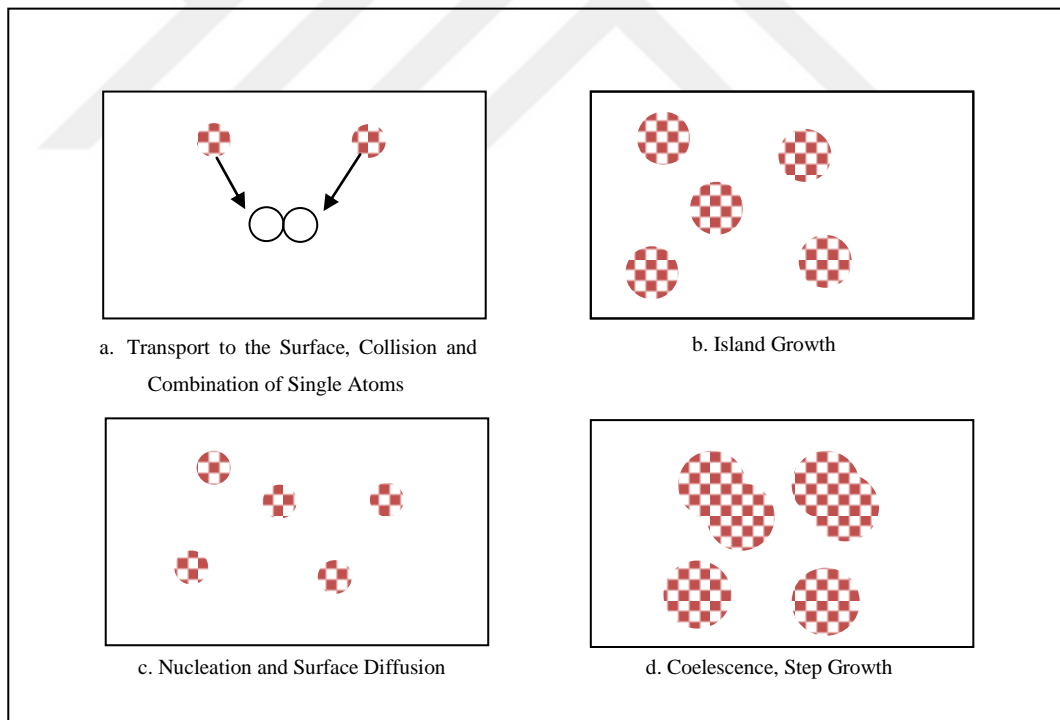


Figure 4.4. Thin film formation

Each island consists of a single crystal or just a few crystals in the island stage. The orientation of each island is random on a polycrystalline substrate. The substrate structure

determines the orientations of the island on a single crystal substrate . They can find low energy positions, as the surface atoms are mobile. If the temperature of the substrate increases, mobility is enhanced. Finding a proper lattice position energetically takes time, low deposition rates enable crystal growth. There is a temperature called as the epitaxial temperature for each deposition rate. Above this temperature, single crystal films can be grown. Polycrystalline films on polycrystalline substrates are more required. There are one or a few crystallites on each island during the island stage. The mechanism of the island growth is the same as a single crystal growth. Thus, large thickness of a film, large grains and crystal defects with low density are obtained with high substrate temperature and low deposition rate. The structure of the growing film depends on the deposition conditions [3].

#### **4.7.2. The Nature of the Substrate**

The thin film depends on the nature of the substrate, content of the impurities, substrate temperature, chemical nature of the substrate.

In a discharge, free electrons gain more energy from the electric field which is applied to the system. There are collisions between the electrons and neutral atoms or molecules and these collisions cause electrons to lose their energies. The energy transfer to the molecules cause the formation of new types of species such as UV radiations, ions, photons and metastable free radicals. Figure 4.5 shows the types of bombardments on a substrate which interact with the surface [14]. Therefore, the environment of the sputtering is very complicated. A typical sputter deposition rate is one monolayer per second.

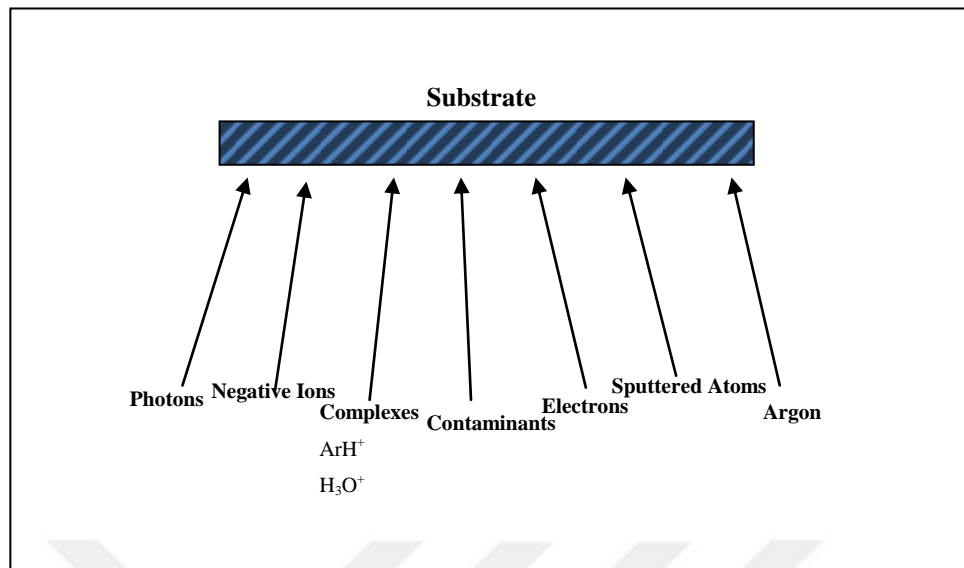


Figure 4.5. Particles which bombard the substrate

#### ***4.7.2.1. Sputtered Atoms and Contaminants***

A contaminant gas with a partial pressure  $10^{-6}$  Torr contributes an equal flux at the substrate. If this contamination is active chemically, it is effective on film property. The flux of contaminant increases with its partial pressure. If the cause of contamination is an internal source such as outgassing from a heated substrate, then its partial pressure can be minimized by maximizing the rate of pumping and gas flow.

#### ***4.7.2.2. Sputtering Gas Atoms***

The argon or other carrying gas flux used in sputtering is very large, if it is compared with the fluxes of contaminants and sputtered atoms at the substrate, so trapping of the argon in the growing film is not usually possible.

#### ***4.7.2.3. Excited Neutrals***

Excited neutrals are also the source of bombardment of substrates in addition to the ground state neutrals. They can lose their energy at the growing film and affect its growth structure.

#### ***4.7.2.4. Positive Ions***

There is also bombardment of charged particles. The most abundant positive ions are argon ions. There are also sputtered material ions which are created by Penning process of collision with the metastables and the electron impact ionization.

These ions are accelerated across the sheath which is too thin at the substrate. There are collisions in the sheath, so the ions are attenuated. There are also more argon ions such as  $\text{Ar}^{++}$ ,  $\text{Ar}_2^+$  and complex ions such as  $\text{ArH}^+$  and short lived ions such as  $\text{H}_3\text{O}^+$  in addition to the species shown in Figure 4.5.

#### ***4.7.2.5. Negative Ions***

Negative target ions may be repelled and slowed down by the space charge sheath. However, if they are adequately energetic, they can still reach to the substrate. However, negative ions are energetic enough to reach the substrate, if they are only formed in the sheath.

#### ***4.7.2.6. Electrons***

Electrons are the most important source of charged particle bombardment at the positively charged substrate. Most of the electrons with a conducting substrate are thermal electrons from the glow, and their energies are a few electron volts. However, more energetic electrons can overcome the sheath at the substrate. Charging of the insulating substrate on the anode in the DC discharge system is up to a floating potential and takes much smaller electron flux which is equal to the ion flux.

There are also fast electron bombardment as well as slow electrons. They are emitted from the target by the impact of ion or others, accelerated across the sheath of the target. After that they travel across the sputtering system without collisions.

The structure and characteristics of the growing film on the substrate is mostly influenced by these fast electrons. They can prevent the growth of the thin film as well as they can provide improvement. Because, large energy input due these electrons may lead to the heating of the substrate and heating closely affects the film structure.

#### ***4.7.2.7. Photons***

Electron or ion bombardment on the surface can cause the production of photons. The energy of a photon can be as much as the ion or electron which creates it. It is almost as the energy of the ion or electron which produces the photon. The photon can be classified as the soft x-ray due to its energy. Photons with lower energy are caused from the relaxation of excited atoms in a glow. Usually the effects of these photon on the thin film formation is minor.

### **4.8. RADIATION DAMAGE**

Various types of radiation damage can result from the metallization of semiconductor devices. Increasing sputtering target voltage increases the magnitude of the damage. Therefore, magnetron sputtering devices with low target voltages below 500 V are preferred for metallization to reduce the damage.

### **4.9. BIAS TECHNIQUES**

The characteristics of the film can be influenced by varying the energy and flux of the particles which are incident. However, the behaviours of the neutral particles can not be controlled easily. The basis of bias sputtering technique is the control of the charged particles by changing the local electric field.

#### **4.10. DEPOSITION OF MULTICOMPONENT FILMS**

Multicomponent films such as compounds, alloys or the mixture of them can be produced by sputtering from a single compound target or from different types of targets at the same time. Four stages are needed to eject an atom from a sputtering target to the thin film. They are sputter ejected from the target, travel through the gas, condensate onto the substrate and join into the film.

#### **4.11. THIN FILM ADHESION**

The thin film is too fragile and the fragility of the film is determined by its substrate for strength. Measuring the adhesion is difficult, and adhesion describes how a film and substrate stays in contact. There are different types of adhesion:

- Film and substrate meet at a well-defined interface and this is known as interfacial adhesion.
- Interdiffusion adhesion arises from the solubility of one or two materials in the other or a solid state interdiffusion between the two materials.
- Intermediate layer adhesion forms the film are bounded with the help of one or more layers of compounds of the materials.

## 5. MAGNETICALLY ENHANCED SPUTTERING SYSTEMS

The magnetic fields in sputtering systems are obtained by permanent magnets and these fields reduce electron bombardment at the substrate surface. These magnetic fields provide an increase in sputtering rate.

The production of a force  $\vec{F}$  on the particle is the result of the primary interaction between a particle with charge  $q$  and velocity  $\vec{v}$  and magnetic field  $\vec{B}$ . The direction of the force is perpendicular to the electric and the magnetic field vectors (see Figure 5.1).

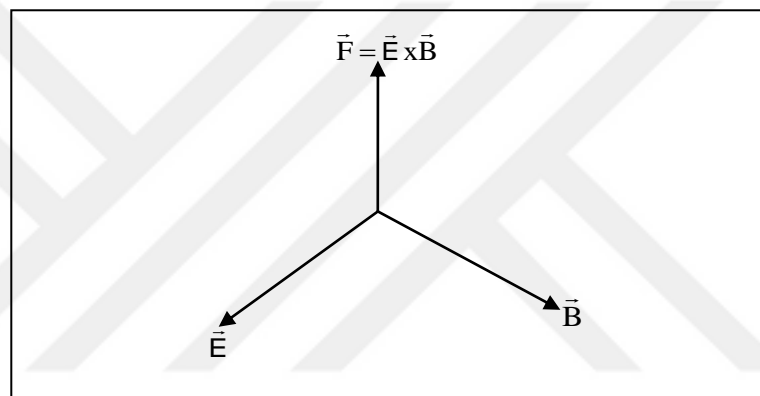


Figure 5.1. The cross product of electric field and magnetic field gives the force

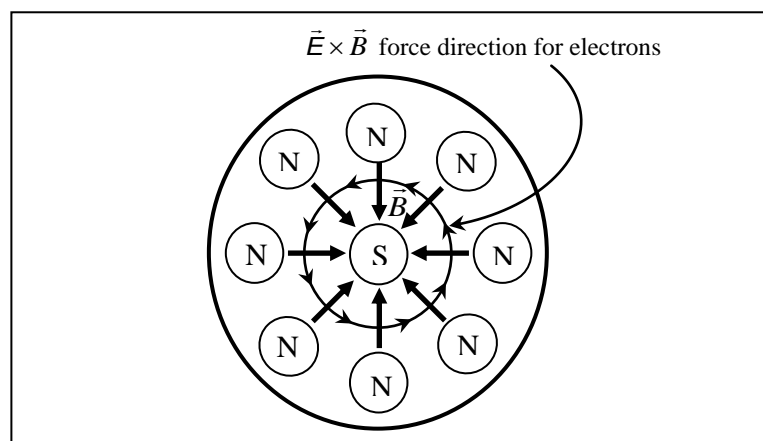


Figure 5.2. Top view of magnetron sputtering system  
(The electric field is from the top to the bottom).

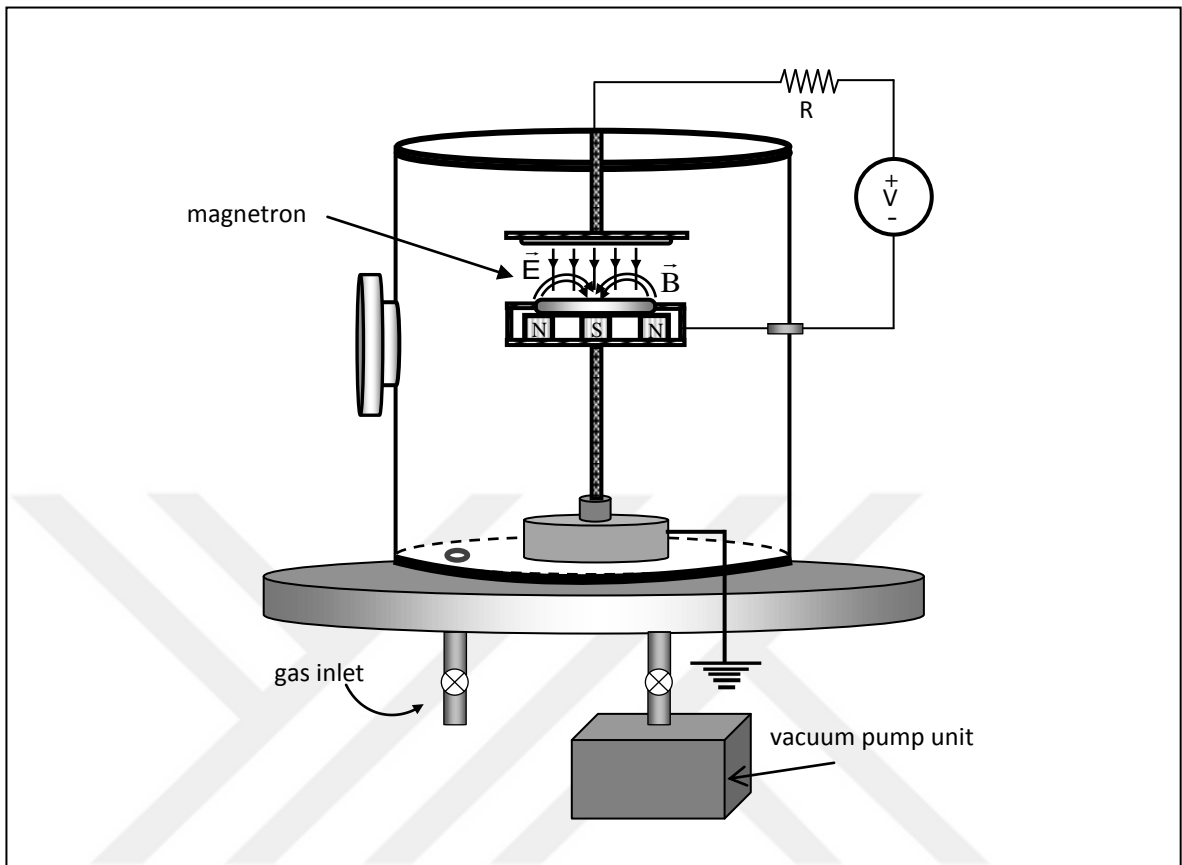


Figure 5.3. The vacuum system with a mechanical and turbo-pump.

Since the force created on the moving charge is  $\vec{F} = q(\vec{v} \times \vec{B} + \vec{E}) = m\vec{a}$ , the acceleration is  $\vec{a} = \frac{q}{m}(\vec{v} \times \vec{B} + \vec{E})$ . This shows that the acceleration which is created by the force is inversely proportional to the mass of the charge. Magnetic field of 100 Gauss by permanent magnets on magnetrons can affect the electrons, but the ions are too big to be affected in the magnetron sputtering systems.

## 5.1. MAGNETIC FIELDS

The purpose of using magnetic field enables the electrons to be used more efficiently and produce more ionization and more sputtering. The recombination at the vacuum walls



cause the electrons to be lost rapidly in a conventional glow discharge. Two types of magnetic field minimizes these losses.

### 5.1.1. Axial Magnetic Fields

The purpose of axial magnetic fields is to keep the electrons away from the walls of vacuum chamber, to decrease recombination and to increase the path length of the electrons before the collection by the anode. If  $B$  and  $v$  are parallel, the vector product is zero. Therefore, an electron which travel along the discharge axis is not affected, but the electrons moving towards walls are affected. This field can be established by winding wires around the vacuum vessel and applying a DC current through them. The force  $Bev\sin\theta$  which is perpendicular to the field is applied to the electron, when the electron travels with an angle  $\theta$  to the magnetic field. Then the electron travel in a circular motion around  $\vec{B}$  with a radius  $r$ , if there are no collisions. In this case, centripetal force is equated to the Lorentz force, and one can write:

$$\frac{m_e (v\sin\theta)^2}{r} = Bev\sin\theta \quad (5.1)$$

and Larmor radius is found by using this equation:

$$r = \frac{m_e v \sin \theta}{Be} \quad (5.2)$$

giving the radius at which electrons move around magnetic field lines. The electron comes back to the same radial position around the axis of the discharge, after each revolution of the helix (Figure 5.4).

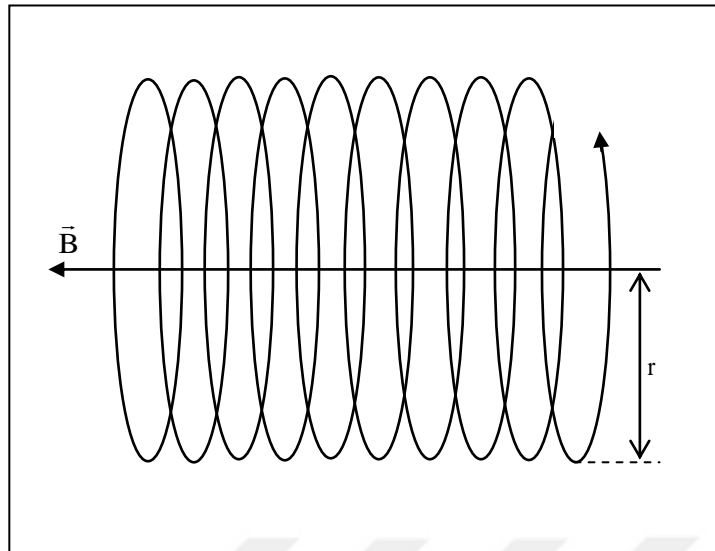


Figure 5.4. Helical motion of particle

The net velocity of the electron towards the wall is decreased to zero by the axial magnetic field, if enough current is applied. Thus wall recombination losses are decreased. In addition to this, more ionization and excitation is obtained by the helical path. Because, the total path travelled by an electron emitted from the filament to the anode is increased. By the application of axial field, the thickness of the discharge decreases and brightens with increasing magnetic field. It causes the increase of electron density in the core.

To summarize, the axial magnetic field can lower the operating pressure or increase ion current and thus sputtering rate at a constant pressure. The substrate is put on the anode in the cold cathode systems in contrast to the hot filament systems.

### 5.1.2. Magnetron Fields

Magnetrons are basically vacuum tube devices. They are used to produce or amplify high frequency signals. Some types of sputtering systems use the same principle of crossed electric and magnetic fields.

Some magnetron systems try to trap electrons near the target to increase the ionizing or sputtering effect. If the electron emitted from the surface with a velocity  $v$  into a region with a magnetic field  $B$  in  $z$  direction and a zero electric field, it travels with a semicircle of

radius,  $r = m_e v / Be$  as in the axial magnetic field case. It comes back to the surface with a velocity  $v$ , if the radius does not exceed surface boundaries (see Figure 5.5).

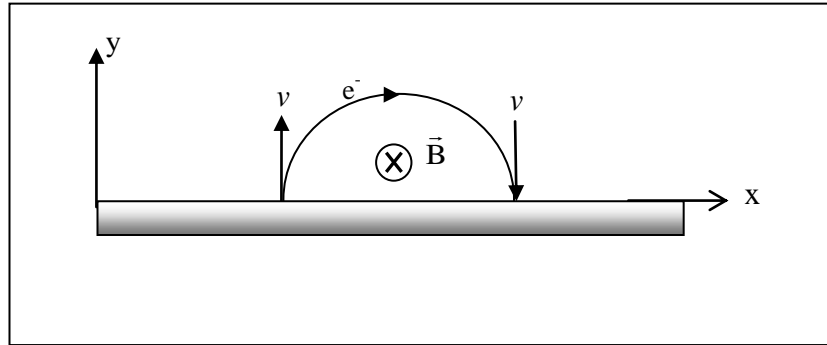


Figure 5.5. An electron with nonzero magnetic field in z direction and zero electric field

Usually, there is a strong electric field,  $\vec{E}$  in the dark space which is perpendicular to the magnetic field,  $\vec{B}$  (magnetic field is parallel to the target surface and electric field is perpendicular to the target surface) for a real magnetron sputtering system. In that case, the circular paths flatten as shown in Figure 5.6:

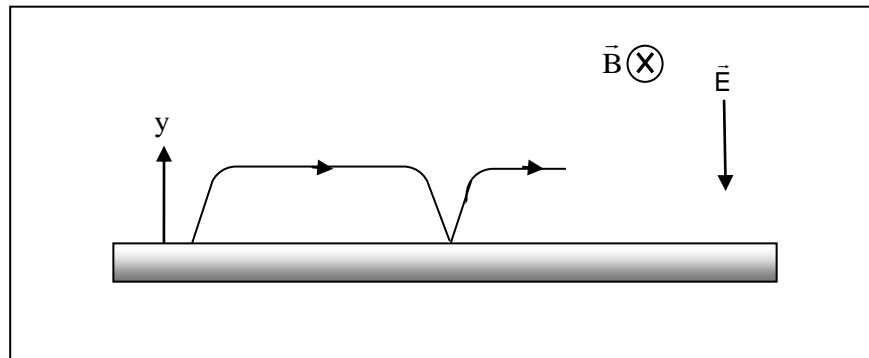


Figure 5.6. An electron with nonzero magnetic field and nonzero electric field

If the electric field,  $\vec{E}$  decreases linearly across the dark space with a thickness  $L$ , this correlation is often used for dark space fields. If  $y$  is the dimension away from the target, the surface of the target is  $y = 0$  and  $E_0$  is the electric field at the target.

From Poisson equation:

$$\nabla^2 V = -\frac{ne}{\varepsilon_0} \Rightarrow \frac{d^2 V}{dy^2} = -\frac{ne}{\varepsilon_0} = -C_1 \quad (5.3)$$

where  $y$  is the dimension from the target, Equation 5.3 yields:

$$\frac{dV}{dy} = -C_1 y + C_2 \quad (5.4)$$

And thus one gets potential and electric field as:

$$V = C_3 + C_2 y - \frac{1}{2} C_1 y^2 \Rightarrow E = -\frac{dV}{dy} = C_1 y - C_2. \quad (5.5)$$

Using the boundary conditions:

$$\left. \begin{array}{l} y = 0, E = E_0 \\ y = L, E = 0 \end{array} \right\}$$

Then electric field can be found as:

$$E = E_0 \left( 1 - \frac{y}{L} \right), \quad y \leq L \quad (5.6)$$

which shows that after dark space, electric field vanishes. If  $x$  is the distance along the target surface from the emission point of a secondary electron, this electron is accelerated away from the target at the start by a strong electric field at the surface. In that case, the equation of motion for electron is:

$$m_e \frac{dv_x}{dt} = e(v_x B)_x = e v_y B \quad (5.7)$$

$$m_e \frac{dv_y}{dt} = eE - ev_x B \quad (5.8)$$

and

$$m_e \frac{dv_z}{dt} = 0 \quad (5.9)$$

which leads to:

$$\frac{dv_x}{dt} = \frac{eBv_y}{m_e} \Rightarrow v_x = \frac{eBy}{m_e} \quad (5.10)$$

The angular velocity  $\omega = eB/m$  is put into Equation 5.10, Equation 5.11. is obtained:

$$v_x = \omega y \quad (5.11)$$

If the value of  $x$  component of velocity and angular frequency is put into Equation 5.8, one gets:

$$\frac{d^2 y}{dt^2} + \omega^2 y = \frac{Ee}{m_e} \quad (5.12)$$

Equation 5.12 looks like a simple harmonic oscillator subjected to a constant external force. The solution of it can be found by:

$$y = \frac{Eq}{m_e \omega^2} + C_1 \cos \omega t + C_2 \sin \omega t . \quad (5.13)$$

If it is differentiated, the equation below is obtained:

$$\frac{dy}{dt} = -\omega C_1 \sin \omega t + \omega C_2 \cos \omega t . \quad (5.14)$$

Initial conditions at the origin with zero initial  $x$  and  $y$  velocities at  $t=0$  is put into Equation 5.13, then  $C_2 = 0$  and  $C_1 = -Ee/m\omega^2$ , and the equation becomes:

$$y = \frac{Ee}{m\omega^2}(1 - \cos \omega t). \quad (5.15)$$

If this equation is put into Equation 5.11, and integrated for  $x$  motion, one gets:

$$x = \frac{Ee}{m\omega^2}(\omega t - \sin \omega t) \quad (5.16)$$

The velocities in  $y$  and  $x$  direction are obtained by differentiating Equation 5.15 and 5.16:

$$v_y = \frac{E}{B} \sin \omega t \quad (5.17)$$

and

$$v_x = \frac{E}{B}(1 - \cos \omega t). \quad (5.18)$$

Note that  $\omega$  is the angular frequency due to electric and magnetic fields.  $\omega$  is equal to  $eB/m_e$  in the absence of the electric field. This is called cyclotron frequency. If there was not emitting surface in this example and in the example of an axial magnetic field before, the electron would be trapped and rotate around the field with the cyclotron frequency. This process shows how external axial field can confine plasma in the middle of vacuum chamber.

If there is an electric field which is perpendicular to the surface, this frequency increases and the orbits change from circular to cycloidal. If the electrons travels further from the surface of the target, the radius of the curvature is reduced. The circular motion in an electric field free region is seen, if it reaches the negative glow by straying further than  $L$ .

The gain in the kinetic energy is equal to the loss of potential energy, then the maximum stray of the electron from the target without collision,  $y_{\max}$  can be calculated.

$$\frac{1}{2} m \dot{x}_{\max}^2 = e(V - V_T) \quad (5.19)$$

$V$  is the potential at  $y_{\max}$ ,  $V_T$  is the voltage at the negative target. i.e. cathode. In that case, one gets  $\ddot{x} = Be\dot{y}/m_e$  and  $\dot{x} = Bey/m_e$ , and from the substitution of them into Eq (5.19), one gets:

$$y_{\max} = \frac{1}{B} \left[ \frac{2m}{e} (V - V_T) \right]^{1/2} \quad (5.20)$$

stating that the maximum height electron reaches is inversely proportional to magnetic field and it increases by increasing voltage. This result is usual for both within and without the dark space, because the electric field is not presented in this equation.

To summarize, the loss of fast electrons and walls are neglected. Because, the electron is trapped close to the target and there is no wall collisions. The trapping is not effective, if there are collisions. However, electrons should make many ionizing collisions to maintain the glow and this is done, when they move amongst argon ions before being lost in the anode. Three types of magnetron sputtering systems are cylindrical magnetrons, circular magnetrons and planar magnetrons.

## 5.2. MAGNETRONS

Magnetrons prevent the bombardment of the substrate by fast charged particles. They can enable high deposition rates .

The localized erosion of the target causes the rates of deposition change with time in the planar and circular magnetrons. They need replacement of the target often, and of arching. The susceptibility of magnetrons to arching is more than any type of sputtering system. A unipolar arc can be set up. Whole discharge current can concentrate into the arc spot on the cathode by the arc. The target can melt due to great amount of heat dissipation at the cathode, if no cooling is used. This type of arc can be seen clearly in the planar magnetron, just before glow starts.

Magnetron systems generally use DC power, if substrates do not allow charge depositions. Otherwise RF power should be used for coating. A lot of problems about the target cooling are seen due to power dissipated at the target by large ion currents. Insulators create more problems in terms of this aspect. Because, they prevent both heat flow and electrical flow.

### 5.3. THE MAGNETRON SPUTTERING SYSTEM

The magnetron sputtering system used in this research is shown in Figure 5.7.

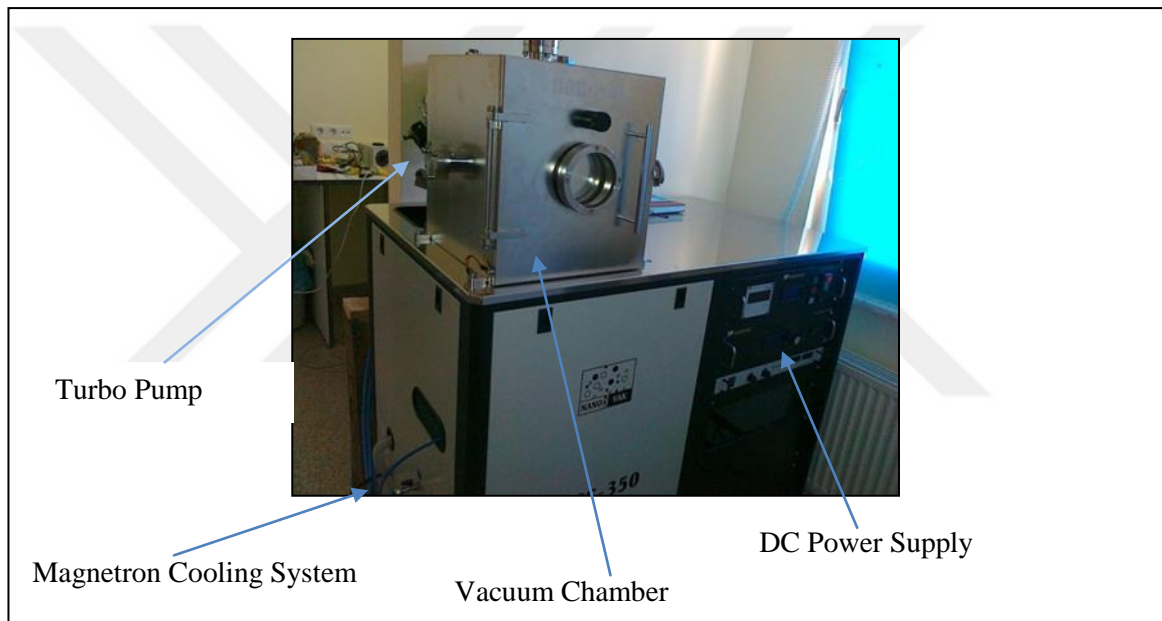


Figure 5.7. The magnetron sputtering system in plasma laboratory

There are two types of pumps connected to the vacuum chamber. One is behind the vacuum chamber and called the turbo pump; another one is below the vacuum chamber and called mechanical pump. The pump connection diagram of the system is shown in Figure 5.8 .



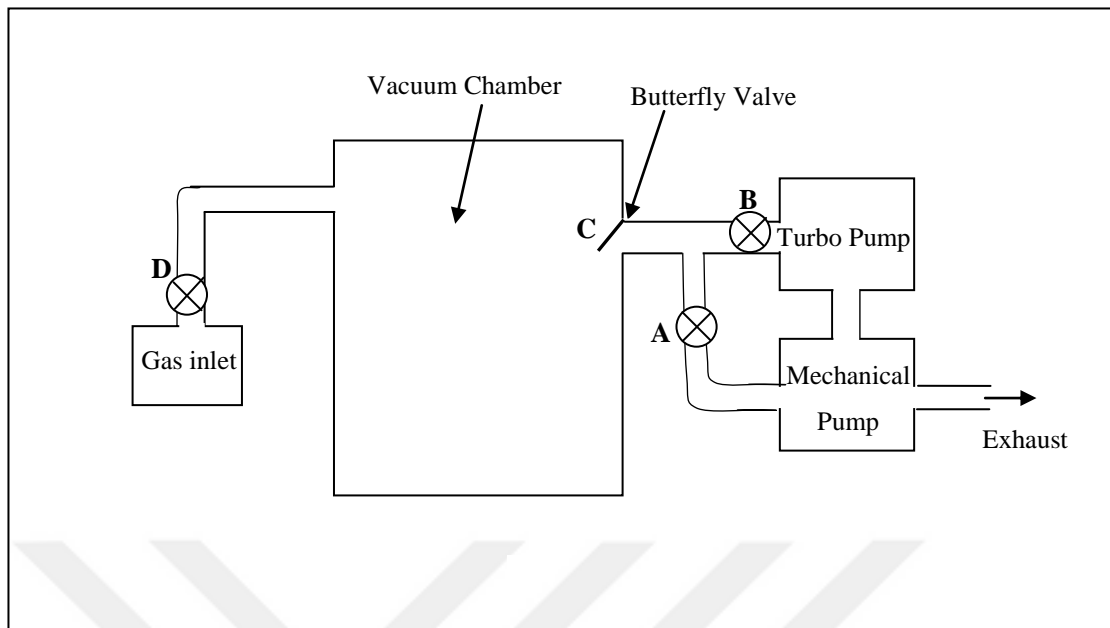


Figure 5.8. Schematic of the Yeditepe magnetron sputtering system

The procedure of running the magnetron sputtering system is presented below:

- At the start, the valves A and C are open and B and D are closed. Since turbo pump should operate below 0.5-0.7 Torr, mechanical pump starts working and pumps the system and interior of turbo pump down to the pressure of about 0.5 Torr.
- When 0.5 Torr is achieved, valve B is opened. Turbo pump starts working and the pressure decreases down to the pressure of about  $10^{-5}$ - $10^{-6}$  Torr. Since pumping is exponential process, it can take a long time. The duration of the pumping process also depends on the cleanliness of the interior walls of the vacuum chamber.
- After achieving low pressure, the butterfly valve C is half closed, turbo pump continues working and then the gas is sent into the system by opening valve D.
- The pressure increases to the pressure of about  $10^{-2}$  Torr, after the gas is sent to the system. Then, the chiller unit that provides the cooler water for magnetron is turned on.
- When desired pressure, and a stable cooling is obtained, the power supply is turned on and magnetron discharge is obtained by adjusting the voltage level of the power supply. By changing the current, the intensity of magnetron discharge can be adjusted.

## 6. DIAGNOSTICS OF LANGMUIR PROBE

### 6.1. PROBE CHARACTERISTICS

Consider a probe inserted in a plasma and it is maintained at a potential  $V$  which is applied by an external energy source. A grounded ( $V=0$ ) conducting wall is selected as a reference voltage, and  $V_p$  is called the plasma potential with respect to the ground potential. The random ion and electron fluxes to the probe are given by  $\Gamma_i = \frac{n_i \bar{c}_i}{4}$  and  $\Gamma_e = \frac{n_e \bar{c}_e}{4}$ . If the probe is at floating potential  $V_f$ , then the net flux becomes zero and current vanishes. The graph of probe current density versus probe voltage is given in Fig. 6.1. Note that the current density is  $j = e\Gamma$  where  $\Gamma$  is the flux. Some electrons can not reach to the probe, but the ion current densities are restricted to the random fluxes of  $\frac{n_i \bar{c}_i}{4}$  for negative applied potential and the electron current densities to the random fluxes of  $\frac{n_e \bar{c}_e}{4}$  for positively applied potential. These are the saturation currents as shown in Figure 6.1.

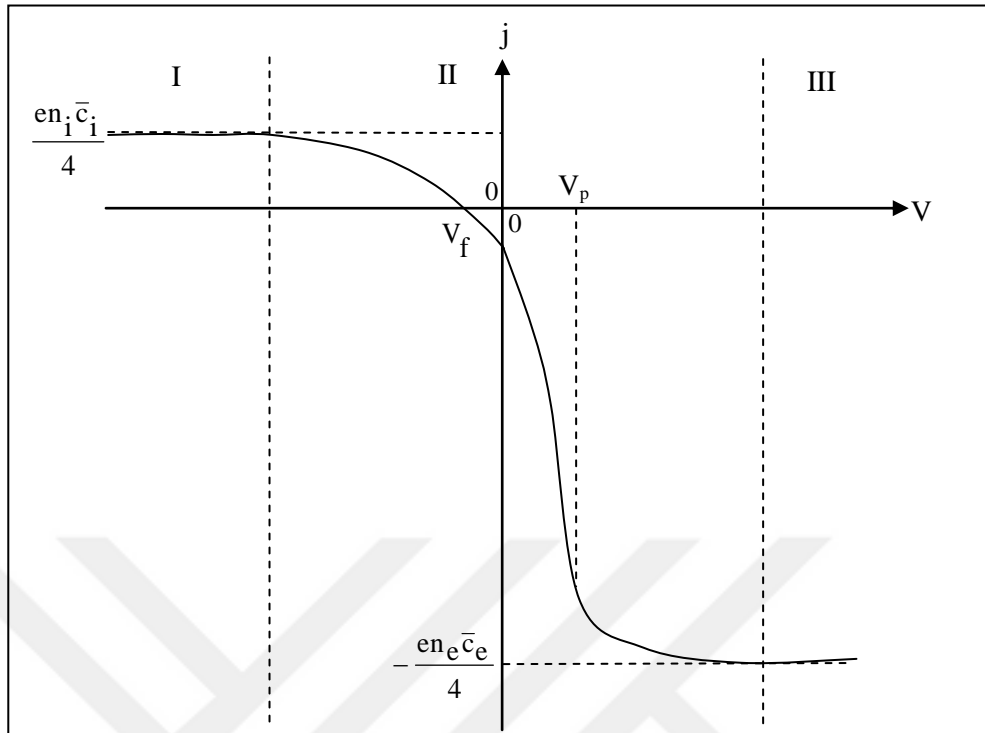


Figure 6.1. Current density versus voltage graph of a probe

Electron current can be prevented completely, if the potential is much more negative than plasma potential. The value  $\frac{n_i \bar{c}_i}{4}$  is called ion saturation current density (region I in Figure 6.1).

The electron current density at the probe can be found from Equation 2.30:

$$\left( j_e = \frac{en_e \bar{c}_e}{4} \exp\left(-\frac{e(V_p - V)}{kT_e}\right) \right), \quad V < V_p \quad (6.1)$$

This equation describes the exponential region II in Figure 6.1 until  $V_p$ . At  $V \geq V_p$ , one gets saturation density of electron, since exponential term in Eq. 6.1 becomes unity.

The sum of  $j_i$  and  $j_e$  gives the net current density to the probe, when  $V < V_p$ . This means that the total current density in region II is given by:

$$j = \frac{en_i\bar{c}_i}{4} - \frac{en_e\bar{c}_e}{4} \exp\left(-\frac{e(V_p - V)}{kT_e}\right). \quad (6.2)$$

Similarly, the net current density, when  $V > V_p$  :

$$j = \frac{en_i\bar{c}_i}{4} \exp\left(-\frac{e(V - V_p)}{kT_i}\right) - \frac{en_e\bar{c}_e}{4}. \quad (6.3)$$

As soon as  $V$  exceeds  $V_p$  (since  $T_i \ll T_e$ ), exponential term is cancelled and the electron saturation current is left.

## 6.2. APPLICATION OF LANGMUIR PROBE METHOD TO FIND ELECTRON

This technique consists on applying a DC voltage and measuring current passing through the thin wire inserted into the plasma as was described by Irving Langmuir and his co-workers (1947). In our studies, the Langmuir probes were used to obtain I-V characteristics of magnetron plasmas.

The spatial and temporal change of the plasma parameters are investigated by the help of Langmuir probes and this method is one of the most important methods to calculate electron temperature, ion temperature and plasma density. The connection diagram is shown in Figure 6.2. Langmuir probe is inserted in the magnetron sputtering system through the right (see Figure 6.4.)

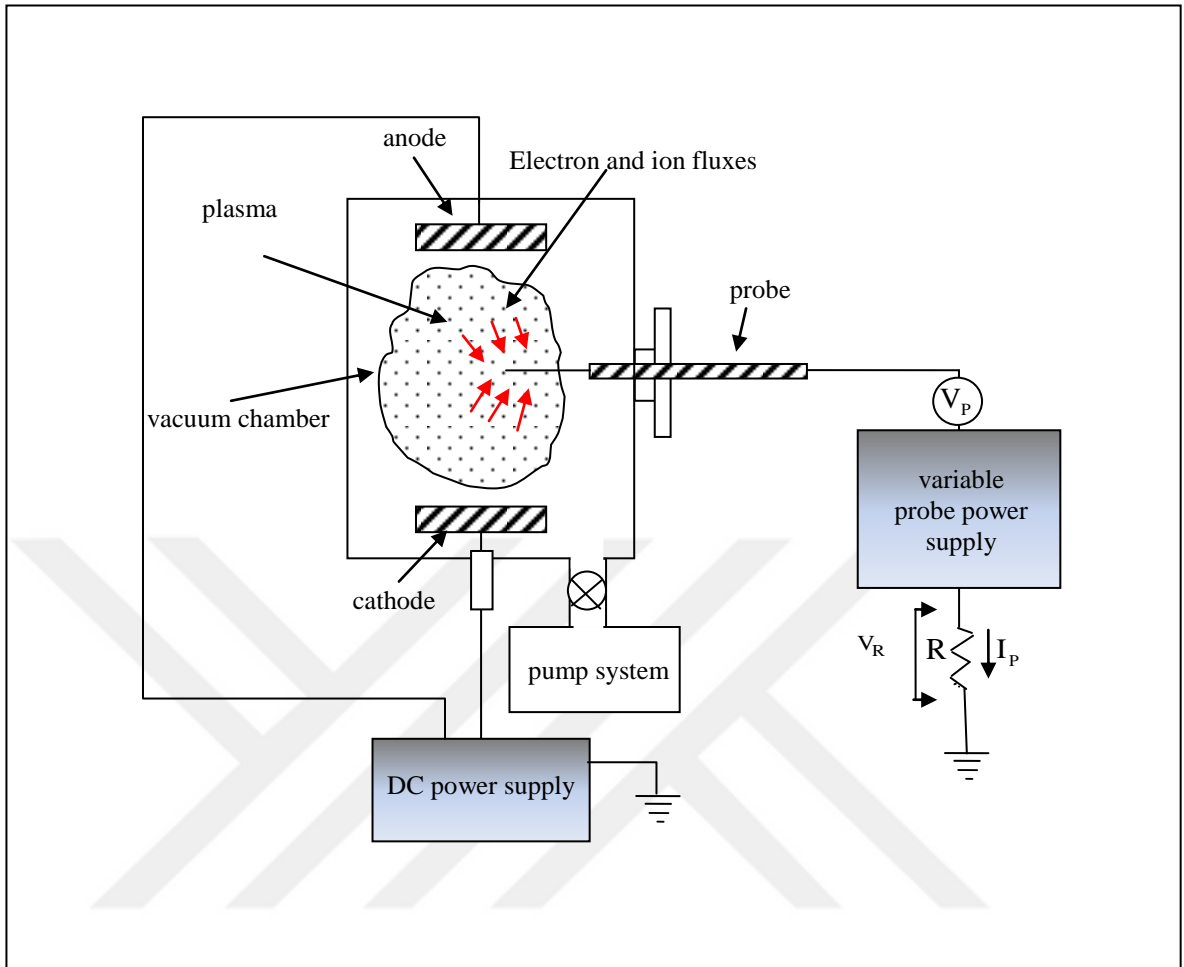


Figure 6.2. Schematic diagram of Langmuir probe system

A biased wire probe is inserted into the plasma system as in Figure 6.2 and the current is measured by changing probe voltage from negative (–) to positive (+) values.



Figure 6.3. Langmuir probe in the plasma environment during sputtering process.

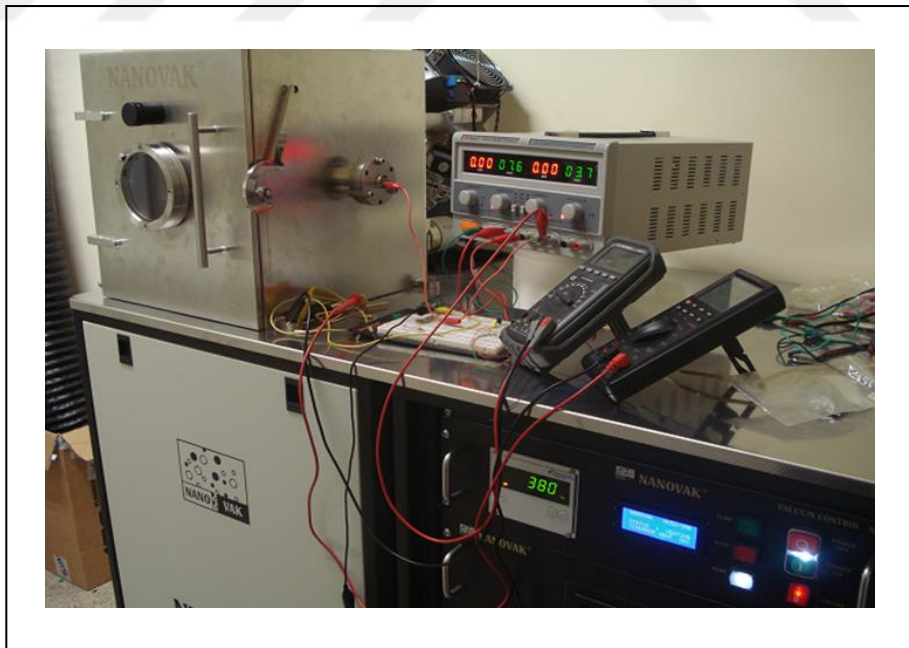


Figure 6.4. The set up of our Langmuir probe measurement system

The current is measured by biasing probe at different voltages. A characteristics graph of current,  $I$  versus  $V_{probe}$  is depicted in Figure 6.5, when there is no any external magnetic

field. Note that Figure 6.5 is the symmetric version of Figure 6.1 with respect to voltage axis.

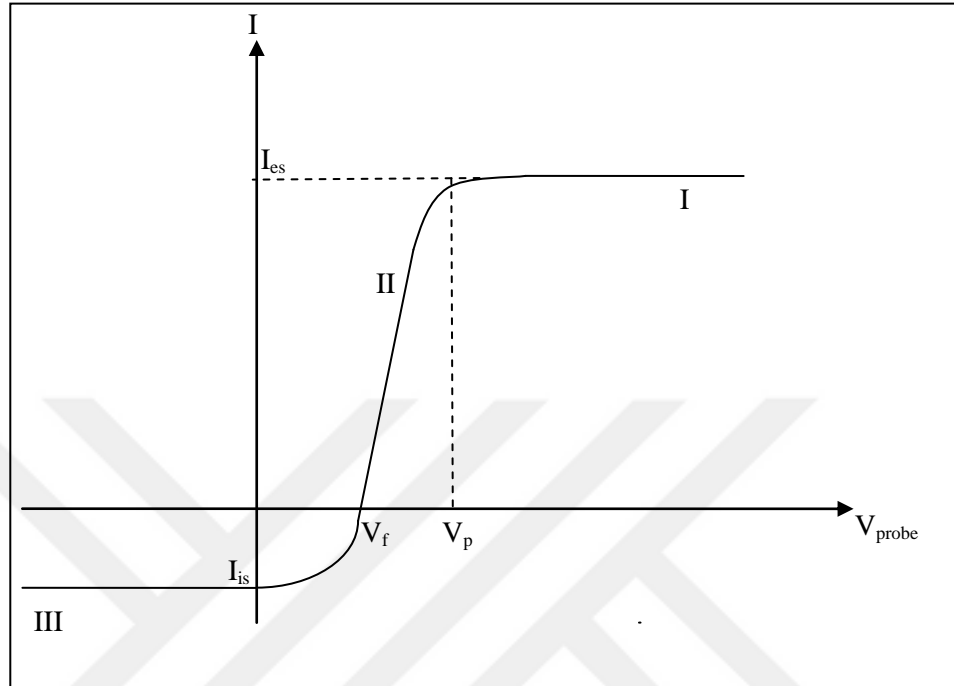


Figure 6.5. Typical current-voltage characteristics of Langmuir probe

In this figure, three different regions are denoted in I-V graph of the probe. When the probe voltage is biased to a sufficiently high positive value, ions are repelled and electrons are attracted so that an electron sheath is generated around the probe in the region I. The thickness of this sheath is equal to the Debye length and electron current is restricted by this sheath. This restricted current is called electron saturation current,  $I_{es}$ . The potential of the probe is nearly equal to the potential of the plasma at space potential,  $V_p$ .

If the voltage is decreased into region II, less number of electrons can reach to the probe and electron current reduces as probe voltage is reduced. The probe current finally drops to zero, if the numbers of electrons and ions which reach to the probe are equal. This potential is called floating potential,  $V_f$ .

If the voltage is further decreased into region III, the probe is biased to a negative voltage. A positive ion sheath is then generated around the probe, since all electrons are repelled. The restricted current in region III is called as the ion saturation current,  $I_{is}$ .

Only electrons with thermal energy exceeding the electrostatic potential energy can arrive to the probe, if we assume that a probe is biased negatively with respect to the plasma, in that case, energy conservation is:

$$\frac{1}{2}(mv_m^2) = -e(V - V_p) \quad (6.4)$$

where  $v_m$  is the minimum approach velocity allowing a probe hit.

The electron current density in terms of the velocity distribution  $f(v)$  is given by:

$$j_e = en_e \langle v \rangle = e \int_{V_m}^{\infty} f(v) v dv \quad (6.5)$$

where  $f(v)$  is assumed to be one dimensional Maxwellian velocity distribution function given by :

$$f(v) = n_e \left( \frac{m}{2\pi k T_e} \right)^{1/2} \exp \left[ -\frac{mv^2}{2k T_e} \right]. \quad (6.6)$$

By doing some calculations (changing variables, integrating and equating the potential energy to the kinetic energy), one gets the current density as:

$$j_e = (n_e e) \left( \frac{k T_e}{2\pi m} \right)^{1/2} \exp \left[ e(V - V_p) / k T_e \right] \quad (6.7)$$

Note that this equation is identical to Eq. 6.1 provided that  $\bar{c}_e = \sqrt{\frac{8k T_e}{\pi m}}$  as shown before.



If the logarithm of ratio of probe electron current is taken at two points from region I and II, one can write:

$$\ln(j_1 / j_2) = (e / kT_e)(V_1 - V_2). \quad (6.8)$$

The electron temperature below can be obtained as:

$$T_e = (e / k)(V_1 - V_2) [\ln(j_1 / j_2)]^{-1} [K]. \quad (6.9)$$

The electron temperature is in units of eV:

$$T_e = (V_1 - V_2) [\ln(j_1 / j_2)]^{-1} [eV] \quad (6.10)$$

The equation 6.5. is integrated over all velocities, when the voltage of probe is much larger than the plasma potential. Because, all electrons can be gathered on the probe. Then the electron saturation current can be calculated :

$$j_e = n_e e (kT_e / 2\pi m_e)^{1/2}. \quad (6.11)$$

The ion saturation current is much smaller than the electron saturation current by a factor of  $m_i / m_e$ . By using the equations (6.9), (6.10), and (6.11), we can find electron temperature and electron saturation current. Then the electron density can be calculated by using them. If the electron and ion densities are assumed the same, then ion temperature can be calculated from equation (6.12) [15].

$$j_i = -n_i e z_i (kT_i / 2\pi m_i)^{1/2}. \quad (6.12)$$

## 7. OPTICAL EMISSION SPECTROSCOPY

These kinds of spectrometers measure the intensity of the peaks as a function of the wavelengths and gives information about the composition of the material.

There is a grating, a CCD detector, a light source, sample beam and reference in an optical emission spectroscopy.

The emission spectrum helps to analyse the substance chemically. If the electrons in an atom make transition from higher energy state to a lower one, electromagnetic radiation is emitted. From this condition, emission spectrum of a chemical compound can be found. The energy difference between two states is equal to the energy of the emitted photon with a specific wavelength. There are a lot of transition levels in an atom which correspond to different radiated wavelengths. The emissions of these wavelengths generate emission spectrum which is different for each element. Therefore, the study of the emission spectrum gives hint about the substance chemically. The plasma is the easiest substance which creates emission spectra, since it includes active and energetic gas molecules.

The plasma of inserted gas is created between the anode and cathode, by the energy of the high voltage which excites the electrons and thus gas atoms so that they emit light. The graph of intensity of these transitions versus wavelength is obtained by emission spectroscopy. The intensity of the peaks can be obtained on the graph easily, and using these, electron temperature of the plasma can be found by the help of Boltzmann plot method.

In our studies, the measurements of the intensity peaks were done by emission spectrometer BAKI developed by BEAM Ar-Ge Optic, Laser Technologies Ltd, Turkey.

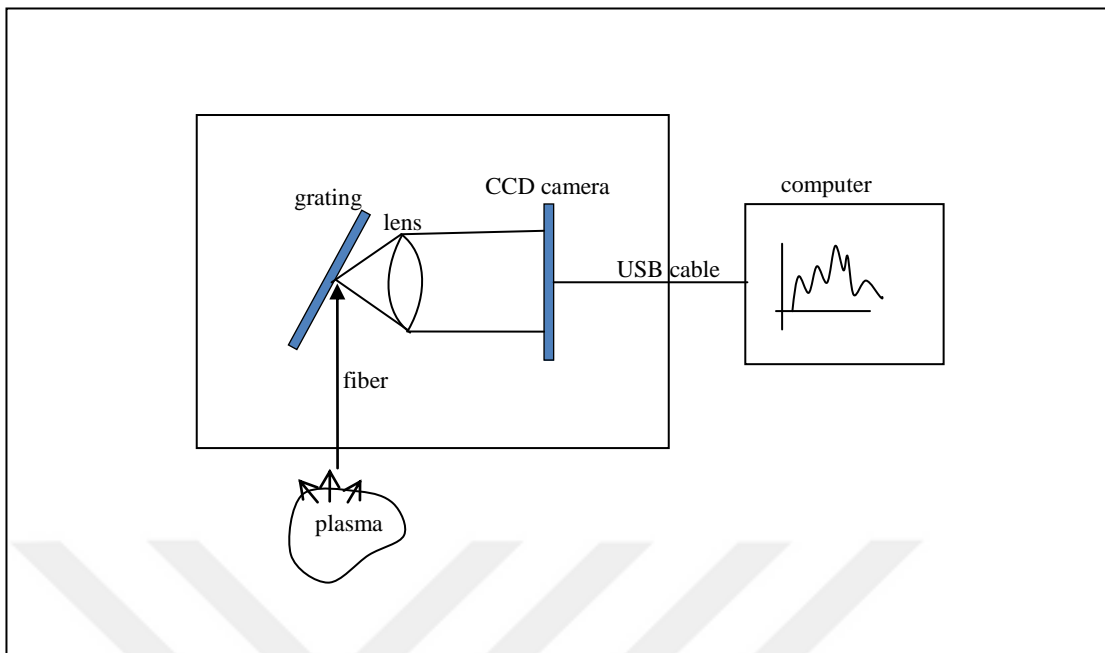


Figure 7. Diagram of optical emission spectroscopy

## 8. BOLTZMANN PLOT FOR TEMPERATURE

If the system of atoms and photons are considered in the thermal equilibrium at a temperature  $T$ ,  $N_1$  and  $N_2$  is the number of atoms in energy states  $E_1$  and  $E_2$  respectively. The number of atoms in other energy states are very small compared to  $N_1$  and  $N_2$  (Figure 8.1).

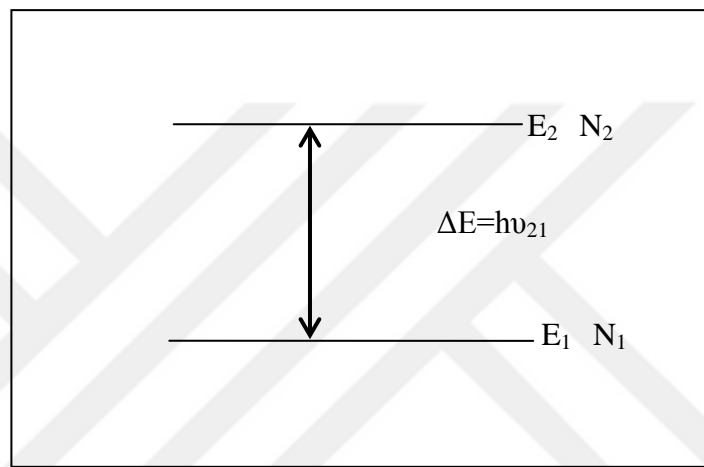


Figure 8.1. Energy level diagram of two level system

Three atomic processes are important in the condition of resonance: induced absorption, induced emission and spontaneous emission (see Figure 8.2).

The atoms absorb one photon of energy and is excited from the ground state  $E_1$  to a higher state  $E_2$  with the stimulated absorption (Figure 8.2.a). This process reduces the number of photons in the radiation field by one. The number of atoms in the ground state which absorb a photon and are excited to  $E_2$  per unit time is proportional to the number of photons with energy  $h\nu_{21}$  and the number of atoms in energy state  $E_1$ , in an assembly of atoms subject to a radiation field with a distribution of  $\rho(\nu)$ . Thus, one gets the rate of change of  $N_1$  due to induced absorption by:

$$\frac{dN_1}{dt} = -B_{12}\rho(\nu_{12})N_1 \quad (8.1)$$

where  $B_{12}$  is the Einstein coefficient for induced absorption.

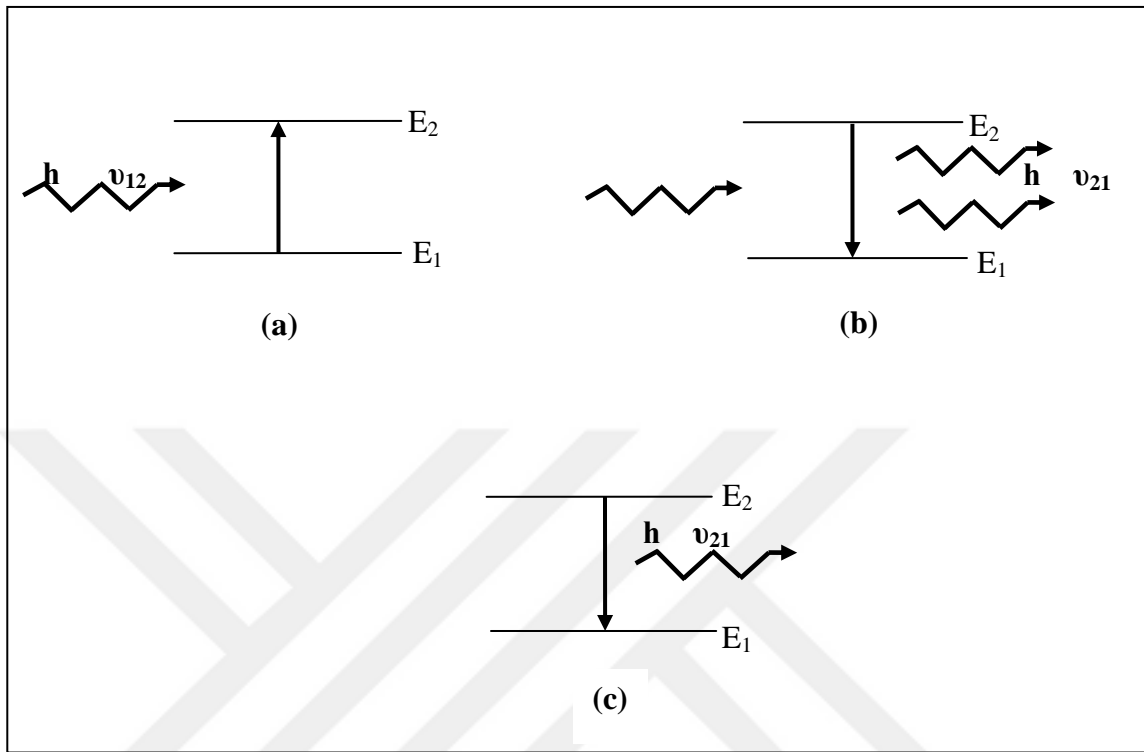


Figure 8.2. (a) Induced absorption, (b) Induced emission, (c) Spontaneous emission

In the process of simultaneous emission of a photon, the radiation field induces transitions from the excited state  $E_2$  to the ground state  $E_1$  (see Figure 8.2.b). There is a net increase of one photon in the radiation field, and the induced photon is emitted with the same frequency as the incoming photon. The rate of change of  $N_1$  due to induced emission can be written by:

$$\frac{dN_1}{dt} = B_{21}\rho(\nu_{21})N_2 \quad (8.2)$$

The proportionality constants,  $B_{21}$  is the Einstein coefficient for induced emission.

It is possible for an atom to emit a photon without the aid of an inducing photon. Because, there is a natural tendency for excited atoms to decay into lowest energy state. This is

called spontaneous emission. An additional photon is added to the radiation field in this process. The rate of change of  $N_1$  due to spontaneous emission can be written as:

$$\frac{dN_1}{dt} = A_{21}N_2 \quad (8.3)$$

$A_{21}$  is Einstein coefficient for spontaneous emission and the number of atoms which spontaneously decay from  $E_2$  to  $E_1$  is dependent only on the selected transition  $E_2-E_1$  and the atomic structure. There is a loss in Eq. 8.1, but a gain in Eq. 8.2 and 8.3. Because, there is a difference in signs.

The sum of the three contributions gives the total rate of change of  $N_1$  per unit time.

$$\frac{dN_1}{dt} = [A_{21} + B_{21}\rho(\nu_{21})]N_2 - B_{12}\rho(\nu_{12})N_1 \quad (8.4)$$

The total rate of change of  $N_2$  can be written by:

$$\frac{dN_2}{dt} = [-A_{21} - B_{21}\rho(\nu_{21})]N_2 + B_{12}\rho(\nu_{12})N_1 \quad (8.5)$$

If Eq. 8.4 is added to Eq.8.5, one gets:

$$\frac{d(N_1 + N_2)}{dt} = 0 \quad (8.6)$$

This shows that the number of atoms in the system is constant in time and  $N_1 + N_2 = N_0$  in a stationary field. If the left hand side of Eq.8.4 is zero, one obtains:

$$\rho(\nu_{21}) = \frac{A_{21}}{B_{21}} \left( \frac{N_1 B_{12}}{N_2 B_{21}} - 1 \right)^{-1} \quad (8.7)$$

The energy level populations of the species can be shown by the Boltzmann distribution for the plasma in a local thermodynamic equilibrium:

$$\frac{N_1}{N_2} = \frac{g_1}{g_2} \exp\left(\frac{h\nu_{21}}{kT}\right) \quad (8.8)$$

$k$  is the Boltzmann constant,  $T$  is the electron temperature and  $g_i$  ( $i=1,2$ ) is the number of degenerate sublevels of the energy state. If Eq.8.7 is put into Eq.8.8, one can find:

$$\rho(\nu_{21}) = \frac{A_{21}}{B_{21}} \left[ \frac{g_1 B_{12}}{g_2 B_{21}} \left( \exp\left(\frac{h\nu_{21}}{kT}\right) - 1 \right) \right]^{-1} \quad (8.9)$$

Planck's black-body radiation law at temperature  $T$  can be written as below:

$$\rho_\nu(\nu, T) d\nu = \frac{8\pi h \nu^3}{c^3} \frac{1}{e^{h\nu/kT} - 1} \quad (8.10)$$

If Eq.8.9 is compared with Planck radiation law (Eq.8.10), the relationship between the Einstein coefficients can be written as:

$$A_{21} = \frac{8\pi h \nu_{21}^3 B_{21}}{c^3} \quad (8.11)$$

The rate of induced absorption is the same as the rate of induced emission for levels  $E_1$  and  $E_2$  with equal statistical weights ( $g_1=g_2$ ).

$$g_2 B_{21} = g_1 B_{12} \quad (8.12)$$

In equations above, a thermal spectrum for which the radiation field was described by a continuous distribution. However, if the fluorescence of a plasma was thought to determine the electron temperature, the problem of non-thermal radiation sources characterized by discrete spectra should be treated. Consider a beam of radiation with intensity  $I_\nu$  between  $\nu_{21}$  and  $\nu_{21} + d\nu$  travelling in the positive  $x$  direction through a layer of atoms with the number of atoms  $N_1$  and  $N_2$  in the energy states  $E_1$  and  $E_2$  respectively.

The change in the intensity of the beam is:

$$\Delta I_{21} = \frac{h\nu_{21}}{4\pi} A_{21} N_2 L + \frac{I_\nu h\nu_{12}}{c} (B_{21} N_2 - B_{12} N_1) L \quad (8.13)$$

Where  $L$  is thickness of the layer,  $A_{21}$ ,  $B_{21}$  and  $B_{12}$  are the Einstein coefficients for spontaneous emission, induced emission and induced absorption respectively. The second term in Eq.8.13 can be neglected for an optically thin plasma. Then, one can write:

$$\Delta I_{21} = \frac{h\nu_{21}}{4\pi} A_{21} N_2 L \quad (8.14)$$

From the Maxwell-Boltzmann distribution, atomic state population at a temperature  $T$  can be written as:

$$N_2 = \frac{N_0 g_2 \exp\left(-\frac{E_2}{k_B T}\right)}{Z} \quad (8.15)$$

$Z$  is the partition function,  $g$  is the degeneracy,  $N_0$  is the total number density of the atomic species, excited and unexcited. For two level system, one can write the partition function:

$$Z = \sum_{i=1}^z g_i \exp\left(\frac{E_i}{k_B T}\right) \quad (8.16)$$

$$\nu_{21} = \frac{c}{\lambda_{21}} \quad (8.17)$$

If Eq.8.17 and Eq.8.15 is put into Eq.8.14, one gets:

$$\Delta I_{21} = \left(\frac{hcN_0L}{4\pi Z}\right) \left(\frac{g_2 A_{21}}{\lambda_{21}}\right) \exp\left(-\frac{E_2}{k_B T}\right) \quad (8.18)$$



There are many different atomic transitions from  $E_k$  to  $E_i$ . This can be achieved by replacing  $k$  instead of 2 and  $i$  instead of 1.

$$\Delta I_{ki} = \left( \frac{hcN_0L}{4\pi Z} \right) \left( \frac{g_k A_{ki}}{\lambda_{ki}} \right) \exp\left( -\frac{E_k}{k_B T} \right) \quad (8.19)$$

$\Delta I_{ki}$  is the integrated intensity of a spectral line which occurs between the upper energy level and the lower energy level  $i$  of the species in the ionization stage  $Z$  in an optically thin plasma ( $c$  is the speed of the light,  $\lambda_{ki}$  is the transition line wavelength,  $L$  is the characteristic length of the plasma,  $h$  is the Planck constant and  $A_{ki}$  is the transition probability).

Taking the natural logarithm of Eq.8.19, one gets:

$$\ln\left( \frac{\Delta I_{ki} \lambda_{ki}}{g_k A_{ki}} \right) = -\frac{1}{k_B T} E_k + \ln\left( \frac{hcLN_0}{4\pi Z} \right) \quad (8.20)$$

If the magnitude on the left-hand side for several transitions is plotted against the energy of the upper level of the species in the ionization stage, this results in Boltzmann plot which is linear. The slope of the Boltzmann plot is the inverse of the temperature.

This last equation can be used only local thermodynamic equilibrium and optically thin plasmas [16].

## 9. SEM ANALYSIS

The scanning electron microscope (SEM) is a kind of microscope which uses high energy electrons instead of light. The resolution of the SEM is much more higher than a light microscope. The degree of magnification can be controlled more, since the SEM uses electromagnets.

It works in a vacuum environment, so a special preparation of nonmetal sample is needed before investigation. Because, they are not conductive, they should be coated with high conductive material such as gold to create a conductive surface and prevent water contamination to the vacuum. A special mini sputtering device is used for coating, and coating time is very short (the coating time of our samples were about 5 seconds). After coating, the samples prepared are put into the SEM, it is evacuated using a pump in 15-20 minutes. The electron beam is formed by an electron gun at the top of the SEM, see Figure 9.1. The electron beam travels through the microscope vertically. There are electromagnetic lenses and coils on its road. The beam is focused by these lenses onto the sample. X-rays and electrons are knocked out of the sample surface by the impact of these accelerated electrons. The beam electrons are decelerated by this impact. Detector inside the chamber collects secondary electrons, backscattered electrons and X-rays. Due to this electron and sample interaction, a signal is created. This signal is sent to a computer for data analysis software image. Especially backscattered and secondary electrons are used for imaging. The morphology of the sample is seen by the help of secondary electrons and contrasts in the composition of the sample is seen by the help of backscattered electrons. See Figure 9.2 [17].

In these studies, SEM analysis were established by Tescan, Mira/LMU Schottky.

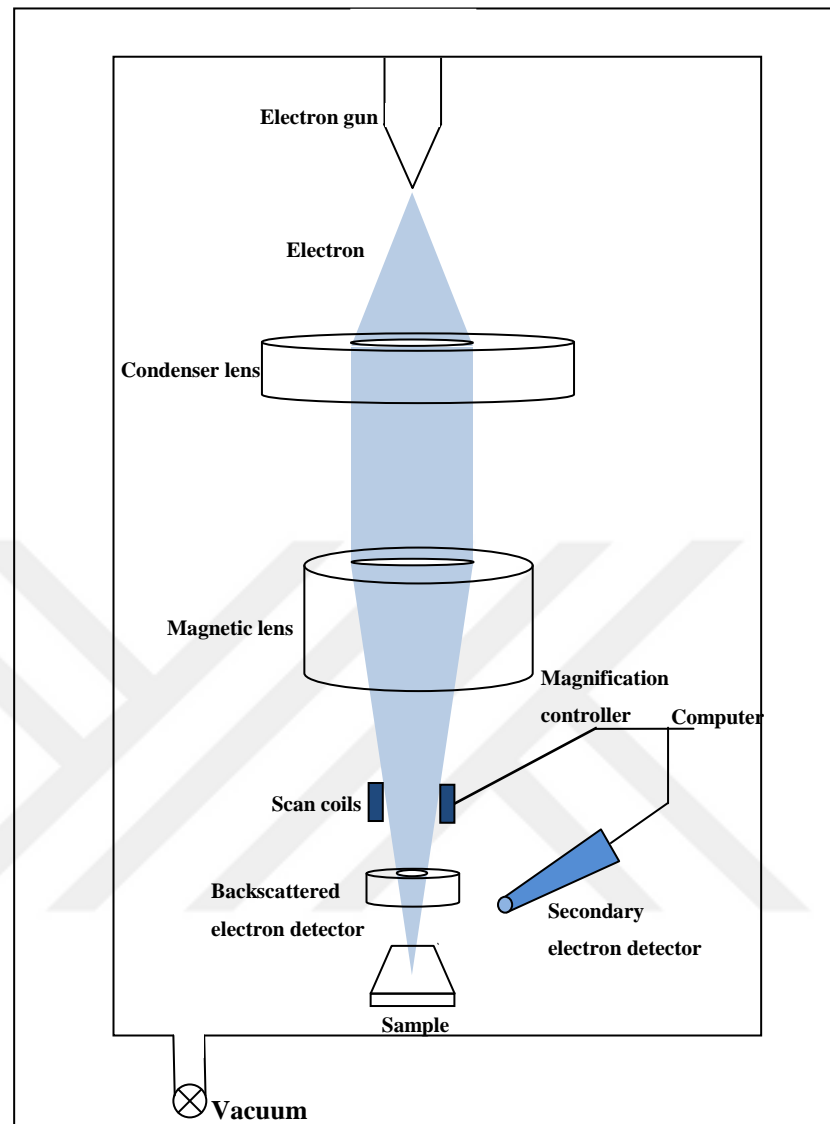


Figure 9.1. Diagram of an scanning electron microscope

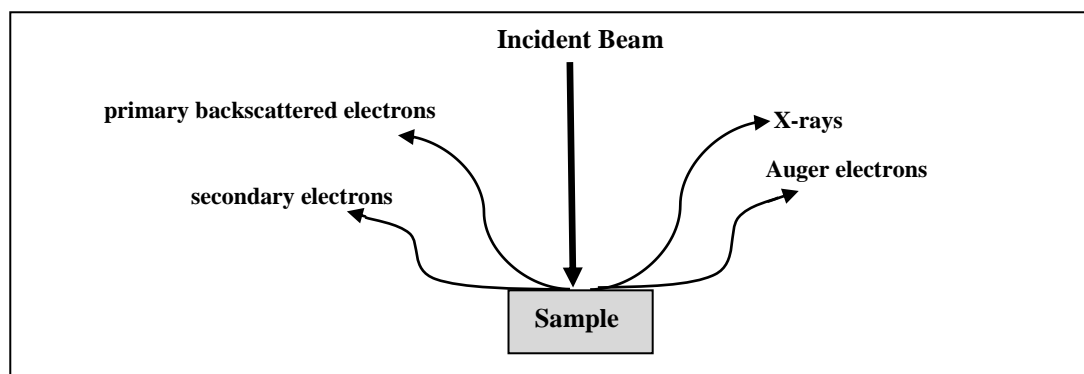


Figure 9.2. Electrons and X-rays which are ejected from the sample [18]

## **10. ENERGY-DISPERSIVE X-RAY SPECTROSCOPY (EDS)**

EDS is a technique which is used to analyze the substance elementally and chemically. The interaction of X-ray excitation and the sample gives information about the sample. A beam of high energy particles (protons or electrons) are send onto the substance surface and X-rays are emitted. Each atom has ground state electrons or electron shells which are bound to the nucleus. When the beam ejects an electron in an inner shell by exciting it, an electron hole is created. If an electron from a higher energy level fills this hole, an X-ray may be emitted due to the energy difference between the higher and lower energy levels. The spectrometer measures the energy of the X-rays emitted from the sample. This gives information about the atomic structure and elemental composition of the specimen. Since, each element has a unique set of peaks on the X-ray spectrum.

## 11. ATOMIC FORCE MICROSCOPY

Atomic force microscopy (AFM) is a high resolution scanning probe microscopy to measure extreme small surfaces in nanometer scale. AFM includes a cantilever, a laser diode, a piezoelectric scanner, a photodetector, and a computer. A sharp probe tip at the end of the cantilever is used to sense surface characteristics. The probe tip of the cantilever scans the surface of the sample, and cantilever is deflected due to the repulsive force between the surface of the sample and tip. Position sensitive photodetector measures the angular deflection of the cantilever, and this gives knowledge about the roughness of the surface. AFM provides three dimensional surface profile, while SEM provides a two dimensional image of sample.

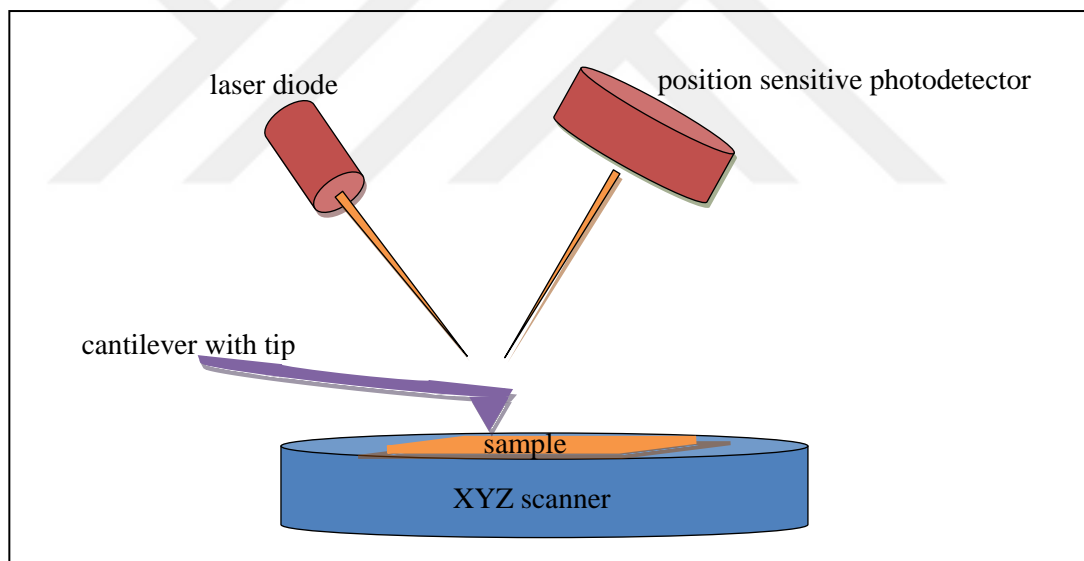


Figure 11. Diagram of an atomic force microscopy

AFM (NanoScope IV, Digital Instrument) was used in this project to study the roughness of the cotton fabrics deposited by silver for 4 minutes after different washing cycles. It was very difficult to investigate the surface of the textiles by using AFM. Because, the fibres of the textiles caused the bending of the probe tips which are very expensive. Therefore, only a few AFM pictures will be presented in this study. Surface roughness was determined by AFM in terms of RMS roughness.

## 12. CONTACT ANGLE MEASUREMENT

While the oxygen atoms have slightly negative charge, hydrogen atoms have positive one in the water molecules. Hydrogen bond binds water molecules to each other in water. However, polar molecules associate with water molecules via hydrogen bond. Therefore, they are hydrophilic. Nonpolar molecules are hydrophobic and repel water molecules. The reason is that these nonpolar molecules do not form hydrogen bond with the water molecules. Thus, the free energy of the system is minimized. Greater contact angle of water drop means greater hydrophobicity.

Contact angle measurement is a technique which determines the wettability of the materials [18]. If there is a drop of liquid on a solid, contact angle is the angle between the interface of liquid-vapor and solid-liquid. Contact angle can be measured by the analysis of drop shape and from this analysis, surface energy can be found. The direction of the view of the drop is not important. Because, it is symmetric about a central vertical axis. The shape of the drop is determined by the inertia or viscosity. That is, the drop is shaped by the gravity and tension.

The slope of the line which is tangent to the drop at the liquid-solid-vapor interface is found [19]. For this purpose, one drop of liquid is put on the sample, and contact angle is measured. It is generally found by using a device called goniometer.

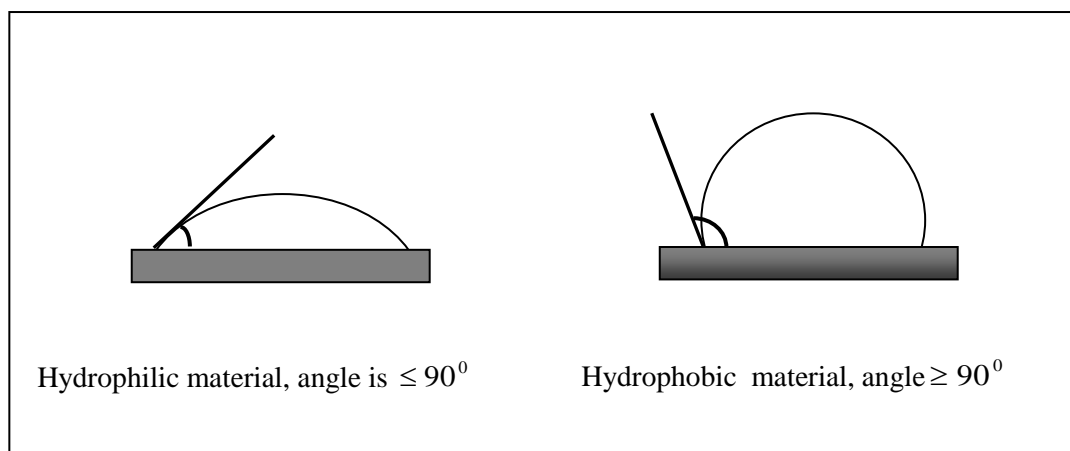


Figure 12. Contact angle measurement method

For the hydrophilic surfaces, the surface free energy is high, wettability and adhesiveness are very good at the hydrophilic materials. Therefore, the contact angle of the hydrophilic material is smaller than  $90^{\circ}$ . On the contrary, solid surface free energy is low, wettability and adhesiveness are poor for the hydrophobic materials. Therefore, the contact angle is greater than  $90^{\circ}$  for the hydrophobic materials. In the past decade, a lot of conventional methods were applied to improve the hydrophobicity of the textiles [20].

There are different types of contact angle measurement methods. The static sessile drop method, dynamic Wilhelmy method, powder contact angle method, single-fiber Wilhelmy method and the dynamic sessile drop method.

The static sessile drop method is the most frequently used method, which was also used in our studies. When the thermal equilibrium of solid, liquid and vapour is reached, then the contact angle is measured.

In our initial studies, whether the textile is hydrophobic or hydrophilic was decided only by taking picture and looking at the profile of the drop. In the later studies, the contact angles on the textiles (cotton and polyester) which were coated by silver and copper were measured by a contact angle goniometer (KSV CAM 200) with a drop image standard software in Institute of Gebze Yüksek Teknoloji. A computer controlled water dispensing system and CCD camera was used in this system. Contact angle measurements on the textiles which were coated by silver and copper were done before and after the abrasion tests to see the effect of abrasion on the hydrophobicity of the coated textile.

### 13. ANTIBACTERIAL TESTS

Nowadays, there are many researchers who work in the area of antibacterial textiles and surgical tools, since textiles and those tools are proper for microorganisms to grow. These microorganisms can cause a lot of illnesses, unpleasant odors, deterioration of textiles and color degradation. A single microorganism which causes the smell of socks can lead to the hospital infections and lots of deaths.

Antibacterial textiles can be used for the production of many things e.g. shoes, sportswears, furnishings, wound care wraps, wipes, towels and sheets. They are very important for high-quality of life and safety. Self-sterilizing fabrics are great advantages to reduce disease transfers among patients and hospital staff. Antibacterial products which are used nowadays, such as triclosan has short active time and high costs. In addition to this, low-molecular weight polymer antimicrobial agents generally leach out from the fabrics towards the environment and to the skin of the wearers [21].

The most important method for the inactivation of bacteria is the coating technique. Silver and copper help the textiles to obtain antimicrobial properties, when they are deposited on the textiles by different methods such as sol-gel coating, chemical washing and magnetron sputtering [21]. The surface properties of textiles can be changed by these coating methods. However, chemical techniques such as sol gel coating can cause toxic effects in the nature. Vacuum techniques are more preferable, because they are nontoxic. Magnetron sputtering system which we used is a safe method as an antibacterial coating.

Each target metal which is used for deposition has different effects on the cells. If the amount of the copper inside the cell increases, oxidative stress is generated and hydrogen peroxide is produced. Copper causes a chemical reaction called as Fenton-type reaction which leads to oxidative damage to the cells. Silver ions cause the death of the cell. Because, they react with thiol group in enzymes and inactivate them. They can also react DNA by preventing replication and enhancing pyrimidine dimerization by the photodynamic reaction.  $\text{TiO}_2$  is also inhibitor, because of the photocatalytic generation of strong oxidizing power with the effect of UV light [21].



Bacteria such as *Staphylococcus aureus* and *Escherichia coli* were used in our studies. *Staphylococcus aureus* is a gram positive bacteria and it causes hospital infections. Gram-positive bacteria has a thick peptidoglycan layer around it, so they do not need any rigid cell wall. They can be stained by crystal violet due to this peptidoglycan layer. *E. Coli* is a gram negative bacteria and it can not retain crystal violet, because it has only a thin layer of peptidoglycan, but has a rigid cell wall to support the cell.

In this thesis, the antibacterial properties of textiles deposited by different metals were examined. These tests were done in Yeditepe University Genetics and Bioengineering Department. Two different methods were used. One of them was parallel streak method. Another one was suspension test. Initially, growth medium was prepared and the bacteria was proliferated. The antimicrobial effects of copper and silver coated textiles on *Escherichia coli* (ATCC25922) and *Staphylococcus aureus* (ATCC25923) were measured by parallel streak method (AATCC TM 147) and by suspension test (ASTM E 2149). Pure bacteria cultures were performed in Luria-Bertani Agar (LB) (Sigma-Aldrich, USA) medium separately for the parallel streak method. The textiles coated with Cu and Ag were laid down onto as streaks which were nearly 60x20 mm. Coated sides which will contact with bacteria were added to these agars and incubated for 24 hours at 37<sup>0</sup>C. Following this incubation process, the diameter of inhibition zones were measured milimetrically, to check if there is an inactivation [22].

Luria-Bertani (LB) broth (Sigma-Aldrich, USA) was prepared for the suspension test. Bacteria cultures were adjusted to 10<sup>8</sup> cfu/ml. Coated and uncoated textile samples were divided as streaks which are nearly 70x30 mm. After that, textiles were added into bacteria and broth mixture and incubated for 1 hour by shaking incubator. After incubation 100 µl was taken from all the solutions and then serial dilution procedure was prepared. After this procedure from 10<sup>-6</sup>, 10<sup>-7</sup>, 10<sup>-8</sup> dilutions, 100 µl was taken and added to prepare LB agars by using drigalski spatula. After 24 hours incubation, colony forming units (cfu) were calculated. All experiments were carried out three times and the mean were calculated [22].

## **14. RESULTS AND DISCUSSION**

Before carrying out experiments, it is better to study the diagnostics of the magnetron sputtering coating system in order to do that several tests were done.

### **14.1. ELECTRICAL PROPERTIES OF PLASMA SYSTEMS**

In order to initiate plasma, pressure, voltage and current must have certain values. Changing any of these parameters can cause difficulty to retain constant plasma properties. This can be done by keeping one or two parameters constant and changing the other parameter.

In this study, hysteresis curves of current-voltage and current-pressure of the plasma system were obtained.

Secondly, Langmuir probe studies helped to calculate local pointwise electron temperatures in the plasma. Electron temperatures were calculated at different pressures by using single Langmuir probe method. In addition to this, electron temperatures on different probes which were placed at a distance of 8 mm with each other were calculated by using multiple Langmuir probes.

The Boltzmann plot method was also used to calculate electron temperature of the bulk plasma. Emission spectrum of plasma was obtained at different voltages with the help of optical emission spectroscopy and electron temperatures were also calculated by using Boltzmann plot method.

#### **14.1.1. Hysteresis**

Hysteresis is a condition in which a system can not go back to its original condition. In this study, the hysteresis effect on I-V and I-P characteristics of magnetron plasma was studied.

The current versus voltage (I-V) characteristics of a plasma system gave the impedance behaviour of plasma system. The inverse of the slope of I-V curve is a measure of the

impedance of the plasma system. The plasma acts as a nonlinear load connected to the power supply. The current versus voltage results were taken in the magnetron plasma at a constant pressure of  $10^{-2}$  Torr.

The voltages between anode and cathode currents were measured. These results are presented in Figure 14.1, Figure 14.2, and Figure 14.3 where the letters A,B,C on these figures mean:

**A:** The power point at which the plasma is initiated.

**A-B:** Linear resistive regime

**B-C:** Nonlinear impedance and hysteresis region

The inverse of the I-V graph gives the resistivity. The inverses of the slopes were found

$\left(\frac{0.04}{80}\right)^{-1} = 2\text{ k}\Omega$  between 320 V-400 V,  $\left(\frac{1.2}{140}\right)^{-1} = 115\ \Omega$  between 400 V to 540 V and

$\left(\frac{0.86}{20}\right)^{-1} \cong 20\ \Omega$  between 520 V- 540 V. It is obvious that from Figure 14.1 that between

A-B (320 V- 400 V) the I-V slope is small so that the impedance of the plasma is high (nearly 2 k $\Omega$ ). In addition this region is not affected from the hysteresis effects. In other words, by changing voltage between 300 V and 400 V, the plasma acts as linear load. Increasing voltage from 400 V to 540 V reduces the impedance to nearly 115  $\Omega$ . If the voltage is reduced back to 520 V from 540 V, the impedance is smallest, i.e, nearly 20  $\Omega$ . Between 320 V and 400 V, the plasma acts more resistively.

This procedure states that for  $P=10^{-2}$  Torr, it is better to increase voltage to 540 V first and then reduce a little to get smallest resistivity, so that faster coating on the sample surfaces.

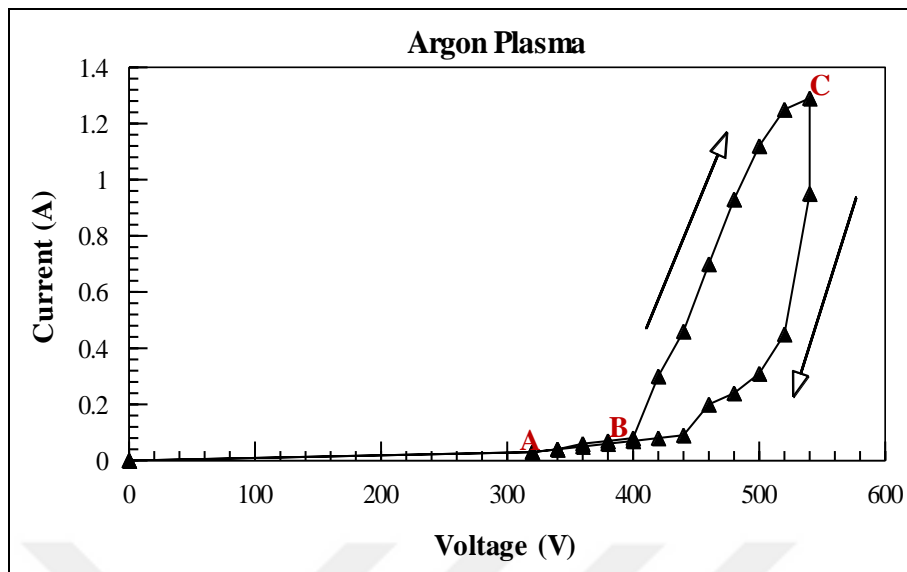


Figure 14.1. The graph of current versus voltage at  $10^{-2}$  Torr with 100% pure argon

Similar effects were observed with the argon gas with 20% air and 50% nitrogen, although the hysteresis effect was smaller in the Ar-N<sub>2</sub> mixture.

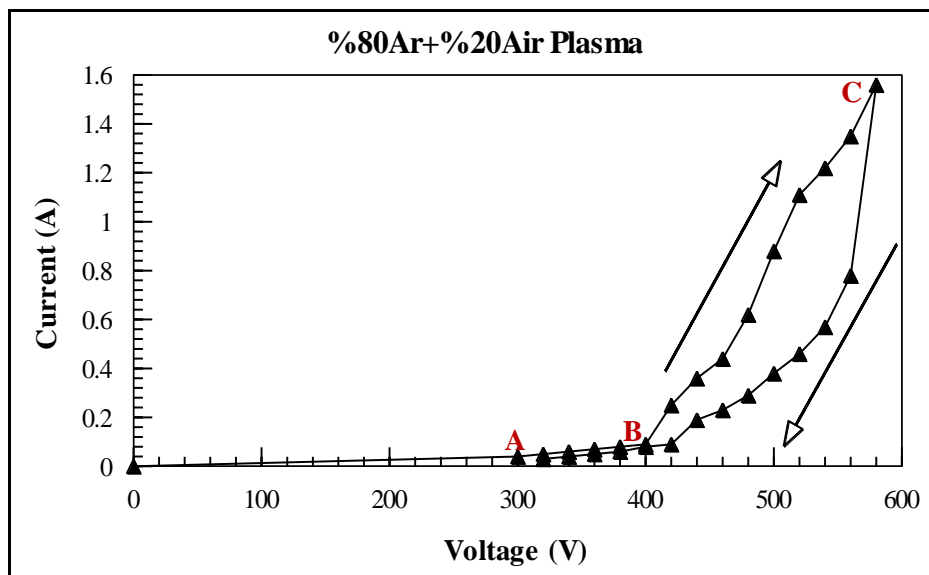


Figure 14.2. The graph of current versus voltage at  $10^{-2}$  Torr with 80% argon and 20% air

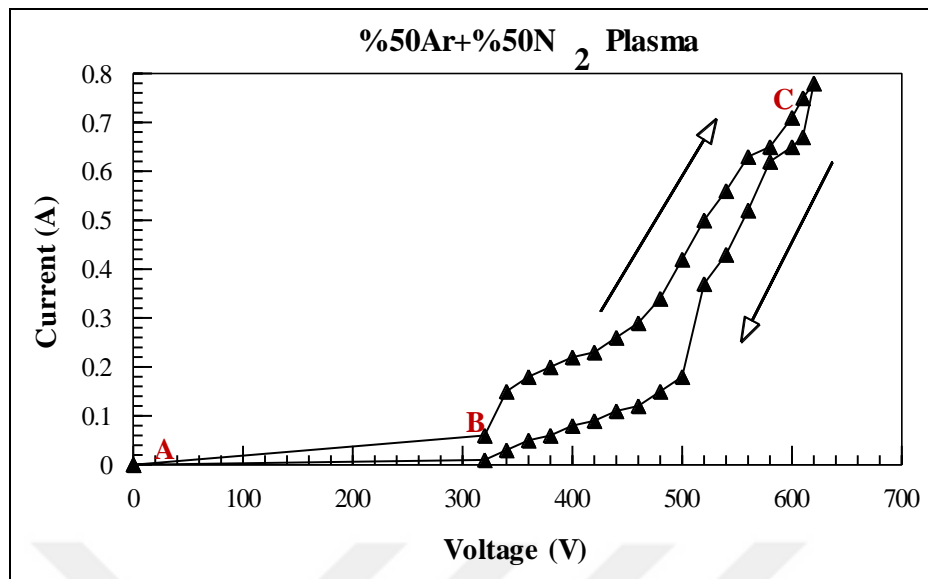


Figure 14.3. The graph of current versus voltage at  $10^{-2}$  Torr with 50% argon and 50% nitrogen.

Plasma is a nonlinear system. Hysteresis effect is the result of the nonlinear behaviour of the plasma system. The differential equations that describe the conservation of particles, momentum and energy in plasmas are generally nonlinear. Plasma has contradictions with other fields such as classical electrodynamics. Because, the main equations in other fields are linear. A lot of parameters affect the plasma behaviour and the results. They lead to a multivariable problem, since the control of all the parameters is not easy enough. Therefore, the interpretation of experimental results are very complicated. It is difficult to maintain plasmas in a steady state, because of their high energy density [6]. The main reason for this is partially due to hysteresis effects. Sudden jumps with the hysteresis in low-pressure argon plasma may be due to the onset of large amplitude plasma oscillations and a change of the plasma density profile.

In this study, it was also observed that the current versus pressure also shows the hysteresis effect in a low-pressure discharge plasma (see Figure 14.4) while Cu is coated. To analyze that the plasma was initiated at 400 V and the pressure increased and decreased between 4 mTorr and 120 mTorr.

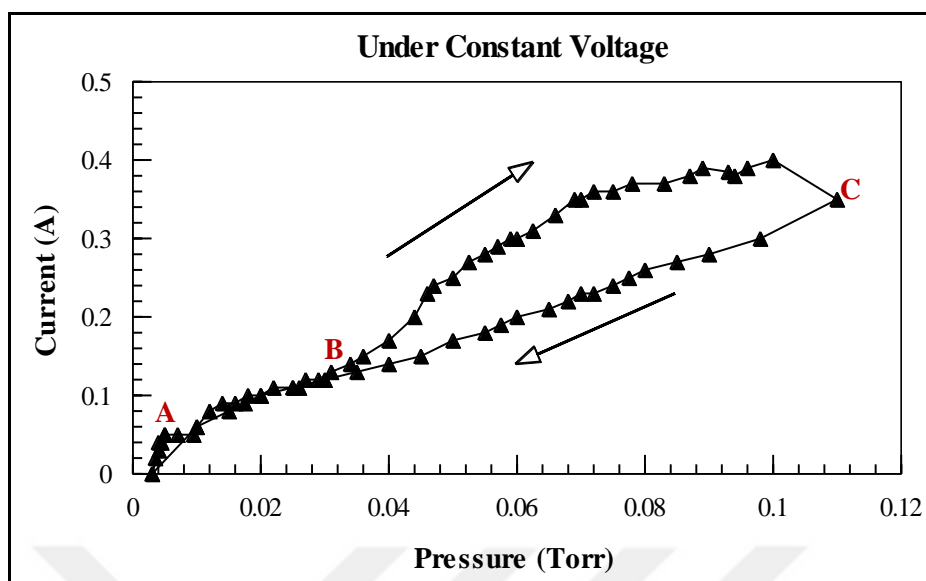


Figure 14.4 . The graph of current versus pressure at 400 V

Figure 14.4 states that between 4-40 mTorr, the plasma current changes linearly with no hysteresis effects. But between 40-120 mTorr, the hysteresis effect is dominant creating current uncertainty of nearly 100 mA. All these results show that the plasma is nonlinear and all the measurements done can have some uncertainty due to the impedance behaviour of the plasma.

Hysteresis effect is also seen in the electric field when magnetic field strength was changed, see Robertson and Currie [23].

## 14.1.2. Langmuir Probe Results

### 14.1.2.1. The Change of Electron Temperature with Pressure

Langmuir probe method can be applied only in the absence of external magnetic field. In the first experiment, the measurements of the current with respect to the voltage were done at different pressures ( $9 \times 10^{-3}$ ,  $2 \times 10^{-2}$  and  $6 \times 10^{-2}$  Torr). The I-V graphs were plotted by using the Stanford Graphics Program.

The most important relation here to apply is:

$$I_{probe} = I_{sat} e^{\frac{q(V-V_f)}{kT}} \quad (14.1)$$

$$\ln(I_{probe} - I_{sat}) = \left( \frac{q}{kT} \right) (V - V_f) + constant \quad (14.2)$$

where  $k$  is Boltzmann constant,  $q$  is the charge and the constant term can be neglected. If Equation 14.2 is compared to  $f(V) = mx + b$  where  $m$  is the slope of line and  $b$  is the intercept,  $x = V - V_f$ , the slope of line gives  $q/kT$ . In this method,  $\ln|I_{sat} - I_{probe}|$  versus  $x = V - V_f$  is plotted, and then a line is fitted to this graph. The slope of this line is inversely proportional to the electron temperature.

In these experiments, the probe voltage was changed from -50 V to +50 V and probe currents were measured. These results at the Argon pressure of  $9 \times 10^{-3}$  Torr was shown on Table 14.1.

Table 14.1. The change of current values with voltage values at  $9 \times 10^{-3}$  Torr

Voltage (V)	Current (A)
-50	-0.0000490
-40	-0.0000500
-30	-0.0000430
-20	-0.0000300
-10	-0.0000120
0	-0.0001916
5	0.0005200
10	0.0012211
20	0.0019385
30	0.0021625
40	0.0023700

The results given on Table 14.1 was plotted as shown in the following figure:

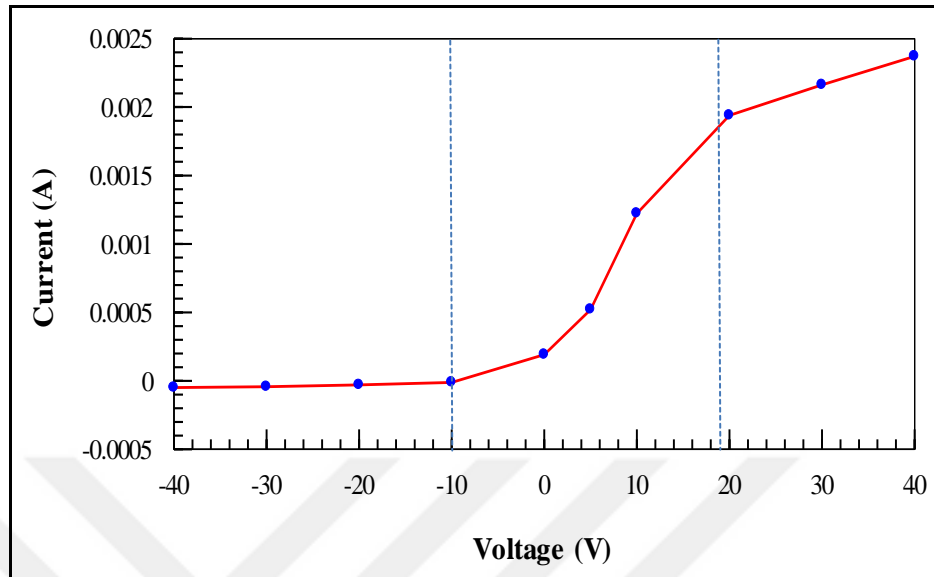


Figure 14.5. Probe current versus voltage at  $9 \times 10^{-3}$  Torr Argon

Then, the value of  $I_{sat}$  was obtained from the graph in Figure 14.5, as  $-0.000049$  A. Then, the values of  $I_{probe} - I_{sat}$  were calculated and the graph of  $I_{probe} - I_{sat}$  vs. voltage was plotted as given in Figure 14.6. By this way, ion contribution to the total current is totally removed. Note that, the graphs in Figures 14.5 and 14.6 seem identical. Since,  $I_{sat}$  is very small.

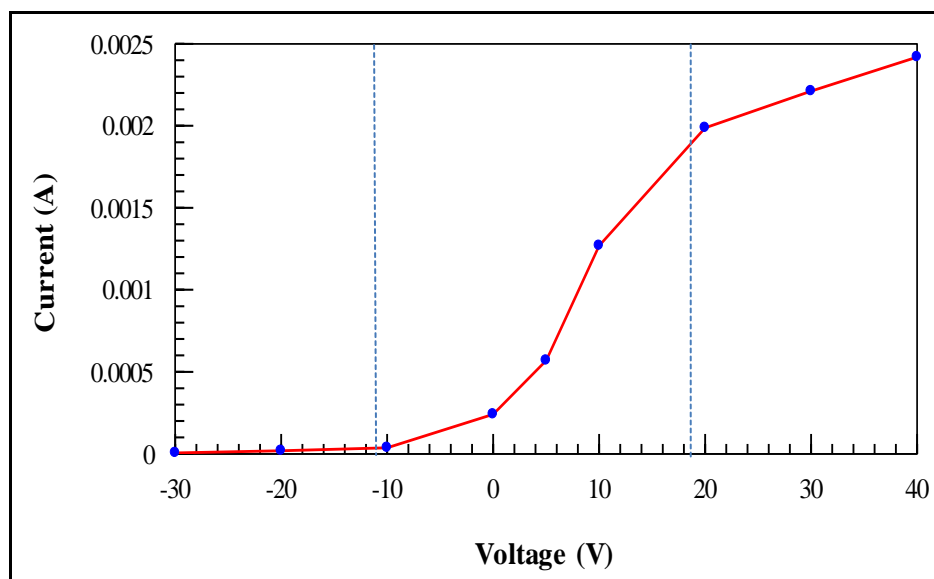


Figure 14.6.  $I_{probe} - I_{sat}$  versus voltage at  $9 \times 10^{-3}$  Torr



Then, the logarithm of  $I_{probe} - I_{sat}$  versus voltage graph was plotted as presented in Figure 14.7.

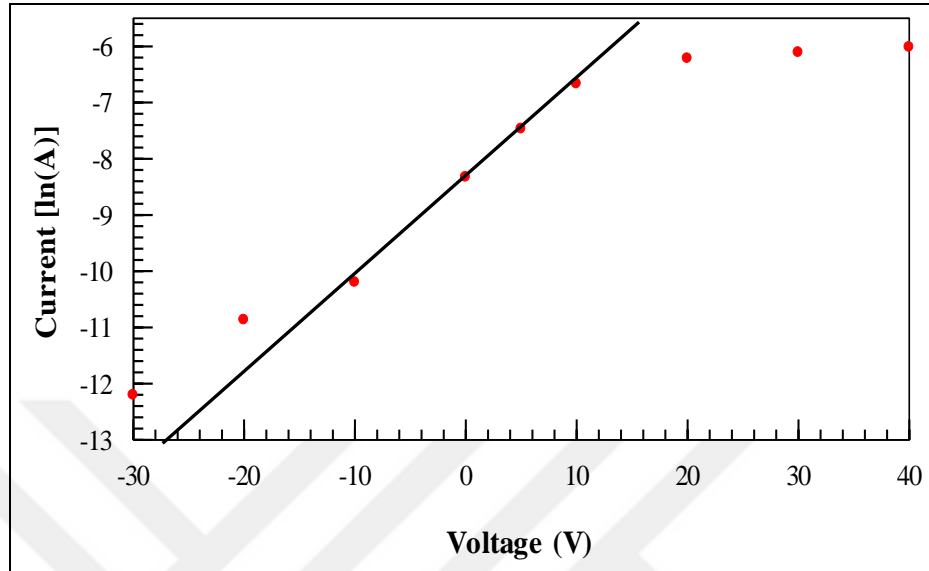


Figure 14.7.  $\ln(I_{probe} - I_{sat})$  versus voltage at  $9 \times 10^{-3}$  Torr

A linear line to the electron saturation current was drawn and, the slope of the line was approximately found as 0.18. One gets  $\frac{e}{kT_e} = 0.18$ . This leads to the following electron temperature:

$$T_e = 64444 \text{ K}$$

of electron temperature.

The same steps were applied for the pressures of  $2 \times 10^{-2}$  Torr, and  $6 \times 10^{-2}$  Torr.

$\ln(I_{probe} - I_{sat})$  versus probe voltage graphs for  $2 \times 10^{-2}$  Torr and  $6 \times 10^{-2}$  Torr were plotted as shown in Figure 14.8 and 14.9 respectively.

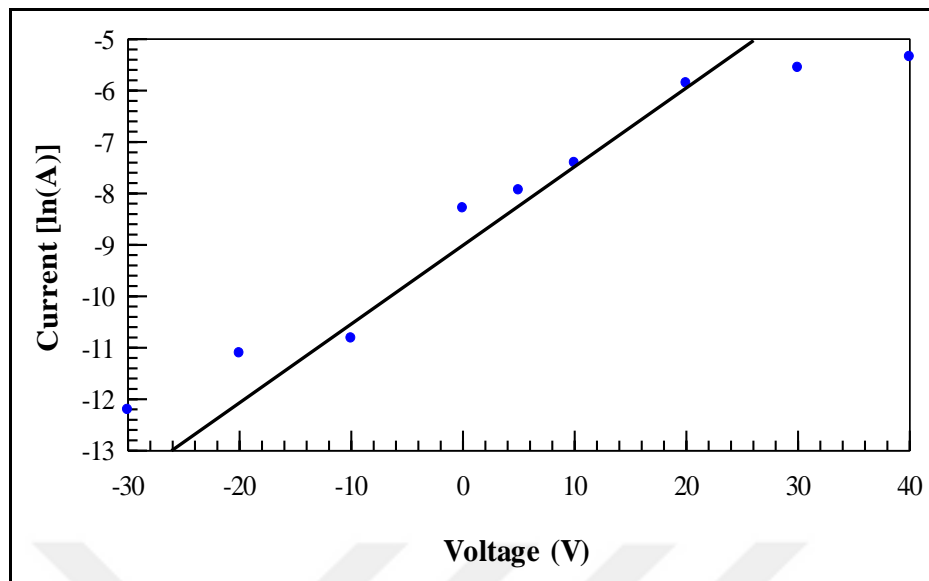


Figure 14.8.  $\ln(I_{\text{probe}} - I_{\text{sat}})$  versus voltage graph at  $2 \times 10^{-2}$  Torr

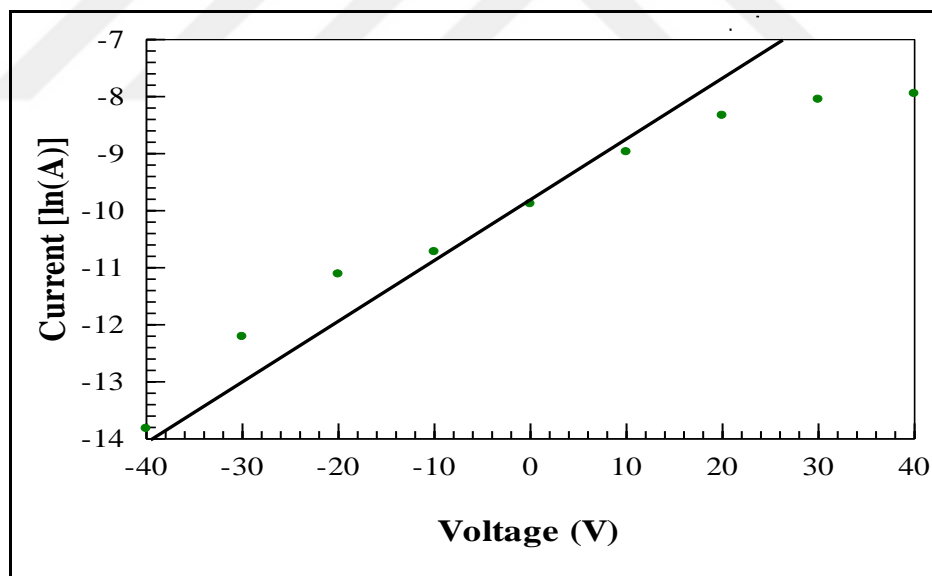


Figure 14.9.  $\ln(I_{\text{probe}} - I_{\text{sat}})$  versus voltage graph at  $6 \times 10^{-2}$  Torr

The slopes for  $2 \times 10^{-2}$  Torr and  $6 \times 10^{-2}$  Torr were found to be 0,155 and 0,09 respectively.

In that case, the electron temperatures can be obtained as follows:

For  $2 \times 10^{-2}$  Torr,  $\frac{e}{kT_e} = 0,155$ ,  $T_e = 74838$  K

For  $6 \times 10^{-2}$  Torr,  $\frac{e}{kT_e} = 0,09$ ,  $T_e = 128888$  K

These results were presented in Table 14.2.

Table 14.2. Electron temperature calculated with respect to the pressure

Pressure (Torr)	Electron Temperature (K)
$9 \times 10^{-3}$	64444
$2 \times 10^{-2}$	74838
$6 \times 10^{-2}$	128888

These results were presented in Figure 14.10:

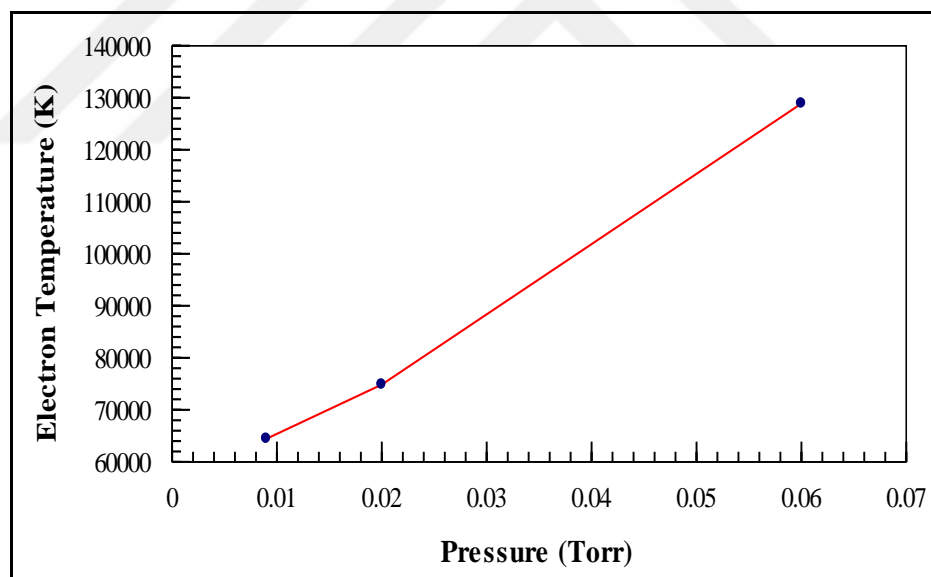


Figure 14.10. The change of electron temperature with pressure

A closer look at the Figure 14.10 shows that an increase of processing pressure leads to the increase of electron temperature of the plasma. This is exactly what is expected. Since, the ideal gas relationship of  $P = \frac{3}{2}nkT$  is approximately valid for electrons in the plasma so that the pressure is linearly dependent on electron temperature.

#### *14.1.2.2. The Change of Electron Temperature from the Cathode to the Anode*

The multineedle probe apparatus contains, eight different probes placed at 8 mm apart with each other as seen in Figure 14.11. This allows the determination of the spatial profile of the electron temperature from cathode to anode.

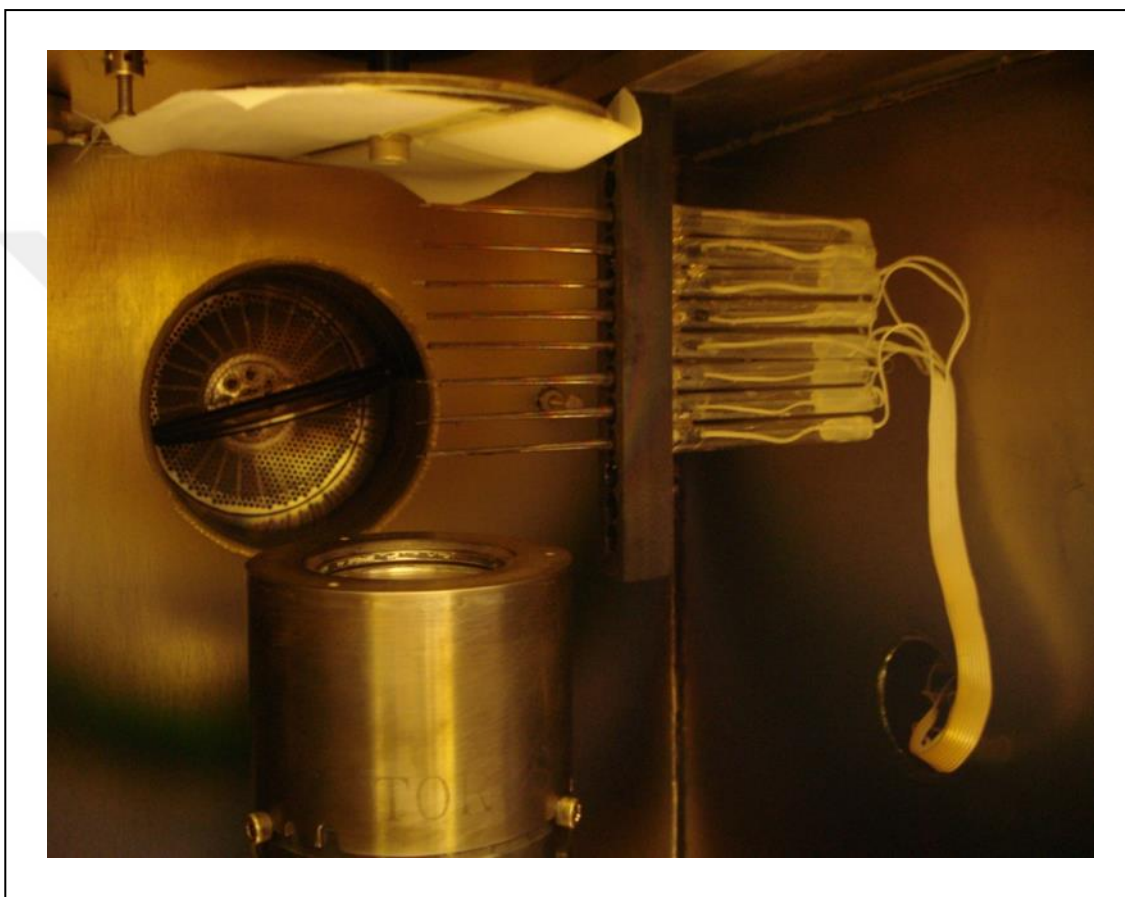
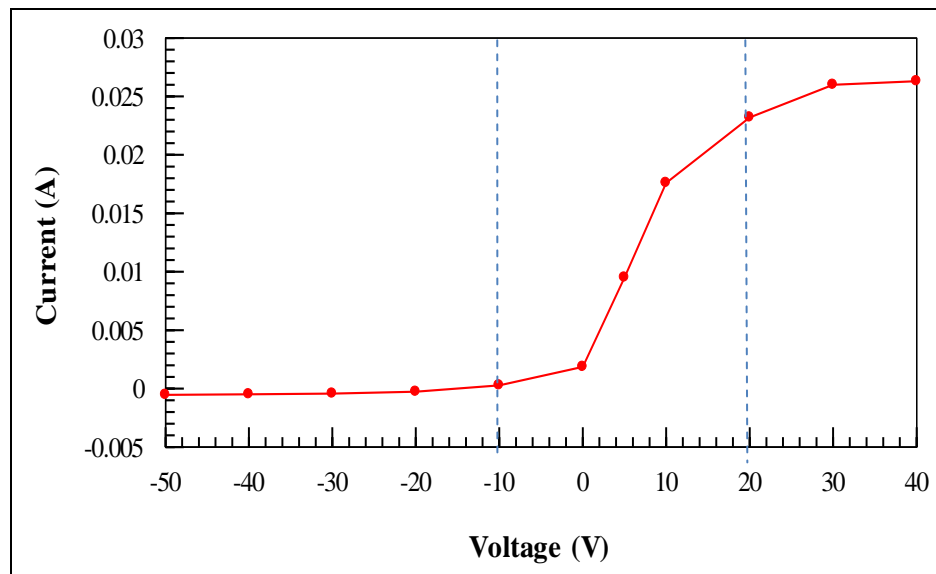


Figure 14.11. Langmuir probe method to measure electron temperature

Only the graphs of first, fourth and eighth probe at a pressure of  $2 \times 10^{-2}$  Torr were plotted in this thesis to prevent time consuming and paper keeping.

Table 14.3. The change of current with voltage on first probe

Voltage (V)	Current (A)
-60	-0.00056
-50	-0.00053
-40	-0.00048
-30	-0.00043
-20	-0.00027
-10	0.00028
0	0.00186
5	0.0095
10	0.01768
20	0.02327
30	0.02606
40	0.0263

Figure 14.12. Current versus voltage graph on the first probe at  $2 \times 10^{-2}$  Torr

The value of  $I_{sat}$  is about -0.00056 A. The values of  $I_{probe} - I_{sat}$  were calculated and the graph of  $I_{probe} - I_{sat}$  versus voltage was plotted as seen in Figure 14.13. The graph of  $\ln(I_{probe} - I_{sat})$

versus voltage was again plotted, and a line is fitted to the electron saturation current as shown in Figure 14.14.

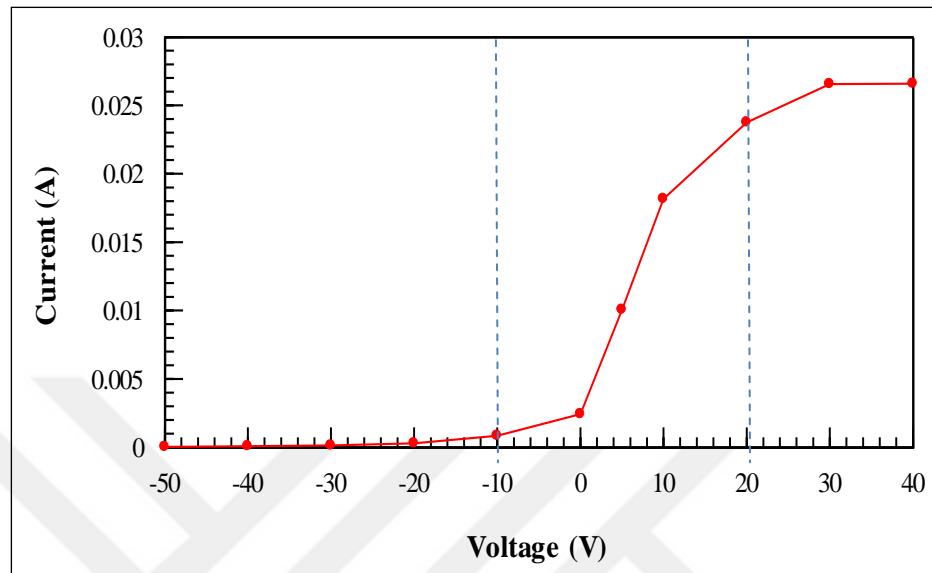


Figure 14.13.  $I_{\text{probe}} - I_{\text{sat}}$  versus voltage graph on the first probe at  $2 \times 10^{-2}$  Torr

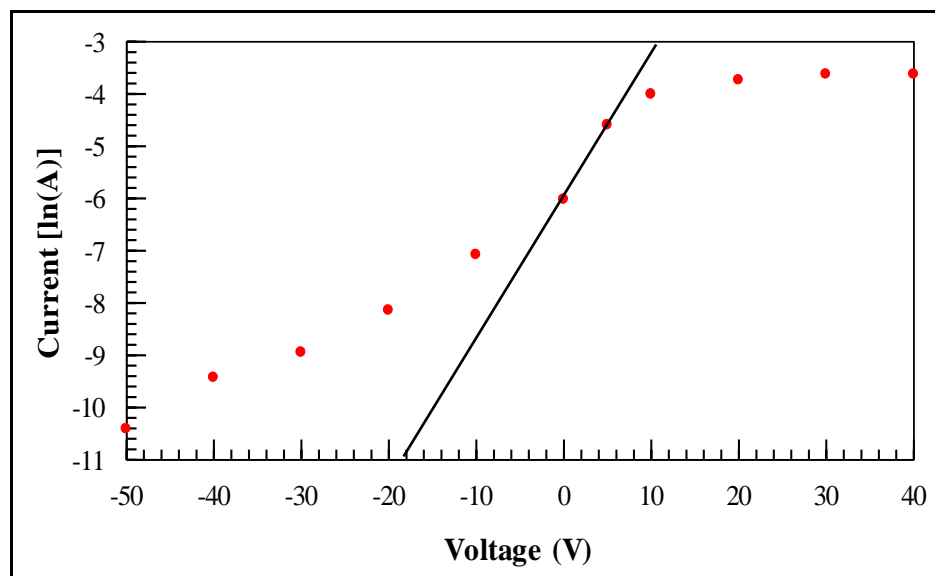


Figure 14.14.  $\ln(I_{\text{probe}} - I_{\text{sat}})$  versus voltage graph on the first probe at  $2 \times 10^{-2}$  Torr

The slope of this line was calculated and approximately found as 0.24 and using the equation, one gets:

$$\frac{e}{kT_e} = 0.24$$

Of electron temperature:

$$T_e = 48333 \text{ K}$$

The same steps were applied for the fourth and eight probes as shown below.  $\ln(I_{probe} - I_{sat})$  versus probe voltage graphs at  $2 \times 10^{-2}$  Torr were plotted as shown in Figure 14.15 and 14.16 respectively.

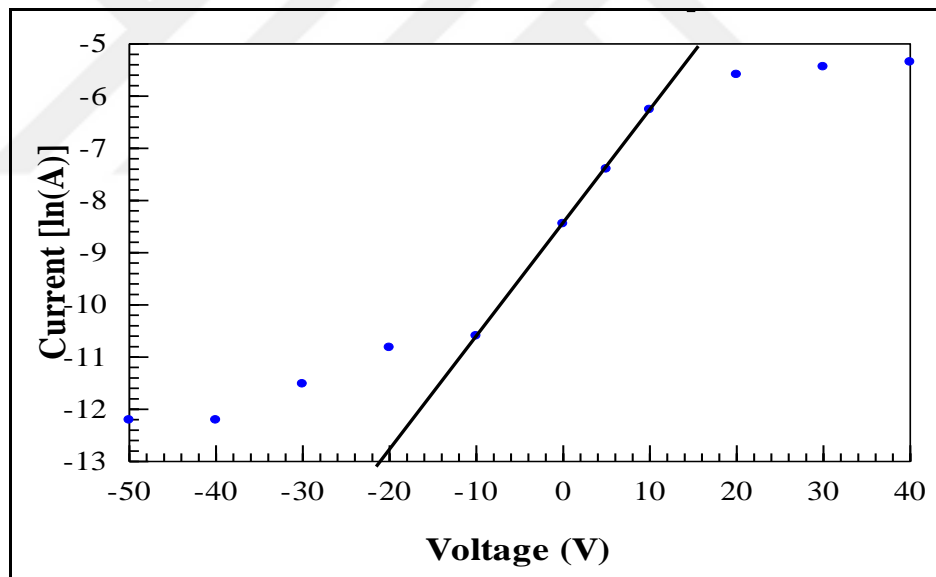


Figure 14.15.  $\ln(I_{probe} - I_{sat})$  versus voltage graph on the fourth probe at  $2 \times 10^{-2}$  Torr

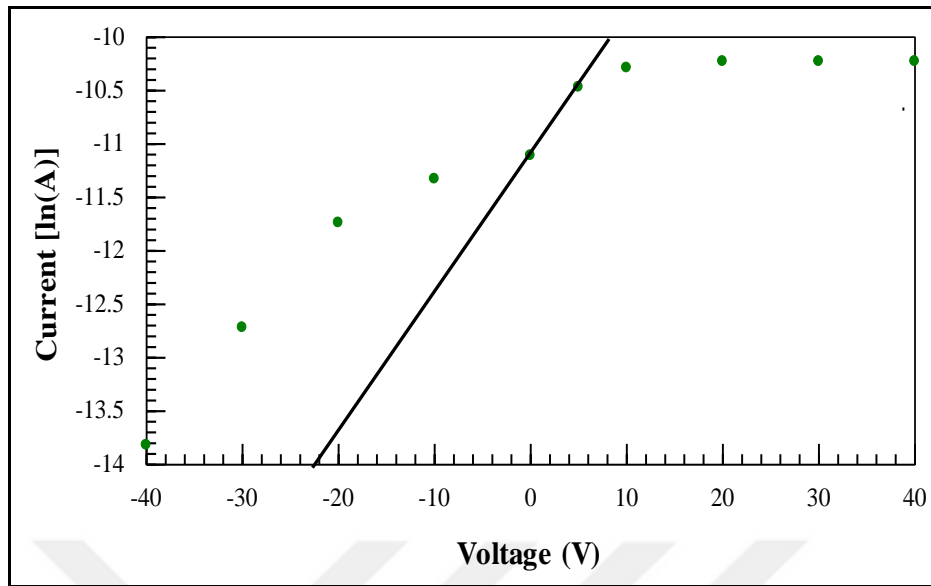


Figure 14.16.  $\ln(I_{\text{probe}} - I_{\text{sat}})$  versus voltage graph on the eight probe at  $2 \times 10^{-2}$  Torr

The slopes for the fourth and eight probe were found to be 0.2 eV and 0.1 eV. In that case, the electron temperatures can be obtained as follows:

For the fourth probe,  $\frac{e}{kT_e} = 0.2$ ,  $T_e = 58000$  K

For the eight probe,  $\frac{e}{kT_e} = 0.1$ ,  $T_e = 116000$  K

Eight of the probes were used to measure the current versus voltages. However, three of them from cathode to anode were shown here for time and paper keeping. It was seen that, the electron temperature increased from cathode to anode, and after that it became constant.



The temperatures which were obtained at the eight probes were written on the Table 14.4.

Table 14.4. The change of electron temperature with the probe number.

Probe	Electron Temperature (K)
1.Probe	48333
2.Probe	48399
3.Probe	53345
4.Probe	58000
5.Probe	79791
6.Probe	116000
7.Probe	116000
8.Probe	116000

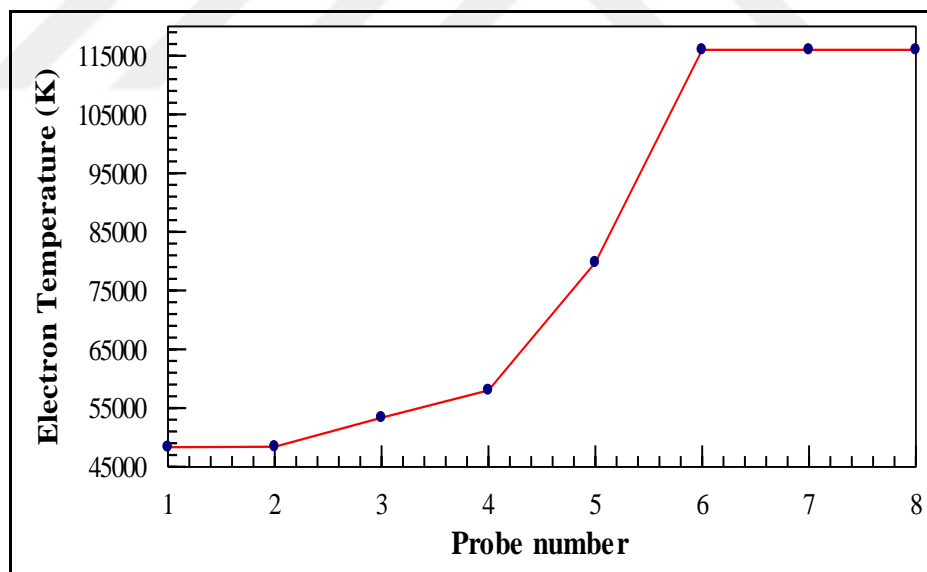


Figure 14.17. The Graph of electron temperature from cathode to anode

As a result, it was seen that the electron temperature increases from the cathode to the anode, at the end it becomes constant. The change of electron temperature with position can relate to the voltage distribution from the cathode to the anode.

### 14.1.3. Measurement of the Electron Temperature by Using Boltzmann Method

Optical emission spectroscopy was used to measure the electron temperature by using Boltzmann plot method. Fiber cable of the spectrometer was put in front of the window of the vacuum chamber as in Figure 14.18.

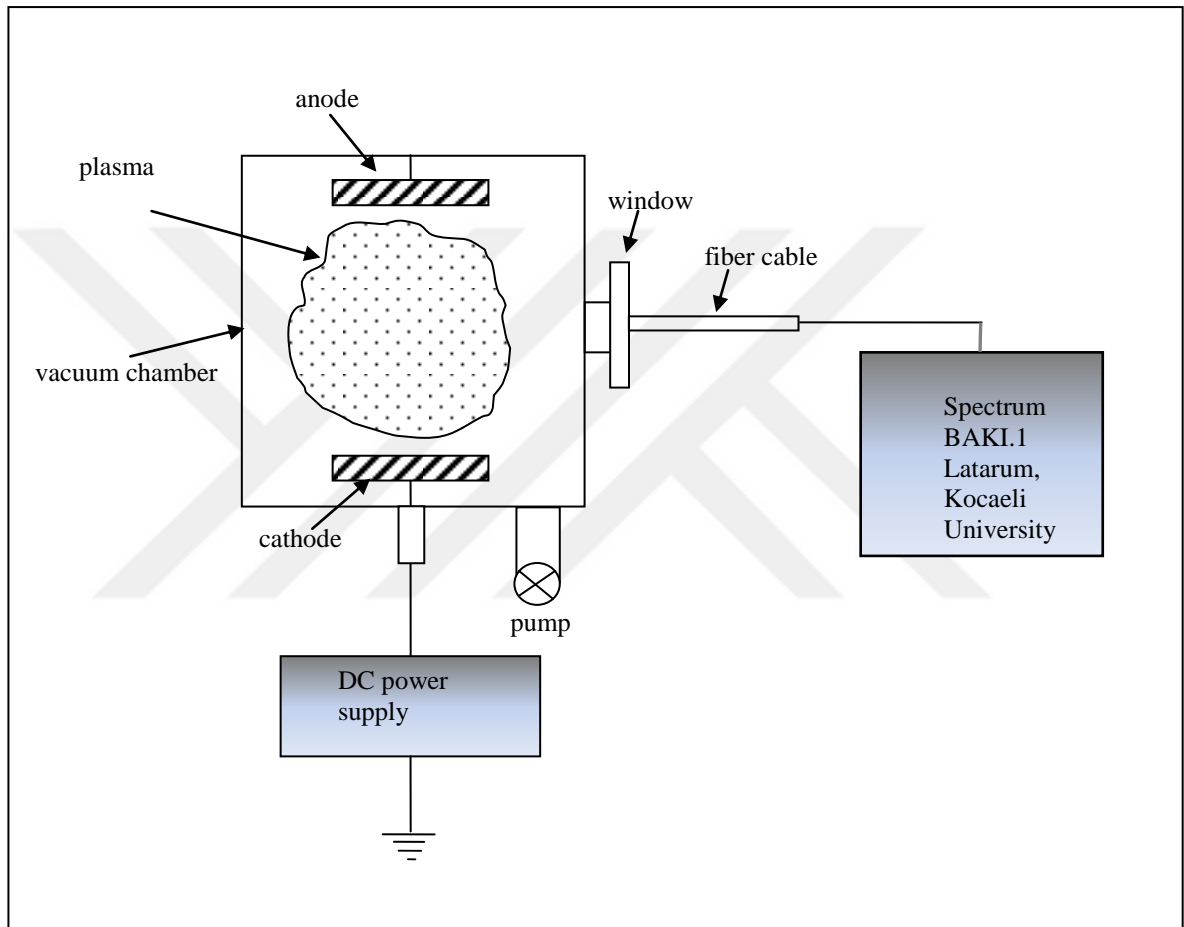


Figure 14.18. Measurement of emission by using Baki spectroscopy in front of the window

The emission spectrum of the magnetron sputtering during silver coating was obtained by using the Baki spectrometer and the results at different DC voltages (and argon as the carrier gas at 100 mTorr) were shown in Figure 14.19.

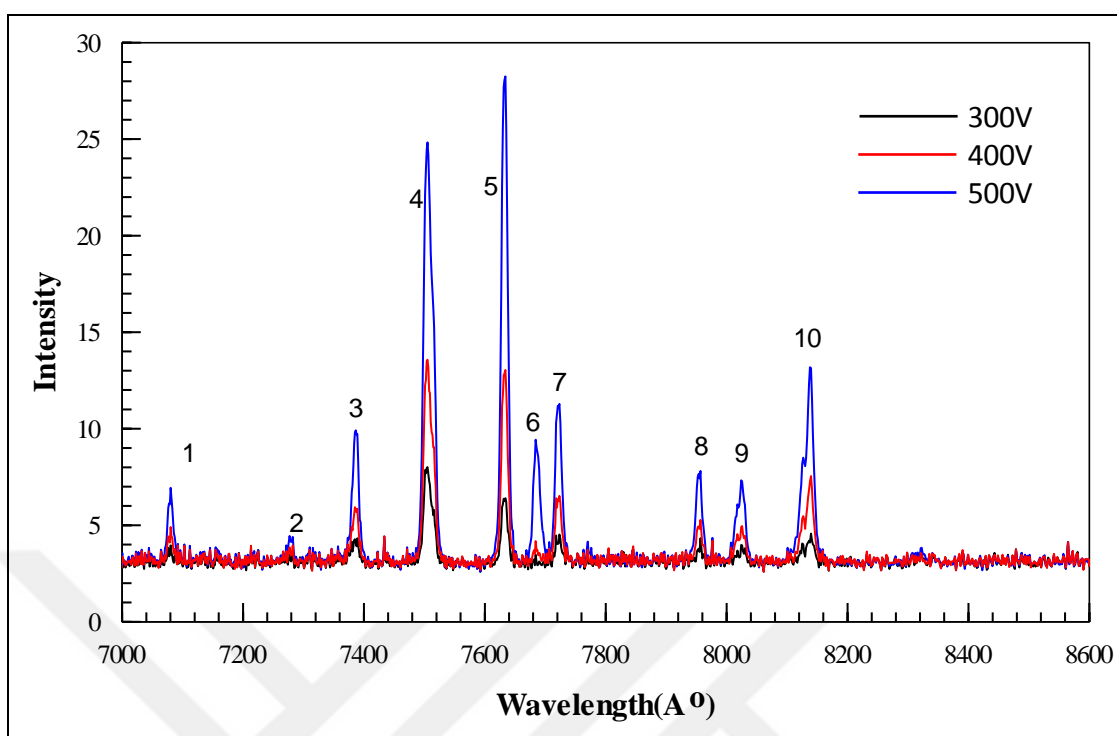


Figure 14.19. Intensity versus wavelength at the voltages 300V, 400V and 500V

When the DC voltage is increased, the intensities of the peaks increase. This is because higher energy causes higher ionization rate in the plasma.

By using the NIST Atomic Spectra Database [24], the peaks observed in Figure 14.19 can be identified to belong to argon ions (first ionization: I, second ionization II). The peaks were observed to be located at the wavelengths from 707.7 nm to 815.1 nm respectively.

After that, the website of NIST was used to find the upper energy  $E_k$  and  $gA$  values.

The page which was open is shown below:

NIST Atomic Spectra Database Lines Form

Best viewed with the latest versions of Web browsers and JavaScript enabled

Spectrum: Ar e.g., Fe I or Na; Mg; Al or mg i-iii

Lower Wavelength: 700 or Upper Wavenumber (in  $\text{cm}^{-1}$ )

Upper Wavelength: 900 or Lower Wavenumber (in  $\text{cm}^{-1}$ )

Units: nm

Reset input Retrieve Data

Figure 14.20. The web page of the NIST

First lower and upper limits were written as in the boxes in Figure 14.20 and then the retrieve button was pushed. In that case, database displays data shown in Figure 14.21.

From these data values,  $E_k$  and  $gA$  values can be obtained.

Ion	Observed Wavelength Air (nm)	Ritz Wavelength Air (nm)	Rel. Int. (?)	$g_k A_{ki}$ (s <sup>-1</sup> )	Acc.	$E_i$ (cm <sup>-1</sup> )	$E_k$ (cm <sup>-1</sup> )	Lower Level Conf., Term, J	Upper Level Conf., Term, J
Ar II	700.144	700.14636	0.5			190 942.7220	- 205 221.512	$3s^2 3p^4 ({}^3P) 5p$ ${}^2S^{\circ}$ $1/2$	$3s^2 3p^4 ({}^3P) 5d$ ${}^2P$ $3/2$
Ar V	700.587	700.583	*	2.6e+00	C	2 028.76	- 16 298.66	$3s^2 3p^2$ ${}^3P$ 2	$3s^2 3p^2$ ${}^1D$ 2
Ar V	700.587	700.583	*	8.0e-03	D	2 028.76	- 16 298.66	$3s^2 3p^2$ ${}^3P$ 2	$3s^2 3p^2$ ${}^1D$ 2
Ar I	703.0251	703.0251	150	1.34e+07	C	105 462.7596	- 119 683.0821	$3s^2 3p^5 ({}^2P^{\circ}_{3/2}) 4p$ $2[{}^3/2]$ 3	$3s^2 3p^5 ({}^2P^{\circ}_{3/2}) 6s$ $2[{}^3/2]$ 2

Figure 14.21. The values which were obtained from the website of the NIST .

The wavelengths which correspond to the peaks are given as follows: 1-707.7 nm Ar-II, 2-727.3 nm Ar-I, 3-738.4 nm Ar-I, 4-750.3 nm Ar-I, 5-763.5 nm Ar-I, 6-768.3 nm Ar-II, 7-772.4 nm Ar-I, 8-794.4 nm Ar-II, 9-801.8 nm Ar-II, 10-815.1 nm Ar-I. Then, the wavelengths which correspond to Ar-I were selected. They were written on the Table 14.5. Intensity values which match with the wavelengths were written on the table. Then,  $\ln(I \cdot \lambda / gA)$  was calculated. The values were calculated for 300 V, 400 V and 500 V differently.

Table 14.5. The values calculated at 300 V

Experimental wavelength (nm)	Experimental Intensity	$gA$ ( $s^{-1}$ )	$E_k$ (eV)	$\ln(I\lambda/gA)$
727,293	3.5	5.49E+06	13,327	-7.68E+00
738,398	4.75	4.24E+07	13,302	-9.40E+01
750,386	8	4.45E+07	13,479	-8.91E+00
763,510	6.5	1.22E+08	13,171	-1.01E+01
772,420	4	3.51E+07	13,327	-9.34E+00
815,118	4.5	9.90E+04	14,848	-3.29E+00

The graph of  $\ln(I\lambda/gA)$  versus  $E_k$  at 300 V was plotted as seen in Figure 14.22.

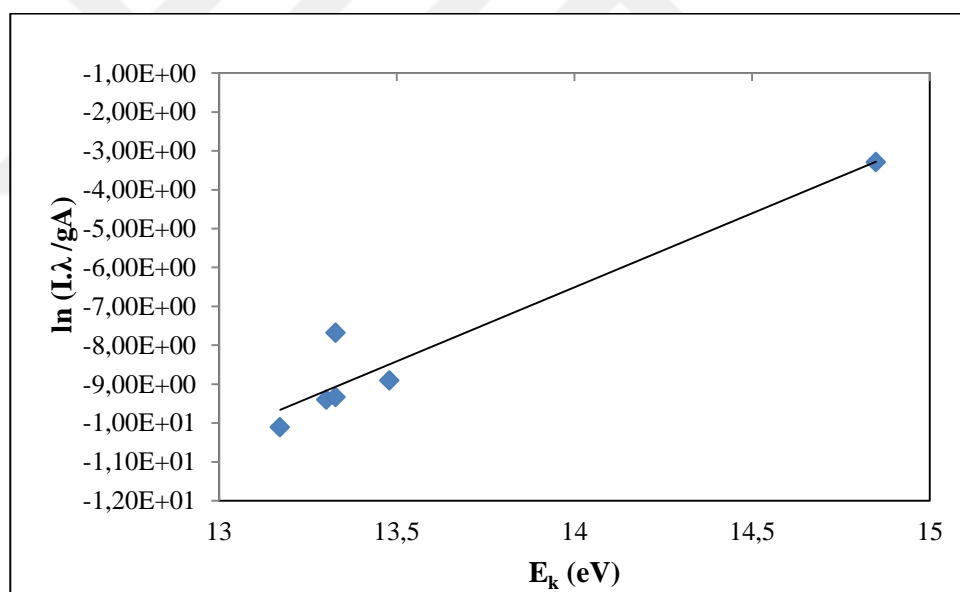


Figure 14.22. The graph of  $\ln(I\lambda/gA)$  versus  $E_k$  at 300 V

The slope of the line was found 3.87. One gets electron temperature :

$$T = 3000.05 \text{ K}$$

Table 14.6. The values calculated at 400 V

Experimental wavelength (nm)	Experimental Intensity	$gA$ ( $s^{-1}$ )	$E_k$ (eV)	$\ln(I.\lambda/gA)$
727.293	5	5.49E+06	13.327	-7.32E+00
738.398	5.8	4.24E+07	13.302	-9.20E+00
750.386	13.6	4.45E+07	13.479	-8.38E+00
763.510	12.8	1.22E+08	13.171	-9.43E+00
772.420	6.4	3.51E+07	13.327	-8.87E+00
815.118	7.4	9.90E+04	14.848	-2.80E+00

The graph of  $\ln(I.\lambda/gA)$  versus  $E_k$  at 400 V was plotted as shown in Figure 14.23.

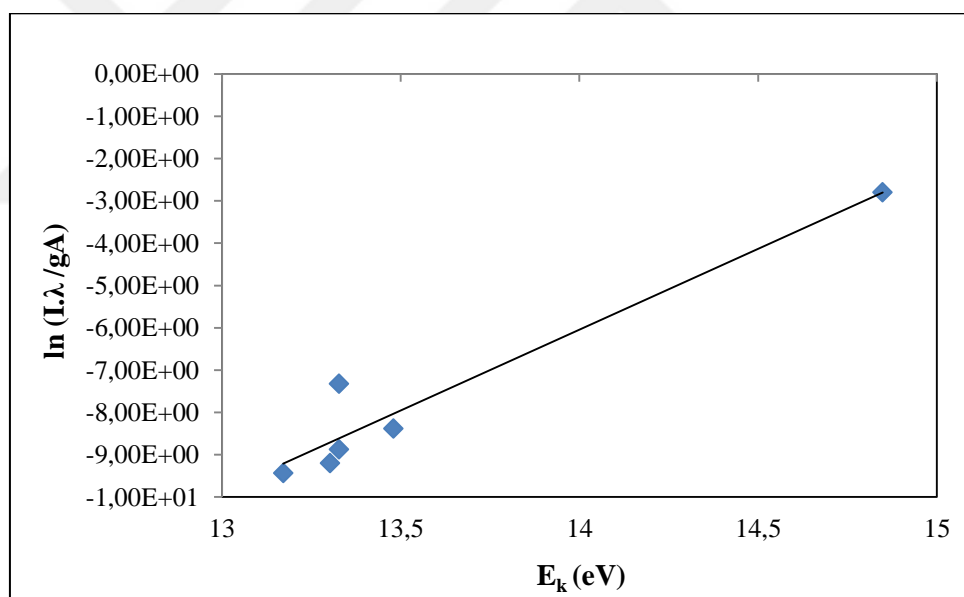


Figure 14.23. The graph of  $\ln(I.\lambda/gA)$  versus  $E_k$  at 400 V

The slope of the line is 3.73. Electron temperature was found as :

$$T = 3109.92 \text{ K}$$

Table 14.7. The values calculated at 500 V

Experimental wavelength (nm)	Experimental Intensity	$gA$ ( $s^{-1}$ )	$E_k$ (eV)	$\ln(I.\lambda/gA)$
727.293	4.4	5.49E+06	13.328	-7.45E+00
738.398	10	4.24E+07	13.302	-8.66E+00
750.386	25	4.45E+07	13.480	-7.77E+00
763.510	28	1.22E+08	13.172	-8.65E+00
772.420	9.5	3.51E+07	13.328	-8.47E+00
815.118	11.5	9.90E+04	14.848	-2.36E+00

The graph of  $\ln(I.\lambda/gA)$  versus  $E_k$  at 500 V was plotted in excel.

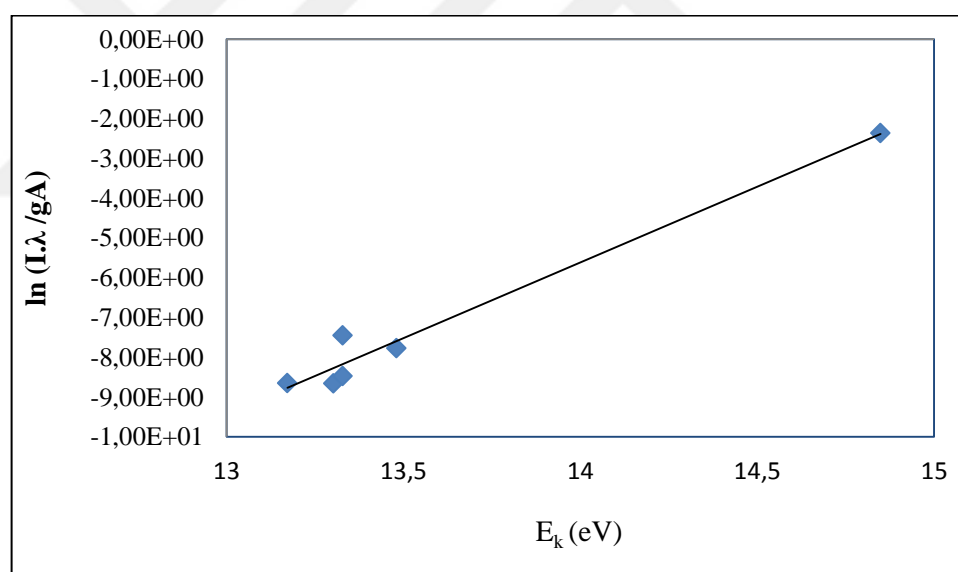


Figure 14.24. The graph of  $\ln(I.\lambda/gA)$  versus  $E_k$  at 500 V

The slope of the line is about 3.5, and one gets electron temperature:

$$T = 3314.29 \text{ K}$$



Table 14.8. The electron temperature change with respect to the voltage

Voltage (V)	Electron Temperature (K)
300	3000.05
400	3109.92
500	3314.29

If the electron temperatures calculated are compared, there is an increase of electron temperature with voltage as shown in Figure 14.24. That is, electron temperature is directly related with voltage.

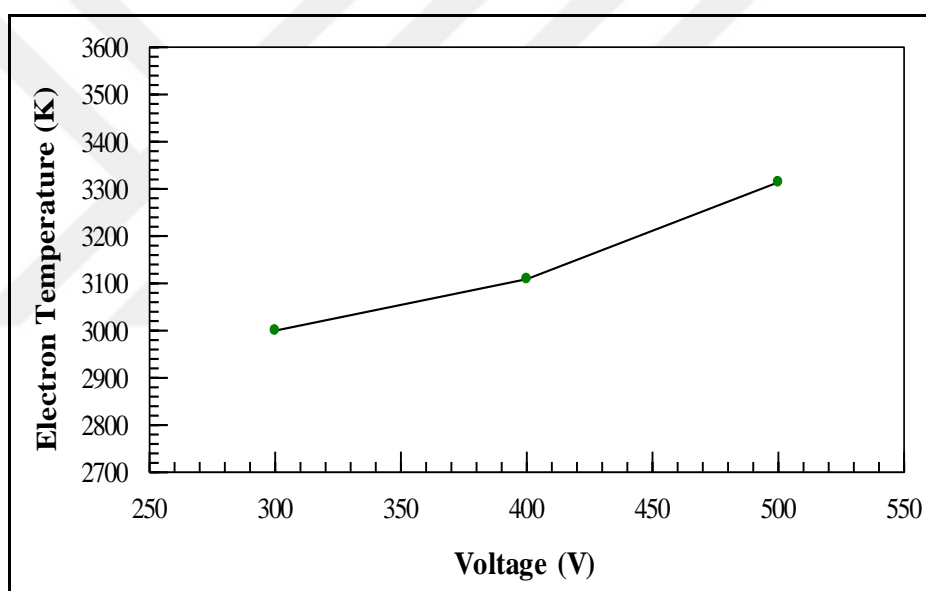


Figure 14.25. Electron temperature versus voltage

Electron temperature of the DC discharge plasma was found about 70000 K and 3000 K in Langmuir probe and in spectroscopy respectively. If Langmuir probe and Boltzmann plot results were compared, electron temperatures were found much more in Langmuir probe method than spectroscopy. Because, the electron temperature calculated by using Langmuir probe method is a local plasma temperature, while the one calculated by using spectroscopy is a spatially averaged plasma temperature [25].

## **14.2. INVESTIGATION OF SURFACE PROPERTIES OF DEPOSITED TEXTILES WITH MAGNETRON SPUTTERING METHOD**

Textiles, metals and glasses with high quality (e.g. corrosion resistant, antibacterial, hydrophobic, wear resistant...) can be obtained by using magnetron sputtering methods.

### **14.2.1. Coating Processes For Textiles**

In order to prepare the textile substrates for coating, the textiles (pure cotton, polyester or polycotton) were put on a mixture which contains 40 ml water, 0.02 g detergent and 0.02 g sodium carbonate for 1 g textile. It was heated up to 70°C, 45 minutes and then the textiles were dried .

The targets (Cu or Ag) were placed on the cathode and the textiles were stuck on the substrate holder by using special stickers. The substrate holder is on the upper part of our magnetron sputtering system. The Cu or Ag ions which were sputtered were deposited separately at the bottom of the textile at room temperature by magnetron sputtering system.

The purity of the targets were 99.99%. The diameter of Ag and Cu targets were 2 inches  $\approx$  50.8 mm. The thickness of them was about 4 mm. The distance between substrate and target was chosen to be between 5 cm and 8 cm.

Initially, the vacuum chamber was evacuated down to the pressure of  $1 \times 10^{-6}$  Torr, before deposition. This low vacuum environment was provided by the turbo pump. The air and all other gases are removed, then the argon gas was sent to the chamber through flow controller and its pressure was increased to the pressure of 10 mTorr.

The parameters for the depositions were given in Table 14.9.

Table 14.9. Deposition conditions for Ag and Cu

Target Type	Silver	Copper
Base Pressure	$1 \times 10^{-6}$ Torr	$1 \times 10^{-6}$ Torr
Working Pressure	$1 \times 10^{-2}$ Torr	$1 \times 10^{-2}$ Torr
Voltage	310-480 V	440-450 V
Current	0.03-0.12 A	0.1-0.15 A
Distance to Target	5-8 cm	5-8 cm
Deposition Time	1-20 min.	1-20 min.

#### 14.2.2. SEM Results

Scanning electron microscope (SEM) is a microscope which uses high energy electron beams for surface scanning. The image obtained is distribution map of the intensity of the signal being emitted from the scanned area of the specimen surface. The SEM analysis were studied by Tescan, Mira/LMU Schottky. Samples were coated with gold before SEM analysis in a short time, nearly 3-5 seconds.

SEM images were used to characterize the morphology and the concentration of the material which were used to coat the textile. The surface composition was determined and how the antibacterial agent was distributed on the coated textile was seen.

Coating of the textile from one side can be more proper for health. Because, some people may have allergy against metal nanoparticles.

The surface characteristics of these depositions on polycotton and cotton textiles were investigated by SEM images of 2K magnification in Figure 14.26.a and Figure 14.26.b SEM results showed that the textile fibers were coated homogeneously and densely by using this sputtering technique as in Figure 14.26.a This can be attributed to the high energy of particles which arrive to the substrate. Small cracks as seen in Figure 14.26.b gave idea about the film thickness. In this study, textiles were coated with very thin layers of copper and silver by magnetron sputtering method.

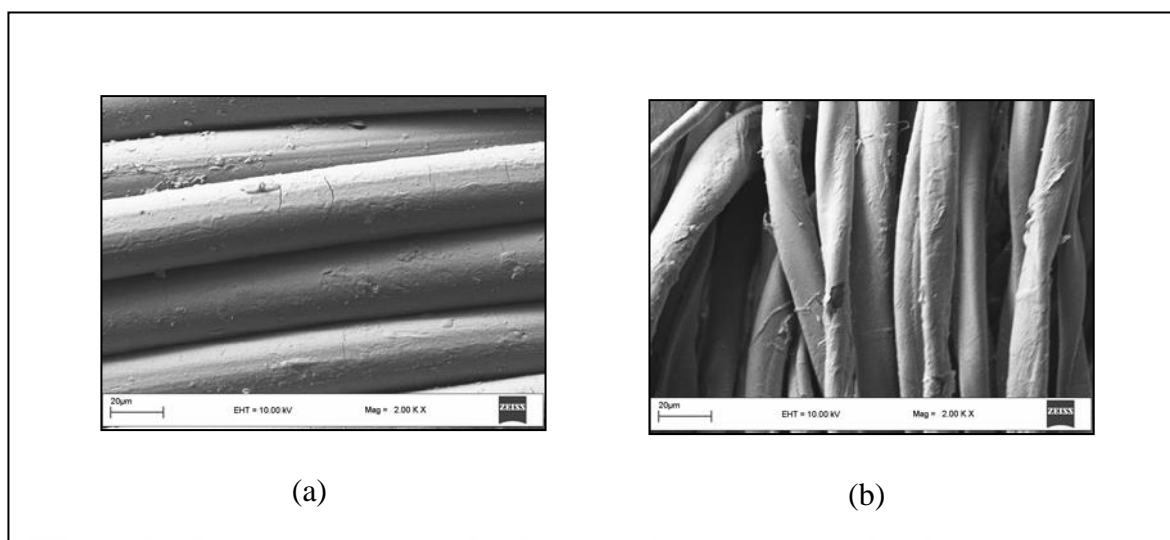


Figure 14.26. SEM images of (a) coated polycotton fiber, (b) coated cotton fiber

Examples of SEM images (5K magnification) of the coatings Cu and Ag on cotton fibers, obtained using magnetron sputtering system are presented by in Fig. 14.27 and 14.28. The differences between the surfaces coated with different metals can be seen easily in the SEM images. Cu deposition leads to the smooth circular zones which are attached to each other. The silver deposition are shiny and smooth with some cracks zones.

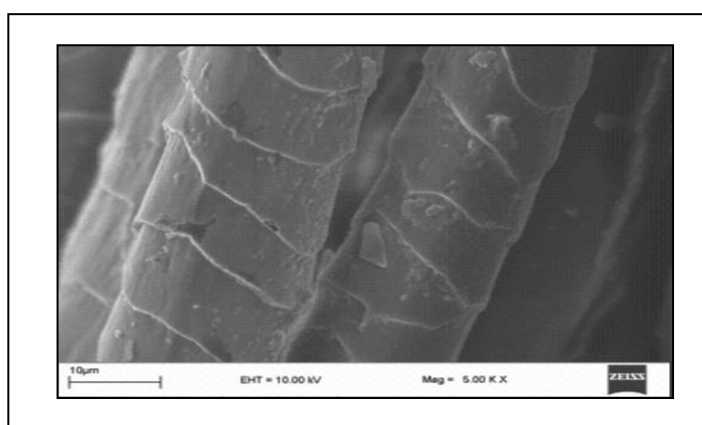


Figure 14.27. SEM images of Cu coatings for 15 minutes

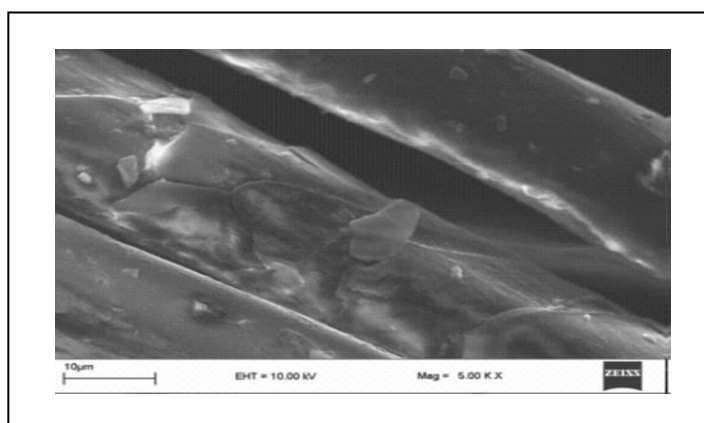


Figure 14.28. SEM images of Ag coatings for 8 minutes

Figure 14.29, Figure 14.30, Figure 14.31 and Figure 14.32 shows the SEM Picture of cotton fibers coated by copper for 4 minutes. The magnifications were 90, 200, 1000, 2000, 5000, 10000, 25000 and 70000 respectively. In order to find out coating thickness, a small region on the surface was deformed intentionally.

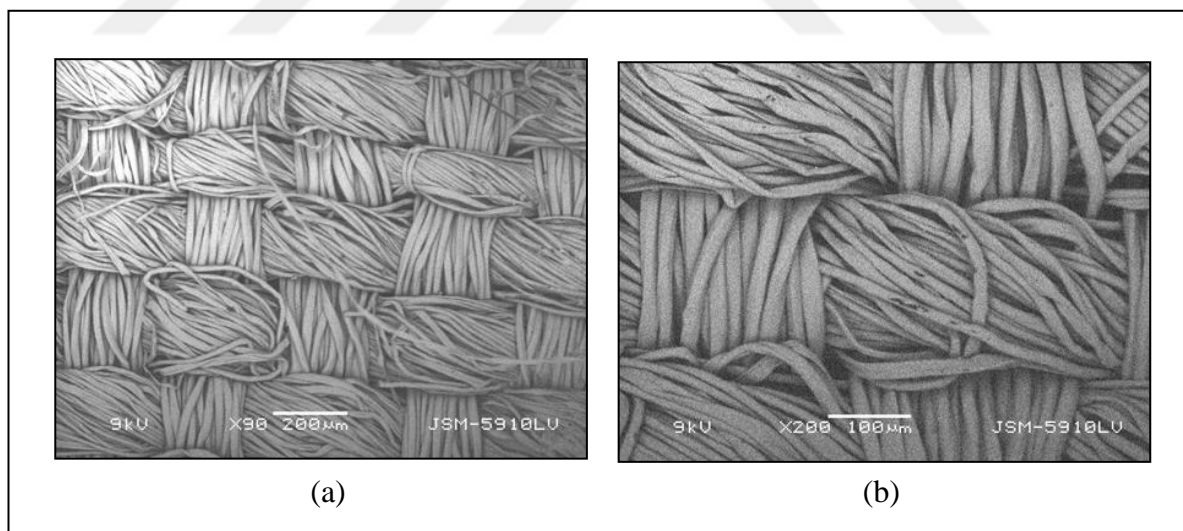


Figure 14.29. The SEM images of the deformed region the cotton fibers coated by copper  
(a) 90 magnification, (b) 200 magnification

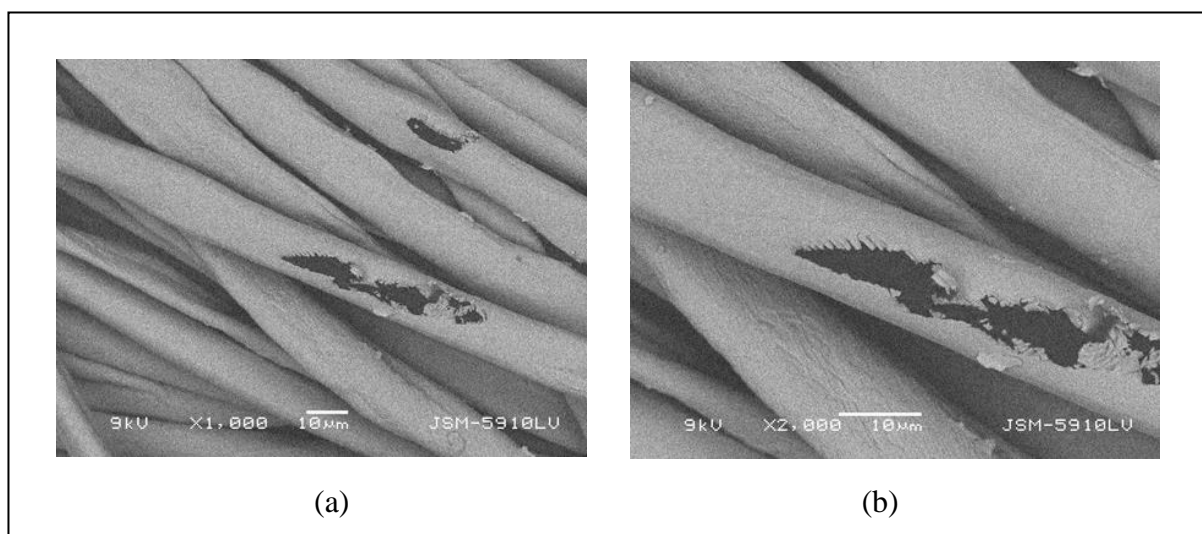


Figure 14.30. The SEM images of the deformed region of cotton fibers coated by copper  
(a) 1000 magnification, (b) 2000 magnification

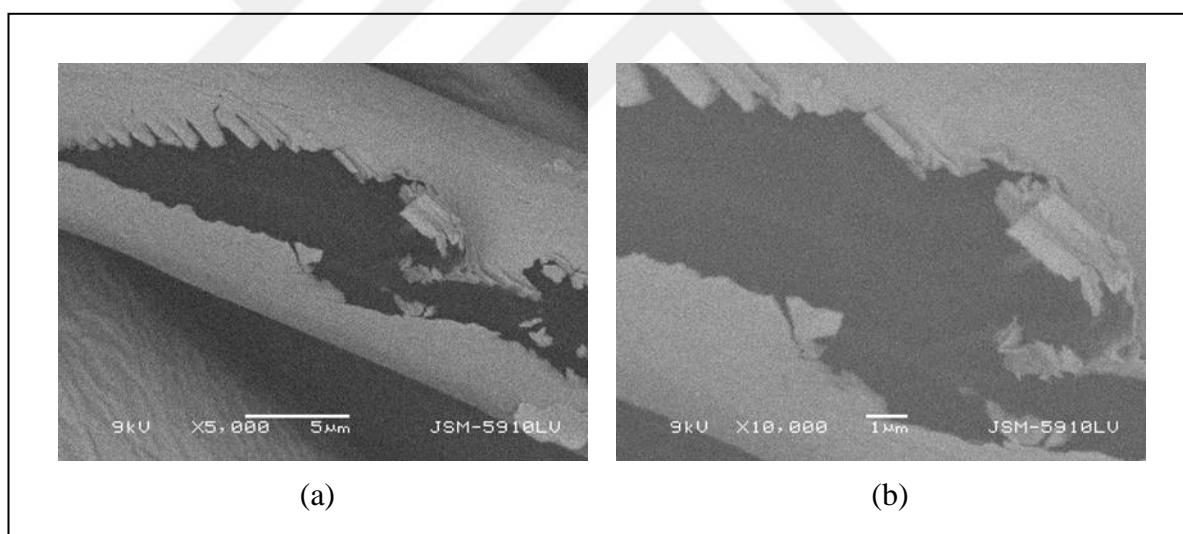


Figure 14.31. The SEM images of the deformed region of cotton fibers coated by copper  
(a) 5000 magnification, (b) 10000 magnification

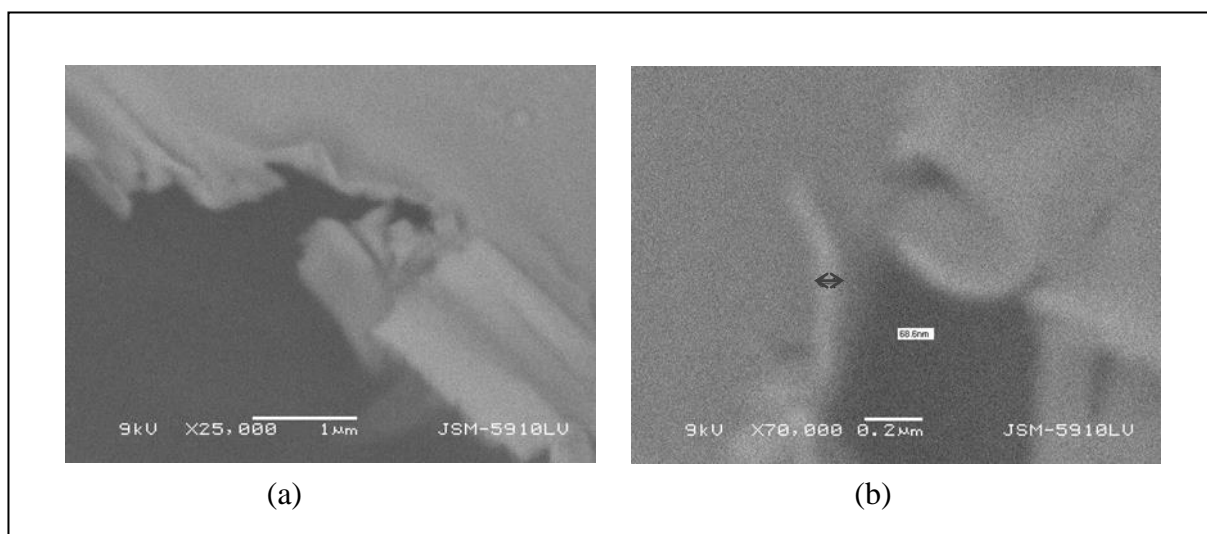


Figure 14.32. The SEM images of the deformed region of cotton fibers coated by copper  
(a) 25000 magnification, (b) 70000 magnification

The cracks on the deposition give an idea about the thickness of the copper. It is seen from the magnification of 70000 that the peeled of coating is approximately 68.6 nm for 4 minutes copper coated textile.

Using the textile fabric, measuring the thickness of the copper coating is not an easy process. Because, textile can bend or stretch. During coating, a glass substrate was put next to the textile, so that it was coated with the same amount of copper. The glass sample coated for 4 minutes was also studied by using SEM. Figure 14.33 shows the side SEM image of the glass coated by copper (100000 magnification).

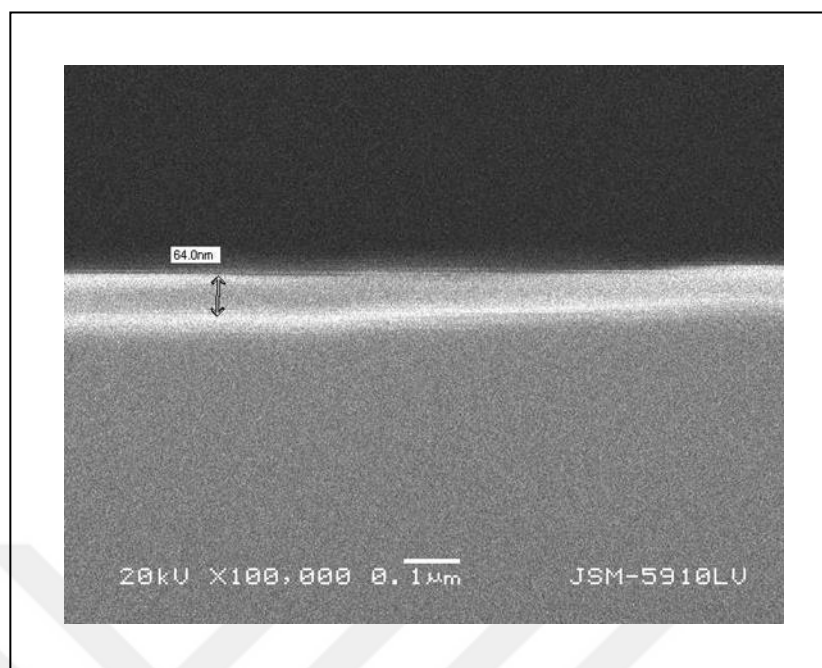


Figure 14.33. SEM Picture of the lateral view of the glass coated by copper

From this figure, it was found that the coating is nearly 64.0 nm. Although, this method gives the thickness more accurately; the thickness which was found by the other technique gave similar results.

In addition to these methods, a new method was applied to find the thickness. In this method, SEM images were not used. The study was done in mass calibration laboratory in Marmara University. Masses of glasses before the deposition was measured in mass calibration laboratory to prevent environmental changes such as humid, and temperature.

Firstly, the temperature and humidity was set on 21.9<sup>0</sup>C and 62% respectively. The masses of the glass samples were measured by an accurate (1µg accuracy) balance in mass calibration laboratory. After that, they were deposited by magnetron sputtering method at different times, and their weights were measured with the temperature of 22.3<sup>0</sup>C and in the humidity 65.2% (nearly same values as before).

Table 14.10 shows the measured masses of the samples before and after deposition. Sample 1, sample 2 and sample 3 are the glasses coated by copper for 1, 4 and 10 minutes respectively.



Table 14.10. The mass of the samples before and after deposition of copper

	The mass before deposition (mg)	The mass after deposition (mg)
Sample 1 (1 minute coated)	1893.019	1893.078
Sample 2 (4 minutes coated)	1898.238	1898.452
Sample 3 (10 minutes coated)	1833.693	1834.828

The difference between the mass of glass before and after the deposition gives us the amount of copper. Figure 14.34 shows the glass sample coated by copper by this technique. One side of the copper deposited by copper is 2.5 cm. The thickness which is the unknown parameter here, one should first calculate the volume of the copper.

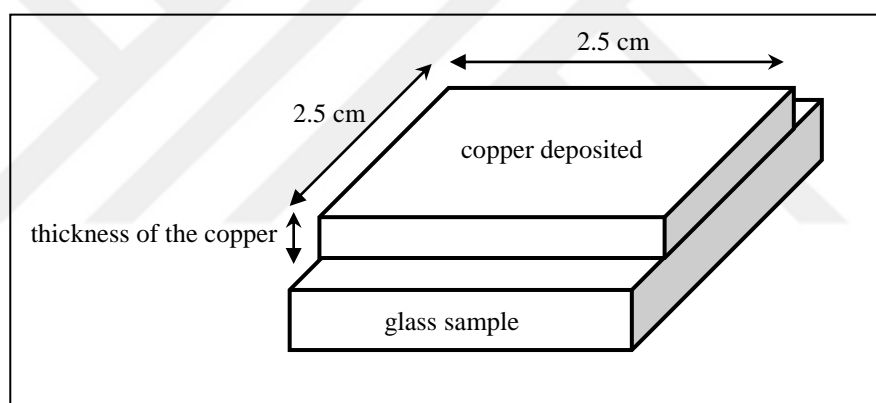


Figure 14.34. The diagram of the glass deposited by copper

For sample 1, the mass of the copper which was coated was found to be  $59.10^{-3}$  mg. By using the density of the copper ( $8.96 \text{ g/cm}^3$ ), the volume of the copper was calculated as  $V = \frac{m}{\rho}$  and  $V = 0.00658448 \times 10^{-3} \text{ cm}^3$ . Using  $V = a.b.c$  and  $V = 2.5 \times 2.5 \times c$ , one gets  $c = 10.53$  nm. For sample 2, the mass of the copper which was coated for 4 minutes was 0.214 mg. Using the same procedure the thickness was found to be 38.2 nm. 10 minutes coated sample, the thickness was calculated as 202.5 nm.

These results are in the same order of magnitude as the one found by SEM. This method can be improved and applied in the future studies to find the approximate thickness of the thin film coating.

Fig. 14.35.a and Fig. 14.35.b shows the SEM picture of (100x magnification) cotton fibers magnetron sputtering coated by Ag for 4 and 10 minutes respectively.

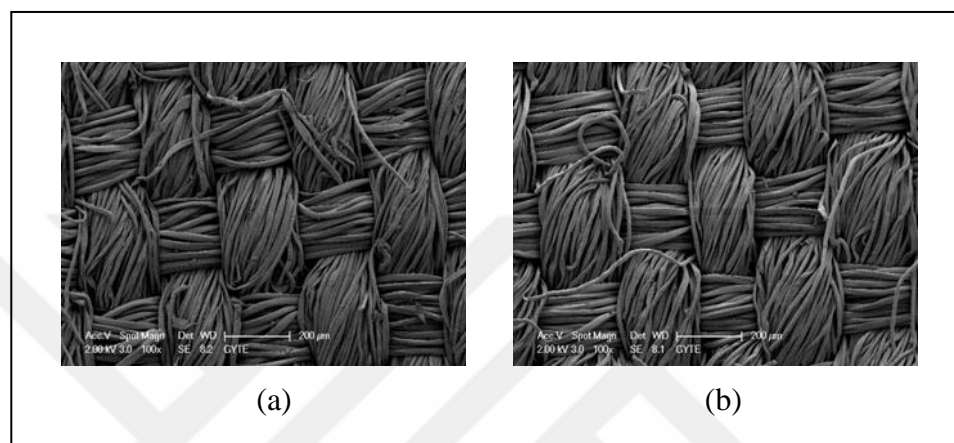


Figure 14.35. SEM images of (a) Ag coatings for 4 minutes and (b) Ag coatings for 10 minutes

The differences between the surfaces coated with silver for 4 min. and 10 min. can be seen easily seen in the Figure 14.35.a and 14.35.b. Longer coating times means shinier appearance.

Although metal which is used to coat the textile is very thin, textiles are colorful. As the thickness of the deposition increases, the transparency of the deposition also decreased. Therefore, coating the textile for a shorter time is more preferable to prevent waste of the metal and toxicity effects [26].

### 14.2.3. EDS Results

Fig. 14.36 and Fig. 14.37 and Fig.14.38 shows EDS results of the cotton coated by silver, the cotton coated by silver and copper, the glass coated by copper.

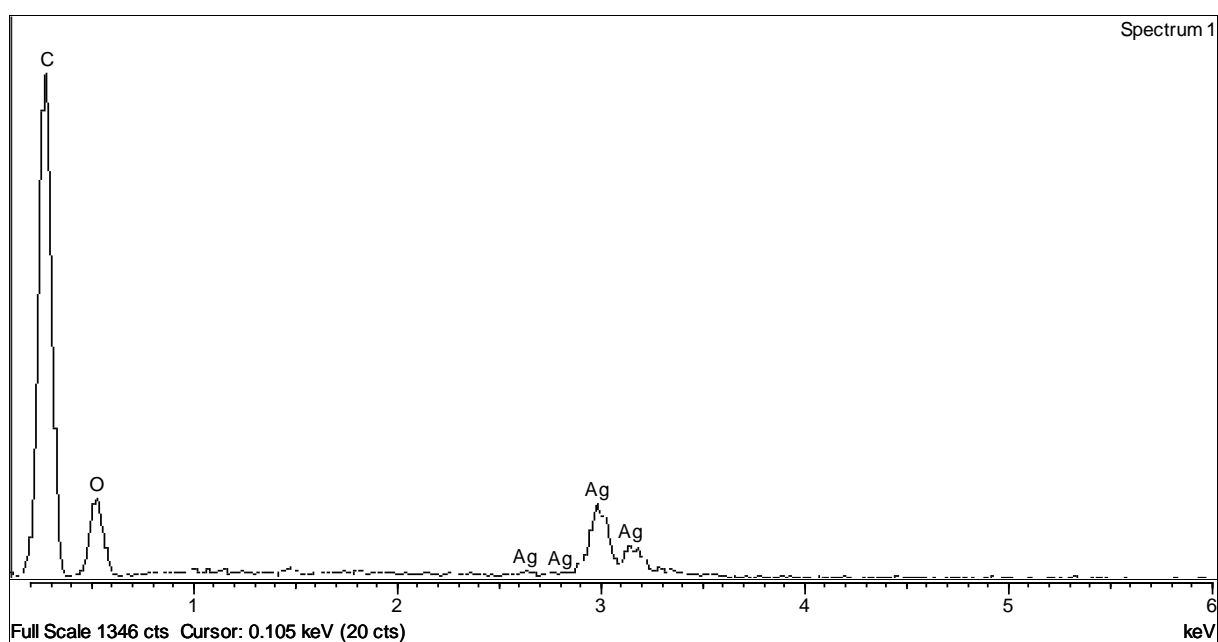


Figure 14.36. The results of EDS which were taken from a cotton textile coated by silver.

The first cotton sample was coated by silver for 20 minutes. The EDS graphs show that the oxygen and carbon weight content in the cotton were 27.52% and 62.75% respectively and the coated silver was 9.73%. Coated textile includes carbon and oxygen in addition to silver peaks in EDS analysis. Because, the cellulose in cotton includes carbon, hydrogen and oxygen as reactive hydroxile groups. EDS results show that the coating is pure silver. As seen from this result, no other material is coated to the fabric proving that this is perfectly clean coating method producing no waste and harmful gases.

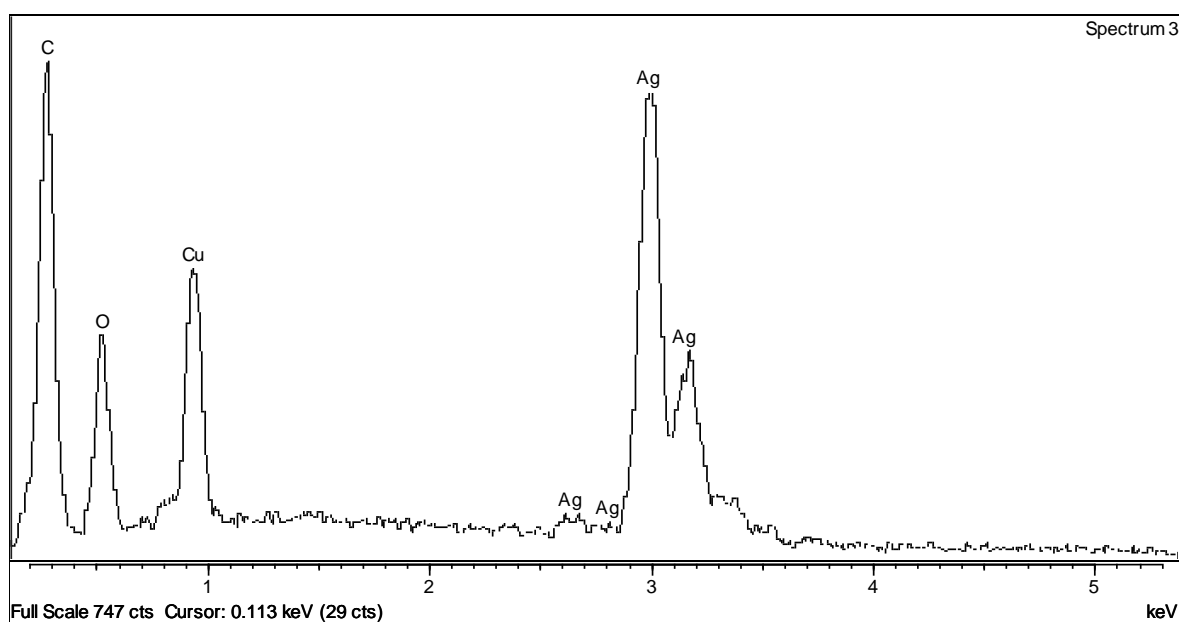


Figure 14.37. The results of EDS of a cotton textile coated by silver and copper

The next cotton sample was coated by firstly copper for 4 minutes and then by silver for 4 minutes. The oxygen and carbon weight content in the cotton were 10.74% and 12.84% and the coated silver and copper to be 60.05% and 16.37% respectively. Coated textile includes only carbon and oxygen in addition to silver and copper peaks in EDS analysis as expected. This EDS result shows that the coating is pure silver and copper, since no peaks due to other elements were observed. It seems that, although the coating time of silver is the same as the coating time of copper, the weight content of the silver is much more than that of the copper. This may be due to the fact that the energy of electron beam in the SEM may not be high enough to pass upper silver layer and reach the bottom of copper coating.

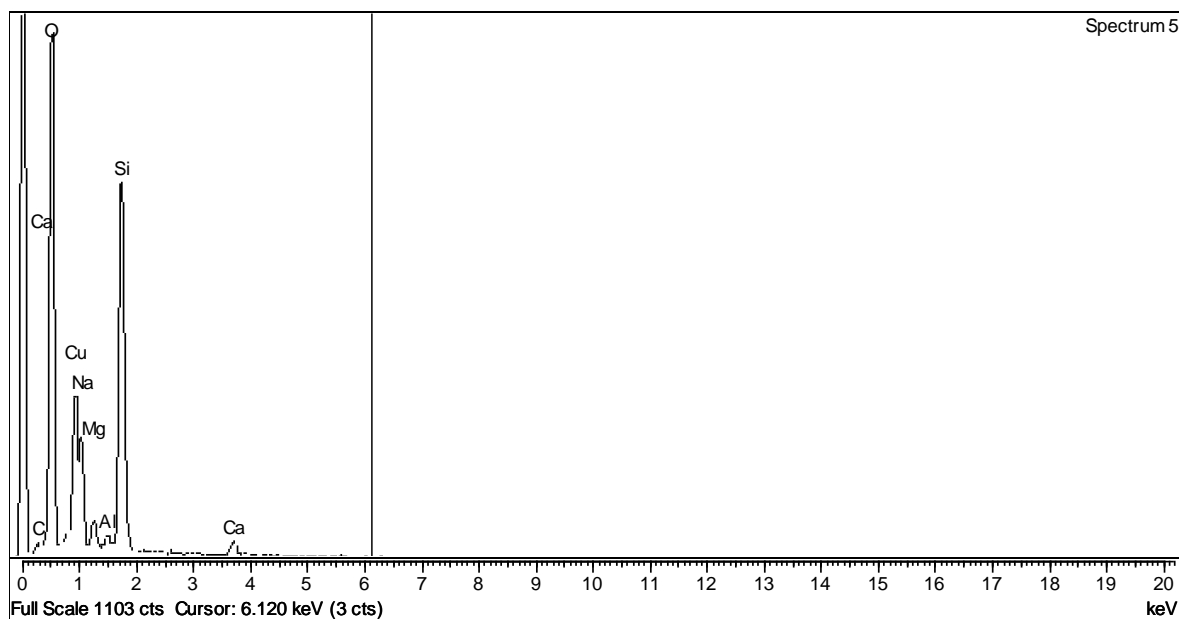


Figure 14.38. The results of EDS which were taken from a glass coated by copper

For the last sample, a 1 mm thick glass was coated by copper for 4 minutes. The EDS analysis (Figure 14.38) shows the peaks due to oxygen, carbon, sodium, aluminium, silisium, calcium and magnesium with weight contents of 39.74%, 1.56%, 4.64%, 0.42%, 21.51%, 2.02% and 1.39% respectively and the upper coated copper weight content was 28.72%. Coated glass includes carbon, oxygen, sodium, silisium, aluminium, calcium and magnesium in addition to copper peaks in EDS analysis. Because, the main element in the glass is  $\text{SiO}_2$ . In addition to this, there is  $\text{Na}_2\text{CO}_3$ ,  $\text{CaCO}_3$ , aluminium and magnesium in the glass due to its manufacturing process. EDS results show that the coating material is pure copper.

All these results show that the main advantage of the magnetron sputtering system is that the coating is too clean and environmentally friendly, comparing with other chemical coating methods.

#### 14.2.4. Results of Wettability of The Surfaces

The change of shape of droplet on the surface gives hint about hydrophobicity or hydrophilicity of the surface. One type of test liquid, pure water is used in this study. First

of all, 100  $\mu\text{l}$  pure water was placed on the deposited textile with an accurate dripper and then contact angles were measured. Initially, we did not have a goniometer in our laboratory, surface tension was out of the scope of interest. However, the influences of the magnetron sputtering deposition on the hydrophobicity of textile were investigated in this study.

Before measurements, uncoated and coated samples were ultrasonically cleaned. Ultra-pure water at 25°C were used to create a droplet. The shapes of droplet on the textiles which were coated and uncoated for different time durations of  $t=0$ ,  $t=3$  and  $t=5$  minutes are shown in Figure 14.39.

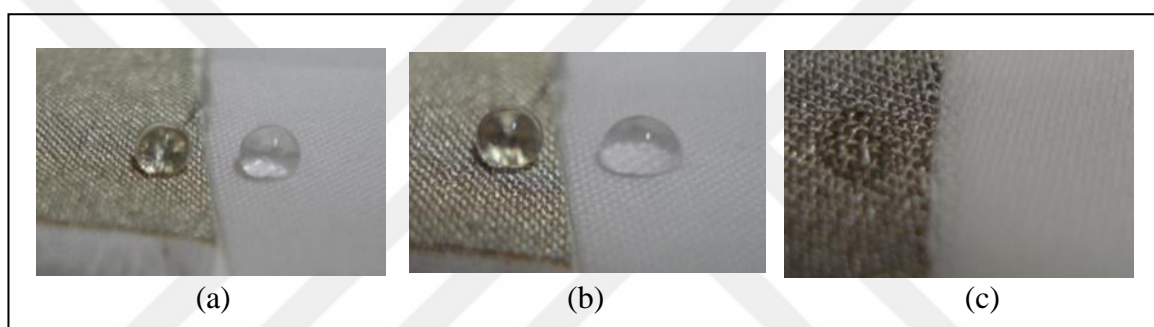


Figure 14.39. The conditions of droplets after (a)  $t=0$  minutes, (b)  $t=3$  minutes, (c)  $t=5$  minutes on Ag coated and non-coated polycotton samples.

It was observed that although water is absorbed by uncoated polycotton in 5 minutes, Ag coated textile did not absorb water. The shapes of droplets on the copper coated textiles and uncoated for different time durations of  $t=0$ ,  $t=2$  and  $t=4$  minutes are shown in Figure 14.40.

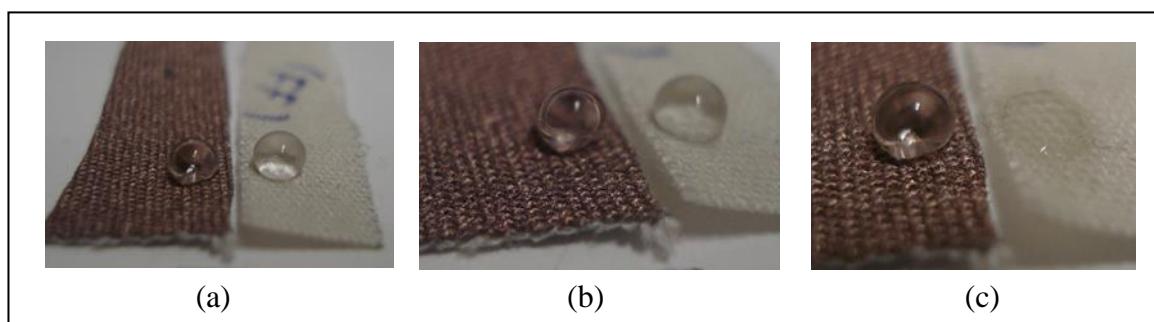


Figure 14.40. The conditions of droplets after (a)  $t=0$ , (b)  $t=2$  minutes, (c)  $t=4$  minutes on Cu coated and non-coated polycotton samples respectively.

Although water is absorbed by uncoated cotton in 4 minutes, Cu coated textile did not absorb water as was the case with Ag coating.

These results showed that the textiles coated by Cu and Ag became totally hydrophobic, while uncoated textiles were hydrophilic [27] and that the hydrophobicity lasted very long time.

The reason why the coated textile is hydrophobic can be air trapped in the metal-cotton surface by producing increase of the surface hydrophobicity. The empty space in the polycotton fabrics is reduced during the magnetron sputtering of metal and decreases the water penetration.

#### **14.2.5. The Measurement of the Resistance**

Textiles can gain certain functionalities by deposition, and conductivity is one of them. Conductive textiles are very important in smart clothing applications such as textile antenna for wireless communication, sensors to monitor body function and transducers for cooling firemen's clothes. Because, electrical conductivity helps the textiles to carry energy and information. Conductive finishings, polymers, fibers, fabrics and yarns are used to produce smart textiles. However, some coating or finishing method are difficult to obtain conductive textiles by using organic thin films, so deposition of inorganic thin films are more preferred [28].

The properties of the textiles, especially the weave structure are important in this study. Only the parts of the textile surface which are exposed to the plasma are deposited. Fig. 14.41 shows the SEM picture of (2K magnification) polycotton fibers coated by magnetron sputtering method. The partial coating of the fiber can be noticed easily. In addition to this, loss of desired conductivity can be seen due to mechanical treatment such as stretching. Therefore, instead of cotton or polycotton textiles, nonwoven textiles were preferred to coat in these resistance measurements.

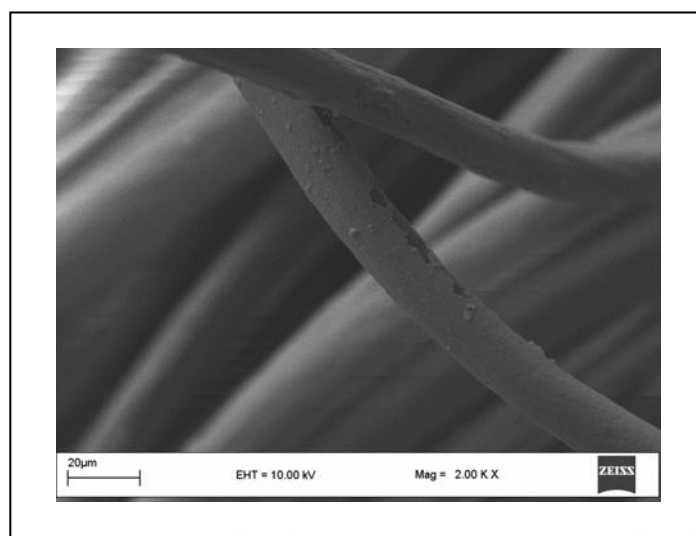


Figure 14.41. SEM images of Ag coatings on polycotton for 4 minutes

For conductive textile applications, the resistivity of silver thin films was investigated. Firstly, the nonwoven fabrics were coated by Ag for 5, 10 and 20 minutes by magnetron sputtering system as mentioned in Table 14.9. To study the effects of deposition times of silver and surface treatment on the resistivity of the textiles, some measurements were done by using a sensitive multimeter by means of stationary and moving probes .

Resistance at different lengths of textile was measured after 1 hr, 24 hrs and 240 hrs as in Figure 14.42. During measurements, it was important to apply the same pressure on the surface, because it could affect the results.



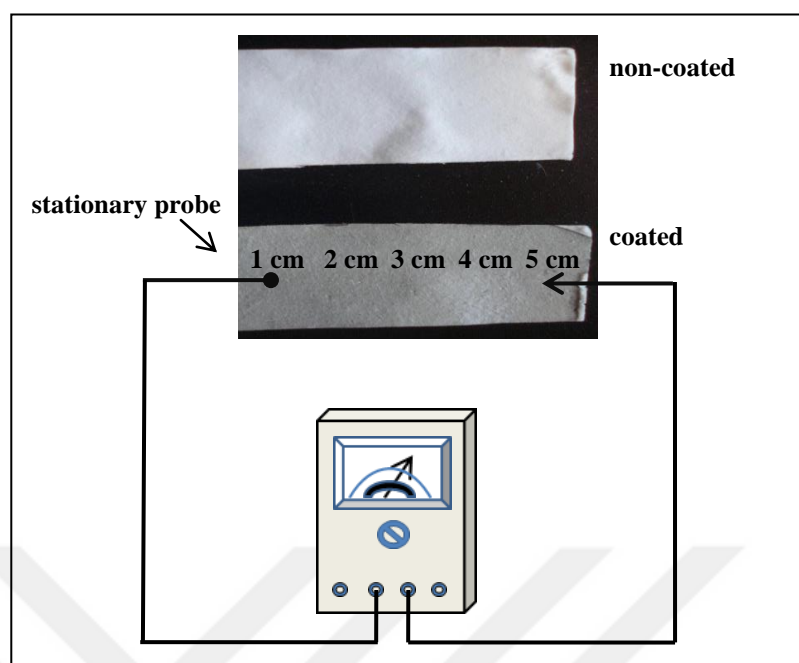


Figure 14.42. The nonwoven fabric before and after coating by Ag and resistance measurement from 1-4 cm apart from the stationary upper electrode.

The graphs of the values of resistance as a function of distance from the stationary probe were plotted. The textiles were coated by silver for 5 minutes, 10 minutes and 20 minutes.

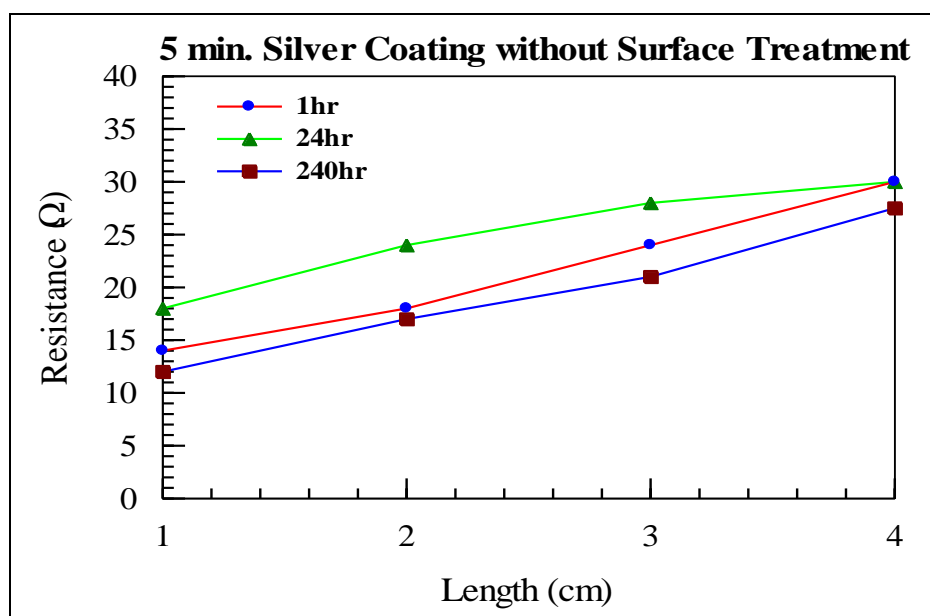


Figure 14.43. Resistances of nonwoven textiles deposited by silver for 5 minutes without surface treatment at different lengths.

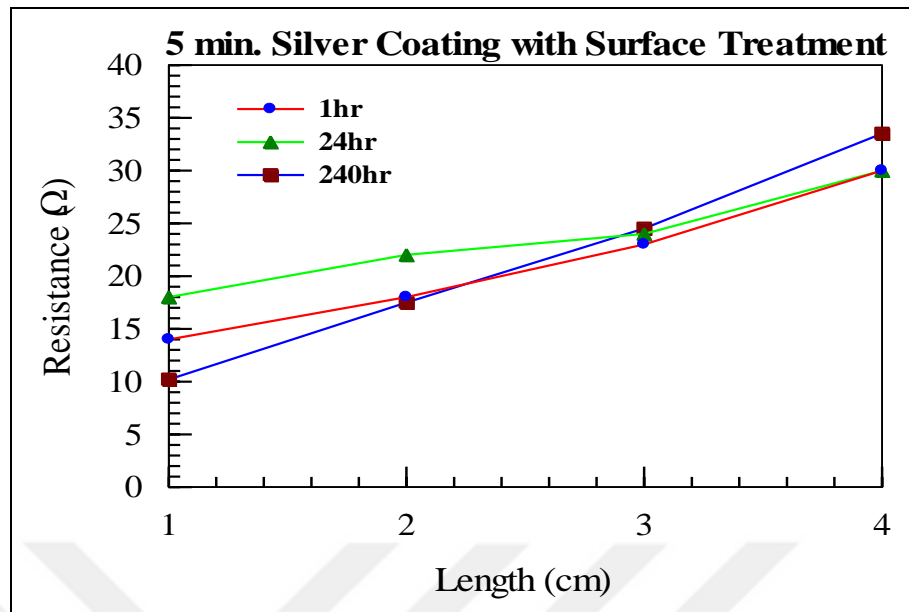


Figure 14.44. Resistances of nonwoven textiles deposited by silver for 5 minutes with surface treatment at different lengths.

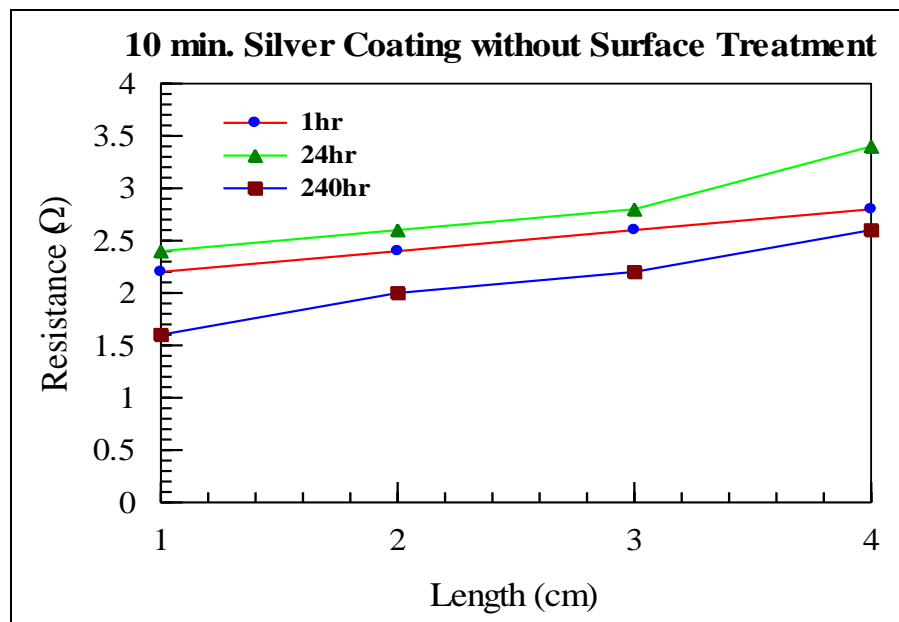


Figure 14.45. Resistances of nonwoven textiles deposited by silver for 10 minutes without surface treatment at different lengths.

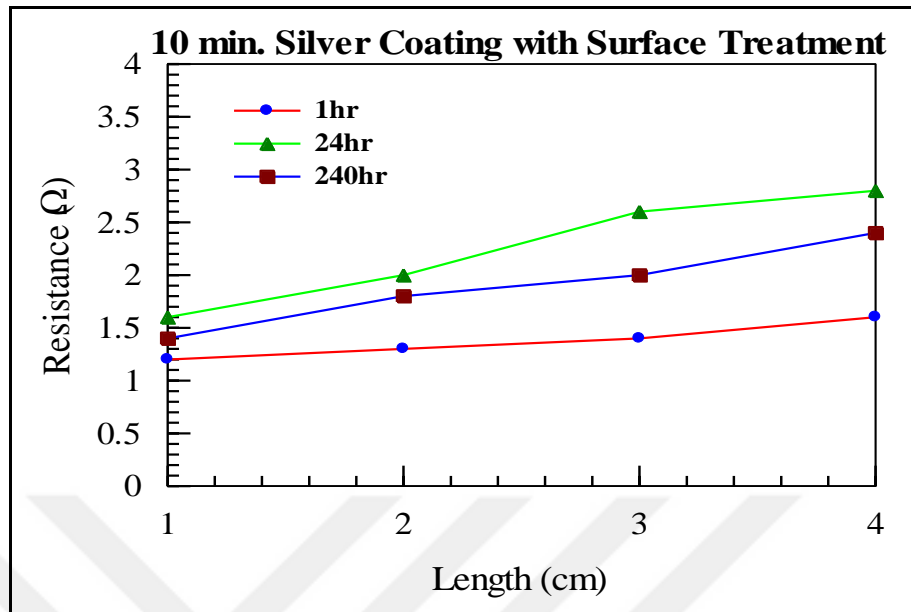


Figure 14.46. Resistances of nonwoven textiles deposited by silver for 10 minutes with surface treatment at different lengths.

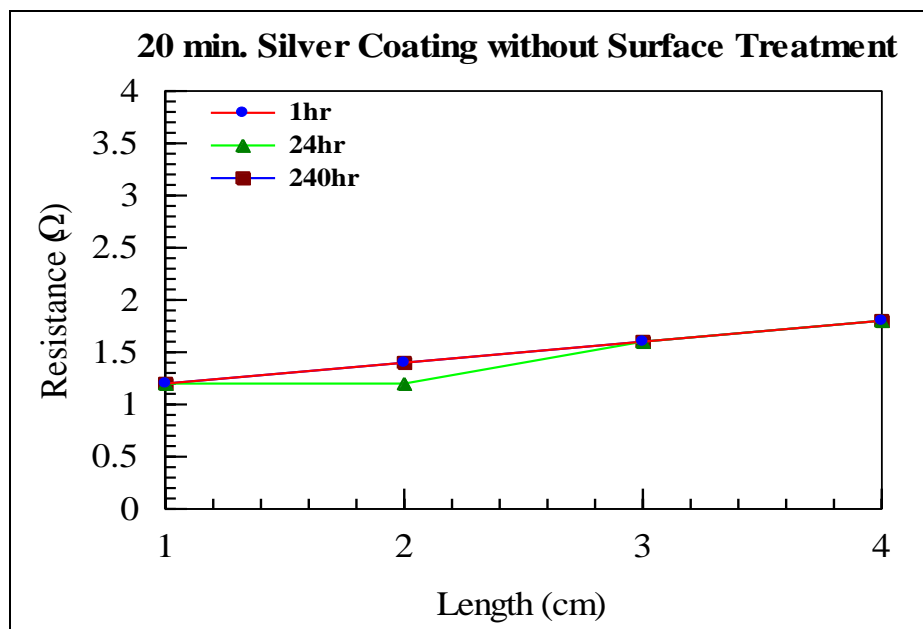


Figure 14.47. Resistances of nonwoven textiles deposited by silver for 20 minutes without surface treatment at different lengths.

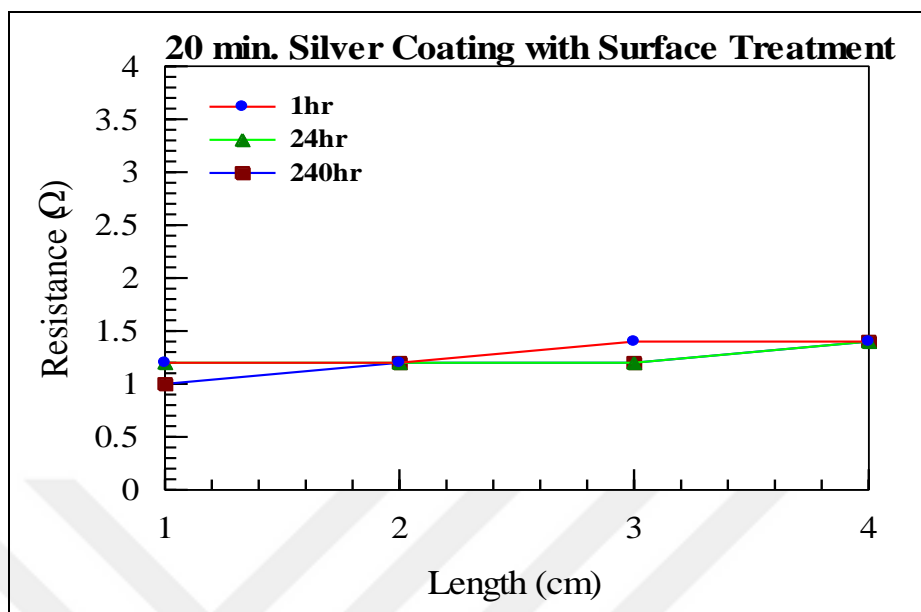


Figure 14.48. Resistances of nonwoven textiles deposited by silver for 20 minutes with surface treatment at different lengths.

The values of resistances on the textiles deposited by silver at different times and with/without pretreatment were shown in Table 14.11.

Table 14.11. The values of resistances with the time of deposition

Resistance ( $\Omega$ )	5 minutes silver coating with no surface treatment			
	Length (1 cm)	Length (2 cm)	Length (3 cm)	Length (4 cm)
After 1 hr.	14	18	24	30
After 1 day	18	24	28	30
After 10 days	12	17	21	27.5
Resistance ( $\Omega$ )	5 minutes silver coating with surface treatment			
	Length (1 cm)	Length (2 cm)	Length (3 cm)	Length (4 cm)
After 1 hr.	14	18	23	30
After 1 day	18	22	24	30
After 10 days	10.2	17.5	24.5	33.5
Resistance ( $\Omega$ )	10 minutes silver coating with no surface treatment			
	Length (1 cm)	Length (2 cm)	Length (3 cm)	Length (4 cm)
After 1 hr.	2.2	2.4	2.6	2.8
After 1 day	2.4	2.6	2.8	3.4
After 10 days	1.6	2	2.2	2.6
Resistance ( $\Omega$ )	10 minutes silver coating with surface treatment			
	Length (1 cm)	Length (2 cm)	Length (3 cm)	Length (4 cm)
After 1 hr.	1.2	1.3	1.4	1.6
After 1 day	1.6	2	2.6	2.8
After 10 days	1.4	1.8	2	2.4
Resistance ( $\Omega$ )	20 minutes silver coating with no surface treatment			
	Length (1 cm)	Length (2 cm)	Length (3 cm)	Length (4 cm)
After 1 hr.	1.2	1.4	1.6	1.8
After 1 day	1.2	1.2	1.6	1.8
After 10 days	1.2	1.4	1.6	1.8
Resistance ( $\Omega$ )	20 minutes silver coating with surface treatment			
	Length (1 cm)	Length (2 cm)	Length (3 cm)	Length (4 cm)
After 1 hr.	1.2	1.2	1.4	1.4
After 1 day	1.2	1.2	1.2	1.4
After 10 days	1	1.2	1.2	1.4

As can be seen in Table 14.11, the values of resistance generally increased with the length. This is expected, since the resistance is directly proportional to the length of a conductor.

It was seen that pretreatment before the deposition of silver affected the resistance of the textiles. The resistance of the thin film generally slightly decreased after pretreatment, and the conductivity of nonwoven textile increased. The importance of pretreatment can be seen in this study, since pretreatment helps the thin film to have a good adhesion to the textile.

As in Table 14.11, there is a dramatic reduction in the resistance (almost 10 times), when the time of deposition is doubled. The textiles were coated by 5, 10 and 20 minutes. As can be seen in Figure 14.44, the resistance is between 10-20  $\Omega$ , in Figure 14.46, between 1-1.5  $\Omega$ , and in Figure 14.48, it is about 1  $\Omega$ . When the time of deposition is increased, the resistance decreased. It is an expected result. Since, if the time increased, the amount of silver on the surface is also increased so that this causes the textile to be a better conductor. These kinds of textiles can be used for the purpose of electromagnetic shielding which the industry needed for electromagnetic compatibility.

#### **14.2.6. Antibacterial Textile Results**

There were two types of antibacterial methods: parallel streak and suspension method was used to check antibacterial effects of coated textiles.

##### ***14.2.6.1. Parallel Streak Method***

Parallel streak method was used to study the bacterial inactivity. In this test, the bacteria are spread on the petri dish filled with agar food, the coated side of the textiles are put on these surfaces and the petri dish are incubated for 24 hours at 37<sup>0</sup>C to allow colonization of bacteria. If the surfaces are antibacterial, the bacteria can not survive on the agar surface under the textile and inactivation zones are created around the textile. The zones around the deposited textile are the regions where the bacteria did not grow. The zone tests were done according to the protocol AATCC TM 147. Two types of bacteria were studied: *Escherichia coli* and *Staphylococcus aureus* .

For all these experiments, one control (non-coated textile) and one coated sample was used to do a correct experiment.

#### 14.2.6.1.1. *Escherichia coli* Inactivation for the Cu Coated Textiles

*E. coli* culture were spread on the petri dish which contains agar as shown in Figure 14.49. A control and Cu coated textile was put on the dishes.

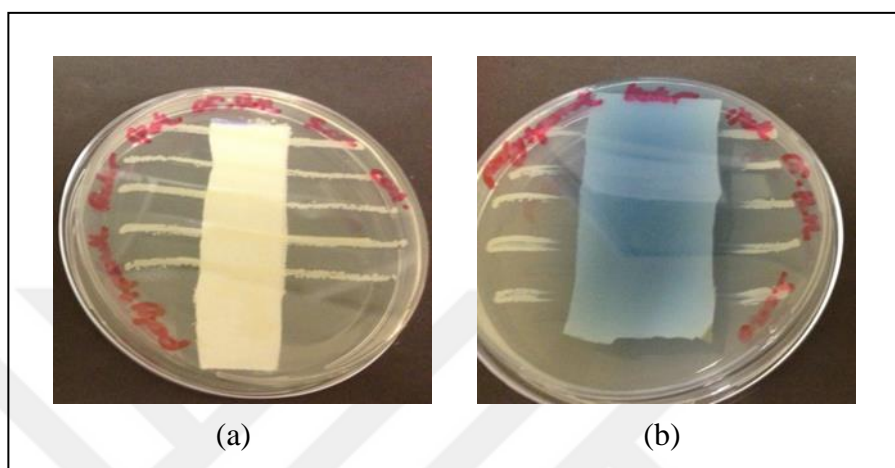


Figure 14.49. *Escherichia coli* inactivation for (a) control sample, (b) Cu coated sample

After incubation for 24 hours at 37<sup>0</sup>C, The petri dishes which contain both uncoated and copper coated textile were observed under the light microscope. The diameters of the zones where the bacteria move away from the both sides of textile were measured by a vernier caliper.

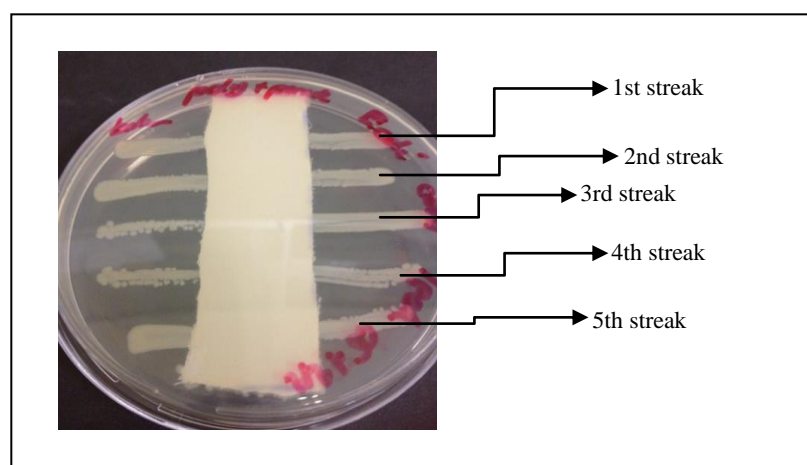


Figure 14.50. *E.coli* control

The diameter of zones are written on Table 14.12.

Table 14.12. Measurement of the distance where the bacteria move away from the both sides of textile

<i>E. coli</i> control				
Streak number	Left (cm)	Right (cm)	Coated side up or down	Surface contain bacteria or not
1	-	-	*	+
2	-	-	*	+
3	-	-	*	+
4	-	-	*	+
5	-	-	*	+
<i>E. coli</i> with Cu coated textile				
1	0.1	-	Y	0
2	0.2	0.1	Y	0
3	0.2	0.2	Y	0
4	0.1	0.1	Y	0
5	0.1	0.1	Y	0

\* : uncoated textile, Y: coated site down , 0: surface does not contain bacteria, + : surface contains bacteria

#### ***14.2.6.1.2. Escherichia coli Inactivation for the Ag Coated Textiles***

In the same way, *E. coli* culture were spread on the petri dish which contains agar as shown in Figure 14.51. A control and Ag coated textile was put on the dishes.



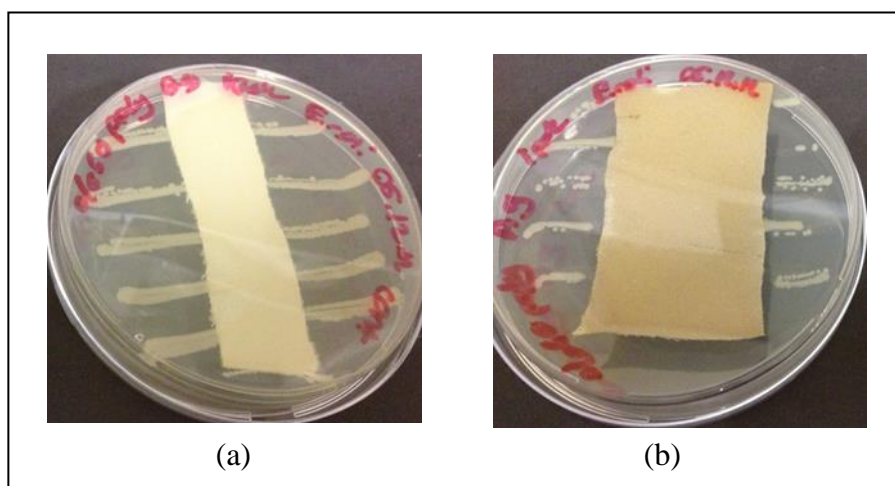


Figure 14.51. *Escherichia coli* inactivation for (a) control sample, (b) Ag coated sample.

The diameter of zones are as shown on Table 14.13.

Table 14.13. Measurement of the distance where the bacteria move away from the both sides of textile

<i>E. coli</i> control				
Streak number	Left (cm)	Right (cm)	Coated side up or down	Surface contain bacteria or not
1	-	-	*	+
2	-	-	*	+
3	-	-	*	+
4	-	-	*	+
5	-	-	*	+
<i>E. coli</i> with Ag coated textile				
1	0.2	0.3	Y	0
2	0.3	0.4	Y	0
3	0.4	0.4	Y	0
4	0.2	0.2	Y	0
5	0.4	0.2	Y	0

\* : uncoated textile, Y: coated site down, 0: surface does not contain bacteria, + : surface contains bacteria

### 14.2.6.1.3. *Staphylococcus aureus* Inactivation for the Cu Coated Textiles

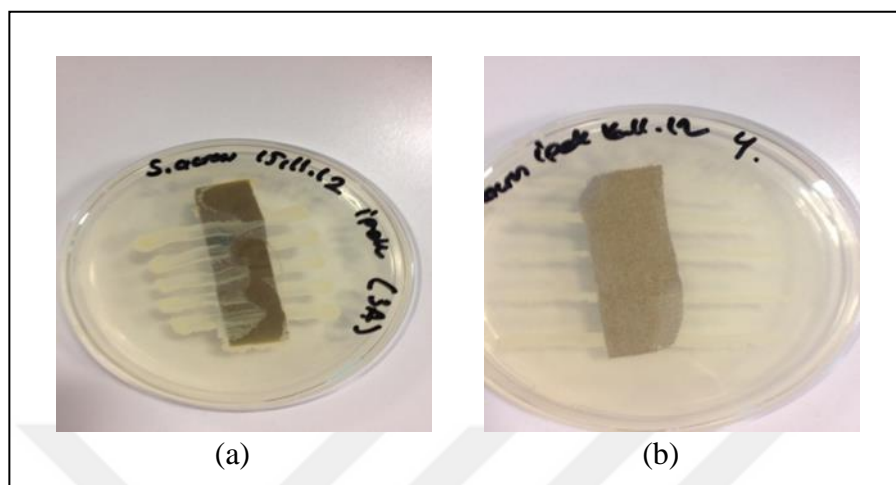


Figure 14.52. *Staphylococcus aureus* inactivation for (a) control sample, (b) Cu coated sample

Table 14.14. Measurement of the distance where the bacteria move away from the both sides of textile

<i>S. aureus</i> control				
Streak number	Left (cm)	Right (cm)	Coated side up or down	Surface contain bacteria or not
1	-	-	*	+
2	-	-	*	+
3	-	-	*	+
4	-	-	*	+
5	-	-	*	+
<i>S. aureus</i> with Cu coated textile				
1	-	-	Y	+
2	-	-	Y	+
3	-	-	Y	0
4	-	-	Y	0
5	-	-	Y	0

\* : uncoated textile, Y: coated site down , 0: surface does not contain bacteria, + : surface contains bacteria

#### 14.2.6.1.4. *Staphylococcus aureus* Inactivation for the Ag Coated Textiles

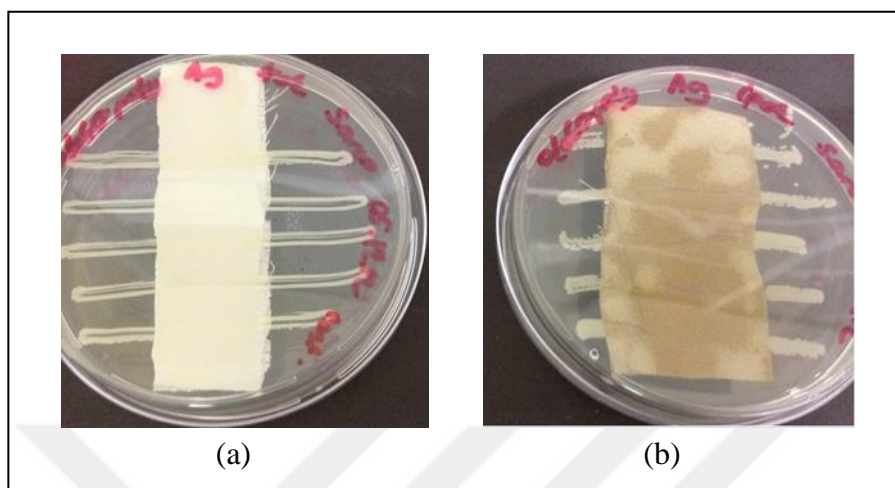


Figure 14.53. *Staphylococcus aureus* inactivation for (a) control sample, (b) Ag coated sample

Table 14.15. Measurement of the distance where the bacteria move away from the both sides of textile

<i>S. aureus</i> control				
Streak number	Left (cm)	Right (cm)	Coated side up or down	Surface contain bacteria or not
1	-	-	*	+
2	-	-	*	+
3	-	-	*	+
4	-	-	*	+
5	-	-	*	+
<i>S. aureus</i> with Ag coated textile				
1	0.1	0.2	Y	0
2	0.2	0.1	Y	0
3	0.2	0.2	Y	0
4	0.2	0.1	Y	0
5	0.2	0.2	Y	0

\* : uncoated textile, Y: coated site down , 0: surface does not contain bacteria, + : surface contains bacteria

#### **14.2.6.1.5. Results of Parallel Streak Method**

As can be seen on the Table 14.12 and Table 14.14, textile which was coated with copper is more effective towards *E. coli* bacteria. The inhibition zones around the textile was about 0.1-0.2 cm. It showed us *E. coli* did not grow around the copper deposited textile, and the surface did not contain bacteria. *S. aureus* grew around the textile which was coated with copper. However, the surface did not contain it. To conclude, the antimicrobial efficiency of copper on *S. aureus* was significantly lower.

Table 14.13 shows that *E. coli* bacteria did not grow on the left and right side of the textiles which were coated with silver. In addition to this, surface did not contain *E. coli* bacteria. The diameters of these zones were measured, and it was about 0.2-0.4 cm for *E. coli*. No *S. aureus* growth onto the silver deposited textile was observed and zone of inhibitions was of 0.1-0.2 cm as can be seen in Table 14.15. It can be seen easily, the antimicrobial efficiency of silver on *E. coli* was significantly higher.

All these results which were written on Table 14.12, 14.13, 14.14 and 14.15 show that both copper and silver coatings can be used for antimicrobial activity on the textile surfaces. However, the textile coated with the silver is more effective towards *E. coli* bacteria and *S. aureus* than the textile coated with copper.

#### **14.2.6.2. Suspension Test**

##### **14.2.6.2.1. Procedure of Suspension Test**

In this method, the number of bacteria was counted to see the effect of coated textiles on the number of bacteria.

5 mL bacteria and 50 mL broth was mixed. There were eight erlenmayer flasks. Four of them were containing *E. coli* and the others were containing *S. aureus*.

Coated and uncoated textiles were added to this mixture and then incubated for 1 hour by shaking incubator. After incubation 100 µl was taken from all the solutions and then serial dilution procedure was prepared. After this procedure from  $10^{-6}$ ,  $10^{-7}$ ,  $10^{-8}$  dilutions, 100 µl

was taken and added to prepared LB agars by using drigalski spatula. After 24 hours incubation, colony forming units (cfu) were calculated. Table 14.16 shows the number of bacteria at different flasks at a dilution of  $10^{-7}$ . Three different measurement were applied and the average of them were written on the Table 14.16.

Table 14.16. Colony forming units (cfu) at  $10^{-7}$  dilution

Flasks	Sample	Number of bacteria at $10^{-7}$ dilution (cfu)	The rate of bacteria
1	<i>E. coli</i> with uncoated textile (control)	$1.75 \times 10^7$	100%
2	<i>E. coli</i> with Cu coated textile	$1.05 \times 10^6$	6%
3	<i>E. coli</i> with uncoated textile (control)	$1.25 \times 10^6$	100%
4	<i>E. coli</i> with Ag coated textile	$1 \times 10^2$	0.008%
5	<i>S. aureus</i> with uncoated textile (control)	$6 \times 10^6$	100%
6	<i>S. aureus</i> with Cu coated textile	$3 \times 10^6$	50%
7	<i>S. aureus</i> with uncoated textile (control)	$7.5 \times 10^6$	100%
8	<i>S. aureus</i> with Ag coated textile	$3 \times 10^5$	4%

#### 14.2.6.2.2. Result of Suspension Test

Table 14.16. shows that the antimicrobial efficiency of copper and silver on *E. coli* was significantly higher, and silver metal is more antibacterial than copper. These results are strongly correlated with the ones which were obtained by parallel streak method.

### 14.3. THE COMPARISON OF SURFACE CHARACTERISTICS OF TEXTILES (COTTON AND POLYESTER) COATED BY SILVER AND COPPER

#### 14.3.1. Antibacterial Activity

In this study, different deposition times were selected for coating of the textiles. The deposition times selected were 1 minutes, 4 minutes and 10 minutes. Effects of deposition times on antibacterial characteristics of the textiles were studied by parallel streak method. In addition to this, effects of fabric type and deposition material on the antibacterial properties were studied. Table 14.17 shows the parameters used for coating by magnetron sputtering.

Table 14.17. Typical deposition parameters for Ag and Cu coatings.

Base Pressure	$1 \times 10^{-6}$ Torr
Working Pressure	$1 \times 10^{-2}$ Torr
Voltage	400-450 V
Current	0.2-0.3 A
Distance to Target	8 cm
Substrate type	polyester, cotton

Firstly, control samples which were not coated by silver and copper (100% cotton and 100% polyester) were studied to check antibacterial effects. It was observed that *E. coli* and *S. aureus* grew on both cotton and polyester fabrics before deposition.

Cotton fabrics deposited by silver for 4 minutes and 10 minutes showed antibacterial effects towards both *E. coli* and *S. aureus*. While cotton fabrics deposited by copper for 4 minutes and 10 minutes were effective toward *E. Coli*, only the one deposited by copper for 10 minutes was antibacterial effect toward *S. aureus*.

The same test was applied to the silver and copper deposited polyester fabrics. Almost the same results were obtained.

To conclude, one can say that the antibacterial effect does not depend on the substrate types, but depends on the type of deposition material. The time of deposition is also an important parameter in terms of antibacterial activity, since this determines coating thickness. In addition to this, fabrics which were coated by silver were more antibacterial than the one coated by copper. 4 Minutes deposition of silver is enough, while 10 minutes deposition of copper is necessary to kill the bacteria. Since copper is cheaper than silver, it would be better to coat surface by copper for 10 minutes initially and by silver for 5 minutes.

#### **14.3.2. Contact Angle Measurements**

In this study, the deposition times were selected to be 1 minutes, 4 minutes and 10 minutes. Effects of deposition times on hydrophobicity of the textiles were studied by drop tests.

For the purpose of investigation of hydrophobicity of the deposited surfaces, tests were done by the camera KSV CAM 200. The contact angle measurement was carried out by using 4 cm x 6 cm of the cotton and polyester fabrics deposited by silver and copper separately. Some ultrapure water were slowly squeezed out by the help of a sensitive pipette at room temperature. A CCD camera took the images of the drop shapes and a computer estimated the contact angles after 10 s. The experiment was repeated ten times and the average was calculated. The maximum error in the contact angle measurement was  $\pm 3 \%$ .

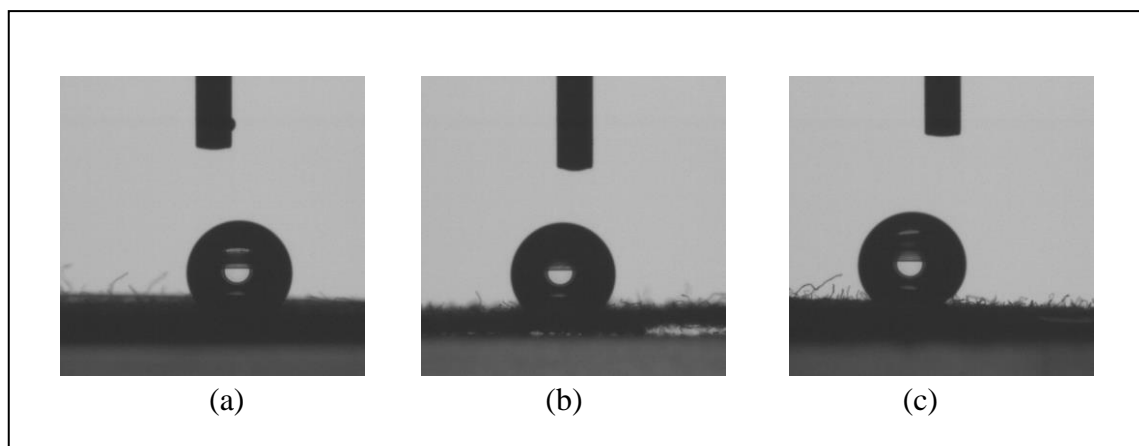


Figure 14.54. The drops on (a) 1 minutes silver deposited cotton, (b) 4 minutes silver deposited cotton, (c) 10 minutes silver deposited cotton

Figure 14.54 shows the drop images on silver coated textiles coated at 1,4 and 10 minutes. Contact angles of cotton textiles deposited by silver for 1 minute, 4 minutes and 10 minutes were  $119^{\circ}$ ,  $125^{\circ}$  and  $134^{\circ}$ . This showed that hydrophobicity of the silver deposited cotton increased with increasing deposition time.

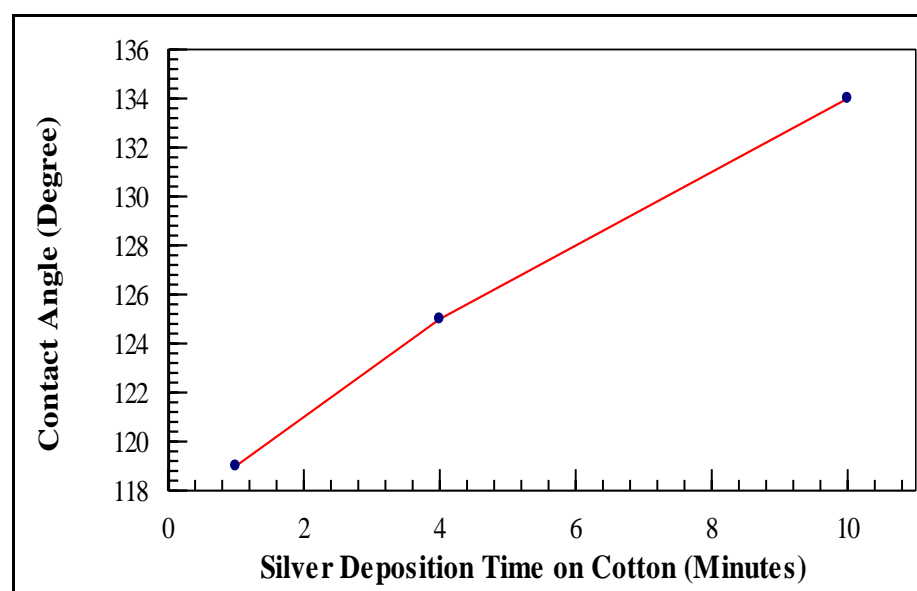


Figure 14.55. Contact angle measurements versus deposition times of silver on cotton



To see the effect of substrate on the hydrophobicity, polyester fabrics were also coated by silver for 1 minute, 4 minutes and 10 minutes. Contact angles of polyester fabrics deposited by silver also increased with increasing deposition time and the conclusion was almost the same as the cotton.

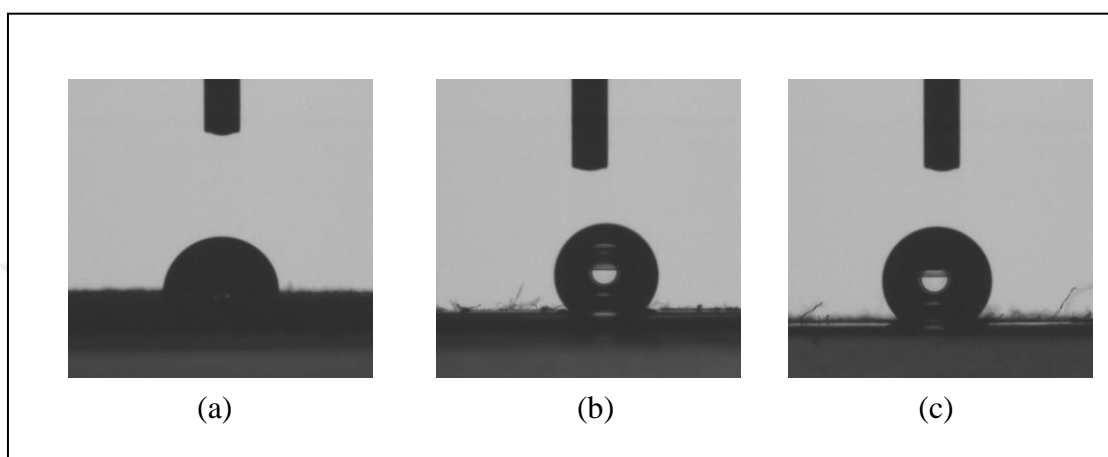


Figure 14.56. The drops on (a) 1 minute copper deposited cotton, (b) 4 minutes copper deposited cotton, (c) 10 minutes copper deposited cotton

Contact angles of textiles deposited by copper for 1, 4 and 10 minutes were found to be  $100^{\circ}$ ,  $114^{\circ}$  and  $120^{\circ}$ . Thus, hydrophobicity of the copper deposited cotton also increased with increasing deposition time, but at smaller rate than cotton coated by silver. This means that, silver coating makes the cotton more hydrophobic. Similar results were observed for the polyester fabric coated by copper.

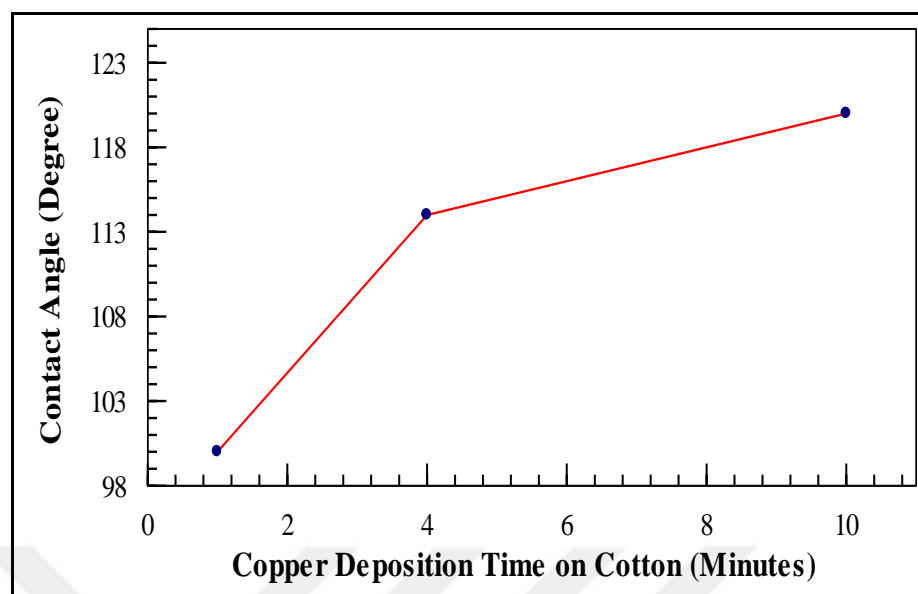


Figure 14.57. Contact angle measurements versus deposition times of copper on cotton

As a result, it was observed that the type of material coated on textile affected the hydrophobicity of its surface and silver makes the textile surface more hydrophobic than copper. Greater deposition time means greater hydrophobicity. In addition to this, it was also found that whether the fabric was cotton or polyester did not effect hydrophobicity of the textiles which were coated.

### 14.3.3. Abrasion Tests

Abrasive resistance of textiles is one of the most important characteristics to improve the surface characteristics. A complex interaction of the forces during wear and maintenance cause the abrasion of a textile surface. The extent of abrasion is affected by the type of activity by the wearer, the construction of the garment and the parts which most involved in the activity. The performance of the textiles is determined by the mechanical finishes (brushing, calendering, sanding, etc.) and finishing processes (finishing agents and their application methods, preparation and dyeing methods, etc.) [11].

Different kinds of chemicals are used to improve abrasion resistance [29]. However, these products have many disadvantages like the modification of fiber surfaces characteristics,

decrease of tensile strength, increased cost and environmental concerns [11]. Therefore, plasma application is an alternative to these chemical methods to increase abrasion resistance of textiles. Applying abrasion is very important, in terms of having an effect on the value of contact angle on the deposited textiles. Abrasion resistance of the deposited textile is determined by the help of an abrasive device. The textile deposited by silver gained hydrophobic characteristics as mentioned in Part 14.3.2. After abrasion tests, it should be still hydrophobic, even after 5000 abrasion cycles [30].

Abrasion tests were applied by Martindale Abrasion Tester in Marmara University, 5000 abrasion cycles were applied on the textiles coated by Ag for 1, 4 and 10 minutes. After abrasion test, drop test was applied on the deposited textiles. A CCD camera and a computer was used in this system. The contact angles on the 10 minutes silver coated textile were measured at different times as seen in Figure 14.58. The contact angle did not change with time.

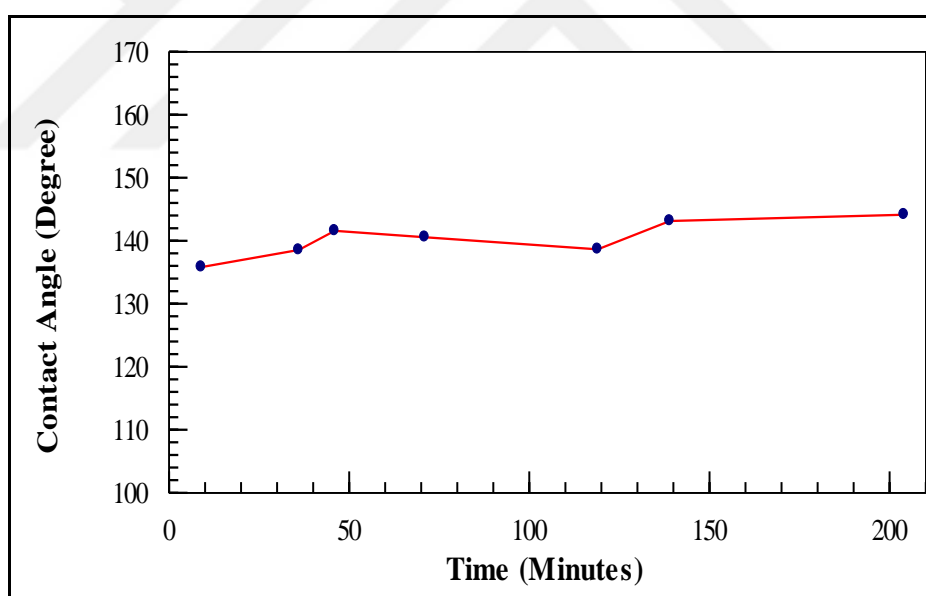


Figure 14.58. Contact angle measurement on 10 minutes silver coated cotton

The comparisons of the contact angles as a function of time on the 1, 4 and 10 minutes silver deposited textiles after abrasion can be seen in Figure 14.59. There was a decrease on the value of contact angle with time. Abrasion (5000 abrasion cycles) leads to the lose of hydrophobicity of the deposited textiles. However, the contact angles on the textiles coated for 1 minute was decreasing in a shorter time, if it is compared with longer treated

time textiles. It showed that after 5000 abrasion cycles, the coated textiles lost the hydrophobic characteristics within 200 minutes.

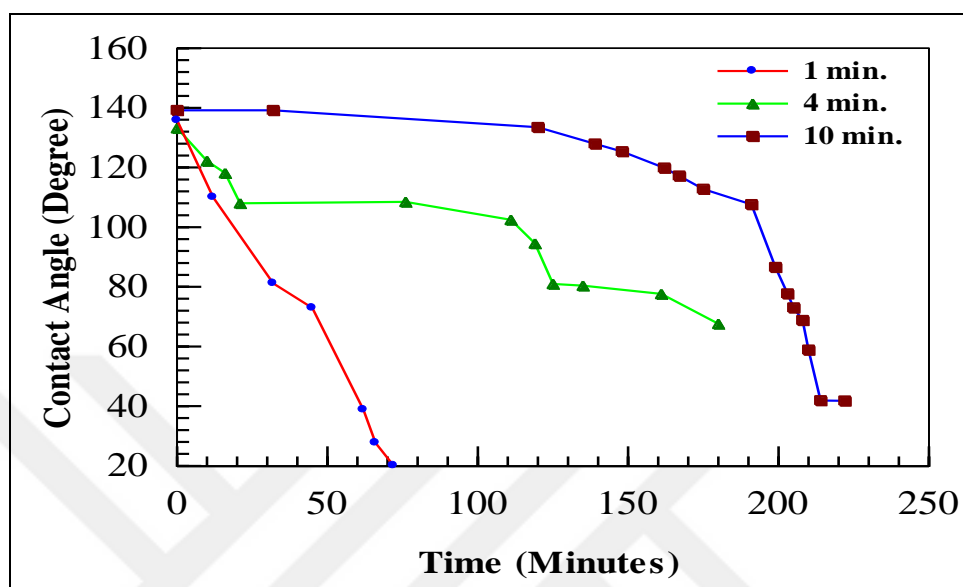


Figure 14.59. Contact angles at different times (a) 1 min. silver deposited cotton after abrasion, (b) 4 min. silver deposited cotton after abrasion, (c) 10 min. silver deposited cotton after abrasion.

This means that silver was not bounded to the textile much. Therefore, to increase the adhesion of silver on the textile, some high-end applications such as a finishing with a polymer coating (varnish or resin) may be used. Then, it is expected that abrasion and washability property can be improved [28].

#### 14.3.4. Washing Tests

##### 14.3.4.1. Antibacterial Results

In order to check the durability of antimicrobial property, washing tests were performed to see the effect of washing cycles (1, 5 and 10 cycles) on antibacterial characteristics. As seen before, 4 minutes deposition of silver on cotton showed antibacterial effect.

Therefore, 4 minutes silver deposited textile was chosen to see the effect of washing on the antibacterial property of textile, since 4 minutes deposition was an ideal deposition time to inhibit the bacteria.

For this study, a washing procedure was applied. 4 g ECE-soap (ISO 105-C06) and 1 g sodium carbonate was put in a tube which contains 1 liter deionized water. The ratio was 1/50. The temperature was set at 60°C. The samples were put in the tubes and they were washed for 20 minutes (ISO6330 standard) [28].

This washing test procedure was applied to the cotton fabrics deposited by silver for 4 minutes. These tests have shown that the deposited textiles were antibacterial toward *E.Coli* and *S.aureus* after 1 washing cycle and 5 washing cycles. However, after 10 washing cycles, antibacterial characteristics of textile disappeared.

#### ***14.3.4.2. Contact Angle Results***

The contact angle measurement was done after washings by the help of a goniometer (KSV CAM200). The contact angles were found to be 119°, 102° and 50° for the deposited textiles which were washed for 1, 5 and 10 times respectively. These results show that while the deposited textiles which were washed for 1 and 5 times were still hydrophobic, 10 times washed textile became hydrophilic, original property.

#### ***14.3.4.3. Roughness Analysis of Washed Textiles***

In this study, AFM (NanoScope IV, Digital instrument Veeco group) was also used to see the roughness of the surfaces after washing procedures. AFM was a very difficult method to study the roughness of the fabric surface due to fabric structure. The pin tool of AFM was sometimes broken due to the fibres of the fabric. Therefore, limited amount of AFM images were obtained.

The following graphs are AFM images taken for the purpose of determining the effect of washing on the silver deposited textiles.

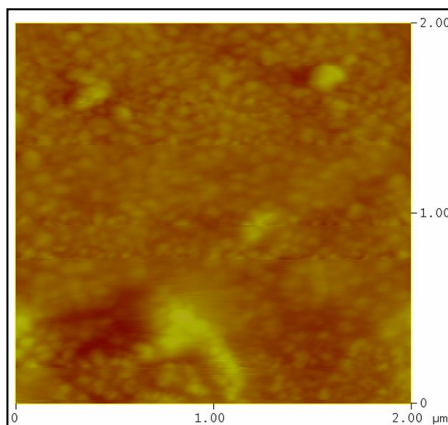


Figure 14.60. Afm analysis after 1 washing cycle

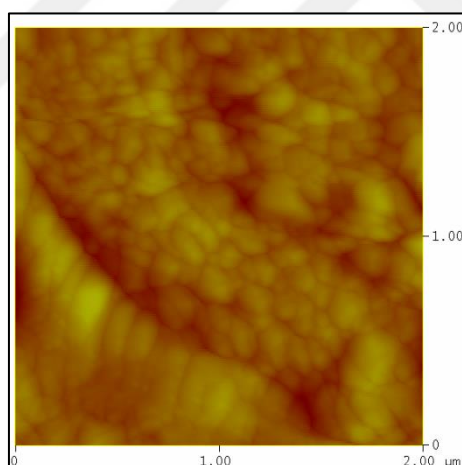


Figure 14.61. Afm analysis after 5 washing cycles

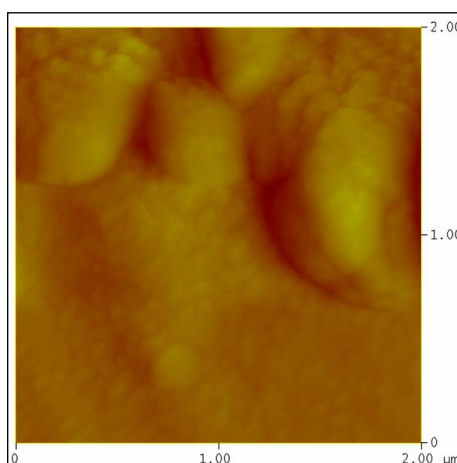


Figure 14.62. Afm analysis after 10 washing cycles

Textiles which were coated by silver on cotton for 4 minutes were washed 1 time, 5 times and 10 times. The roughness of them were measured by using AFM. RMS value of textiles which were washed for 1 time, 5 times and 10 times were 3.345 nm, 4.352 nm and 10.390 nm respectively. It is obvious that when the number of washing procedure increases, roughness of the surface of the deposited textiles increases. It means that silver on the surfaces disappears, after washing procedures. It must be noted that antibacterial activity of these coatings disappeared after 10 times washing cycles procedure. That is adhesion of silver particles on the textile was not very well. To optimize the adhesion, some chemicals and special methods would be used before and after deposition.

While the contact angles were decreasing, the values of surface roughness were increasing. It was also seen that roughness had strong influence on the wettability [31].

Table 14.18. The relationship between the roughness and the contact angle

Washing cycles	Roughness (nm)	Contact angle (degrees)
1	3.345	119
5	4.352	102
10	10.390	50

#### 14.4. OPTICAL EMISSION SPECTROSCOPY OF GLASS, ALUMINIUM AND TEXTILE COATED WITH COPPER AND SILVER

For this work, halogen lamp was used in optical emission spectroscopy. Spectrum was between 700-800 nm wavelengths. The measurements were done in the plasma laboratory in Yeditepe University.

In order to examine reflectivity, the BAKI spectrometer was used, see Figure 14.63. and Figure 14.64. for the measurement setup.

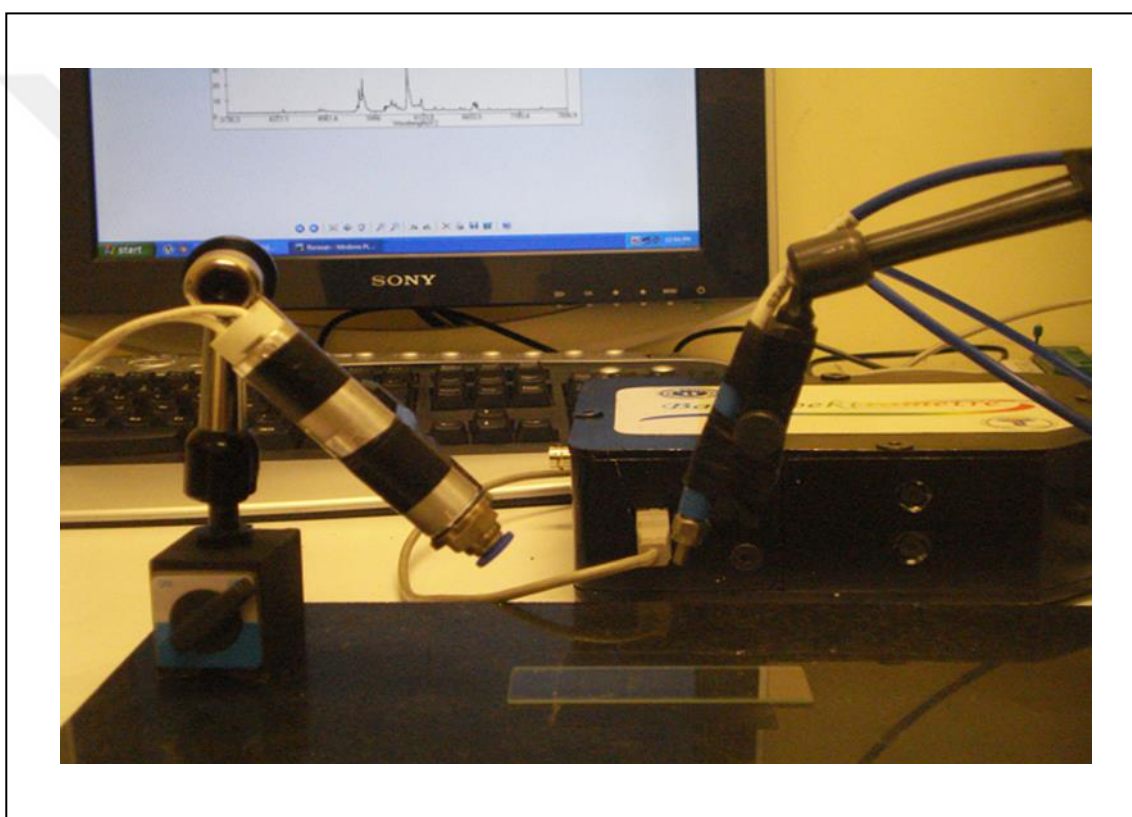


Figure 14.63. Measuring reflectivity of glass by using optical emission spectroscopy



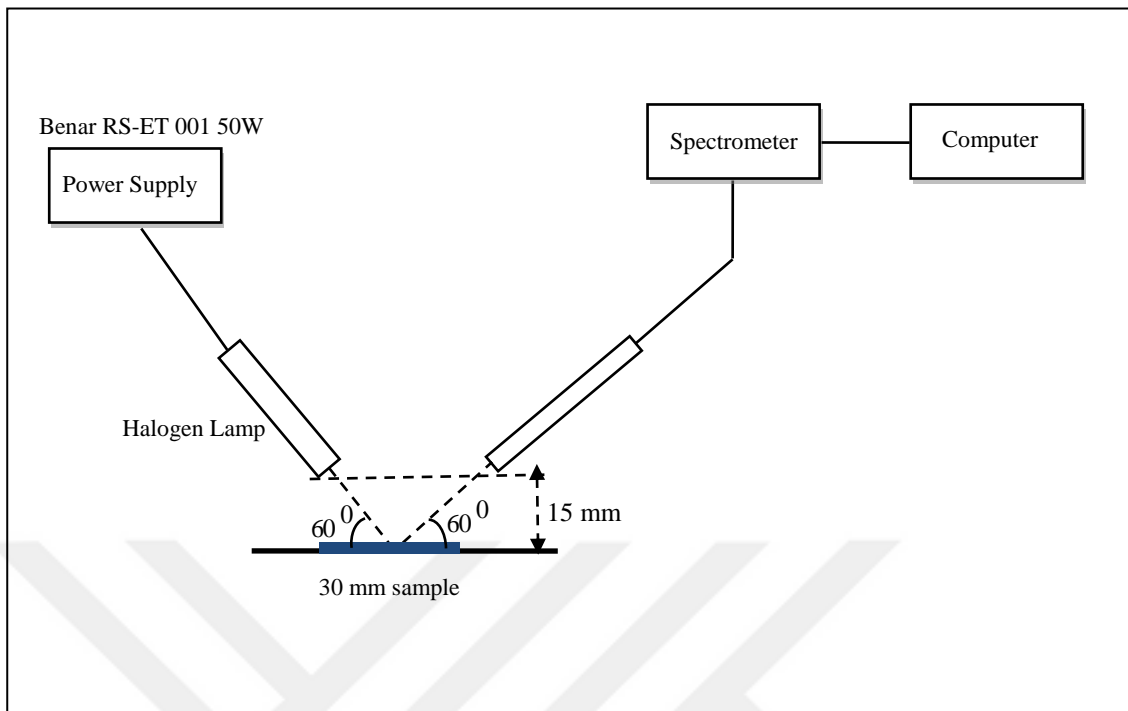


Figure 14.64. Diagram of measuring reflectivity

The observation of the emission intensity versus wavelength graph gives information about the reflectivity of the materials. The spectroscopic analyses of a single glass, and 20 minutes copper coated glass were observed as seen in Figure 14.65.

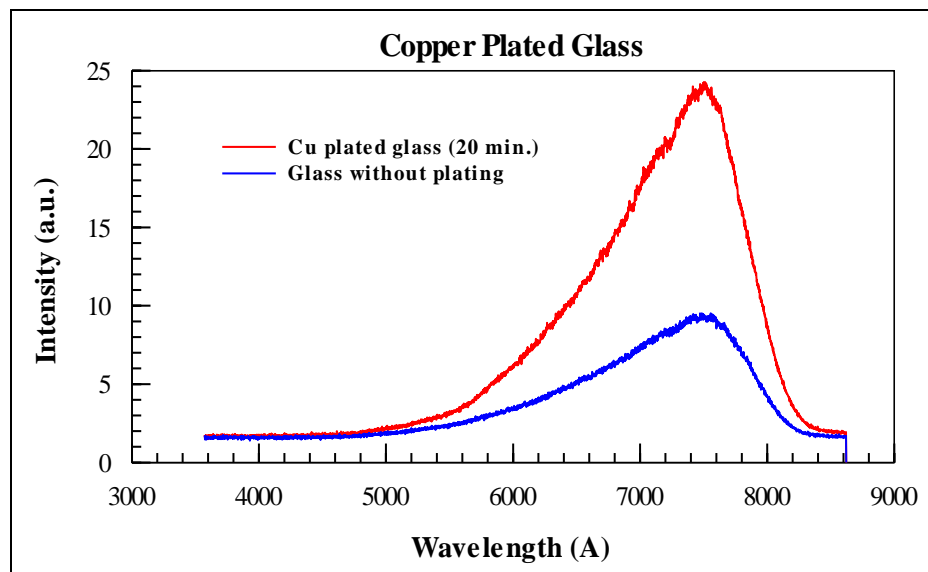


Figure 14.65. Intensity versus wavelength for single glass and copper coated glass

The spectroscopic analyses of a single aluminium, and 20 minutes copper coated aluminium were also observed as in Figure 14.66.

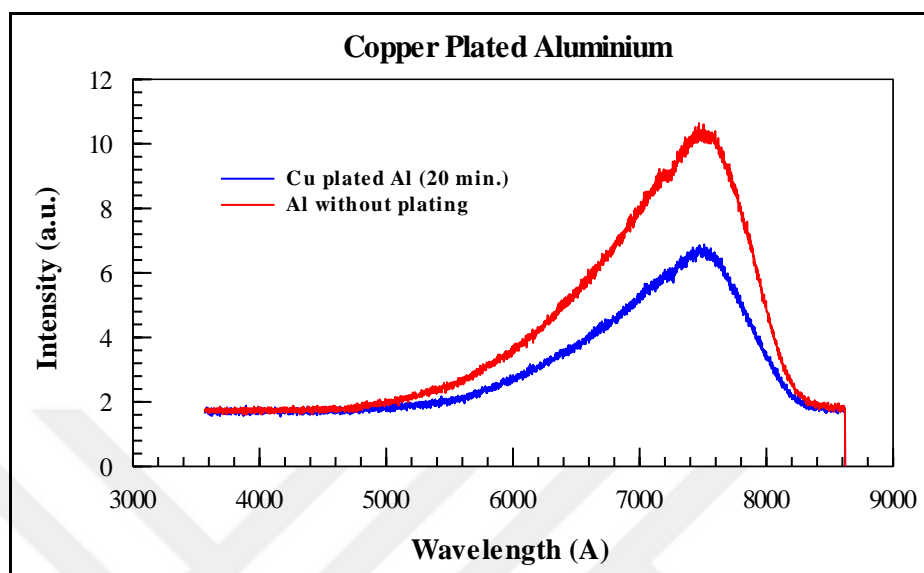


Figure 14.66. Intensity versus wavelength graph for single aluminium and copper coated aluminium

The values of intensity which correspond to the wavelengths of 360 nm, 460 nm, 560 nm, 660 nm and 760 nm were written on the tables below.

Table 14.19. The comparison of the intensity versus wavelength values of the samples

	360 nm	460 nm	560 nm	660 nm	760 nm
Intensity for single glass	1.562	1.611	2.441	5.444	8.545
Intensity for 20 min. copper-glass	1.489	1.758	3.630	12.915	22.876
Intensity for Single aluminium	1.733	1.709	2.661	5.688	9.985
Intensity for 20 min. copper-Al	1.660	1.658	2.173	3.833	6.372

If a single glass and 20 minutes copper coated glass was compared, the emission will generally increase as the glass coated by copper. Firstly, there was a decrease in the intensity at 360 nm. After 360 nm, the rises were seen at the intensity values. The increment rates were 9.11%, 48.71%, 137% and 168% at 460 nm, 560 nm, 660 nm and

760 nm respectively. As can be clearly seen, the increment rate raised at higher wavelengths and it shows that reflectivity of glass deposited by copper increased at higher wavelengths more. Therefore, it can be a good way to make the glass more reflective.

If a single aluminium and 20 minutes copper coated aluminium was compared, There are decreases at the intensities, as the aluminium coated by copper. The decrease rates were 4.21%, 2.98%, 18.34%, 32.61% and 36.18% at 360 nm, 460 nm, 560 nm, 660 nm and 760 nm. As can be seen clearly, the decrease rate generally raised at higher wavelengths and it shows that reflectivity of aluminium is higher than copper.

As the single glass and aluminium was compared, aluminium is more reflective. Since aluminium is metal and it has free electrons to make it more reflective.

The spectroscopic analyses of a single glass, 5 minutes and 20 minutes silver coated glasses were observed as shown in Figure 14.67.

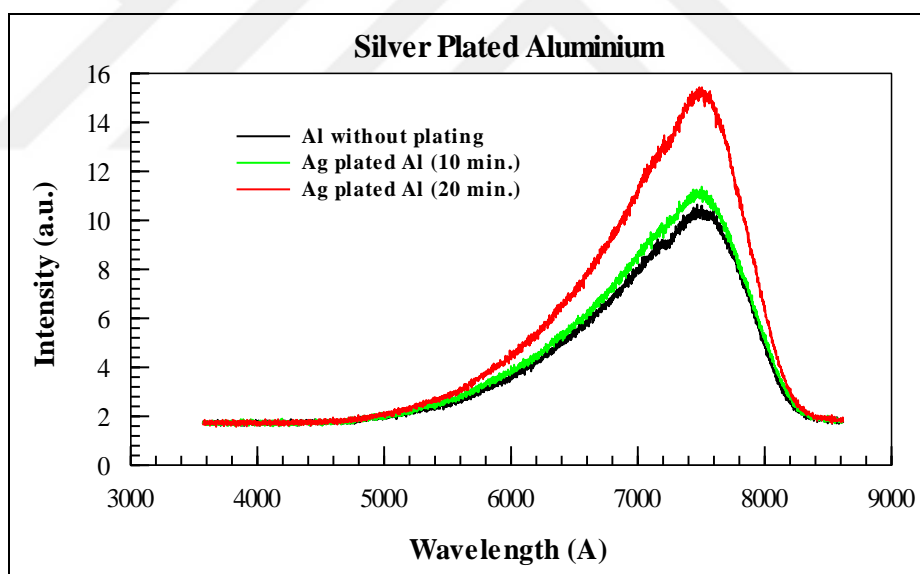


Figure 14.67. Intensity versus wavelength graph for single glass, 10 and 20 minutes silver coated aluminium

The values of intensity which correspond to the wavelengths of 360 nm, 460 nm, 560 nm, 660 nm and 760 nm were written on the Table 14.20.

Table 14.20. The comparison of the intensity versus wavelength values of samples

	<b>360 nm</b>	<b>460 nm</b>	<b>560 nm</b>	<b>660 nm</b>	<b>760 nm</b>
Intensity for only aluminium	1.733	1.709	2.661	5.688	9.985
Intensity for 10 min. silver on Al	1.709	1.782	2.734	6.104	10.547
Intensity for 20 min. silver on Al	1.709	1.758	3.052	7.715	14.453

As can be observed from the table, the emission decreased at 360 nm and increased at 460 nm, 560 nm, 660 nm and 760 nm as a single aluminium is deposited by silver. The rate of change of intensity is 4.27%, 2.74%, 7.69% and 5.62% at 460 nm, 560 nm, 660 nm and 760 nm respectively, if it is coated for 10 minutes. As can be seen, the rate of change did not increase regularly, as the wavelength increase. However, the reflectivity of the aluminium increased, as it is deposited by silver.

The emission decreased at 360 nm and increased at 460 nm, 560 nm, 660 nm and 760 nm as a single aluminium is deposited by silver for 20 minutes. The rate of change of intensity is 2.87%, 14.69%, 36.12% and 44.75% at 460 nm, 560 nm, 660 nm and 760 nm respectively, if it is coated for 20 minutes. As can be seen, the rate of change of intensity generally increased, as the wavelength increased.

These results demonstrate that, the rate of change of intensity on the silver deposited aluminium for 20 minutes is much more than the one on the the silver deposited aluminium for 10 minutes at high wavelengths. More silver means more reflectivity. Therefore, it can be more advantageous to deposit the aluminium materials for 20 minutes with silver to obtain more reflectivity. And the spectroscopic analyses of a single glass and 5, 10 and 20 minutes silver coated glass were observed as in the Figure 14.68

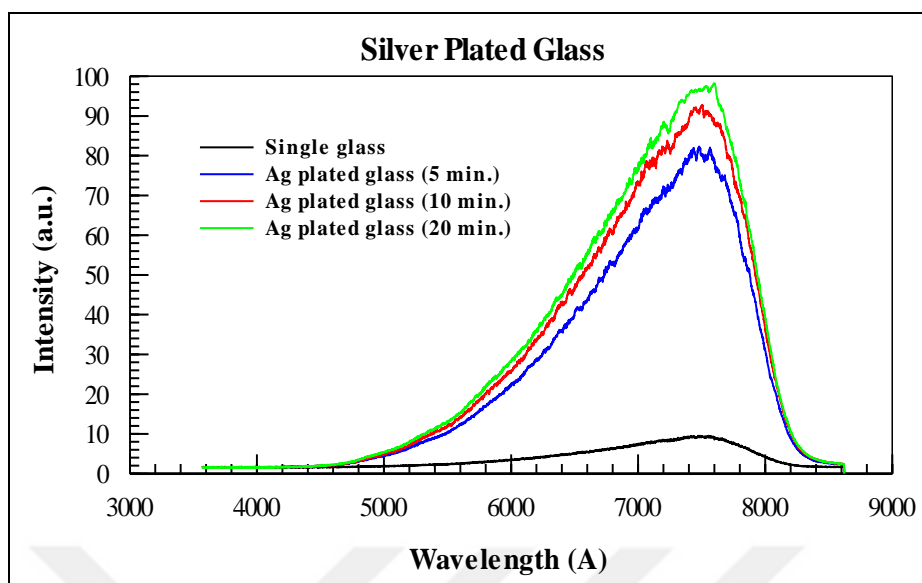


Figure 14.68. Intensity versus wavelength for single glass and 5, 10 and 20 minutes silver coated glasses

The values of intensity which correspond to the wavelengths of 360 nm, 460 nm, 560 nm, 660 nm and 760 nm were written on the Table 14.21.

Table 14.21. The comparison of the intensity versus wavelength values of the samples

	360 nm	460 nm	560 nm	660 nm	760 nm
Single glass	1.562	1.611	2.441	5.444	8.545
5 min. silver on glass	1.611	2.099	12.573	43.604	78.149
10 min. silver on glass	1.562	2.125	14.258	51.88	87.793
20 min. silver on glass	1.514	2.173	15.186	55.103	98.145

As can be seen clearly on the Table 14.21, the emission increased at all of the higher wavelengths. The rate of change of intensity is 3.14% , 30.29%, 415%, 700% and 815% at 360 nm, 460 nm, 560 nm, 660 nm and 760 nm respectively, if it is coated for 5 minutes. As can be seen, the rate of change increased regularly, as the wavelength increased.

As can be observed clearly on the Table 14.21, the emission did not change at the 360 nm for 10 minutes silver coated glass. The rate of change of intensity is 31.91%, 484% , 853% and 927% at 460 nm, 560 nm, 660 nm and 760 nm respectively, if it is coated for 10 minutes. The rate of change increased regularly, as the wavelength increased.

The emission decreased at 360 nm for 20 minutes silver coated glass. The rate of increase of intensity is 34.88% , 521% , 912% and 1049% at 460 nm, 560 nm, 660 nm and 760 nm respectively, if it is coated for 20 minutes. The rate of change increased regularly, as the wavelength increased.

The results demonstrates that silver is more reflective at higher wavelengths. They also show that the reflectivity of the glass increases a lot, as it is deposited by silver for 20 minutes. Since the silver is expensive, if a reflective glass is needed, it can be enough to deposit it for 5 minutes to decrease cost.

The spectroscopic analyses of a single textile and 1, 4 and 10 minutes silver coated textile were observed as in the Figure 14.69. The reflectivity of the textile increases, if it is deposited by more silver.

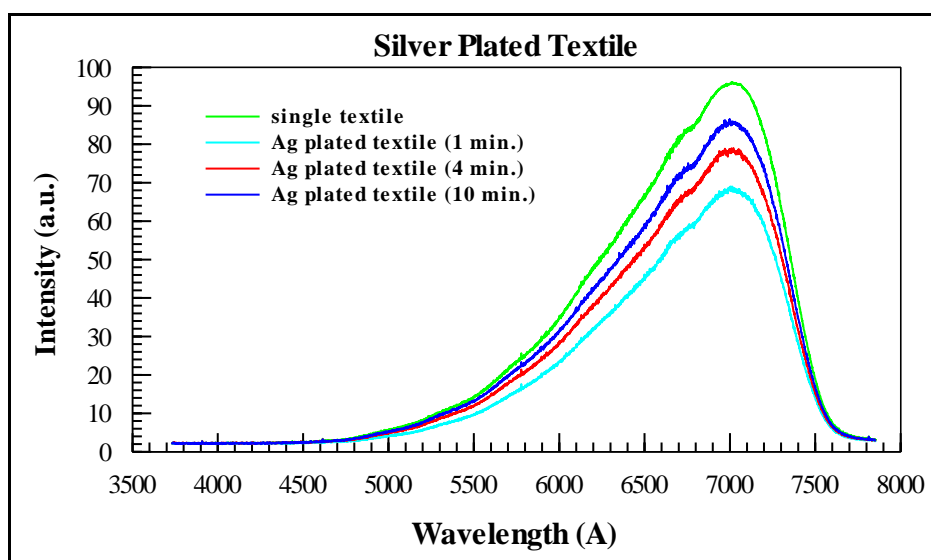


Figure 14.69. Intensity versus wavelength for single textile and 1, 4 and 10 minutes silver coated textiles

The values of intensity which correspond to the wavelengths of 360 nm, 460 nm, 560 nm, 660 nm and 760 nm were written on the Table 14.22.

Table 14.22. The comparison of the intensity versus wavelength values of the samples

	360 nm	460 nm	560 nm	660 nm	760 nm
Single textile	2.148	2.783	17.407	74.487	7.422
1 min. silver on textile	2.221	2.611	11.719	51.172	5.858
4 min. silver on textile	2.271	2.759	14.893	59.839	6.566
10 min. silver on textile	2.271	2.661	16.016	66.382	6.836

The reflectivity of non-coated textile is higher than silver coated textiles. Because, the colour of the textile is white and it reflects all of the colours. The decrease rate of intensity is 31.300%, 19.667%, and 10.881%, if it is coated for 1, 4 and 10 minutes respectively at 660 nm. The change of intensity at 660 nm can be seen on the Figure 14.70. Intensity values increase linearly, if is coated by silver more time.

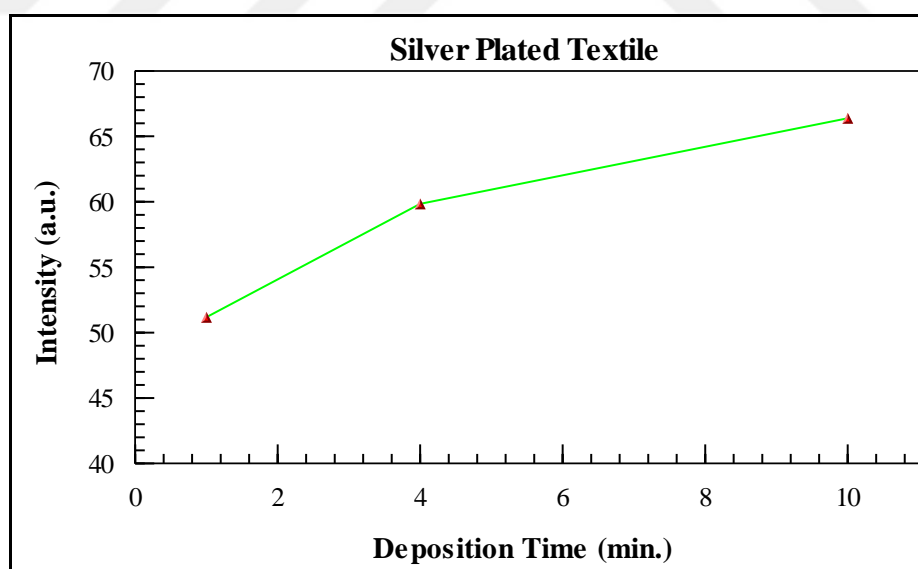


Figure 14.70. The graph of intensity versus deposition time (1, 4 and 10 minutes silver coated textiles at 660 nm)

## 15. CONCLUSION AND FUTURE WORK

As a conclusion, the purpose of this thesis was the application of magnetron sputtering method on the deposition of metals such as silver and copper on to the textiles (cotton and polyester), metals and glasses.

Firstly, the electrical properties of magnetron sputtering system were studied. The current versus voltage graphs and current versus pressure graphs were plotted and hysteresis effect was seen in Figure 14.1, 14.2, 14.3 and 14.4. These graphs were not obeying to the ohm law. This is the result of the nonlinear behavior of the plasma system.

Langmuir probe method was used to calculate electron temperatures with single and multineedle probes. In single probe, at higher pressures, higher electron temperatures were obtained as can be seen in Figure 14.10. There is a linear relationship between the electron temperature and pressure of the system. In multineedle probes, eight different probes were placed at a distance of 8 mm with each other. Electron temperatures at different probes were calculated. Figure 14.17. shows electron temperatures increase from cathode to anode and then become constant. Boltzmann plot method is a spectroscopic method to calculate the electron temperature. Using an emission UV spectrometer, electron temperatures were calculated at different voltages. When the voltages increase, the electron temperatures also increase as can be seen in Figure 14.25. Electron temperatures which were obtained by using Langmuir probe method were higher than the one which were obtained by using Boltzmann plot method. Because, electron temperature calculated by using Langmuir probe method is a local plasma temperature, while the one calculated by using Boltzmann plot method is a spatially averaged plasma temperature.

Morphology studies of surfaces were done by Scanning electron microscopy. SEM results showed that, if the deposition time increased, the thickness of the deposition increased. The deposition of the textiles with different materials changed the pattern of the SEM images. How the antibacterial agent was distributed on the coated textile was seen by SEM images. Figure 14.26.a shows the textile fibers were coated very well by using this sputtering technique. From Figure 14.27 and 14.28, the differences between the SEM analysis of the textiles which were coated with different metals were observed. Some cracks were seen on



the deposited textiles as in Figure 14.30, 14.31 and 14.32 and these cracks give hint about the thickness of the deposited metal. Measuring the thickness of the metal on the textile accurately was not an easy process. Because, the fibres of the textile can bend. Glass sample was coated by copper at the same conditions of textile deposition and studied by using SEM. The thickness of copper on the glass was easily measured as seen in Figure 14.33. In addition to this, Figure 14.34 shows the new method to find the film thickness. It is very successful method to measure the thickness. Because, the results which were obtained with this new method is very near to the results which were obtained by SEM analysis. Further work can be done in the future for more accurate measurements.

Magnetron sputtering is a very clean method and does not create any chemicals. Figure 14.36 shows EDS result of a cotton textile coated by silver, and there was only oxygen, carbon and silver on the surface. Carbon and oxygen are due to the cellulose in cotton. This result showed that the deposition material contains only silver. The deposition of the textile by using magnetron sputtering method is very clean and from the ecological point of view, the surface modification of textile by plasma application is superior to chemical methods.

In addition to these studies, wettability tests were done. Firstly, we did not have a goniometer in that part, therefore, we used a digital camera to take the photos of the drops. Figure 14.39 and 14.40 shows the textiles coated by Ag and Cu became hydrophobic, while uncoated textiles were hydrophilic. Air trapped in the metal-cotton surface can increase the surface hydrophobicity by preventing water penetration on the textile.

The resistances of the textiles coated with silver were also studied. Table 14.11 shows the comparison of the nonwoven textiles coated by silver at different times. When the time of the deposition is increased, the resistance was seen to be decreased. It caused the textile to be a good conductor that can be used for EMC studies. A further research can be done in electromagnetic shielding materials. Nowadays, industry has a great interest to the smart textiles .

Two types of antibacterial tests; parallel streak method and suspension test were applied to investigate the antibacterial characteristics of the textiles coated by silver and copper. Textile coated with the silver was more effective towards E.coli bacteria than the textile coated with copper. That is, silver is more antibacterial.

In section 14.3, antibacterial and hydrophobic characteristics of cotton and polyester different time deposited by copper and silver were compared. The cotton and polyester textiles were coated by silver and copper for 1, 4 and 10 minutes. Effects of deposition times and textile type on antibacterial characteristics of the textiles were studied by parallel streak method. These results showed that the time of deposition is an important parameter in terms of antibacterial activity, and 4 minutes deposition of silver is enough, while 10 minutes deposition of copper is necessary to kill the bacteria. Therefore, greater time deposition of textiles can cause the waste of time and money. It was also seen that, antibacterial effects do not depend on the type of substrate. Instead, it depends on the type of deposition metal.

Figure 14.55 shows hydrophobicity of the silver deposited cotton increased with increasing deposition time. Hydrophobicity of copper deposited cotton also increased as can be seen in Figure 14.57. If the copper deposited cotton is compared with the silver deposited cotton, contact angles are smaller. This means that, silver makes the cotton more hydrophobic. In addition to this, whether the fabric was cotton or polyester did not effect hydrophobicity of the deposited textiles.

In addition to this, abrasion tests (5000 cycles abrasion) were also applied to the the cotton textiles which were coated by silver for 1, 4 and 10 minutes. Comparisons of abraded tests were then studied. Figure 14.59 indicated that, contact angles on silver deposited textiles were decreasing with time, however contact angles on 1 minute silver was decreasing in a shorter time, after 5000 cycles abrasion. Losing its hydrophobic character, it also showed that adhesion of the metal to the cotton surface should be increased for a long term antimicrobial property.

The washing procedures (1 cycle, 5 cycles and 10 washing cycles) applied to the 4 minutes deposited cotton textiles. After that, antibacterial properties and contact angle values were also measured and compared. 1 and 5 cycles washed deposited textiles were still antibacterial, but 10 cycles washed deposited textiles lost antibacterial property. In addition to this, it was also observed that 10 cycles washed deposited cotton lost the hydrophobicity characteristics. This showed that there was a relationship between antimicrobial property and hydrophobic property, and after 10 times washing procedure, silver was found to be lost to the water. Further to this work, washing effect on the silver deposited cotton was

also investigated by using AFM. These results showed that roughness (RMS) increased with increasing washing cycles, and the distribution of the silver on cotton decreased. In addition to this, while the contact angles were decreasing, the values of surface roughness were increasing as can be seen in Table 14.18. It was seen that roughness had strong influence on the wettability. From washing and abrasion cycles, it was understood that adhesion of the metal to the cotton textile needs to be optimized. To optimize the adhesion, some chemicals and special glues would be used before and after deposition. Further research can be done in these optimization studies.

Figure 14.63 shows the reflectivity measuring system, and an optical emission spectroscopy, a halogen lamp was used in this system. Emission intensity versus wavelength graphs were plotted by the help of a computer and reflectivity analysis were done. Silver coated materials were more reflective compared to copper coated materials. Silver coated textiles for 1, 4 and 10 minutes were also studied in terms of reflectivity. Noncoated white textile was more reflective than the coated textiles, and reflectivity increases if the textiles were coated by silver more time.

## REFERENCES

1. R. Feynman. There is Plenty of Room at the Bottom. *Annual Meeting of the American Physical Society*, Caltech, 22-36, 1960.
2. M. Ratner and D. Ratner. *Nanotechnology*, Prentice Hall Professional, Technical, and Reference, New Jersey, 2003.
3. B. Chapman. *Glow Discharge Processes*, A Wiley-Interscience Publication, New York, 1980.
4. F. F. Chen. *Introduction to Plasma Physics and Controlled Fusion*, Plenum Press, New York, 1974.
5. M. P. Gashti, F. Alimohammadi, G. Song and A. Kiumarsi. Characterization of Nanocomposite Coatings on Textiles: a Brief Review on Microscopic Technology. In: Méndez-Vilas, editor, *Current Microscopy Contributions to Advances in Science and Technology*, pages 1424-1437. Formatex Research Center, Spain, 2012.
6. J. Reece Roth. *Industrial Plasma Engineering*, Institute of Physics Publishing, Knoxville, 1995.
7. Electric Egg, “Static Electricity”,  
[http://www.physics.kenyon.edu/EarlyApparatus/Static\\_Electricity/Electric\\_Egg](http://www.physics.kenyon.edu/EarlyApparatus/Static_Electricity/Electric_Egg)  
[retrieved 24 September 2014].
8. Hittorf Double Tube, “Early Tech”,  
<https://earlytech.com/earlytech/item?id=205>. [retrieved 23 October 2015].
9. Electron Microscope Laboratory, “Northern Arizona University”,  
<http://www.nau.edu/microanalysis/Microprobe-SEM/History.html>  
[retrieved 26 November 2015].

10. W. Crookes. *On Radiant Matter*, The Popular Science Monthly, Sheffield, 1879.
11. G. Rosace, R. Canton and C. Colleoni. Plasma Enhanced CVD of SiO<sub>x</sub>CyHz Thin Film on Different Textile Fabrics, Influence of Exposure Time on the Abrasion Resistance and Mechanical Properties, *Applied Surface Science*, 256:2509-2516, 2010.
12. D. Sun and G. K. Stylios. Fabric Surface Properties Affected by Low Temperature Plasma Treatment, *Journal of Materials Processing Technology*, 173:172-177, 2006.
13. A. Guthrie, R. K. Wakerling, M. Hill and D. Bohm. *In the The Characteristics of Electrical Discharges in Magnetic Fields*, McGraw-Hill Book Company Inc., Newyork and London, 1949.
14. K. Navaneetha Pandiyaraj and V. Selvarajan. Non-thermal Plasma Treatment for Hydrophilicity Improvement of Grey Cotton Fabrics, *Journal of Materials Processing Technology*, 199:130-139, 2008.
15. R. L. Merlino. Understanding Langmuir Probe Current-Voltage Characteristics, *American Association of Physics Teachers*, 75:1078, 2007.
16. V. K. Unnikrishnan, K. Altı, V. B. Kartha, S. Chidangil, G. P. Gupta and B. M. Suri. Measurement of Plasma Temperature and Electron Density in Laser-Induced Copper Plasma by Time-Resolved Spectroscopy of Neutral Atom and Ion Emissions, *Journal of Physics*, 74:983-993, 2010.
17. Scanning Electron Microscopy, "Radiological and Environmental Management", <http://www.purdue.edu/rem/rs/sem.htm> [retrieved 27 December 2013].
18. K. N. Pandiyaraj and V. Selvarajan. Non-thermal Plasma Treatment for Hydrophobicity Improvement of Grey Cotton Fabrics, *Journal of Materials Processing Technology*, 199:130-139, 2008.

19. R. P. Woodward. Contact Angle Measurements Using the Drop Shape Method, <http://www.firsttenangstroms.com/pdfdocs/CAPaper.pdf> [retrieved 23 October 2015].
20. E. Temmerman and C. Leys, Surface Modification of Cotton Yam with a DC Glow Discharge in Ambient Air, *Surface Coating Technology*, 200:686-689, 2005.
21. N. Aslan, K. Şentürk, T. Şen, T. Çoruhlu, İ. Vartürk, S. Şeker, S. Shahidi, A. M. Dobrovolskiy, V. V. Tsiolko, S. V. Matsevich, S. S. Keskin and M. Korachi. Investigation of Antimicrobial Activity and Morphological Properties of Metal Coated Textile Surface, *Problems of Atomic Science and Technology*, 20:208-211, 2014.
22. N. Aslan , K. Şentürk , T. Şen, T. Çoruhlu, İ. Vartürk, S. Şeker, S. Shahidi, A. M. Dobrovolskiy, V. V. Tsiolko , S. V. Matsevich, S. S. Keskin and May Korachi. Investigation of Antimicrobial Activity and Morphological Properties of Metal Coated Textile Surfaces, *International Conference School on Plasma Physics and Controlled Fusion*, Ukrayna, 256-258, 2014.
23. H. S. Robertson and E. H. Currie. Onset of the Helical Instability in Weakly Ionized Discharge Plasmas, *Physics of Fluids*, 12:200, 1969.
24. Y. Ralchenko, A. E. Kramida and J. Reader. NIST ASD Team, NIST Atomic Spectra Database (version 3.1.5), National Institute of Standards and Technology, <http://physics.nist.gov/asd3> [retrieved 2 October 2013].
25. M. Maeyama, Y. Akashi and K. Nagano. Electron Temperature and Density Measurement of Cylindrical Parallel MCS Discharge Plasma in Atmospheric Pressure, *Journal of Plasma Fusion Research Series*, 8:711-744, 2009.
26. C. Brunon, E. Chadeau, N. Oulahal, C. Grossiord, L. Dubost, F. Besueille, F. Simon, P. Degraeve and D. Leonard. Characterization of Plasma Enhanced Chemical Vapor Deposition Transparent Deposits on Textiles to Trigger Various Antimicrobial Properties to Food Industry Textiles, *Science Direct*, 519:5838-5845, 2011.

27. P. Osorio-Vargas, R. Sanjines, C. Ruales, C. Castro, C. Pulgarin, A. J. Rengifo-Herrera, J. C. Lavanchy and J. Kiwi. Antimicrobial Cu-Functionalized Furfaces Prepared by Bipolar Asymmetric DC-pulsed Magnetron Sputtering (DCP), *Journal of Photochemistry and Photobiology A: Chemistry*, 220:70-76, 2011.
28. D. Depla, S. Segers, W. Leroy, T. V. Hove and M. V. Parys. Smart Textiles: An Explorative Study of the Use of Magnetron Sputter Deposition, *Textile Research Journal*, 81:1808-1817, 2011.
29. W. D. Schindler and P. J. Hauser. Chemical Finishing of Textiles, *Woodhead Publishing*, Cambridge, 2004.
30. Y. Bulut and V. Sular. Kaplama veya Laminasyon Teknikleri ile Üretilen Kumaşların Genel Özellikleri ve Performans Testleri, *The Journal of Textiles and Engineers*, 6-16, 2015.
31. K. J. Kubiak, M. C. T. Wilson, T. G. Mathia and P. Carval. Wettability versus Roughness of Engineering Surfaces, *12th International Conference on Metrology and Properties of Engineering*, 271:523–528, 2011.

## APPENDIX A: PUBLICATIONS AND DOCUMENTS

### INVESTIGATION OF ANTIMICROBIAL ACTIVITY AND MORPHOLOGICAL PROPERTIES OF METAL COATED TEXTILE SURFACES

*Necdet Aslan<sup>1</sup>, Kenan Şentürk<sup>2</sup>, Tuba Şen<sup>1</sup>, Turgay Çoruhlu<sup>3</sup>, İpek Vartürk<sup>4</sup>, S. Şeker<sup>5</sup>, S. Shahidi<sup>6</sup>, A.M. Dobrovolskiy<sup>7</sup>, V.V. Tsiolko<sup>7</sup>, S.V. Matsevich<sup>7</sup>, S.S. Keskin<sup>8</sup>, May Korach<sup>6</sup>*

<sup>1</sup>*Yeditepe University- Physics Department-Kayışdağı/Istanbul, Turkey;*

<sup>2</sup>*Beykent University- Energy Systems Engineering Department-Ayazağa/Istanbul, Turkey;*

<sup>3</sup>*Beykent University-Vocational School- Dept. of Technical Programmes-Beykent /Istanbul;*

<sup>4</sup>*Yeditepe University-Genetics and Bioengineering Department- Kayışdağı /Istanbul, Turkey;*

<sup>5</sup>*Gebze Institute of Technology, Materials Science & Engineering Dept. Gebze Istanbul, Turkey;*

<sup>6</sup>*Department of Textile, Arak Branch, Islamic Azad University, Arak, Iran;*

<sup>7</sup>*Institute of Physics NASU, Kyiv, Ukraine;*

<sup>8</sup>*Marmara University, Environmental Engineering Department, Turkey*

*E-mail: tsiolko@iop.kiev.ua*

The results of investigation antimicrobial and surface properties of the textiles metal coated by means of magnetron or the cleaning-deposition system, which is based on sequentially arranged DC anode layer accelerator and hollow cathode, are presented. The antimicrobial properties against bacteria *E. coli* and *S. aureus* of cotton and polyester/cotton textiles coated by Cu, Ti and Ag with the use of two different systems were examined and compared.

PACS: 52.77.Dq, 81.15.Cd

#### INTRODUCTION

In recent years the production of a textiles with antimicrobial properties caused an increasing interest from industry because of their potential to provide beneficial health effects leading to a higher quality of human life. It is connected to the fact that textile products provide a suitable environment for the growth of many microorganisms, including pathogens, which could be the source of infection transfer, unpleasant odors, color degradation and general deterioration of the textile.

Current antimicrobial products, such as triclosan, quaternary ammonium and metallic salts have disadvantages such as short active durations and high costs. Moreover, they have been known to leach out from the fabric towards the environment and diffuse into the skin of the wearers.

It is known that many metals by themselves (primarily silver and copper) also have antimicrobial properties (though the mechanisms of their antimicrobial activity are not yet known precisely [1]). Therefore, the deposition of metal films on fabrics is a promising method for creating antimicrobial coatings. Currently, the most suitable way of the antimicrobial metal films deposition on a textile is the sputtering technique. Recently, quite a number articles on this topic have been published [2-8]. Metal film deposition was carried out using a variety of devices—direct current (DC) magnetron, direct current pulsed (DCP) magnetron and high intensity power impulse (HIPI) system. SiO<sub>2</sub> fabrics [2], polyester textile [3, 6, 7], cotton [4, 5] were used as substrates in the studies. In

[2] it was found that Cu was effective against bacteria and fungi, while Ag was effective only against bacteria, since its effect was limited against fungi. The effectiveness of other used metal (Pt, Pt/Rh and Au) was much lower. So most of the studies was devoted to the investigation of antimicrobial properties of Ag, Cu, TiO<sub>2</sub>, Cu/TiO<sub>2</sub> sputtered films.

An interesting phenomenon has been described in [8]. Antimicrobial activity of Cu films, deposited by DCP magnetron was found to be significantly higher than the activity of the films produced by DC magnetron. The reason for this effect may be that the Cu ions produced by DCP with an energy up to 100 eV create Cu films with different structure compared with the films deposited by DC magnetron Cu ions with lower energy 5...15 eV.

An important point in the sputtering technique on textile is the adhesion of the deposited metal film and, correspondingly, wearability and washability of the resulting fabrics. It is known that, for obtaining high-quality coatings on substrates, efficient methods of cleaning and activation of the surface to be coated is required immediately prior to the deposition. Polarity switch in magnetron discharge for cleaning the treated surface by ion flow is generally possible only in case when the last one is conductive. Therefore, for the plasma pretreatment of substrates ignite the gas discharge or the entire volume of the chamber, or by using a special electrode between the magnetron and the substrate as the cathode [9, 10].

The aim of this study was to investigate the antimicrobial activity and morphological properties of cotton and cotton/polyester textiles with Cu, Ag and Ti film coated by DC magnetron sputtering and cleaning-

ISSN 1562-6016. BAHT. 2014. №6(94)

Figure A.1. Article



deposition system, which is based on sequentially arranged DC anode layer accelerator and hollow cathode. Using the second system we were able first to clean the sample with Ar ions with an energy of 400...600 eV, then deposit of the metal films with help of metal ions with energy about 200 eV. Selection of titanium due to the fact that although the Ti itself does not exhibit antimicrobial activity [1], in the ambient air at the surface of the Ti film  $\text{TiO}_2$  layer is fairly quickly formed, which already has antimicrobial properties.

### 1. EXPERIMENTAL SET-UPS AND METHODS

The DC/RF magnetron, used during the sputtering, had no specific differences from equipment used in other researches. The dimensions of the cathode (Ag, Cu and Ti of 99.99 % purity) were 50.8 mm in diameter and 4 mm in thickness. The magnetron sputtering coating was established at 10 mTorr of Ar pressure and a DC voltage of  $V=400$  V and  $I=0.3$  A producing ion current density nearly  $11 \text{ mA/cm}^2$ .

The cleaning-deposition system is based on sequentially arranged DC anode layer accelerator with permanent magnets and hollow cathode, which is coupled to accelerator cathode. The surfaces to be coated are situated inside the hollow cathode. At low gas pressure in the system, cleaning of the surfaces is performed by Ar ions accelerated in crossed magnetic field  $B$  and electric field  $E$ . Increase of working gas pressure above certain value results in discharge glow between the accelerator anode and hollow cathode, and to intense sputtering of material of the targets attached to the accelerator cathode and material of the hollow cathode. The sputtered target atoms (Ti, Cu) are ionized additionally in the hollow cathode plasma and deposited on the substrate surfaces. For deposition of Cu and Ti onto textile samples, accelerator cathode cover plates, made of copper and titanium (99.9 % purity) foil with a 50...100  $\mu\text{m}$  thickness were used. The hollow cathode was made of the same materials as the ones used for the accelerator cathode cover plates. Textile samples (50x20 mm) were placed inside the hollow cathode at about 150 mm distance from the bottom plane of the accelerator electrodes during the deposition. The cleaning of the textile samples inside the vacuum chamber was carried out for 5...6 min of discharge voltage  $V=900$  V and Ar ion current density of  $\sim 0,1 \text{ mA/cm}^2$ . The coating was then established for 20 mins of voltage  $V=600$ ...650 V and current of  $I=500$ ...600 mA.

In order to prepare the textile substrates for coating, they were pretreated by washing in water, cleaning detergent (OMO, Turkey 1 g/l) and 1 g/l of sodium carbonate compound for 15 min at  $70^\circ\text{C}$  and then air dried for 45 min. The same cleaning procedure was carried out for all substrates to be coated by both magnetron sputtering and cleaning-deposition system.

The antibacterial properties of the Ag, Ti and Cu coated fabrics were qualitatively evaluated using a gram-negative bacterium *E. coli* (ATCC 25922) and gram-positive bacterium *S. aureus* (ATCC 25923) provided from the culture collection of Microbiology laboratory, Yeditepe University. Bacterial inoculum

with a suitable concentration was prepared in the Tryptone soya broth (Fisher Scientific). For the antimicrobial tests the parallel streak method (AATCC-TM 147) was used. Briefly, plates of Luria-Bertani Agar (Sigma-Aldrich) were streaked with a loopful of the bacteria. The coated side of the textile strips was placed face down onto the agar and aerobically incubated (Binder, USA) for 24 h at  $37^\circ\text{C}$ . Following this incubation the zone of inhibition was determined and the textile surface microscopically examined (Leica, Germany) to check for growth on top of the textile surface. All experiments were carried out three times and the mean values were calculated.

### 2. EXPERIMENTAL RESULTS AND DISCUSSION

Examples of SEM images (5 K magnification) of the coatings Cu, Ti, Ag on cotton fibers, obtained using magnetron sputtering and cleaning-deposition system are presented by in Fig. 1.

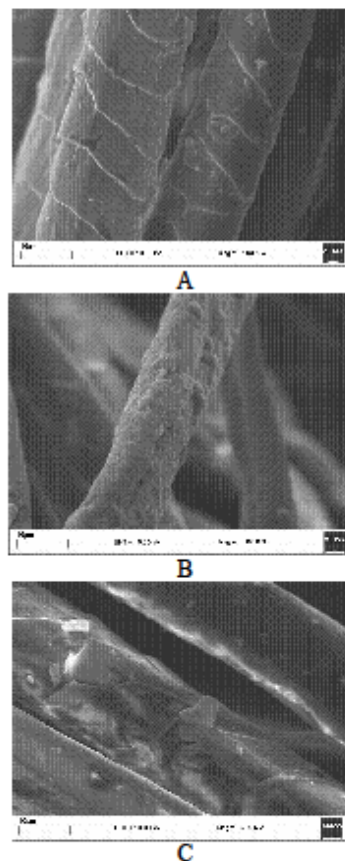


Fig. 1. The SEM pictures of cotton fibers coated by Cu, Ti, and Ag. A – Cu coatings for 15 min; B – Ti coatings for 30 min; C – Ag coatings for 8 min

When these coatings are examined, it is seen that the Cu coating creates smooth circular zones which are attached to each other while Ti coatings are more uniform but not smooth. The silver coatings are weak, but smooth and shiny. The SEM pictures (5K magnification) of Ti coating (20 minutes) on the cotton/polyester textile obtained by magnetron sputtering and cleaning-deposition systems under the same conditions are presented in Fig. 2.

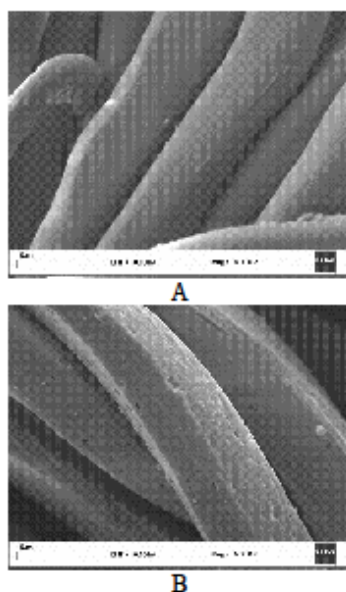


Fig. 2. The SEM pictures of cotton/polyester fibers coated by Ti. A – magnetron sputtering; B – cleaning-deposition system

As seen, cotton/polyester fibers allow more smooth surface against Ti and the magnetron sputtering coating is more uniform than cleaning-deposition system coating.

Fig. 3 shows the SEM picture (5K magnification) cross section of cotton/polyester fibers magnetron sputtering coated by Ag for 20 min coating.

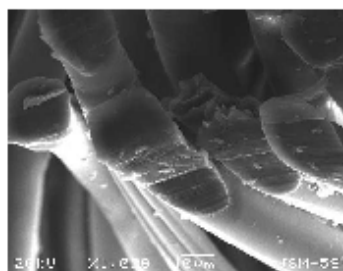


Fig. 3. The SEM pictures of the cross section of cotton/polyester fibers magnetron sputtering coated by Ag

The coating seems homogeneous and its thickness appeared to be nearly 200 nm.

The results of the antimicrobial property of Cu, Ti, Ag films on cotton textile coated by magnetron sputtering and cleaning-deposition systems against *S. aureus* and *E. coli* bacteria are shown in Table. This table was produced by measuring the thickness of inhibition zones around coated textiles.

#### Antimicrobial activity of the coating on cotton textile

Metal/bacteria	Inhibition zone, mm	
	<i>S. aureus</i>	<i>E. coli</i>
Cu	0	0.1...0.2
Ti	0	0
Ag	0.2...0.3	0.2...0.3

It has been found that in the case of Cu coating no growth of *E. coli* on the surface of the samples was observed and the value of the inhibition zone around the samples was 0.1...0.2 mm. At the same time, the antimicrobial efficiency of copper on *S. aureus* was significantly lower. Ti coating demonstrated similar antimicrobial activity as Cu one although no inhibition zones were formed. Sufficiently high activity of the titanium (comparable with the copper activity) can be connected, as we have indicated above, with the formation a TiO<sub>2</sub> film on the surface of Ti films. It was also found, that silver coating is more effective than others – no bacteria growth onto the substrate surface was observed and zone of inhibitions was of 0.2...0.3 cm for all studied substrates. The comparison of sputtering and hallow cathode systems revealed that nearly identical results are obtained although the coating morphologies were slightly different.

## CONCLUSIONS

It was shown that cotton and cotton/polyester textiles coated by DC magnetron sputtering and hollow cathode systems produced similar antimicrobial activity. The coated Cu, Ag and Ti films by both methods can produce total elimination of the bacteria of *E. coli* and *S. aureus* from the textile surfaces while only Cu and Ag coated fabrics produced up to 0.2 mm inhibition zone around the surfaces. These results show that all these metal coatings can be used for antimicrobial activity on the textile surfaces.

## ACKNOWLEDGEMENTS

This work was partially supported by the company ELES-Electromechanics, Istanbul-Turkey and mainly by Yeditepe University, Istanbul-Turkey and by joint TÜBİTAK (The Scientific and Technological Research Council of Turkey) and National Academy of Sciences of Ukraine (NASU) project number 110T578.

## INVESTIGATION ON SURFACE, ELECTRICAL AND OPTICAL PROPERTIES OF ITO-AG-ITO COATED GLASS

*Necdet Aslan<sup>1</sup>, Tuba Şen<sup>1</sup>, Turgay Çoruhlu<sup>1</sup>, Kenan Şentürk<sup>2</sup>, Sinan Keskin<sup>3</sup>,  
Sedat Şeker<sup>4</sup>, Andrey Dobrovolskiy<sup>5</sup>*

<sup>1</sup>*Yeditepe University, Physics Department, Istanbul, Turkey;*

<sup>2</sup>*Beykent University, Energy Systems Engineering Department, Istanbul, Turkey;*

<sup>3</sup>*Marmara University, Environmental Engineering Department, Istanbul, Turkey;*

<sup>4</sup>*Gebze Institute of Technology, Materials Science & Engineering Department, Istanbul, Turkey;*

<sup>5</sup>*Institute of Physics, Kyiv, Ukraine*

The aim of this work was to study the optical and electrical properties of thick ITO-Ag-ITO multilayer coating onto glass. ITO-Ag-ITO coatings with thickness of ITO layers 110 nm, 185 nm and intermediate Ag layer thickness 40 nm were prepared by magnetron sputtering. The optical, electrical and atomic properties of the coating were examined by scanning electron microscope, atomic force microscope, X-ray diffraction analysis and ultraviolet-visible spectroscopy.

PACS: 78.20.-e, 78.66.Sq.

### INTRODUCTION

Indium tin oxide (ITO) films, which are transparent and conductive, have attracted a growing interest in many industrial devices, such as solar cells, liquid crystal displays, and organic light emitting diodes due to their low resistance and high optical transparency in the visible region of spectrum. However, their resistivity is rather high in some cases for improved practical applications, particularly, at their use as a transparent electrode of a color filter in the case of an improved display panels.

One of the ways of resistivity reduction of transparent conductive electrodes is the use of thin metal films in combination with ITO [1-3]. However, optical and electrical features of such multilayer films essentially depend on their structure. Used metal films should have a continuous structure and high transmittance. Otherwise, presence of island structures in the film body can lead to both resistivity increase and transmittance decrease. One of the most suitable metals is Ag due to its high conductivity, and good transmittance of thin Ag films in visible spectrum range.

The aim of this work was to study the optical and electrical properties of thick ITO-Ag-ITO multilayer coating. ITO-Ag-ITO coatings with thickness of ITO layers 110, 185 nm and intermediate Ag layer thickness 40 nm have been prepared by magnetron sputtering.

### 1. EXPERIMENTAL PART

#### 1.1. MATERIALS AND METHODS

Glass microscope slides (RE-WA Lehmann-Schmidt, 55x25 mm) that were amorphous, transparent to visible and near-infrared light were used in our experiments. To prepare a clean adhesion surface, the glass slides were washed by water and then treated by water-ethanol solution (20%, Greenfield Ethanol Inc.) for 10 min. After that the glass slides were cleaned by ultrasonic cleaner (MTI Corp., USA) for 20 minutes and finally left to dry for 10 min before sticking it to the substrate holder. The coating materials (targets for magnetron sputtering) used in this study were Ag, and ITO (all of 99.99% purity, 50.8 mm diameter, 4 mm thickness).

### 1.2. CHARACTERIZATION AND MEASUREMENT METHODS

The film thicknesses on glass coatings were measured (by Dektak Profilometer, Germany); cross sections of the films were examined in the SEM images.

In order to examine the optical properties of the ITO-Ag-ITO coating, a 50 W halogen lamp (producing a continuous light intensity between 300...900 nm) and the BAKI spectrometer (BEAM Ar-Ge Optic, Laser Technologies Ltd, Turkey) were used.

The AFM measurements were carried out by the AFM machine (Park systems, USA).

The X ray diffraction (XRD) measurements were established by Rigaku D-Max/2200 PC model system. The measurements were carried out at 40 kV and 40 mA with 2 degrees scanning/minutes.

At studies of the features of obtained films, energy dispersive X ray (EDX) analysis and scanning electron microscopy (SEM) (Tescan, Mira/LMU Schotky) were also used.

The conductivity tests on the coated glass surface were done by four probe method (4 channel digitizing oscilloscope from TEKTRONIX TDS 510A).

### 2. RESULTS AND DISCUSSION

One of the problems arising at the way of creating high-quality uniform coatings is ITO cluster formation during the coating. Due to that, at creation of multilayer ITO-Ag-ITO coating by magnetron sputtering method especially great attention was paid to operation mode choice, particularly, the coating time. It was determined that the average cross section diameters of these clusters increased from 200 to 400 nm after 5 and 25 min of coating (Fig. 1). The film thickness was found to change from 150 nm (for 5 min) to 350 nm (for 25 min). It was found that the coating thickness increased linearly with the coating time. This cluster formation can be reduced after annealing in a temperature range of 200...300°C. It should be also noted that the EDX analysis of these clusters and flat regions between clusters showed identical results, so that the atoms in flat regions and those in clusters are the same.



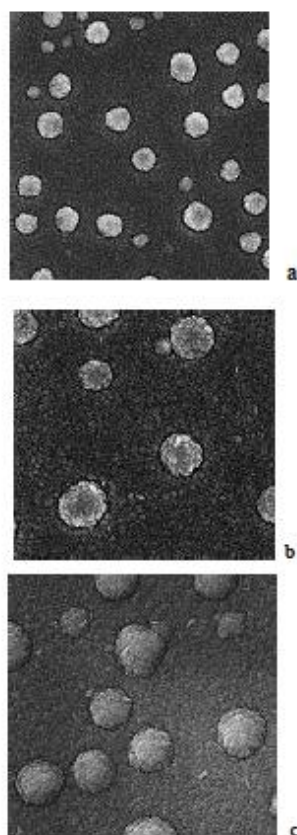


Fig. 1. The SEM pictures ( $\times 20K$  magnification) ITO coating onto glass for different exposition times: 5 min (a); 15 min (b); 25 min (c)

Layers of 1<sup>st</sup> ITO, Ag and top ITO were deposited stepwise for both surface morphology control and convenience of performing optical measurements (Fig. 2). The film thickness of the first ITO layer (21 min. coating) was measured to be 110 nm and the Ag and final ITO layer thicknesses were measured to be 40 nm and 185 nm, respectively. Fig. 3 shows the SEM images of these coatings taken at the points a-c, as shown in Fig. 2.

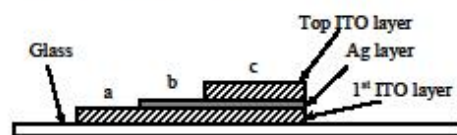


Fig. 2. The multilayer coating of ITO-Ag-ITO onto microscope slide glass

As one can see from this Figure, initial ITO coating produces clusters, Ag coating smoothes the surface, but the clusters at final ITO coating become larger. Similar clustering formation has been also previously observed [4].

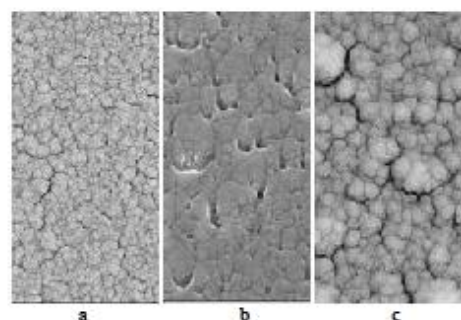


Fig. 3. The SEM pictures ( $\times 75K$  magnification) ITO-Ag-ITO coating on microscope slide: First ITO coating (a); Ag coating onto first ITO (b); top ITO coating onto Ag (c)

At creation of such multilayer coating, the structure of single layers was also controlled. Fig. 4 shows the single ITO coating side view SEM picture of 75K magnification. One can see from the figure that deposited ITO layer has regular columnar structure.

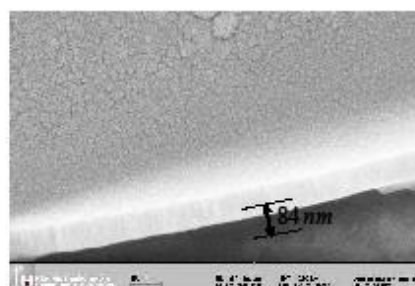


Fig. 4. The SEM pictures ( $\times 75K$  magnification) of cross section of glass-ITO film coated for 12 minutes

Morphological feature of this ITO thin film was also monitored using atomic force microscopy (AFM) (Fig. 5). One can see from the Figure that the surface of deposited layer is smooth enough – its roughness does not exceed several tens of nanometers.

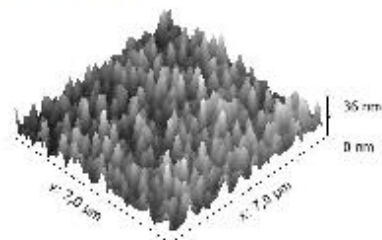


Fig. 5. The AFM image of single 84 nm thickness layer of ITO coating

Results of researching the transmission of created multilayer ITO-Ag-ITO coating in 400 to 900 nm range

are presented in Fig. 6. Deposition of the first ITO layer with 110 nm thickness practically has no influence on transmission spectrum of the film, whereas adding 40 nm thick Ag layer leads to transmission decrease in visible range by almost 30% (transmission minimum is located at about 650 nm wavelength). Adding top 185 nm thick ITO layer does not change the transmission value in 400...650 nm range, but decreases it at longer wavelengths. Such behavior of transmission spectrum differs from data presented in [3], where transmission spectrum is bell-shaped (with the transmission maximum at  $\approx 600$  nm) at Ag layer thickness variation from 10 to 20 nm.

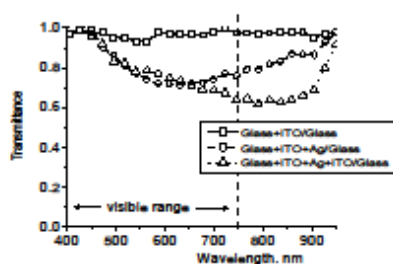


Fig. 6. The transmittance spectra for ITO-Ag-ITO multilayer consisting of 110 nm thick ITO, 40 nm Ag and 185 nm ITO

Clarification of a reason of such discrepancy is planned in subsequent researches.

The resistances of ITO monolayer and ITO-Ag-ITO multilayer structures deposited on the glass slide by magnetron sputtering was measured by 4-probe method, and it was found that the resistance of ITO-Ag-ITO (measured from top) reduces to only 1  $\Omega$  from initial ITO resistance of nearly 70  $\Omega$ . The low resistance is due to the immersion of Ag layer between the ITO layers. It should be noted that, owing to light transmittance reduction with the increase of Ag coating thickness, it is important to carefully adjust Ag thickness, if ITO layers are to be used for optical purposes.

#### ИССЛЕДОВАНИЕ ПОВЕРХОСТНЫХ, ЭЛЕКТРИЧЕСКИХ И ОПТИЧЕСКИХ ХАРАКТЕРИСТИК ИТО-АГ-ИТО-ПОКРЫТИЙ НА СТЕКЛЕ

*Needet Aslan, Tuba Şen, Turgay Çoruhlu, Kenan Şentürk, Sinan Keskin, Sedat Şeker, Andrey Dobrovolskiy*

Целью работы было изучение оптических и электрических характеристик толстых ИТО-АГ-ИТО многослойных покрытий на стекле. ИТО-АГ-ИТО-покрытия с толщиной ИТО-слоев 110, 185 нм и промежуточным слоем Аг толщиной 40 нм были изготовлены с помощью магнетронного напыления. Оптические, электрические и атомные характеристики были исследованы с помощью сканирующего электронного микроскопа, атомного силового микроскопа, рентгеновского дифракционного анализа и оптической спектроскопии.

#### ДОСЛІДЖЕННЯ ПОВЕРХНЕВИХ, ЕЛЕКТРИЧНИХ ТА ОПТИЧНИХ ХАРАКТЕРИСТИК ИТО- АГ -ИТО-ПОКРИТТІВ НА СКЛІ

*Needet Aslan, Tuba Şen, Turgay Çoruhlu, Kenan Şentürk, Sinan Keskin, Sedat Şeker, Andrey Dobrovolskiy*

Метою роботи було вивчення оптичних та електричних характеристик товстих ИТО-АГ-ИТО багатослойних покриттів на склі. ИТО-АГ-ИТО-покриття з товщиною ИТО-шарів 110 і 185 нм та проміжним шаром Аг товщиною 40 нм було виготовлено за допомогою магнетронного напылення. Оптичні, електричні та атомні характеристики такого покриття були досліджені із застосуванням скануючого електронного мікроскопа, атомного силового мікроскопа, рентгенівського дифракційного аналізу та оптичної спектроскопії.

#### CONCLUSIONS

The optical, electrical and atomic properties of multilayer ITO-Ag-ITO coating were examined by SEM, AFM and XRD analysis. It was measured that the average cross section diameters of these clusters increased from 200 to 400 nm after 5 and 25 min of coating. The film thickness of the first ITO layer (21 min coating) in ITO-Ag-ITO coating was measured to be 110 nm and the Ag and final ITO layer thicknesses were measured to be 40 nm and 185 nm respectively. It was found that the sheet resistance of ITO-Ag-ITO (measured from top) reduces to only 1  $\Omega$  from initial ITO resistance of nearly 70  $\Omega$  ohms. The low sheet resistance is due to the immersion of Ag layer between the ITO layers.

#### ACKNOWLEDGEMENTS

This work was partially supported by Yeditepe University, İstanbul-Turkey and by joint TÜBİTAK (The Scientific and Technological Research Council of Turkey) and National Academy of Sciences of Ukraine (NASU) project number 110T578.

#### REFERENCES

1. K.H. Choia, J.Y. Kima, Y.S. Leeb, H.J. Kima. ITO/Ag/ITO multilayer films for the application of a very low resistance transparent electrode // *Thin Solid Films*. 1999, v. 341, p. 152-155.
2. C. Guillen, J. Herrero. ITO/metal/ITO multilayer structures based on Ag and Cu metal films for high-performance transparent electrodes// *Solar Energy Materials & Solar Cells*. 2008, v. 92, p. 938-941.
3. C. Guillen, J. Herrero. Transparent conductive ITO/Ag/ITO multilayer electrodes deposited by sputtering at room temperature// *Optics Communications*. 2009, v. 282, p. 574-578.
4. A. Klöppel, W. Kriegseis, B.K. Meyera, et al. Dependence of the electrical and optical behaviour of ITO-silver-ITO multilayers on the silver properties// *Thin Solid Films*. 2000, v. 365, № 1, p. 139-146.

Article received 10.11.2014



## Antibacterial Surface Modification for Medical Purposes by Magnetron Sputtering and Plasma Torch Systems

Necdet Aslan<sup>1</sup>, May Korachi<sup>2</sup>, Kenan Senturk<sup>3\*</sup>, Turgay Coruhlu<sup>1,4</sup>, Tuba Sen<sup>1</sup>, Sedat Şeker<sup>5</sup>, İpek Vartürk<sup>2</sup>,

<sup>1</sup> Physics Department, Yeditepe University, Istanbul 34755, Turkey

<sup>2</sup> Genetics and Bioengineering Department, Yeditepe University, Istanbul 34755, Turkey

<sup>3</sup> Energy Systems Engineering Department, Beykent University, Istanbul 34396, Turkey

<sup>4</sup> Textile Technologies Programme, Beykent University, Istanbul 34500, Turkey

<sup>5</sup> Materials Science and Engineering, Gebze Institute of Technology, Kocaeli 41400, Turkey

**Abstract**— The aim of this study is to modify the surfaces of different materials by using two different methods which are magnetron sputtering coating technique and atmospheric plasma torch. The antibacterial properties after magnetron sputtering deposition with Copper and Silver thin films of textiles against *Staphylococcus aureus* and *Escherichia coli* bacteria were investigated by using parallel streak method. Inactivation of *Candida albicans* fungi on denture acrylic discs after atmospheric plasma torch application was also studied. The electron microscope images, antimicrobial properties and wettability properties of textiles were also investigated after modification of surfaces.

The need for new and environment friendly products has attracted and affected the studies of researchers and scientists. The potential health risks due to some bacteria and fungi are increasing concerns in public [1]. Since they are able to cause disease and change the mechanical and hydrophobic properties of materials such as textiles, the development of surface activation and thin film deposition techniques are becoming promising methods for eliminating the bacterial contaminations. Magnetron sputtering system which was used in this study includes a rotary and turbo pumps for obtaining low pressure in the vacuum chamber. The system utilizes a DC power supply and carrier Argon gas. The targets of Silver (Ag), Copper (Cu) and Titanium (Ti) at 99.99% purity, 50.8 mm diameter, 4 mm thickness were used in this work. They were placed on the magnetron head (Figure-1) below the textile substrate and coated at  $10^{-2}$  torr. Argon (Ar) gas was introduced and the coating was done.

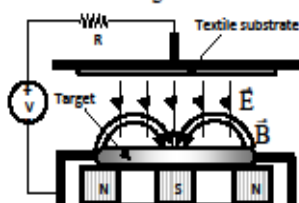


Figure-1: The magnetron head. E is electric B is magnetic field.

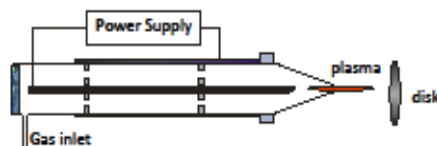


Figure-2: The torch system with a high voltage power supply.

The results showed that this environmentally clean coating technique can be used for inactivation of micro-organism on textile surfaces against *Staphylococcus aureus* and *Escherichia coli* bacteria. It was shown that instead of well known Ag coating, one can also use Cu and Ti coatings for antimicrobial property.

Unlike commercially used coating deposition methods, there are also many different types of cold (nonthermal) atmospheric pressure plasmas used for bacterial inactivation [3,4]. One of the methods include the atmospheric plasma

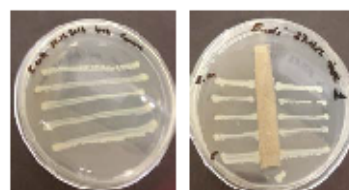


Figure-3: The control and coated / activated samples .

torch surface activation (no coating) operating in atmospheric conditions, see Figure-2. As it is well known, 40% of the total human population and 75% of people with dentures suffer from the oral cavities colonized with *Candida albicans* forming biofilms [5]. These biofilms are also resistant to antimicrobial agents [6] and the increase in antifungal resistance results in a decrease in the efficacy of conventional therapies, longer treatment time and higher costs. In this study, the acrylic disks were activated (not coated) by plasma torch and magnetron plasma for 5 and 10 minutes by incorporating Argon gas into the torch tube and magnetron system driven by a high frequency high voltage power supply. The torch/plasma activated and non-activated denture acrylic disks were transferred into the *Candida albicans* solutions which were adjusted to  $10^8$ cfu/ml, incubated at 37°C for 24h and 48h. The parallel strike procedures were followed for checking the colony formation of *Candida albicans* on magnetron coated textiles as well as torch and magnetron plasma activated acrylic disks. It was observed that there were no growth after 24h incubation as well as 48h incubation. No colonies were observed on discs that were activated (for 5 and 10 minutes) by atmospheric plasma torch as well as magnetron plasma. It was observed that nearly 2 min of activation is required for totally eliminating colonies on surfaces, see Figure.3..

The encouraging results presented here show that utilization of plasma technology in medical area is very promising.

\*Corresponding author: ksanturk99@gmail.com

- [1] R. Dasjardi *et al.*, Colloids and Surfaces B: Biointerfaces 79, 1,(2010)
- [2] O. Baghriche *et al.*, Surface and Coatings Technology, 206, 8–9, (2012)
- [3] C. Hoffmann *et al.*, Medical Gas Research, 3 (2013)
- [4] V. Arora *et al.*, Dentistry, 4 (2014)
- [5] I. Kobayashi *et al.*, New Journal of Physics, 12 (2010)
- [6] T. Maisch *et al.*, Applied and Environmental Microbiology, 78 (2012)



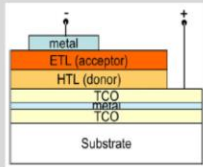
# Fabrication and characterization of magnetron sputtered TCO-metal-TCO multilayers

T. Çoruhlu<sup>1,2,3</sup>, N. Aslan<sup>1</sup>, T. Şen<sup>1</sup>, G. Gürsoy<sup>1</sup>, K. Şentürk<sup>2</sup>, N. Barnhard<sup>3</sup>, P. Pokrowsky<sup>3</sup>  
<sup>1</sup>Department of Physics, Yeditepe University, İstanbul, Turkey e-mail: tcoruhlu@gmail.com  
<sup>2</sup>Department of Energy Systems Engineering, Beykent University, İstanbul, Turkey  
<sup>3</sup>Department of MIST, University of Applied Sciences, Zweibrücken, Germany

## Motivation

### Transparent conductive oxides (TCO)

- low electrical resistivity
  - high optical transmittance
- ### Indium Tin Oxide (ITO)
- high luminous transmittance (>80%),
  - high infrared reflectance,
  - good electrical conductivity (~0.0001 Ω.cm),
  - excellent substrate adherence,
  - hardness, and chemical inertness.



### ITO-metal-ITO (IMI) Multilayer Structures

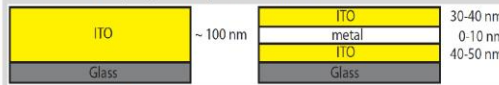


Figure 1: Single ITO layer (left), IMI multilayer (right) and solar cell (above)

- further improvement of conductivity
- ITO-Ag-ITO (IAI), ITO-Cu-ITO (ICI), and ITO-Ti-ITO (ITI) multilayers

## Method and Materials

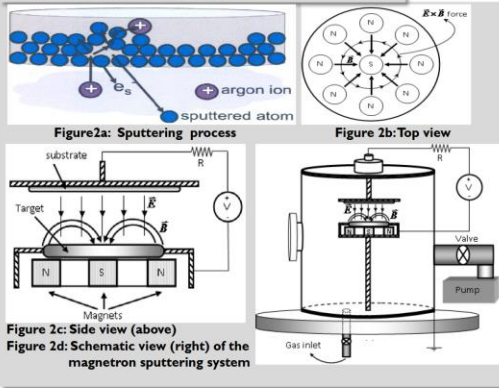


Figure 2c: Side view (above)  
 Figure 2d: Schematic view (right) of the magnetron sputtering system

## Scanning Electron Microscopy

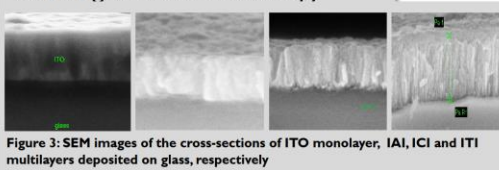


Figure 3: SEM images of the cross-sections of ITO monolayer, IAI, ICI and ITI multilayers deposited on glass, respectively

## Energy-Dispersive X-Ray Spectroscopy

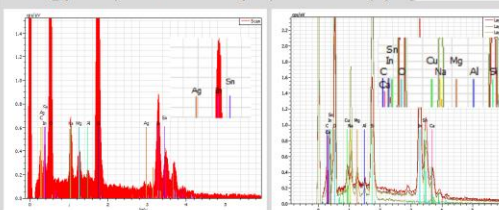


Figure 4: EDX analysis of IAI (left) and ICI (right) multilayer structures

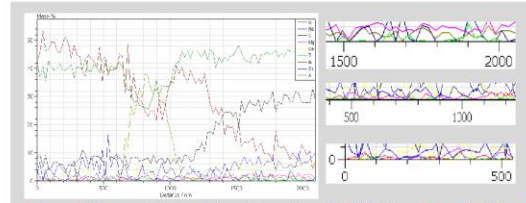


Figure 5: EDX analysis (mass % vs distance [nm]) of ITI trilayer (Green for Ti)

## Atomic Force Microscopy

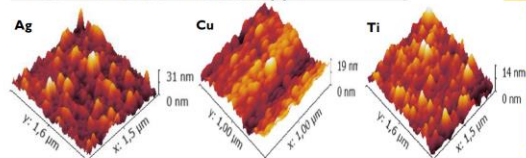


Figure 6: AFM images of intermediate layer of IAI, ICI and ITI trilayers

## Optical Characterization

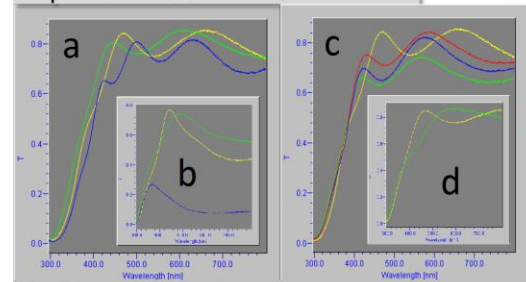


Figure 7: Transmission spectra of (a) ITO monolayers with different thickness (100 nm-330 nm-540 nm); (b) IAI trilayers with increasing amount of silver (10-20s-3m); (c) ITO monolayer (300 nm) and ITI trilayers with increasing amount of titanium (1m-2m-3m); (d) ICI trilayers with increasing amount of copper (10-20s and m refer to the coating time in terms of second and minute).

## Electrical Characterization

Surface resistances of single ITO layer and ITO-Ag-ITO deposited on glass were measured by 4-probe method.

$$\sigma = \frac{1}{\rho} \quad \frac{\rho}{d} = R_s = \frac{U}{I} \cdot \frac{\pi}{\ln 2} \quad \frac{\sigma_{IAI}}{\sigma_{ITO}} \approx 10$$

where d is the thickness of the film.

## Conclusion

The structural and electrical characteristics of ITO monolayer and IMI trilayer deposited on glass by DC magnetron sputtering are examined by using stylus profilometry, spectroscopic ellipsometry, SEM-EDX, AFM and 4-point probe. The islands growth of thin film formation or diffusion into ITO layer could cause the difficulty in measuring the metal layer thickness. We have shown that IMI sandwich structures are more conductive than single ITO layers without losing transparent property (around 80%).

## Reference

- Guillen and Herrero, Thin Solid Films 420 (2011) 1-17.
- Chapman, Glow Discharge Processes, Wiley, 1980.

Partial support from Scientific and Technological Research Council of Turkey (TÜBİTAK) under grant 110T578 is acknowledged. The characterization studies were conducted at the microsystems department of UASK.



Informatik und Mikrosystemtechnik  
 Zweibrücken



Figure A.8. Poster